54

Bulletin 37
Part 4
(of 7 Parts)

THE SHOCK AND VIBRATION BULLETIN

JANUARY 1968

A Publication of
THE SHOCK AND VIBRATION
INFORMATION CENTER
Naval Research Laboratory, Washington, D.C.

Office of
The Director of Defense
Research and Engineering

222

BLANK PAGES
IN THIS
DOCUMENT
WERE NOT
FILMED

SYMPOSIUM MANAGEMENT

THE SHOCK AND VIBRATION INFORMATION CENTER

William W. Mutch, Director
Henry C. Pusey, Coordinator
Rudolph H. Volin, Coordinator
Katherine G. Jahnel, Administrative Secretary

37th Program Committee

David Askin, U.S. Army Frankford Arsenal
Jerry Sullivan, Naval Ship Systems Command Hdq.
Robert F. Wilkus, Systems Engineering Group, W-PAFB
Dennis J. Martin, NASA Langley Research Center

Navy Liaison

Naval Training Device Center

William Powell
Allan Collier

Bulletin Production

Graphic Arts Branch, Technical Information Division,
Naval Research Laboratory

Bulletin 37
Part 4
(of 7 Parts)

THE SHOCK AND VIBRATION BULLETIN

JANUARY 1968

A Publication of
THE SHOCK AND VIBRATION
INFORMATION CENTER
Naval Research Laboratory, Washington, D.C.

The 37th Symposium on Shock and Vibration was held in Orlando, Florida, on 24-26 October 1967. The U.S. Navy was host.

Office of
The Director of Defense
Research and Engineering

CONTENTS

PART 4

Shock Analysis and Simulation

Air Blast and Ground Shock

PAPERS APPEARING IN PART 1
Part 1 - Classified
(Titles Unclassified)

*This paper appears in Shock and Vibration Bulletin 37, Supplement.

PAPERS APPEARING IN PART 2

Instrumentation and Analysis

PAPERS APPEARING IN PART 3

Vibration Testing

Test Facilities

PAPERS APPEARING IN PART 5

Large Vibro-Acoustic Test Facilities

*This paper appears in Shock and Vibration Bulletin 37, Supplement.

PAPERS APPEARING IN PART 6

Helicopter Environments

*This paper appears in Shock and Vibration Bulletin 37, Supplement.

PAPERS APPEARING IN PART 7

Environmental Data

*This paper appears in Shock and Vibration Bulletin 37, Supplement.

SHOCK ANALYSIS AND SIMULATION

MEASUREMENT AND ANALYSIS OF SPACECRAFT SEPARATION TRANSIENT RESPONSE FOR MARINER-TYPE SPACECRAFT*

Phillip Barnett
Jet Propulsion Laboratory
Pasadena, California

The Mariner spacecraft separation transient event and the efforts of the Jet Propulsion Laboratory to design ground tests for this event for both proof test model and flight spacecraft are described. A test program is described for measuring and evaluating the structural response of the spacecraft for the separation transient event is presented.

Measured spacecraft acceleration transient-response data in the form of time histories, shock spectra, and Fourier transforms are presented for a series of ground tests of pyrotechnically initiated spacecraft V-band separation events. Conclusions are drawn pertaining to the relative magnitude of the spacecraft transient-response parameters for the range of V-band tensions used during the test program and to the feasibility of generating proof test model and flight spacecraft ground tests for this event. Instrumentation, data acquisition, and data handling techniques are briefly discussed.

INTRODUCTION

A significant shock transient is experienced by the Mariner spacecraft (Fig. 1) as a result of spacecraft separation. Prior to separation, the spacecraft is secured to an adaptor atop the booster by means of a tensioned V-band that secures the eight feet of the spacecraft to eight mating surfaces on the adaptor. To separate the spacecraft from the adaptor, two pyrotechnic release devices spaced 180 deg apart around the V-band are fired simultaneously, suddenly releasing the 2500-lb V-band tension, and preloaded springs in the adaptor separate the spacecraft from the booster. This action, of pyrotechnic firing and the sudden release of the V-band tension resulting in the rapid release of stored energy in the structure, represents a significant shock transient for the spacecraft structure and the electronic assemblies mounted throughout the vehicle. For a transient environment as significant as this (or for that matter any significant environment), ground tests to reproduce the effects of this environment on both proof test models (PTM) and flight spacecraft are necessary to demonstrate spacecraft design compatibility and flight worthiness, respectively. This requires a method of controlling the transient-response parameters (which would be a measure of the test severity) throughout the spacecraft. Then test levels and test margins for PTM and flight spacecraft consistent with the overall environmental test philosophy and methodology at the Jet Propulsion Laboratory could be obtained: PTM test levels would be 1.5 times flight test levels, which in turn would be obtained from the 95th percentile of measured flight data.

To determine the feasibility of such a ground test sequence, a test program was conducted by the Jet Propulsion Laboratory to evaluate the spacecraft transient response for various V-band tensions and pyrotechnic configurations using an instrumented structural test model (STM) of the Mariner Venus 67 spacecraft. The objectives of this program were to:

1. Empirically determine if a relationship could be derived between the measured

*This research was carried out under Contract NAS 7-100 from the National Aeronautics and Space Administration.

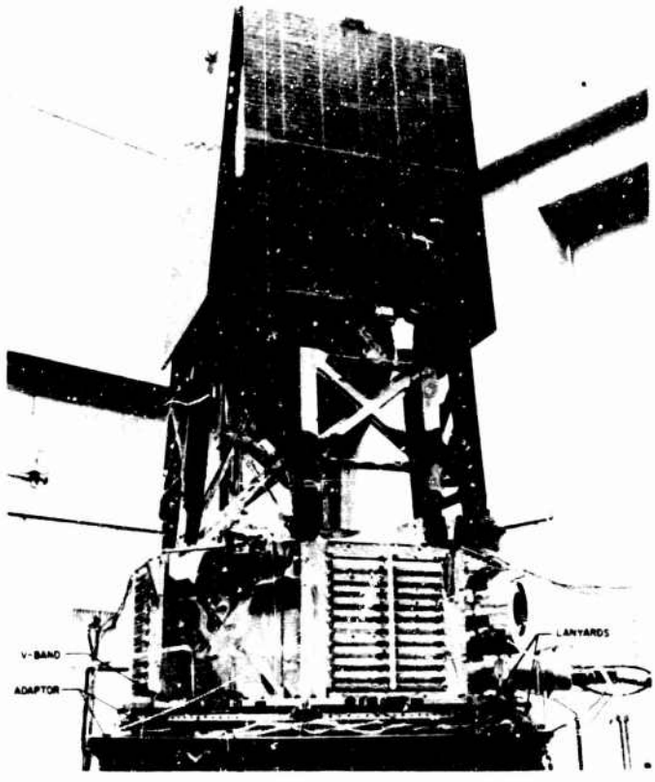

Fig. 1. Mariner Venus 67 spacecraft

transient response of the structure (acceleration vs time, shock spectra, or Fourier transform magnitude) and the initially applied V-band tension;

2. Determine the effect, if any, of the size of the pyrotechnic charge in the release mechanism of the V-band on the transient response of the structure;

3. Enhance the general knowledge and state of the art in the areas of instrumentation, data acquisition, and data handling and analysis for pyrotechnic shock testing to be better able to cope with the unique problems of pyrotechnic shock phenomena.

TEST DESCRIPTION

The test vehicle for this program was a Mariner structural test model, shown in Fig. 2. The solar panels and omniantenna were omitted since it was felt that the absence of these assemblies would not affect the high-frequency structural response. The STM was structurally complete with dummy assemblies in the bays, wiring harnesses, midcourse motor, and high-gain antenna.

All testing was performed with the Mariner STM atop an adaptor, which was similar to the adaptor used to secure the spacecraft atop the Agena booster. The spacecraft was secured to this adaptor with a V-band fabricated of 7075 aluminum. This V-band secured the eight feet of the spacecraft to eight mating surfaces on the adaptor. The tension in each of the eight individual segments of the V-band was continuously adjustable and measurable (with 8 strain-gage bridge circuits, one in each segment of the V-band), providing uniform load distribution at each of the eight mounting feet. The transient shock was generated by tensioning the V-band to the prescribed value and rapidly releasing this tension by means of the two pyrotechnic devices on the V-band positioned 180 deg apart at bays II and VI (see Fig. 3).

There were nine V-band releases during this test program using three different V-band

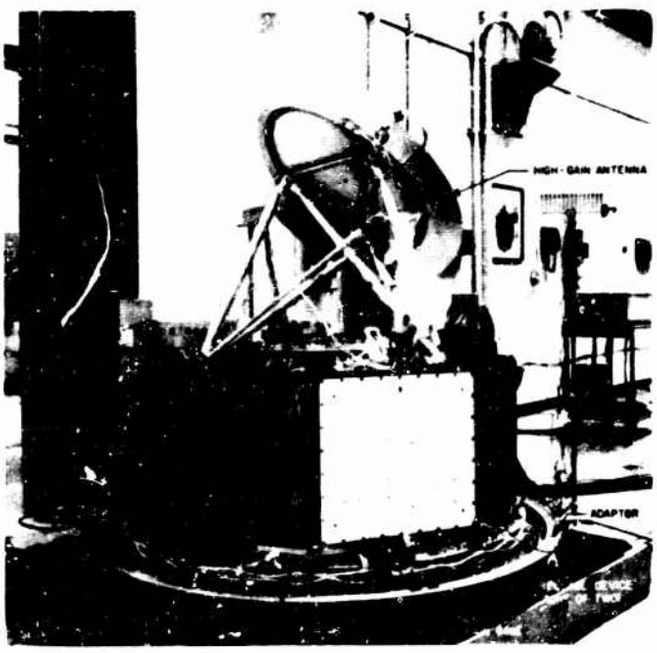

Fig. 2. Mariner Venus 67 structural test model: overall view of test setup

TABLE 1
V-Band Separation Test Sequence

Run	V-Band Tension (lb)	Pyrotechnic Configuration
1	1900	2 live pyros per release device
2	1900	2 live pyros per release device
3	2200	2 live pyros per release device
4	2200	2 live pyros per release device
5[a]	2500	2 live pyros per release device
6[a]	2500	2 live pyros per release device
7	2500	1 live pyro per release device
8	2500	1 live pyro per release device
9	2500	1 release device inert and 2 live pyros in the other

[a] Flight configuration

tensions and various pyrotechnic configurations as shown in Table 1. The range of V-band tensions was 1900-2500 lb. The lower limit is the minimum load that can be applied to the release device and still be assured of separation. The upper limit was governed by spacecraft structural and V-band limitations.

Tensioning operations proceeded as follows:

1. The eight segments of the V-band and release devices were assembled, loosely placed around the spacecraft, and secured.
2. Tension in each of the segments was increased gradually to approximately 500 lb.
3. At a tension of 500 lb, a rubber protective covering was placed over the V-band and the lanyards connected from the adaptor to the V-band. These lanyards pull the V-band down into the adaptor after separation and prevent the V-band from flying off uncontrolled.
4. The V-band tension was increased in 200-lb increments to the prescribed tension. At each 200-lb increment, all strain gages on the V-band and the structure were recorded.
5. After the desired tension was obtained, the rubber protective device was removed and the live pyros installed into the release device and wired.
6. The room was cleared of all personnel and the pyrotechnics fired by a remote switch in an adjacent room.

INSTRUMENTATION

To record and analyze the transient response, the structure and V-band were instrumented with accelerometers and strain gages. The spacecraft structure was instrumented with triaxial accelerometers and strain gages. The accelerometers were cemented onto structural webs of the upper and lower rings of the spacecraft (Fig. 3). Three strain-gage pads were

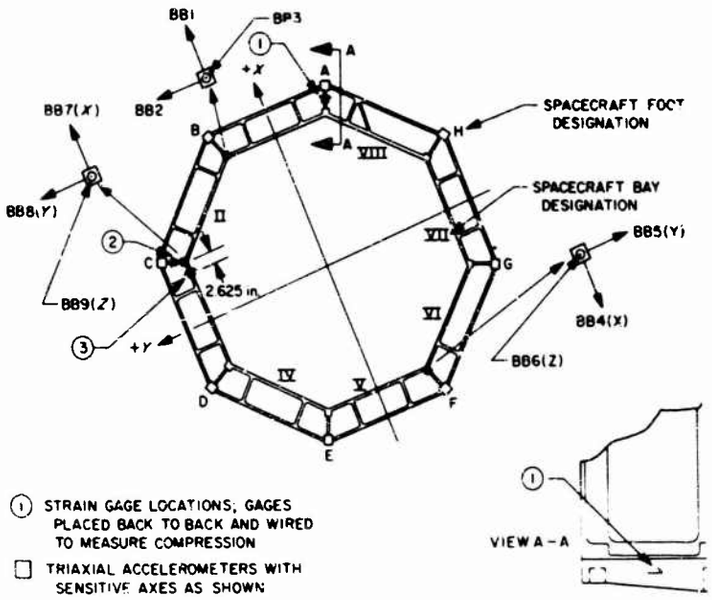

Fig. 3. Spacecraft instrumentation lower ring: bottom view

located on the lower ring of the structure to record the load taken by the structure during tensioning operations and also to record the stress release during the V-band separation. There were gages located on the radial webs at foot A and foot C (Fig. 3). The third gage was located on the inner channel between foot C and foot D (Fig. 3) at bay III. These gages were wired to cancel all bending loads and to sense tension and compression only. In addition, they were temperature compensated.

The V-band instrumentation (Fig. 4) consisted of 10 strain gages. There was one 1/2-in. gage in each of the eight V-band segments. These gages were used to measure and record V-band tension during tensioning operations prior to the V-band release. Two additional 1/8-in. gages were located as shown (Fig. 4), in the bay II segment (with one of the release devices). Data from these 1/8-in. gages, along with the existing gage in bay II, were recorded during the release to measure V-band response. These gages were also wired to cancel all bending loads and were temperature compensated.

The accelerometer data were limited by the natural frequency of the accelerometers used (28 kHz). Therefore, the accelerometer data presented here are considered accurate up to 7.0 kHz only.

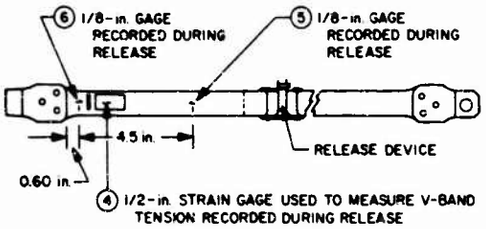

Fig. 4. V-band instrumentation: bay II segment

DATA HANDLING

Data Acquisition

All strain-gage data (10 V-band gages and 3 structure gages) were recorded on digital readout and chart paper during the V-band tensioning operation. Prior to testing, the V-bands were pulled in a tensile-testing machine and the strain gages were calibrated in pounds. The structure gage calibrations were derived from the known gage factors and the modulus of elasticity of the magnesium structure. During the V-band release, the accelerometer and six strain gage outputs were recorded on FM magnetic tape with frequency response flat to 20 kHz.

Data Reduction and Analysis

The transient accelerometer data were reduced digitally to plots of time history, shock spectra (primary and residual), and energy-density spectra. The shock spectra and energy-density spectra were derived from the tape-recorded signal using JPL programs 5628 [1] and 5695, respectively. Phase data were obtained for the Fourier transform of the transient pulses, but are not presented here. The energy-density spectrum is the square of the magnitude of the Fourier transform of the response pulse plotted against frequency. Hence, if the response pulse is expressed as $g(t)$, then the magnitude of the Fourier transform of this response can be called $|G(f)|$ and the energy-density spectra may be expressed as $|G(f)|^2$. The area under $|G(f)|^2$ vs frequency curve is

$$\int_{-\infty}^{\infty} |G(f)|^2 df = \int_{-\infty}^{\infty} g(t)^2 dt$$

and is a measure of the "total energy" of the pulse.

The shock-spectra data presented here represent the peak response of a single-degree-of-freedom oscillator (Fig. 5) to the shock transient. The peak response of the oscillator is presented as a function of the natural frequency of the oscillator over the frequency range of interest. There are two shock-spectra curves associated with each transient: the primary and the residual. The primary spectrum represents the peak response of the single-degree-of-freedom oscillator during the time the transient exists. The residual spectrum represents the peak response of the oscillator after the pulse has passed. The analysis can be performed for any chosen value of oscillator damping; the damping ratio used in this analysis was 0.025 (Q = 20). Figure 5 is a simplified single-degree-of-freedom oscillator model of the shock-spectra analysis process. All data presented here are primary shock-spectra data.

RESULTS

During each of the tensioning operations previously described, the stress response in several structural members of the spacecraft lower ring and in each of the eight segments of the V-band was recorded. Figure 6 is a presentation of the scatter of the measured tension around the eight V-band segments prior to the pyrotechnic release. Except for run 5, all tensions fall within ±2 percent of the tension desired.

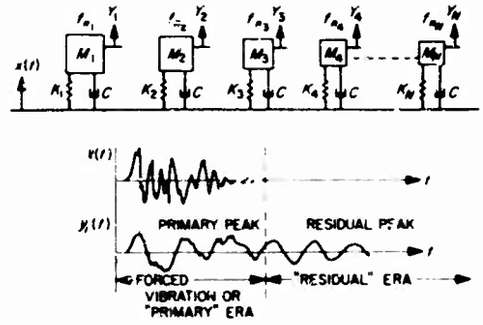

Fig. 5. Single-degree-of-freedom oscillator model for shock-spectra representation

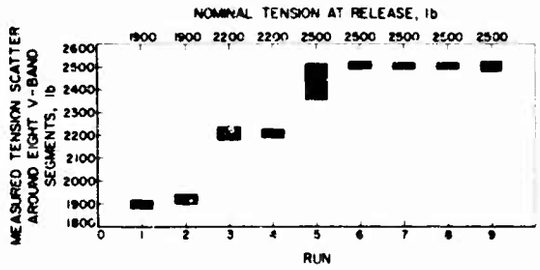

Fig. 6. Measured tension scatter around eight V-band segments vs nominal tension

Figure 7 presents a sample of the stresses recorded in the structural members for one of the five "similar" tensioning operations up to 2500 lb (flight tension). In spite of the attempt to control carefully the spacecraft loading by means of the tensioning operations, there were noticeable differences in the stresses produced in the structure for each of the runs at the same nominal V-band tension. Figure 8 presents the scatter in the spacecraft stress for the nominal value of V-band tension for the five runs to 2500 lb. The largest stress variation just prior to V-band release occurred in the gage at the radial web of foot C, showing approximately a 500-psi spread from run 6 (4550 psi) to run 8 (4050 psi), or about a 12.5 percent variation in stress at this location for these runs.

Sample strain-gage data recorded during the V-band release are shown in Fig. 9. These data indicate that:

1. There is a time lag of nominally 100 to 200 μsec between the release of the V-band tension and the subsequent "relaxation" of the structure.

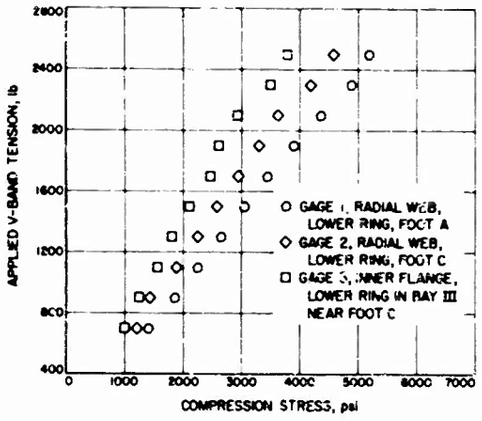

Fig. 7. Compression stress in lower ring of spacecraft versus applied V-band tension for 2500-lb maximum V-band tension

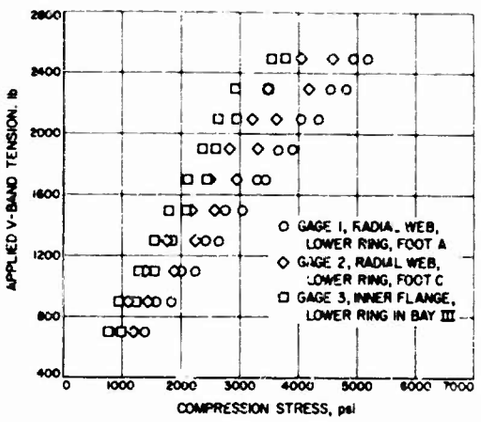

Fig. 8. Measured stress spread at spacecraft strain gages for runs 5 to 9

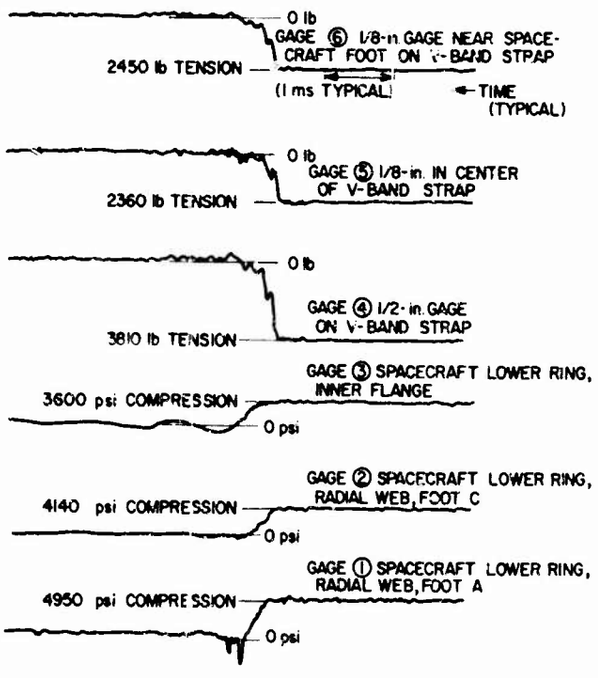

Fig. 9. Real-time strain-gage response: run 5, 2500-lb nominal V-band tension

2. During the energy release era, the slope of the stress-time response of the structure is less than the slope of the tension-time response of the V-band.

The time history of the response acceleration (samples shown in Fig. 10, a and b) resulting from the V-band releases are characterized by very complex oscillatory transients with relatively high peak g levels, jagged irregular decay rates, and a low net velocity change. Typical peak g values recorded during this test ranged from 100 to 1000 g at the bottom ring and from 40 to 125 g at the top ring. The predominant part of the pulse lasted for approximately 5 to 10 msec.

Comparison of sample response spectra at the top and bottom of the spacecraft structure for the V-band tensions (Figs. 11-13) of 1900 and 2500 lb and various pyrotechnic configurations reveal the following pertinent results:

1. The scatter in response spectra for two tests of "identical" test conditions can be expected to be at least 10 db (approximately 3:1 ratio of shock spectra) at some frequencies throughout the range of interest.

2. The variation in the shock-spectrum response between a 1900-lb release and a 2500-lb release is of the same order of magnitude as between two identical tension releases. The magnitude of these individual spectrum responses does not increase "nicely" with increasing V-band tension, and it can be stated that no empirical relationship could be found relating V-band tension and response spectra. However, the data show that a higher shock-spectrum response is more probable with the highest V-band tension than with the lowest tension.

3. The size of the pyrotechnic charge bears no measurable relationship to the magnitude of the structural response.

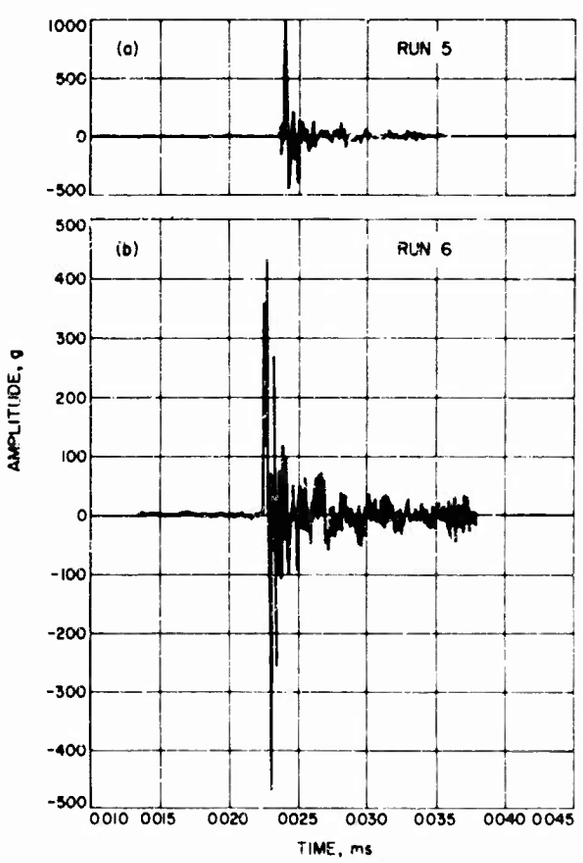

Fig. 10. Acceleration transient time history for V-band release (2500 lb): bottom of structure

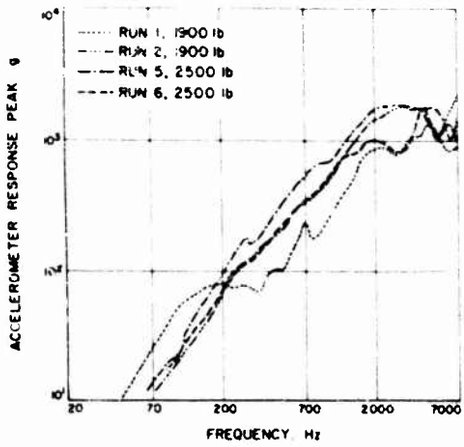

Fig. 11. Composite shock spectra for two runs of 1900-lb tension and two runs of 2500-lb tension: lower ring of spacecraft

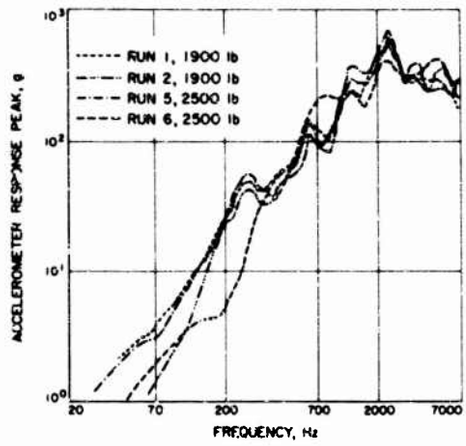

Fig. 12. Composite shock spectra for two runs of 1900-lb tension and two runs of 2500-lb tension: upper ring of spacecraft

4. The spectral response at the top of the structure (farthest from the V-band) is typically one half to one fifth of the response at the lower ring of the structure (approximately in the plane of the V-band). In addition, there appears to be no agreement between the shock-spectrum response scatter and the relative magnitudes of the compression stress recorded in the spacecraft lower ring prior to release for runs of similar tension.

Typical of the shock-spectrum responses was the "knee" in the curve at approximately

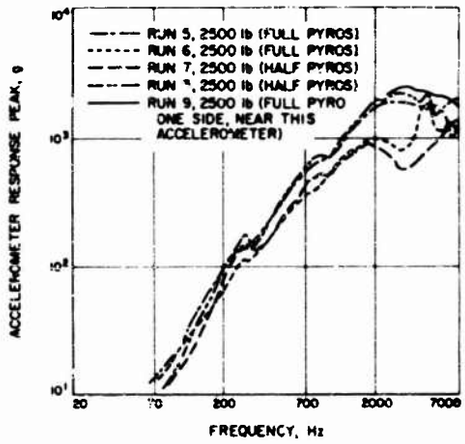

Fig. 13. Composite shock spectra for 2500-lb V-band tension, three different pyrotechnic configurations: lower ring of spacecraft

3000 to 5000 Hz, where the spectra peaked and leveled out at approximately 150 to 700 g at the top of the spacecraft and between 1000 and 5000 g at the lower ring.

All shock-spectrum data for runs of similar tension and pyrotechnic configuration were averaged independently of accelerometer location and orientation, and a composite plot of average response spectra for each test configuration was generated (Figs. 14 and 15). These curves are a gross presentation of the spacecraft spectra response as a function of V-band tension and are another indication of the lack of sensitivity of the spacecraft response to the initially applied V-band tension or pyrotechnic configuration.

Energy-density-spectrum data were also derived from the response transients in an attempt to determine if some definable trend in the response could be discerned. Samples of these data are shown in Figs. 16 and 17. As might be expected, these data reveal basically the same results as the shock-spectrum data when comparing spacecraft structural response for the 1900- and 2500-lb V-band tensions at the top and bottom of the spacecraft:

1. Similar scatter for identical events and for two separations of 1900- and 2500-lb tension;

2. No detectable relationship between pyrotechnic charge size and response transient.

However, there is another parameter associated with the Fourier transform or energy density (aside from phase) that may be useful

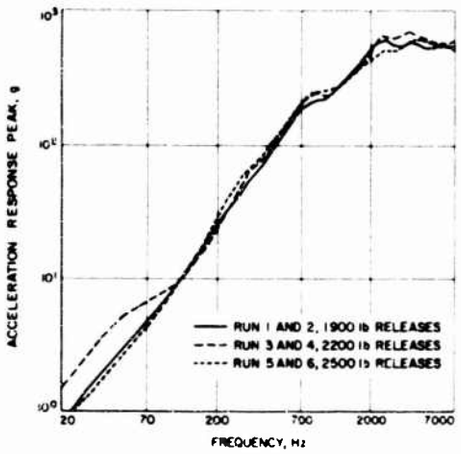

Fig. 14. Composite average shock spectra for runs of different V-band tension and similar pyrotechnic configuration (two live pyros per release device)

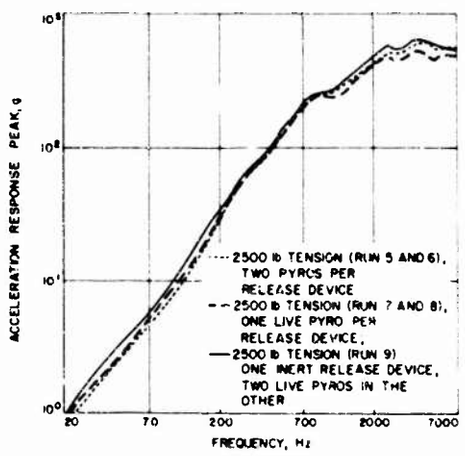

Fig. 15. Composite average shock spectra for runs of similar V-band tension and various pyrotechnic configurations

in expressing the "severity" of the response transient. This is a measure of the "total energy" as expressed by

$$\int_{-\infty}^{\infty} |G(f)|^2 df = \int_{-\infty}^{\infty} g(t)^2 dt \quad \text{area under energy density spectrum}$$

where

$g(t)$ = transient time history,

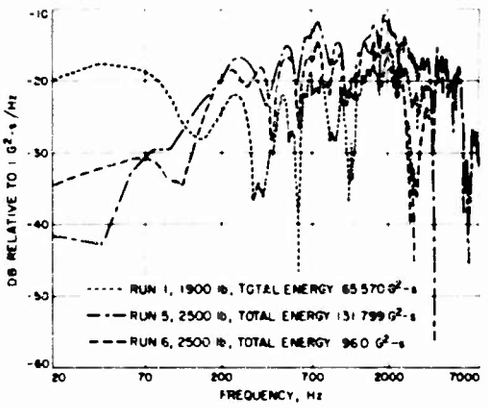

Fig. 16. Composite energy-density spectra for 1900-lb and 2500-lb releases: lower ring of spacecraft

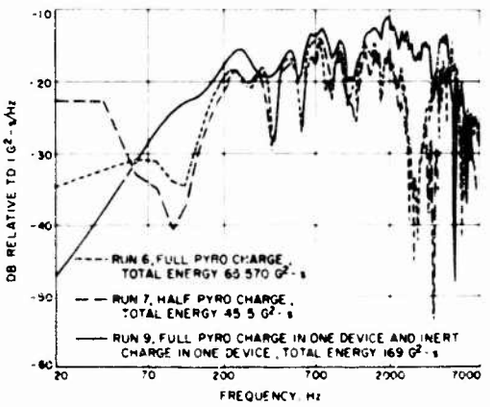

Fig. 17. Composite energy-density spectra for 2500-lb runs comparing three different pyrotechnic configurations

and

$$G(f) \quad \int_{-\infty}^{\infty} g(t)\, e^{-j2\pi ft}\, dt \quad \text{Fourier transform of } g(t)$$

It is of interest to examine and compare the areas under the energy-density spectra, derived from the response transients at the various spacecraft locations for each run, to see if a trend exists in this parameter. Table 2 presents all "total-energy" data derived from the transient response for all test configurations. As before, a scatter between data of similar runs exists, and this scatter is consistent with the energy-density data.

TABLE 2
Total Energy Recorded at Response Accelerometer Locations

Run:			1	2	3	4	5	6	7	8	9
V-Band Tension (lb):			1900	1900	2200	2200	2500	2500	2500	2500	2500
Accel. Code	Sensitive Axis	Location[a]	Total Energy (g^2-sec)								
B3	Z	Top	7.9	7.3	10.8	9.8	11.9	7.4	4.1	12.9	12.7
B1	X	Top	7.0	7.4	9.7	9.4	9.8	6.9	3.4	10.5	14.0
B2	Y		4.6	5.7	6.0	—	6.7	4.6	2.9	6.9	9.4
B3A	Z		5.9	5.6	8.6	—	12.1	7.2	3.9	10.4	12.4
B4	X	Top	2.2	3.8	4.1	—	3.2	5.9[b]	3.8	3.8	2.6
B5	Y		1.5	2.4	1.6	—	1.8	2.5[b]	1.5[b]	1.6	1.4
B6	Z		1.2	1.4	1.8	—	2.0	2.6	1.3[b]	1.7	1.4
BB1	X	Bottom	96.0	97.8	141	—	132	65.6	45.6	156	170
BB2	Y		44.2	58.4	76.3	37.1	68.5	17 3	12.9	77.3	74.7
BB3	Z		—	21.8	27.4	24.3	28.1	12.5[b]	7.2	30.0	31.8[b]
BB4	X	Bottom	64.1	87.5	—	—	—	110.3	68.2	58.1	42.5
BB5	Y		19.8	36.0	—	—	—	46.4	27.3	17.7	11.6
BB6	Z		7.2	9.6	—	—	—	12.3	8.5	6.8	5.6
BB7	X	Bottom	19.1	21.0	27.4	29.3	31.2	25.0	15.2	30.9	27.6[b]
BB8	Y		56.8	55.1	60.2	94.0	62.7	40.5	24.8	53.0	68.5
BB9	Z		6.8	6.6	10.0	15.0	9.8	9.5	6.1	9.6	12.7[b]

[a]Measurements taken at top or bottom of spacecraft structure.
[b]Data taken from shortened sample length due to V-band rebound.

Table 3 presents the "total-energy" parameters averaged for those runs of similar tension and pyrotechnic configuration. This table is particularly revealing in that the lowest tension runs never produce maximum "total-energy" responses and rarely exceed the flight tension-pyrotechnic configuration of runs 5 and 6. Also, the runs employing the half-pyro charge in the V-band release devices never result in maximum "total-energy" responses and exceed the flight configuration "total energy" at only 2 of 16 locations. Further analysis of this table reveals the apparent anomaly that the "total energies" of runs 3 and 4 (2200-lb tension) exceed those of runs 5 and 6 for more than 50 percent of the response locations.

CONCLUSIONS

1. Increasing V-band tension for this test configuration does not produce a controllable increase in the transient response as described by the parameters discussed here: shock spectra, Fourier transform, or "total energy." However, the chances of producing a greater response appear to be increased when a larger V-band tension is applied.

2. The pyrotechnic configuration (full charge or half charge in the release devices) does not appreciably alter the frequency-response characteristics of the structure. The "total-energy" parameter suggests that there may be a relationship between pyrotechnic size

TABLE 3
Total Energy Averaged for Runs of Similar Tests

Run:			1, 2	3, 4	5, 6	7, 8	9
V-Band Tension (lb):			1900	2200	2500	2500	2500
Accel. Code	Sensitive Axis	Location[a]	Full Pyro Charge			Half Charge	1 full 1 inert
			Average Total Energy (g^2-sec)				
B3	Z	Top	7.5	10.3	10.9	8.5	(12.7)
B1	X	Top	7.2	9.6	8.4	7.0	14.0
B2	Y		5.2	6.0[b]	5.2	4.9	(9.4)
B3A	Z		5.8	8.6[b]	10.9	7.2	(12.4)
B4	X	Top	3.0	4.1[b]	(4.6)[c]	3.8	2.6
B5	Y		2.0	1.6[b]	(2.2)[c]	1.6	1.4
B6	Z		1.3	1.8[b]	(2.3)	1.5[c]	1.4
BB1	X	Bottom	97.0	141.0[b]	98.8	101	(170)
BB2	Y		51.3	56.7	42.9	45.1	(75)
BB3	Z		21.8	25.8	20.3[c]	18.6	(32)[c]
BB4	X		75.8	—	(110.3)[b,c]	63	42.5
BB5	Y		27.9	—	(46.4)[b,c]	22.5	11.6
BB6	Y		8.4	—	(12.3)[b,c]	7.7	5.6
BB7	X	Bottom	20.1	(28.4)	28.1	23.1	27.6[c]
BB8	Y		56.0	77.1	51.6	38.9	(60.8)
BB9	Z		6.7	12.5	9.7	7.9	(12.7)[c]
Percentage of accelerometer locations where total energy exceeds or equals that of runs 5 and 6:			25	61.5	100	12.5	50

Note. — Data within parentheses give maximum value for all runs.

[a]Measurements taken at top or bottom of spacecraft structure.
[b]Data from only one run available.
[c]Data taken from shortened sample length due to V-band rebound.

and response, but this appears remote and requires further consideration.

In spite of the failure of this evaluation to produce a more controllable ground test for the spacecraft separation event, this type of test is considered extremely important in the environmental test program for spacecraft employing this type of separation. This test method provides an excellent simulation of the actual in-flight phenomenon experienced by the spacecraft during separation. It might be necessary of course, to repeat a ground test several times, taking advantage of the wide response variations, to achieve the desired responses; but after the initial setup each release can be accomplished in a matter of hours.

REFERENCE

1. D. C. Snyder and D. B. Wiksten, "Shock-Spectrum Analysis Program," Jet Propulsion Lab. Tech. Memo. 33-326, Mar. 1967.

DISCUSSION

Mr. Gertel (Allied Research): You do not have to apologize for an operational type of explosive test such as this. Even though the shock spectra from one condition to the next do not really repeat, it looks like an excellent type of service test to prove that something functions as it should. In connection with the shock spectra that were plotted, I noticed in at least one of the shock time histories that the peak acceleration of the complex shock motion was about 400 g. Yet at the extreme high frequency end of the shock spectrum, where one normally anticipates an asymptotic approach to the peak acceleration of the input, your spectra showed approximately 1000 g instead of the expected 400 g. Would you comment on that?

Mr. Barnett: If I understand your question correctly, you are wondering why the ratio of the shock spectrum to the peak g response is around two or a little bit more. We were a little bit surprised at that ourselves since we have data not only from this test, but from the flight spacecraft for which we did derive these same ratios. Typically, a ratio larger than three would be unusual as far as our data is concerned.

Mr. Schell (WPAFB): May I say something about this question? It is generally asymptotic when you have a simple peak, but a great deal of oscillatory motion in your input gives you resonant buildup which amplifies the spectrum above unity.

Mr. Carpenter (Radiation Inc.): In your shock spectrum analysis, were you considering residual response? What were you really looking at?

Mr. Barnett: These are primary shock spectra. All of these data were reduced digitally on a 7094 with our shock spectrum program.

Mr. Mustain (Douglas Aircraft Co.): Did you experience any failures of equipment or structure during these tests?

Mr. Barnett: We were using a test model. There were no structural failures. However, in addition to running this test, we conducted pyrotechnic tests on both of our Mariner flight spacecraft and experienced no failures.

Mr. Mustain: I don't think we have ever had any real structural failures, but there have been a few reported equipment failures. On the Saturn program we have had much higher explosive values than you had on our shock tests, yet we failed almost on equipment. Fortunately, we had a lot of isolators on our equipment which attenuated the shock beautifully. I think the best thing of all is to test the functional ordnance item with the type of test that you've done. But, if you can't do this, how would you specify the test? This is the question that people are always asking.

Mr. Barnett: I was hoping that you wouldn't ask that question.

Mr. Mustain: It is a good one.

Mr. Barnett: Well, at JPL we have answered it for ourselves and I think this is the key. You have to do the best that you can with what you have. It certainly wouldn't be feasible to mount the spacecraft on a shaker or a shock machine and try to perform a meaningful shock test to take care of this particular environment. That still doesn't mean that this environment is not considered significant.

Mr. Mustain: Suppose we had to specify a test for a vendor to test his equipment to a shock spectrum or some other type of shock input, such as a Fourier spectrum or time history. How would you best specify for that vendor?

Mr. Barnett: We specify a test that can be done uniformly by all vendors which does not by any means encompass this pyrotechnic shock event. It does give us some increased confidence that the component will survive when we get it on the spacecraft. I would like to hear a better idea, frankly.

Mr. Harvey (Goodyear Aerospace Corp): We did a similar test on our base diameter at the interface of the V-band to the heat shield. It was 5 feet in diameter and we used a stainless steel band. As a word of caution I might add that initially we had 2 or 3 strain gages on the band to check tension and later we put on eight. We found that the tension is in no way uniform around the band. This may be one reason that you could see no difference between the 1900 and the 2500 lbs. In some cases there was a variation of from 2500 lbs to 1200 lbs on the band. As a result we developed a method for the Air Force with which we tensioned the band checking all eight gages during the tensioning process. We did have a lot of trouble getting uniform tension in the bands before our first pyrotechnic test. Incidentally, our results were very similar to yours.

Mr. Barnett: We did monitor tension continuously during tensioning operations and up to the instant of pyro firing. For this configuration we detected at most a 2 percent difference in tension around the entire eight segments of the vehicle. We had one gage in each segment and three gages in that bay two segment with the release device. The tensions were fairly uniform, again, within two percent.

Mr. Harvey: That's what I was saying. We initially had about three gages on the band as you did. After we put eight gages on, we found out that our tension distribution around the band varied considerably without clapping the band into place each time.

Mr. Barnett: That is one thing that I will look into.

Mr. Burton (Martin-Marietta Corp.): With respect to the occasion when the accelerometers for two similar tests did not respond in the same manner, was time enough allowed for the accelerometer to recover? In other words, after being shocked, what was the time lag between that test and the next one?

Mr. Barnett: I couldn't tell you to the hour, but in some cases we ran the test and then shut down for the night. At no time was there ever less than 2 or 3 hours between runs.

Mr. Burton: We have done many similar tests and have found that the accelerometer was not able to recover, sometimes within a period of 24 hours. Do you have any comments in this respect?

Mr. Barnett: Immediately after the test was over, we recalibrated all accelerometers and found them to be satisfactory.

Mr. Regillo (MIT Lincoln Lab): On the plots of your acceleration-time history you showed one peak at about 1000 g and the other about 400 g. Do you recall the duration of the initial peak on each one?

Mr. Barnett: We feel the important part of the pulse is nominally 5 milliseconds. I don't recall offhand what that slope was on the rising g curve, but I could get it for you.

Mr. Regillo: Did you use triaxial accelerometers?

Mr. Barnett: No, they were single axis accelerometers mounted as closely as possible in one location.

Mr. Regillo: Do you recall the frequency response?

Mr. Barnett: Yes, they had natural frequencies of 25,000 Hz. Our tape recorders were flat to 20 kHz, and, as you might have noticed, we plotted our data up to 7000 Hz.

Mr. Parmenter (Naval Weapons Center): What was the digitizing rate that you used?

Mr. Barnett: For the shock spectra, it was 320,000 samples per second.

Mr. Painter (Lockheed California Co.): Your shock spectrum plots looked rather smooth. I would assume you used some value of damping rather than undamped spectra. Is that true?

Mr. Barnett: We need a Q of 20.

Mr. Painter: Do you have any explanation as to why things leveled off as you increased the power of the explosion? Certainly if one dropped it low enough you would think that eventually the spectra would shift and start falling.

Mr. Barnett: This is our feeling, too. If, for example, we could tension the V band to two pounds, then to four pounds, we certainly would expect to see a corresponding change in the response. However, you could see that when we applied our load, it was fairly linear. The structure was not designed for this kind of a test. If we were to design a structure to do what we would like it to do, I'm sure we would design it quite differently.

Mr. Foley (Sandia Corp): With your particular digitization rate of 320,000, how much computer time is required for your program to turn out one of these shock spectrum presentations?

Mr. Barnett: 1-1/2 minutes per spectrum.

Mr. Richardson (Consolidated Electrodynamics Corp.): How does the pyro device act to release the tension?

Mr. Barnett: It shears a disc in the release mechanism. The two pyros are screwed into their chamber. They ignite, filling the chamber with gas which pushes on a piston that shears the thin disc. There is a diaphragm in there that is supposed to contain all the combustion and not allow any of it to escape.

* * *

MECHANICAL SHOCK OF HONEYCOMB STRUCTURE FROM PYROTECHNIC SEPARATION

J. R. Olsen, J. R. West Jr., H. Himelblau
North American Rockwell Corporation
Los Angeles, California

and

C. D. Knauer, Jr., and P. E. McHorney, Jr.
Hughes Aircraft Company
El Segundo, California

Mechanical shock was measured at various locations on a half-section of the Apollo service module, a structure of mainly honeycomb construction. The shock was generated by twin strands of mild detonating fuse which simulated the separation of the service module from the spacecraft/lunar-module adapter. Shock (or response) spectra of approximately 10,000 g were measured in the vicinity of the separation line. There was not as much attenuation with distance from the separation line as that reported previously for conventional sheet-stringer construction. The structure, the test program and data acquisition performed by North American Rockwell, and the data reduction and shock spectral analysis performed by Hughes Aircraft are described.

INTRODUCTION

The Apollo spacecraft, shown in Fig. 1 in its earth orbital configuration, uses a number of ordnance devices to accomplish separation of various modules or subsystems throughout the phases of the Apollo mission. The largest of these separations is the deployment of the four panels of the spacecraft/lunar-module adapter (SLA), shown in Fig. 2; separation is performed by detonating twin strands of 7 grains per foot mild detonating fuse (MDF). For the lunar mission, this event occurs shortly after the Saturn S-IVB stage boosts the spacecraft from its earth orbit into a translunar trajectory. After separation, the command and service modules (CSM) dock with the lunar module (LM) and extract it from the spent S-IVB, as shown in Fig. 3. At the present time, the SLA deployment constitutes the largest pyrotechnic separation occurring in an aerospace vehicle in terms of the total energy expended and the total length of the separation line. The details of the separation line configuration are shown in Fig. 4.

Over the past four years, several papers have appeared in the literature which have discussed the "pyro shock" problem, reporting that very high intensity, high-frequency transients are transmitted from these ordnance devices [1-11]. Occasionally, equipment items which have successfully passed conventional shock and vibration tests have failed or malfunctioned during exposure to mechanical shock from these devices [3, 6, 9]. Because of the proximity of service module (SM) equipment to the SLA separation lines, especially the upper circumferential line (A in Fig. 4), it was decided to perform a ground test on an SM with equipment items installed to determine their possible susceptibility to the mechanical shock transmitted from the separation line. Previously reported shock measurements were made on conventional sheet-stringer structure, with the exception of those reported in Ref. [10], where there was ablative material on the structure. Since the Apollo SM is almost entirely of honeycomb construction, the decision to perform the test was reinforced by the lack of data on its shock transmission properties.

The SM structure, shown in Fig. 5, comprises six outer panels, six radial beams, a forward bulkhead, and an aft bulkhead. The overall diameter is 154 in. and the length (from forward to aft bulkheads) is 155 in. The outer panels are bonded aluminum honeycomb with 16-mil facesheets of 7178-T6 and 1-in.-thick core of 3/16-in. by 3-mil 5052 H39. (The core dimensions refer to the distance across the

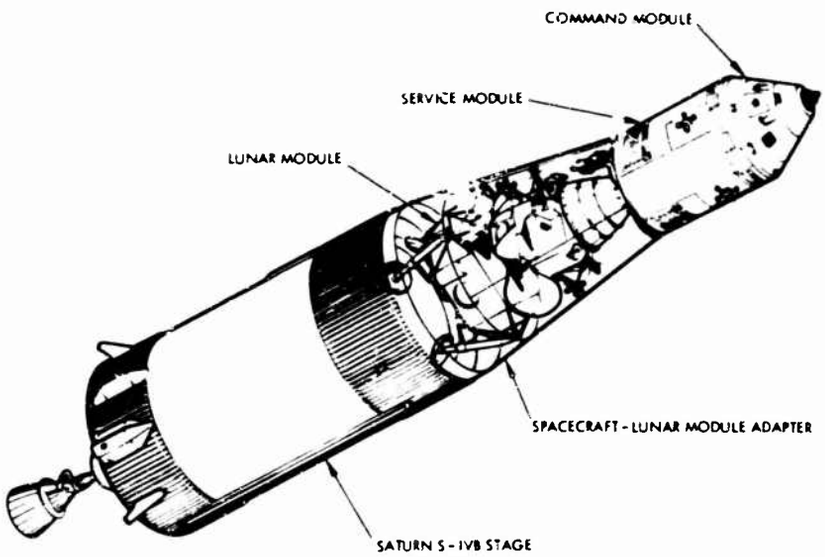

Fig. 1. Major modules of the Apollo Spacecraft shown in its earth orbital configuration with the Saturn S-IVB stage

Fig. 2. Deployment of SLA panels

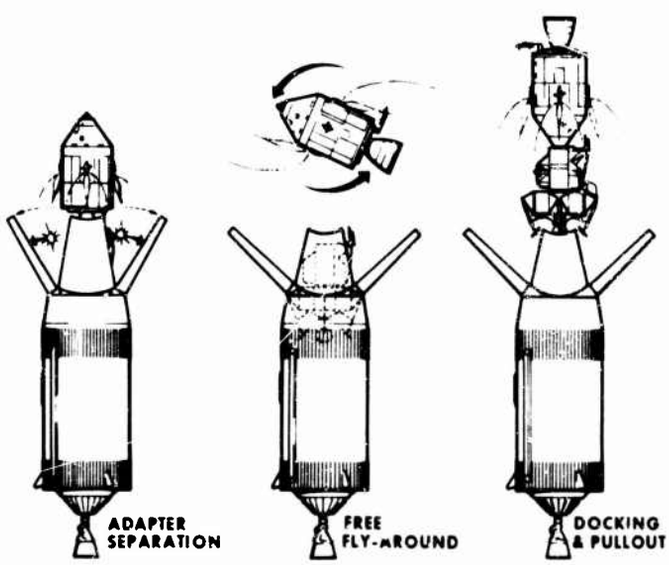

Fig. 3. Transposition of the CSM, docking with the LM, and extraction of the LM from the Saturn S-IVB stage

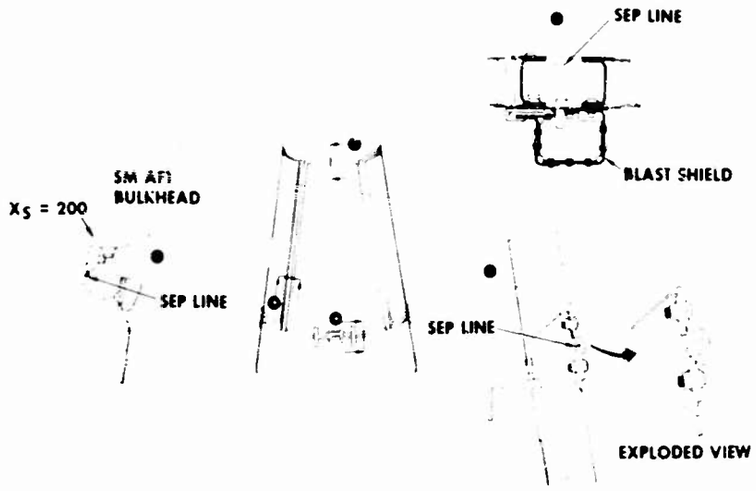

Fig. 4. Details of the separation lines of the SLA

hexagon flats and the wall thickness, respectively.) Some outer panels contain thermal radiators, using a double outer facesheet on the honeycomb. Each radial beam is 7075-T6 aluminum chem-milled to form stiffeners 2 in. deep and a web thickness of only 18 mil. The forward bulkhead comprises six segments, each of bonded aluminum honeycomb with 16-mil facesheets of 7178-T6 and 1.1-in. core of 0.25 in. by 1-mil 5052 H39. The aft bulkhead is bonded aluminum honeycomb with 63-mil facesheets of 7178-T6 and 2.88-in. core of 0.25-in. by 4-mil 5052 H39. Figure 5 shows that the SM holds many items of equipment necessary for the Apollo mission. Four cylindrical propellant tanks (two fuel and two oxidizer) are located in the largest four of six pie-shaped sectors. (The sectors are not of equal size. They are 50° + 60° + 70° + 50° + 60° + 70° = 360±.) Two spherical pressurization tanks and the combustion chamber of the SM rocket engine partially fill the "hole" in the center of the SM. Most of the remaining equipment is located in the two 50-deg sectors, some on shelves and bulkheads, and others on radial beams. The equipment items considered most susceptible to mechanical shock are located in these two sectors.

TEST PROGRAM

When CSM program management gave its approval to the shock test, no SM's were available. However, vibroacoustic testing was being performed at that time on half of an SM, which is called a 180-deg segment. Figures 6 and 7 show the segment installed in the acoustic test facility at the Los Angeles Division of North American Rockwell. The segment was supported off of the floor of the facility by resilient pads. It was estimated that the segment would adequately simulate the SM dynamic behavior if the equipment to be tested was installed at a sufficient distance from the resiliently supported edges. On this basis, and because the SM segment was available, the decision was made to use the segment for the shock test. The test was performed between phases of the vibroacoustic test program.

Rather than expose all SM equipment to the shock, it was decided to test only those items that were considered most susceptible to high-intensity, high-frequency transients. These items contained such possibly sensitive elements as relays, inertial switches, IF and RF circuits, and certain brittle materials, such as ceramics and glass. Since the major part of the SM shock was expected from the SLA upper separation line, it was decided to use a simulated upper line for the test. Figure 8 shows the details of this line, which may be compared with the details of the flight separation line shown in Fig. 4. It was estimated that the differences in the installation would produce only minor differences in the shock transmission to the SM.

DATA ACQUISITION

With the exception of the accelerometers conventional instrumentation was used for data acquisition: charge amplifiers and tape

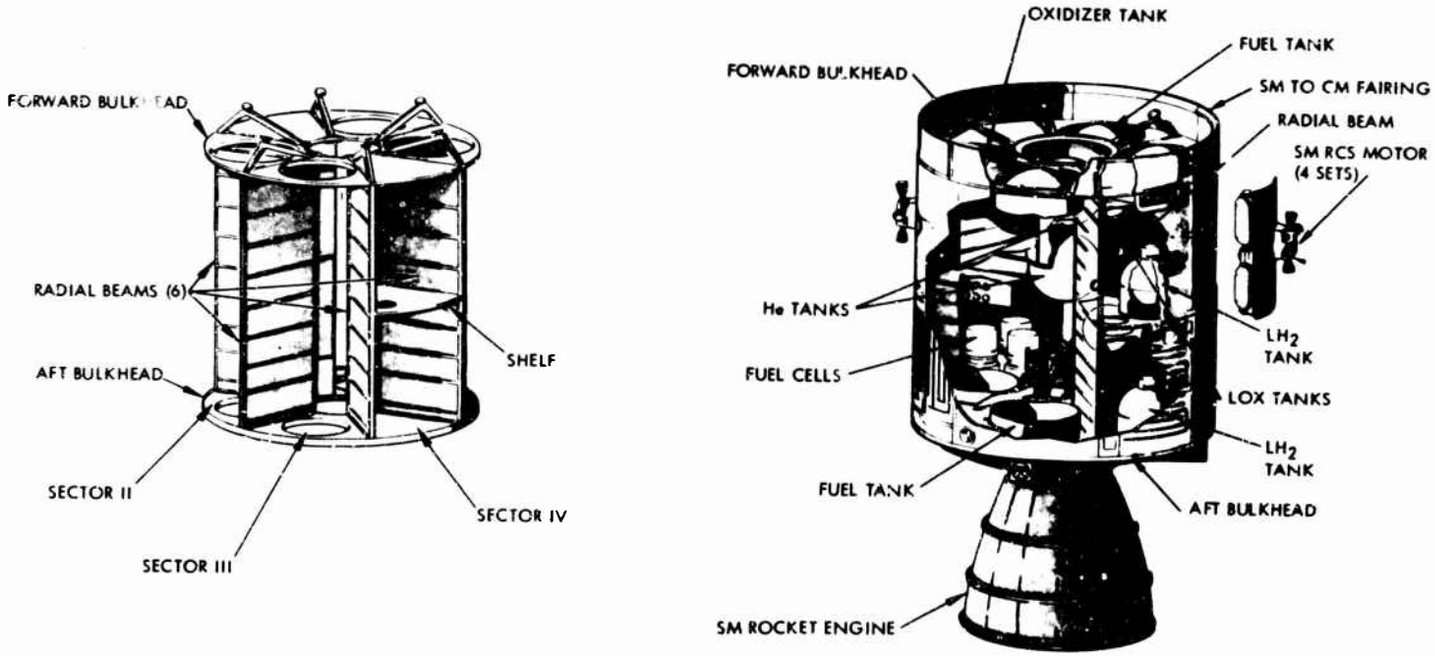

Fig. 5. Apollo SM structure and equipment

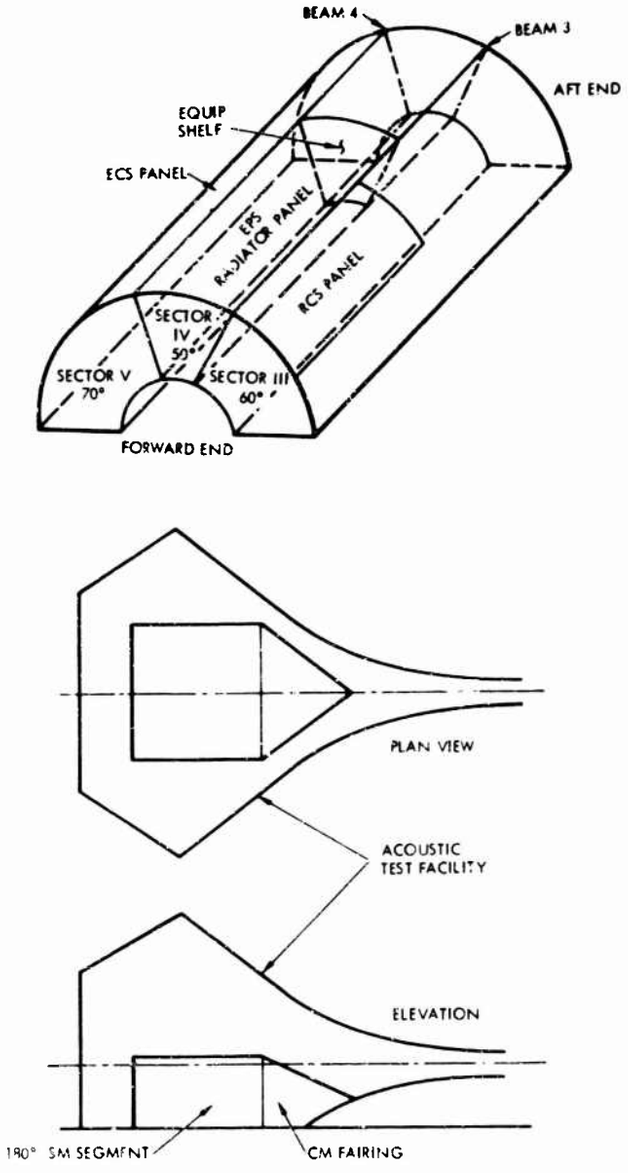

Fig. 6. Service module 180-deg segment in the acoustic test facility

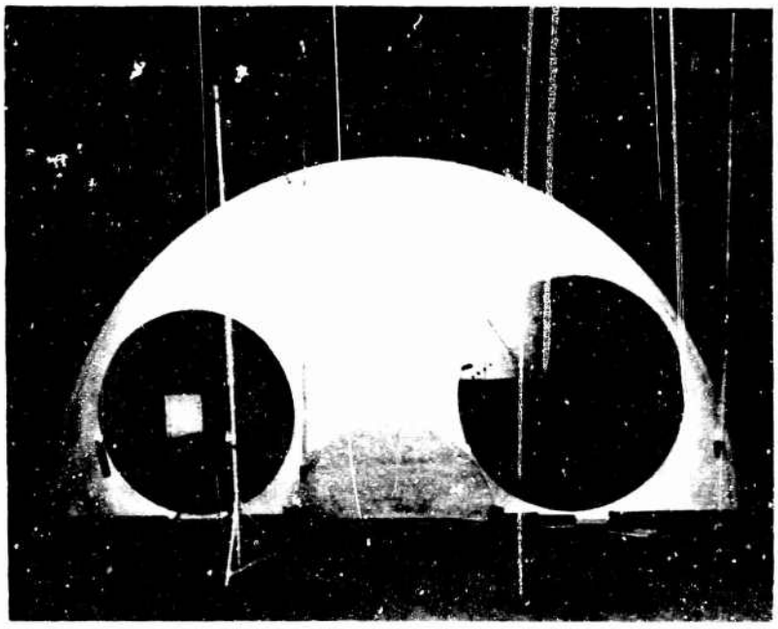

Fig. 7. Service module 180-deg segment in the acoustic test facility prior to installation of equipment

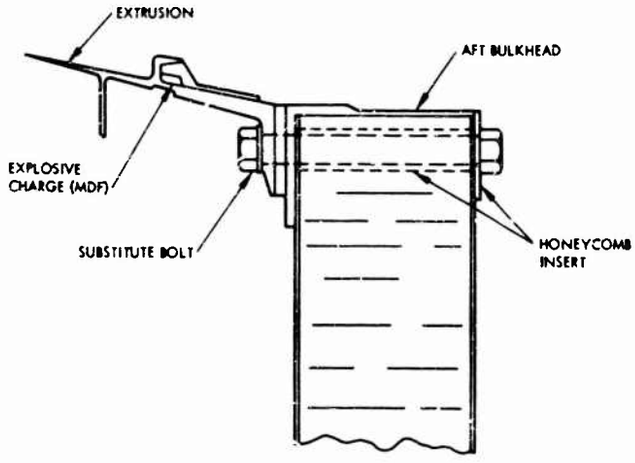

Fig. 8. Details of the simulated SLA separation line of the SM 180-deg segment

recorders (operating in the FM mode), producing a frequency range of 20 Hz to 20 kHz. Endevco model 2225 accelerometers were used, at the recommendation of McDonnell-Douglas, because of their high resonant frequency (approximately 80 kHz). Previous experience with accelerometers of lower resonant frequency showed that they had an unacceptable resonant response and zero shift under mechanical shock from pyrotechnic devices [2, 4]. (However, previous tests on a small honeycomb cylinder, using tape recording in the direct record mode to cover the frequency range of 100 Hz to 300 kHz, showed no substantial excitation above 20 kHz.) Nineteen accelerometers were attached at various locations on the segment, as shown in Figs. 9, 10, and 11. Nine of these were located adjacent to or on equipment, like those shown in Fig. 12.

DATA REDUCTION

Magnetic tape copies of the acceleration signals were transmitted from North American Rockwell to Hughes Aircraft with appropriate identification and calibration information. From these, oscillograms of the accelerometer signals were made. A few reproductions of these data are shown as Fig. 13. A tape speed of 7.5 ips was used for playback, as opposed to 60 ips for recording, to lower the apparent frequency regime of the data. The effective frequency response of the oscillograph galvanometers was thereby increased from 3 to 24 kHz. The maximum amplitudes of all 19 oscillogram traces were well below (less than half of) the calibration level, but most of these maximums were greater than one fifth of the calibration.

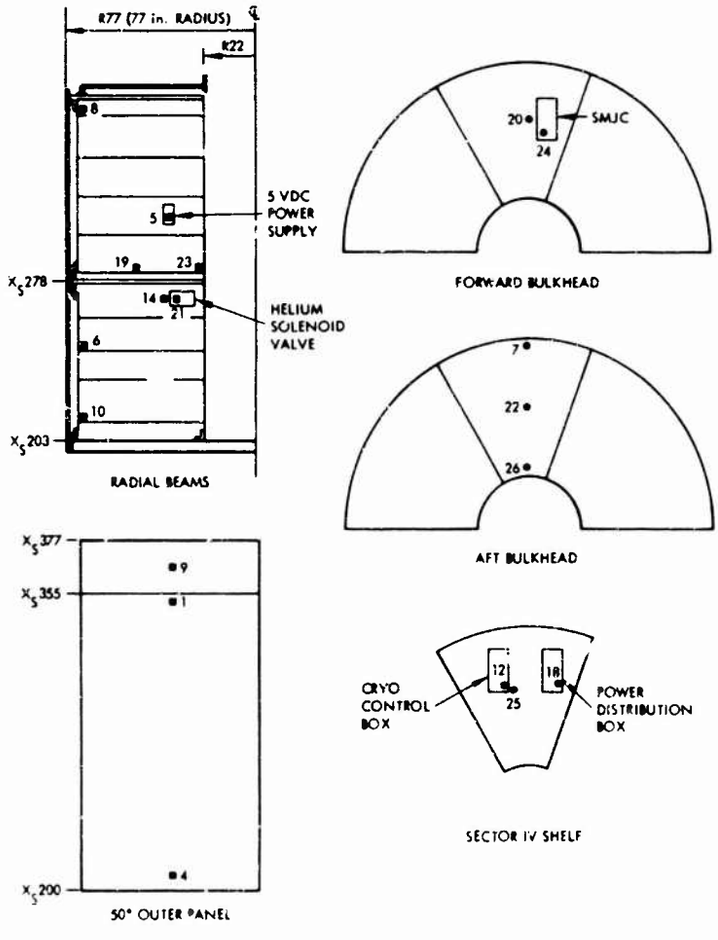

Fig. 9. Accelerometer locations on the SM 180-deg segment

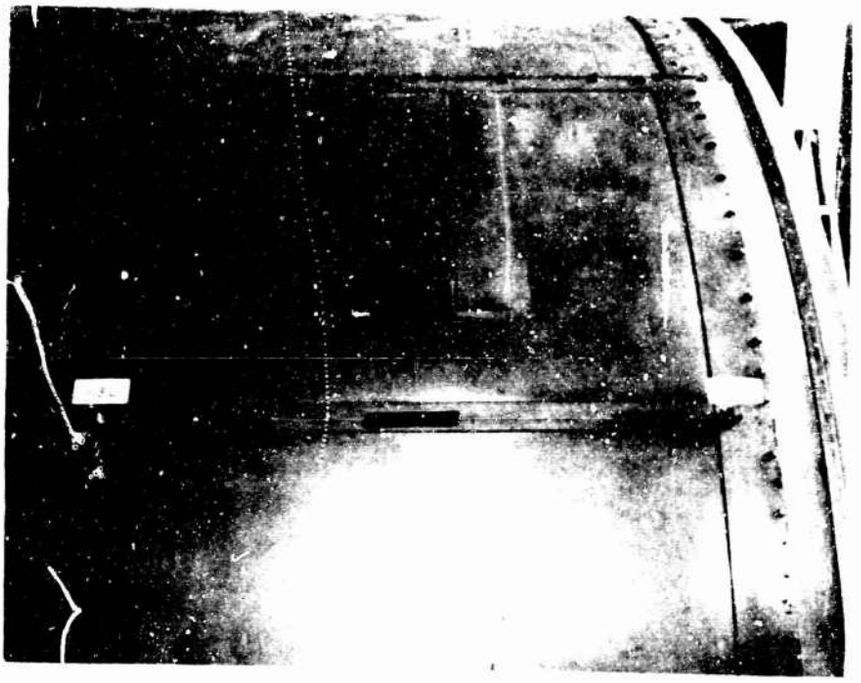

Fig. 10. Accelerometers installed on the outer panels (simulated SLA separation line is also shown)

Fig. 11. Accelerometers installed on the aft bulkhead

Fig. 12. Accelerometers installed on the radial beam and equipment items

The positive and negative maximum values were read from each trace and are shown in Table 1. In some cases significant accelerations persisted for long durations (about 100 msec), but the "duration" of the shock varied greatly with location on the structure. Except for one trace (accelerometer 21), the maximum amplitudes associated with sustained high-frequency oscillation (above 10 kHz) appeared relatively low.

Eleven accelerometers were selected for reduction to shock (or response) spectra by virtue of their locations and high signal quality. These locations (with one exception) are on structure, rather than on items of equipment, and are identified in Table 1. An MB Electronics N980 shock spectra analyzer was used. This machine obtains maximum positive and negative response peaks at natural frequencies spaced one-sixth octave apart. A tape loop was used to input the raw data. A time-reference pulse was recorded on a separate track of the tape loop and was used to trigger the analyzer during each cycle of the loop so that only a specific portion of the loop (excluding the splice) was analyzed. The plus and minus response peaks were machine plotted, and then enveloped to obtain the final shock spectrum, as shown on Figs. 14 through 24. A Q of 10 (5 percent of critical damping) and natural frequencies ranging from 10 Hz to 10 kHz were used for determining shock spectra.

TEST RESULTS

The various items of equipment were monitored for operational performance during the test. No performance degradation was observed despite the high shock levels. No structural failures (other than the separation line!) were observed after the test.

The complete set of 11 shock spectral plots, as shown in Figs. 14 through 24, are plotted with a linear acceleration scale. In addition, 10 of the spectra were replotted with a logarithmic scale in groups on Figs. 25 through 28 for comparison purposes. In general, the reduced data are a mixture of the expected and the unexpected, and may be considered typical of pyrotechnic shock data in this respect.

The outer panel data, shown in Fig. 25, show relatively little attenuation from X_s 206 to X_s 366, a distance of over 13 ft. This lack of attenuation is considered a result of the uniformity of the panels and the lack of numerous joints, corners, and attached equipment.

The spectra from the aft bulkhead locations are shown on Fig. 26. The highest levels occur at R45, although the R75 accelerometer is closer to the shock source. This result is discussed more fully in a subsequent paragraph.

Figure 27 shows data from four locations on the radial beam. The attenuation of the highest acceleration levels, above 1000 g, at the more distant locations is readily apparent. The reasons for other differences between the curves are not so obvious. For example, the close proximity of the two forward accelerometers is not reflected in their spectral levels.

Spectra for the forward bulkhead and a piece of equipment mounted on the bulkhead are plotted on Fig. 28. The decrease in levels associated with the transition from structure to component are apparent. These data contrast sharply with the aft bulkhead spectra, which are much lower in the lower frequency range. This may be justified in terms of the resonant modes of the bulkheads and the accelerometer orientations. The aft bulkhead measurements are radial (in-plane), while the forward bulkhead

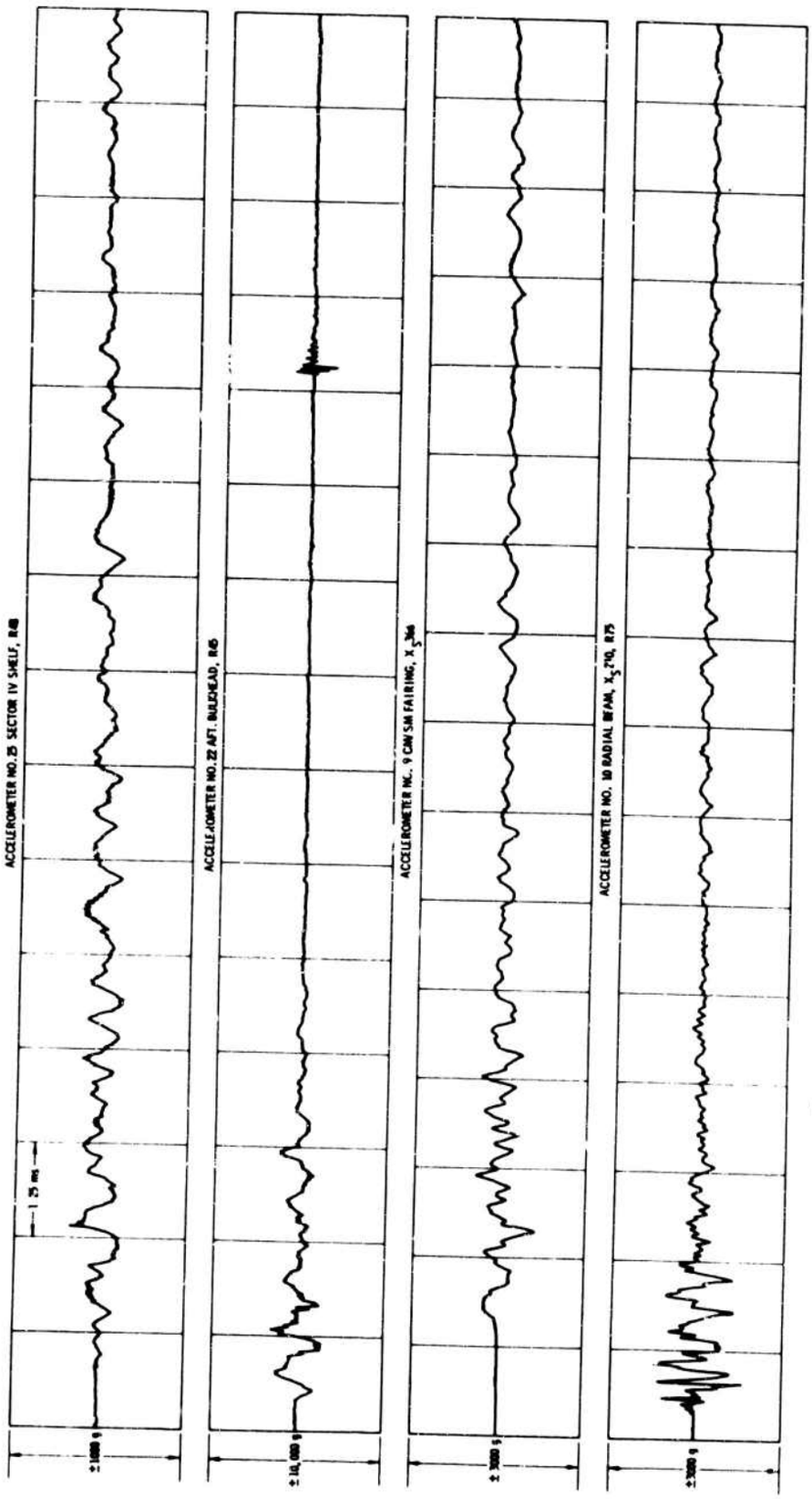

Fig. 13. Typical shock acceleration histories, from oscillograms

TABLE 1
Apollo Service Module Shock Test Maximum Acceleration Values

Accelerometer Number	Location	Orientation	Maximum Instantaneous Accelerations (from oscillograms) (g)		Maximum Shock Spectrum Value (g)
			(Positive)	(Negative)	
1	50° outer panel, X_s 352	Longitudinal	1190	1320	—
4	50° outer panel, X_s 206	Longitudinal	3830	2920	11,560
5	Power supply	Longitudinal	141	115	—
6	Radial beam X_s 242, R 75	Longitudinal	980	823	3,120
7	Aft bulkhead, R 75	Radial	1620	1760	4,220
8	Radial beam, fwd end, R 75	Longitudinal	354	276	—
9	CM-SM fairing, X_s 366, R 77	Longitudinal	894	1230	3,190
10	Radial beam X_s 210, R 75	Longitudinal	1490	1290	7,120
12	Control box, sector IV shelf	Longitudinal	162	216	—
14	Radial beam X_s 270, R 35	Longitudinal	321	363	970
18	Power box, sector IV shelf	Longitudinal	84	130	—
19	Radial beam X_s 278, R 45	Longitudinal	275	196	—
20	Fwd bulkhead, R 45	Longitudinal	306	357	1,680
21	Solenoid valve	Longitudinal	222	222	—
22	Aft bulkhead, R 45	Radial	2990	2730	9,810
23	Radial beam X_s 278, R 23	Longitudinal	316	276	1,250
24	SM jet controller, fwd bulkhead	Longitudinal	231	206	1,110
25	Sector IV shelf, R 48	Longitudinal	363	252	1,134
26	Aft bulkhead, R 23	Radial	1600	3600	—

measurements are longitudinal (transverse to the bulkhead) and may be expected to show more low-frequency response.

The maximum value from each spectrum was plotted against the maximum peak value of the corresponding measured acceleration history (Fig. 29) to show the correlation of these two "amplitude" parameters. All of the ratios are between 2.5 and 5.0, and 5 of the 11 are between 3.0 and 4.0. It may be seen that the relation between history and spectrum is relatively consistent for a wide range of levels and locations. Also, the ratios are well below the maximum obtainable value of 10, which corresponds to a steady sinusoidal input, even though the various shock histories persist for periods of time which are equivalent to many cycles.

A single shock spectrum using a Q of 100 was obtained for accelerometer 14. This curve and the "Q = 10" spectrum for the same location are plotted on Fig. 30 for comparison. Typically, the effect of using a higher Q for shock spectral analysis is an increase in the general level which is less than the increase in Q, and more emphasis of the peak values.

The test results are summarized by two plots, Figs. 31 and 32, showing attenuation as a function of distance. Figure 31 was obtained by reading the maximum acceleration value from each spectrum and calculating distance as the sum of longitudinal and radial distances from the shock source. The normalized attenuation curve published by Lockheed Missiles and Space Company (LMSC) [9] for aluminum skin-and-stiffener structure is shown for comparison. This curve was actually derived from acceleration history peaks, but is also a good representation of attenuation for shock spectra. Another attenuation curve was generated from normalized spectra data points reported in Ref. [10], for the Martin Company SV-5D lifting reentry vehicle, and is also plotted.

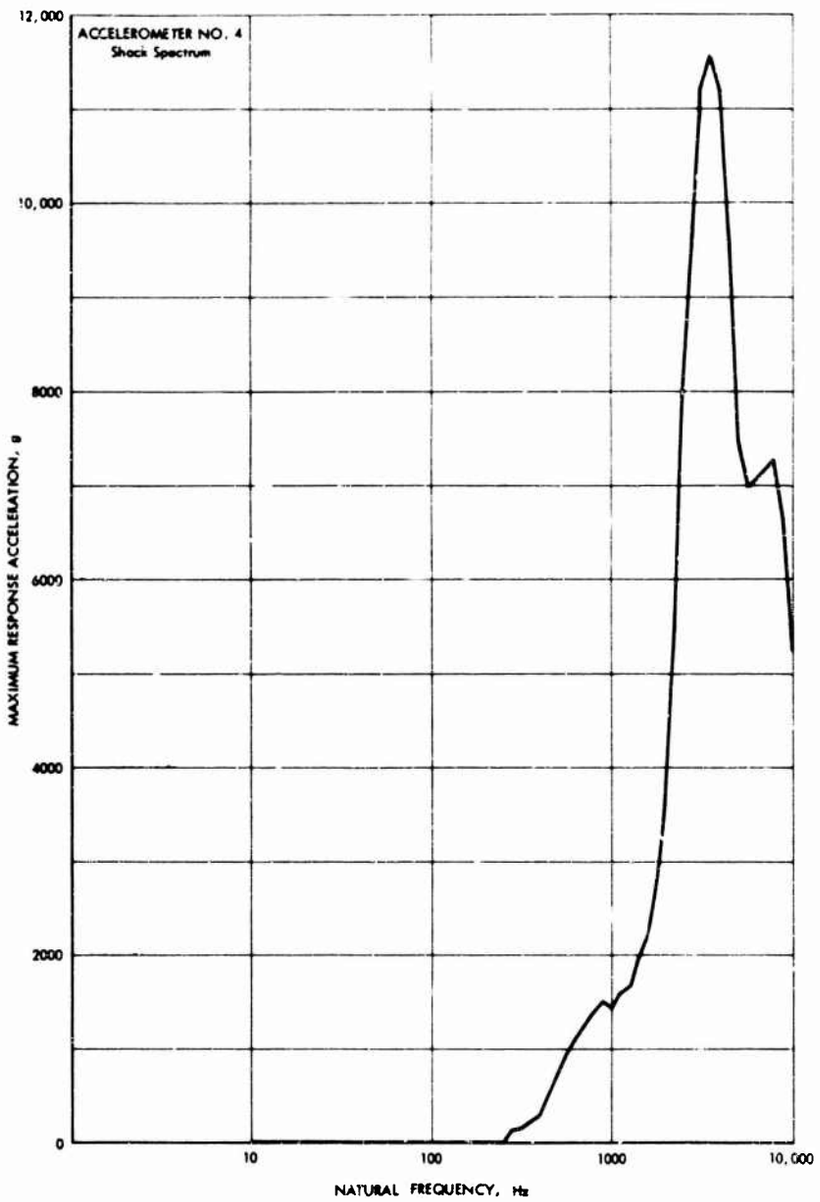

Fig. 14. Shock spectrum for 50-deg outer panel, X, 206

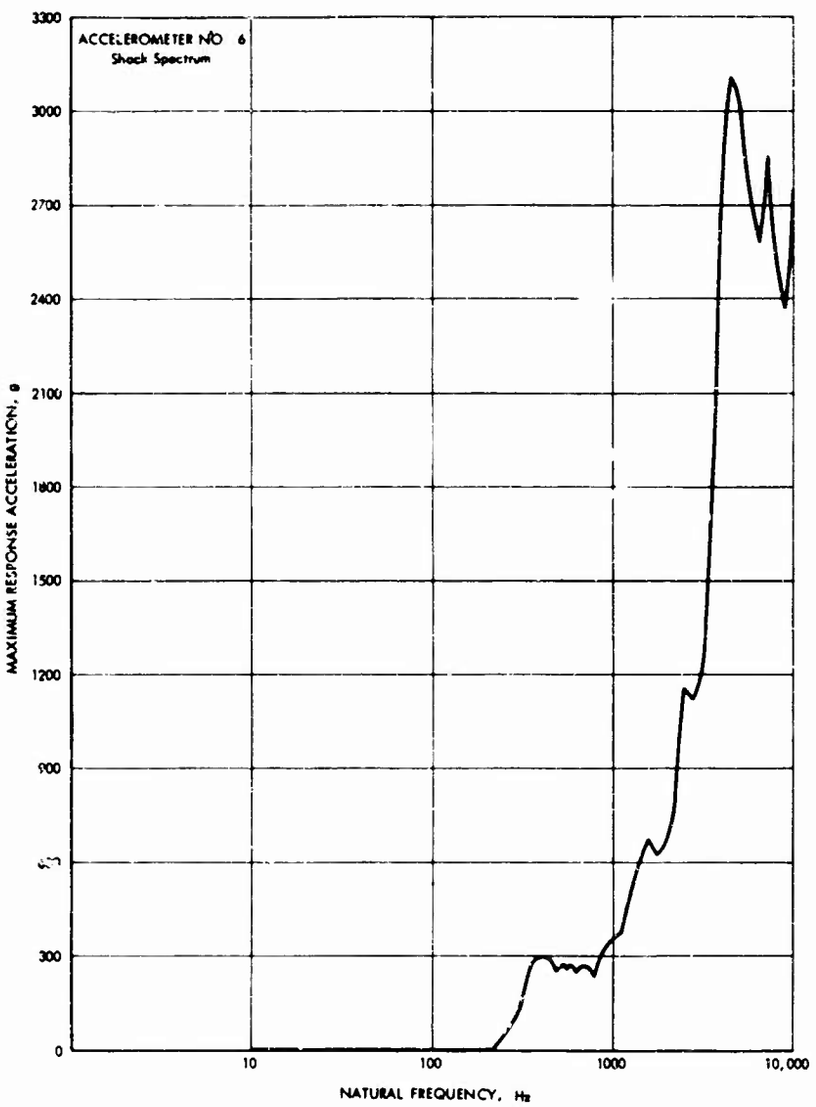

Fig. 15. Shock spectrum for radial beam, X_s 242, R 75

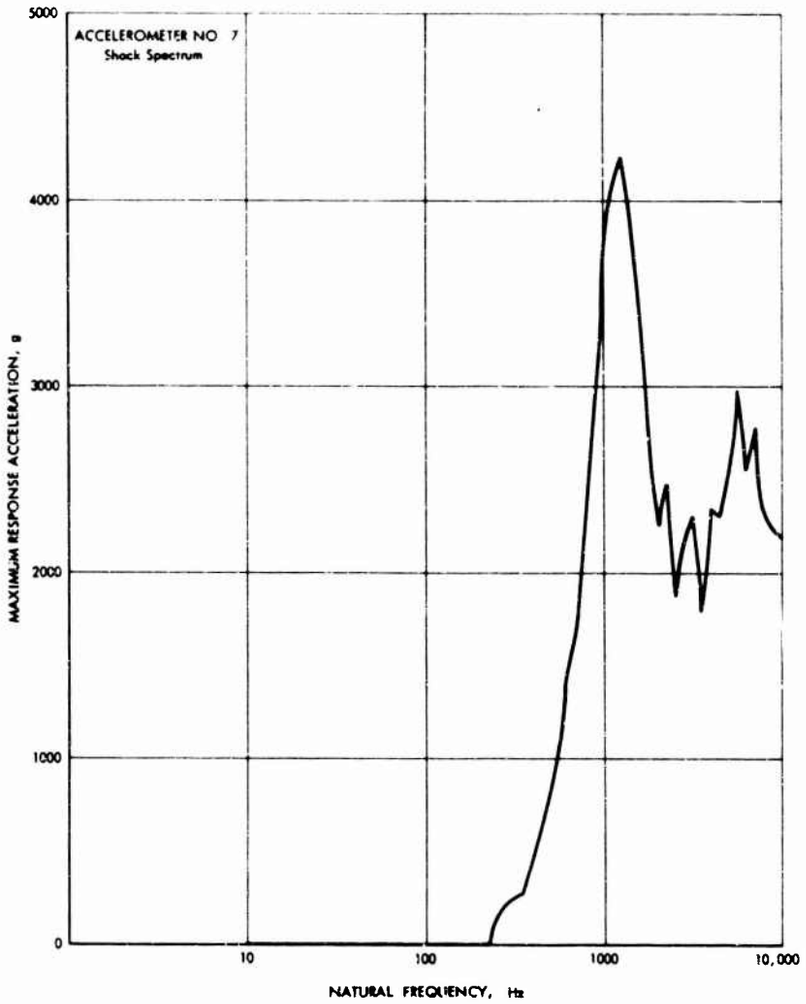

Fig. 16. Shock spectrum for aft bulkhead, R 75

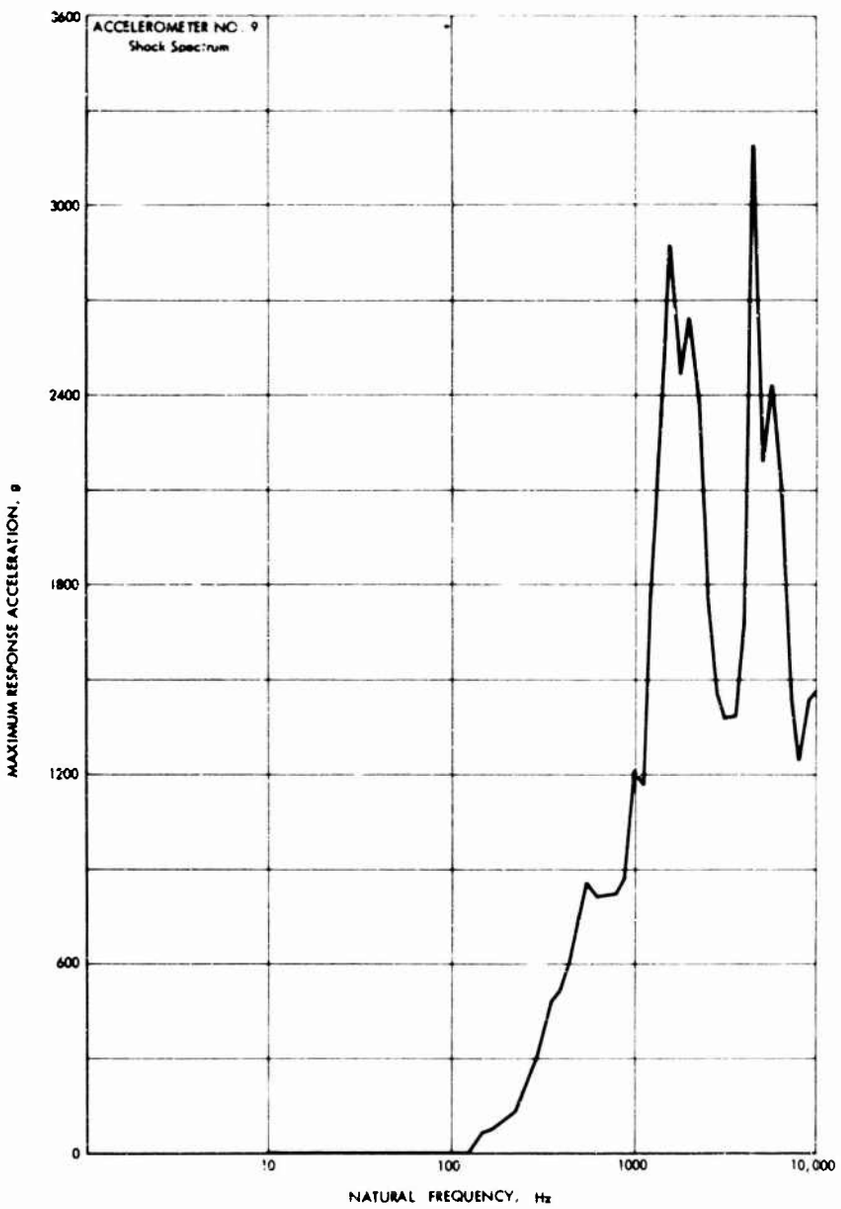

Fig. 17. Shock spectrum for CM-SM fairing, X, 366, R 77

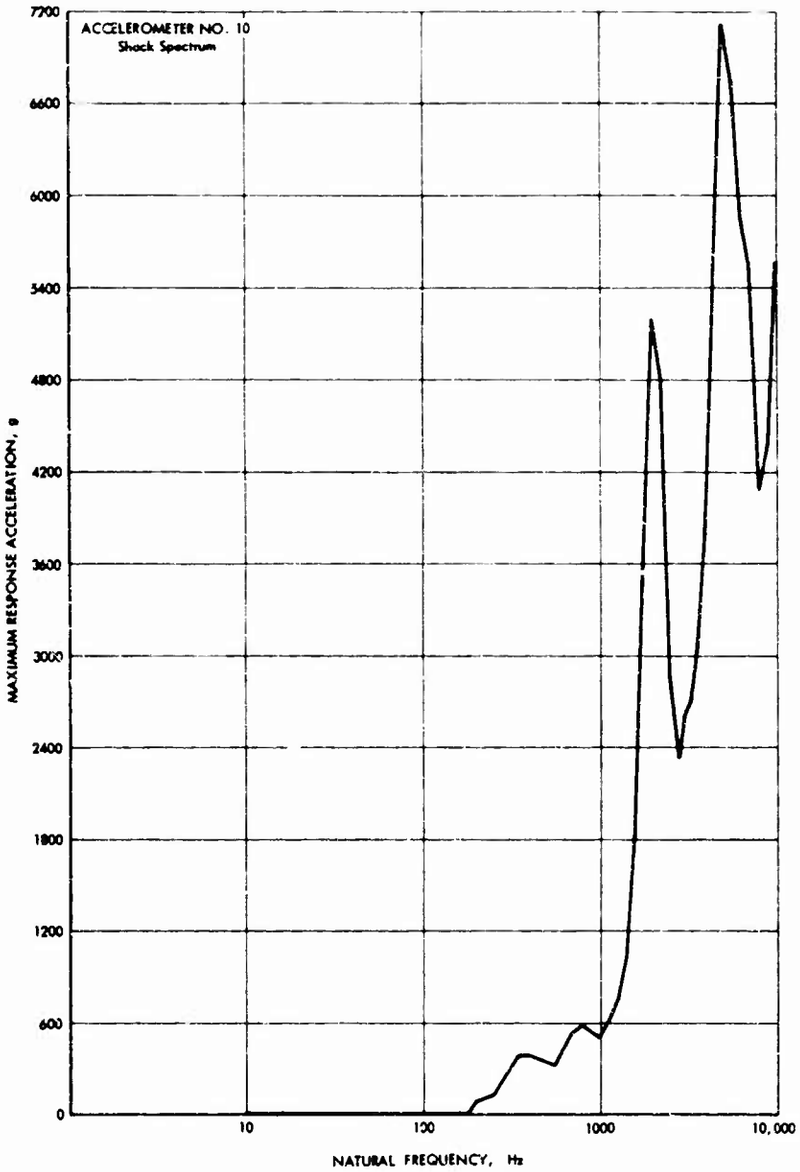

Fig. 18. Shock spectrum for radial beam, X_s 210, R 75

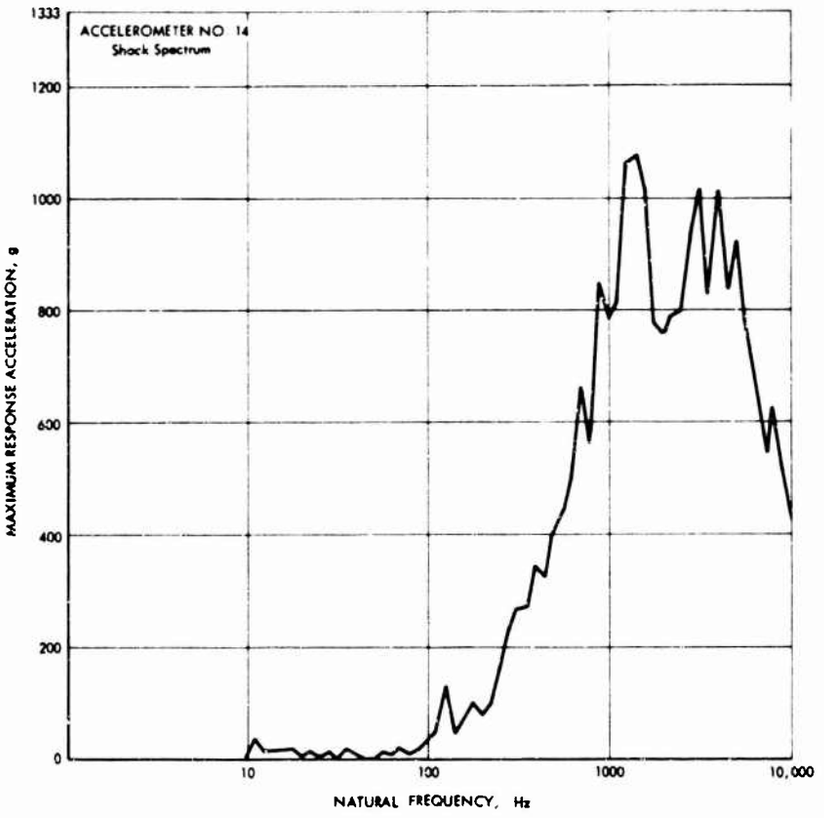

Fig. 19. Shock spectrum for radial beam, X, 270, R 35

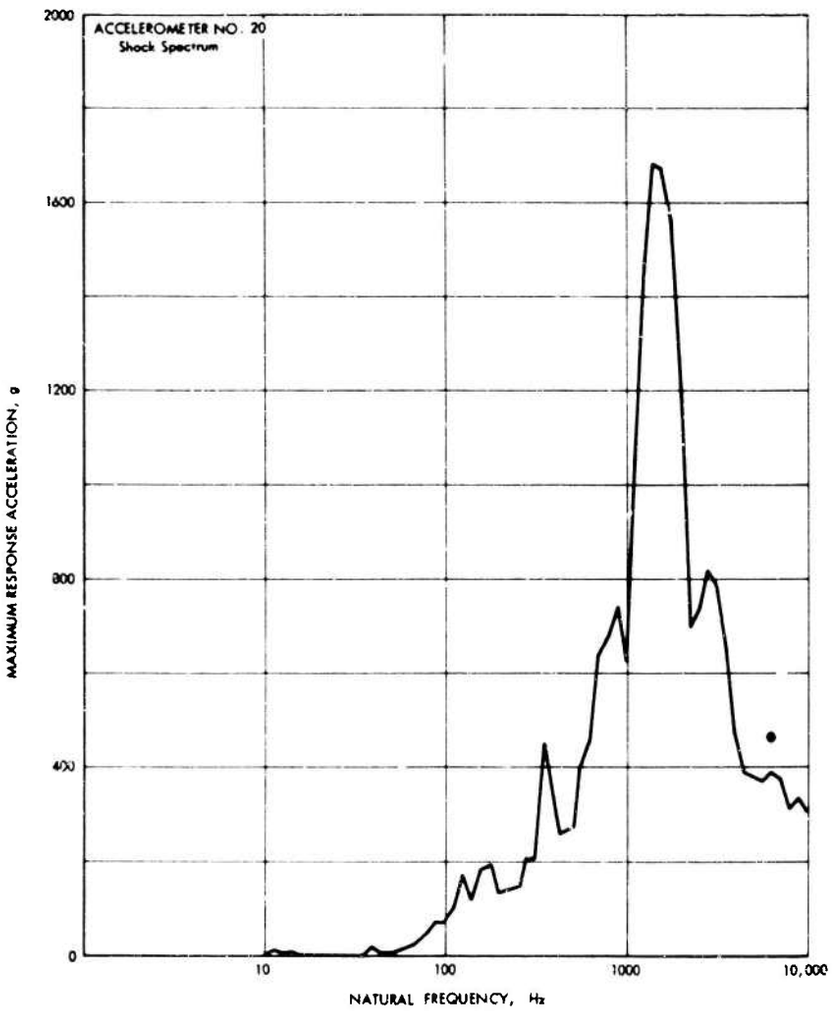

Fig. 20. Shock spectrum for forward bulkhead, R 45

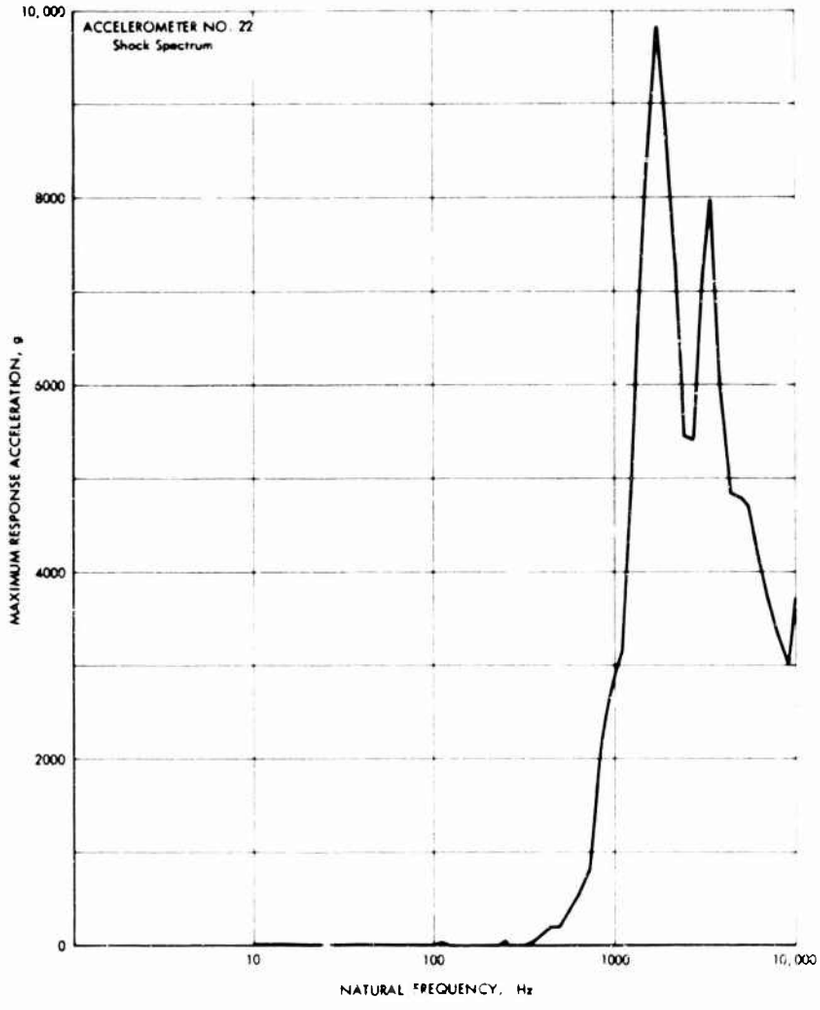

Fig. 21. Shock spectrum for aft bulkhead, R 45

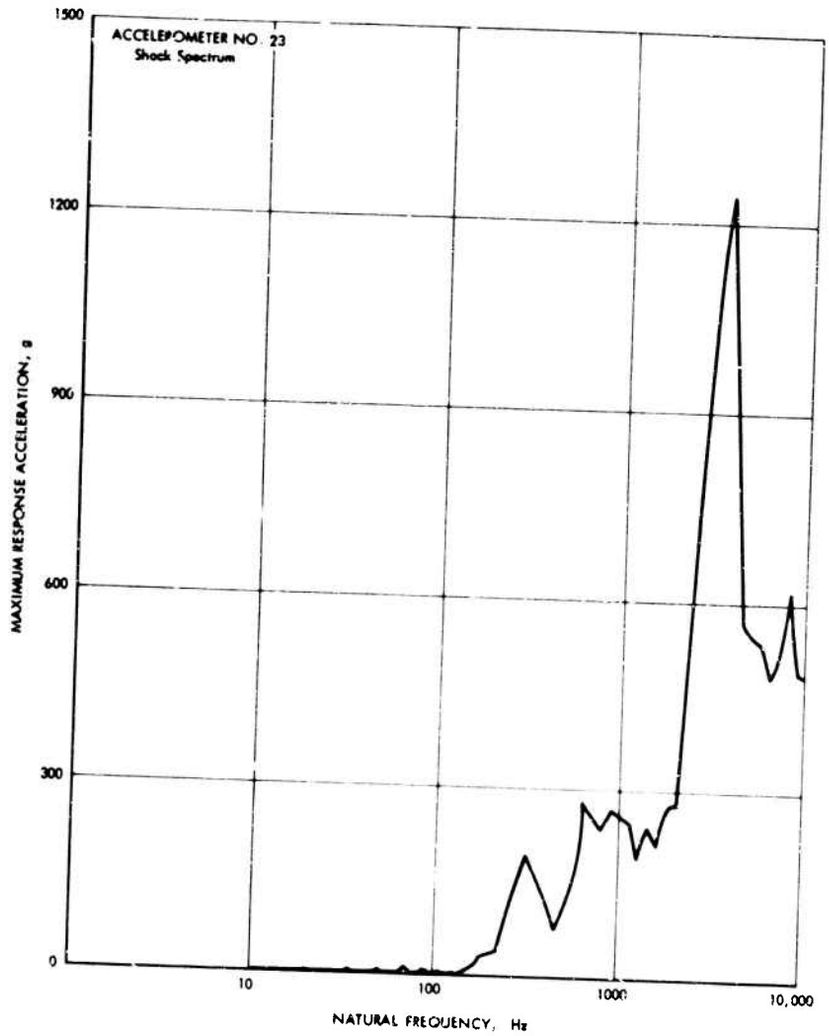

Fig. 22. Shock spectrum for radial beam, X_s 278, R 23

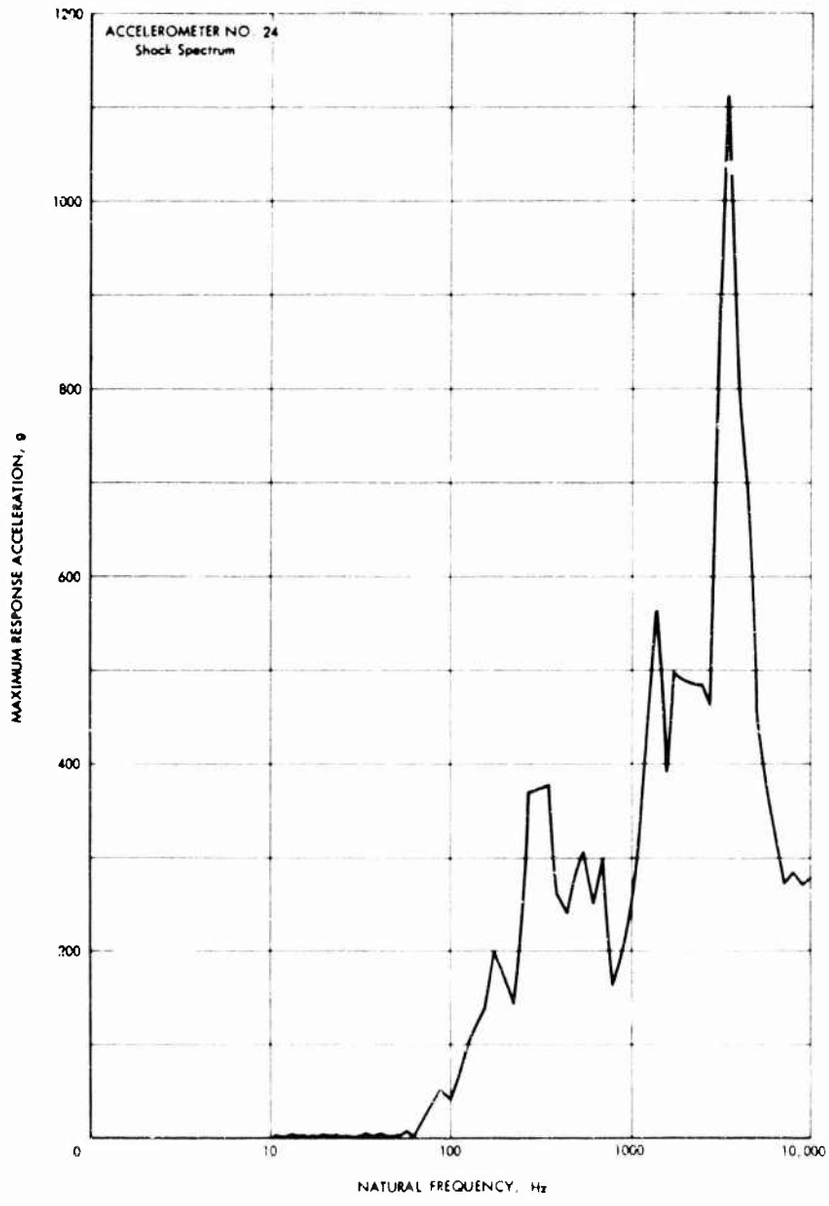

Fig. 23. Shock spectrum for SM jet controller, forward bulkhead

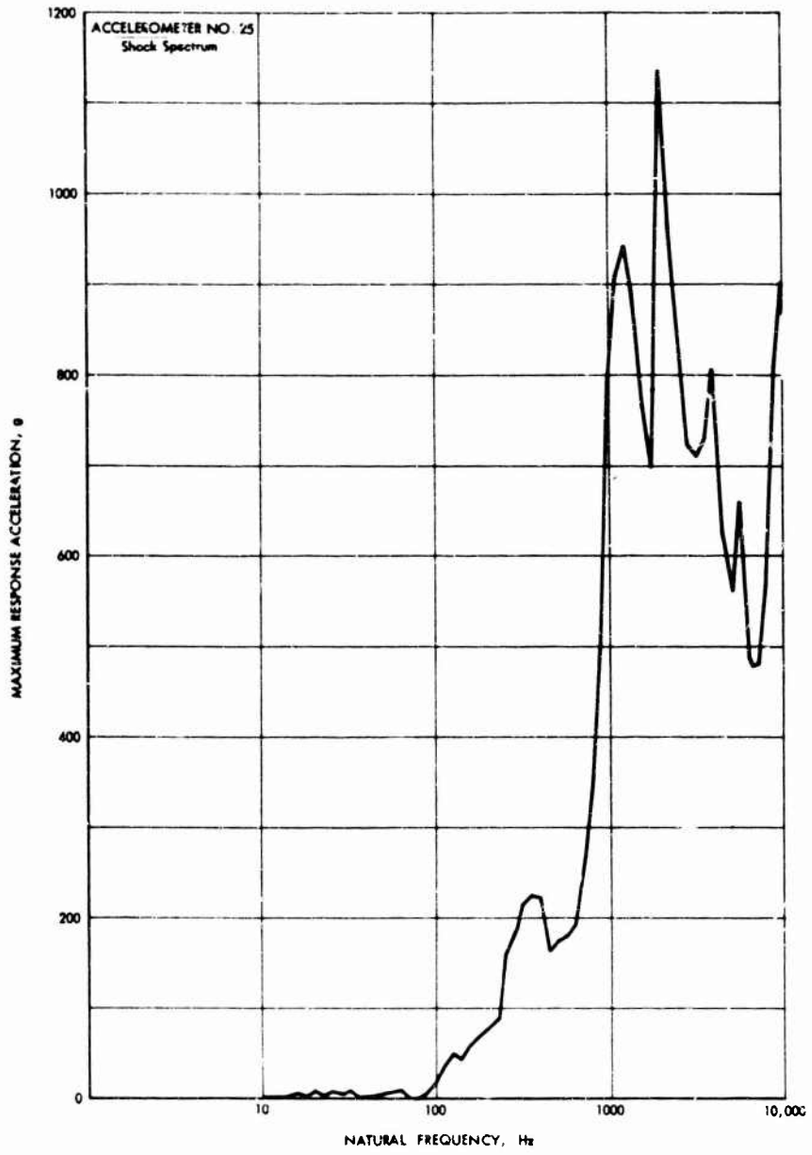

Fig. 24. Shock spectrum for sector IV shelf, R 48

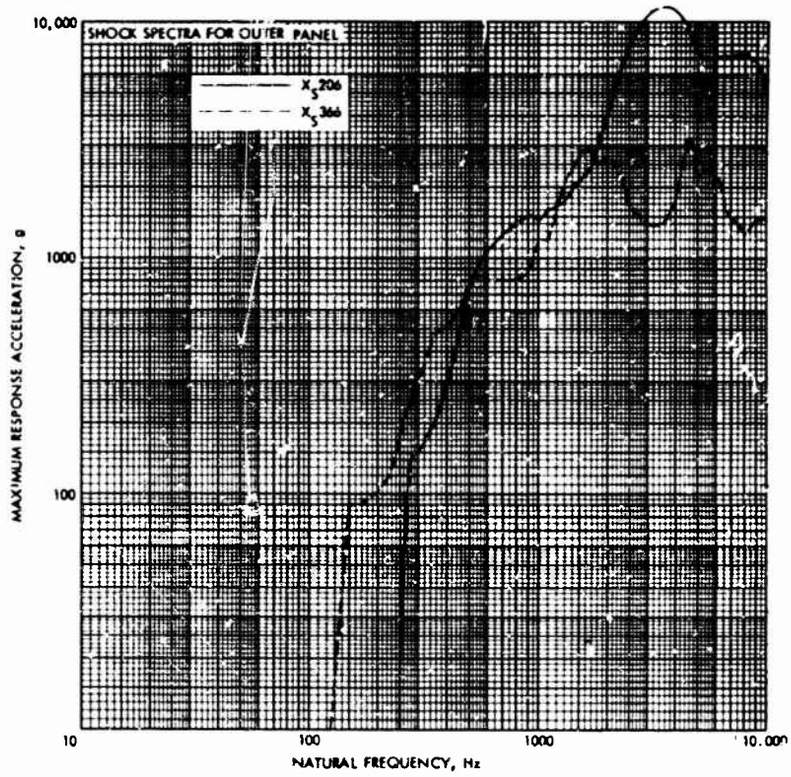

Fig. 25 Shock spectra for outer panel

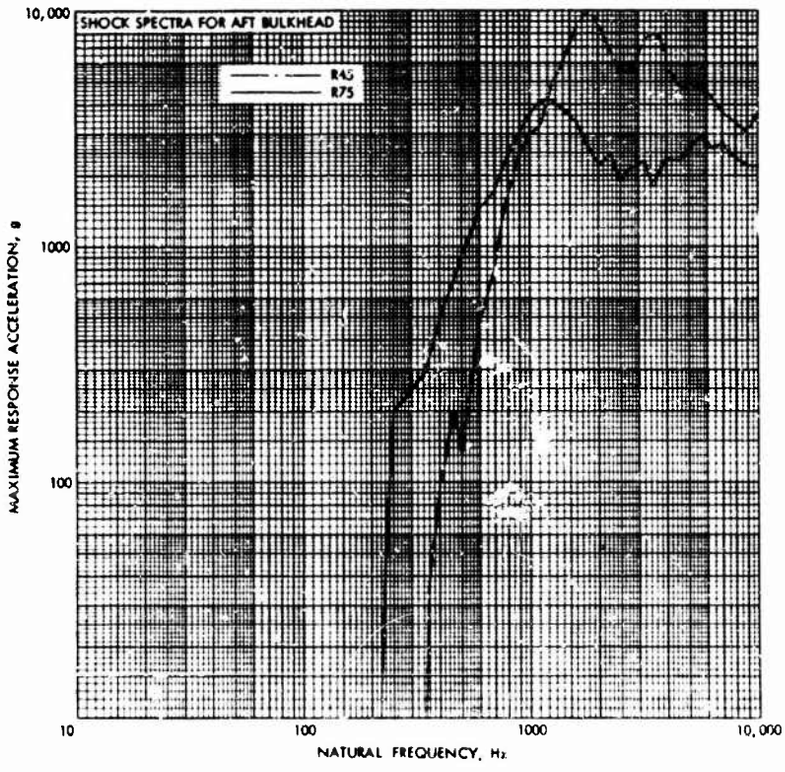

Fig. 26. Shock spectra for aft bulkhead

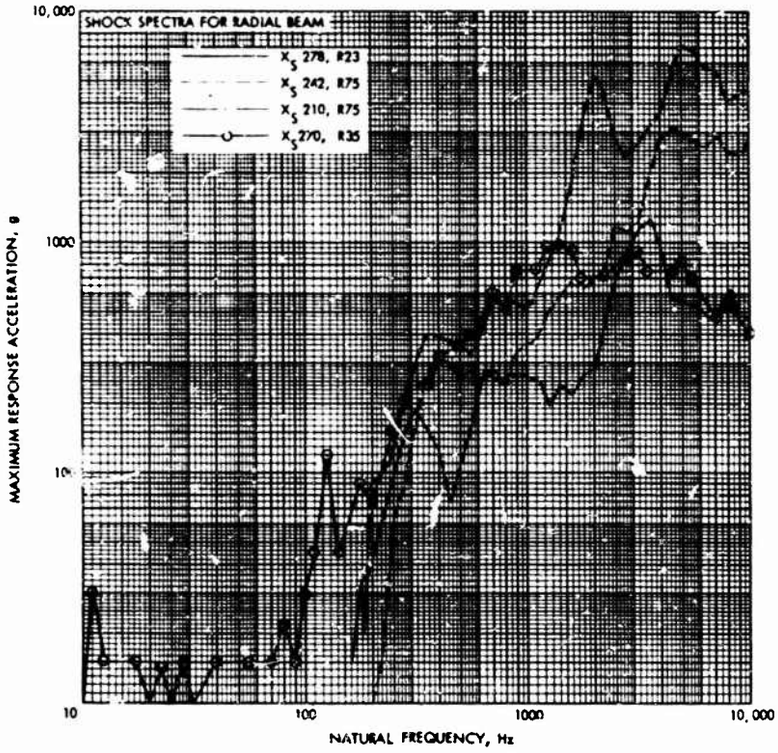

Fig. 27. Shock spectra for radial beam

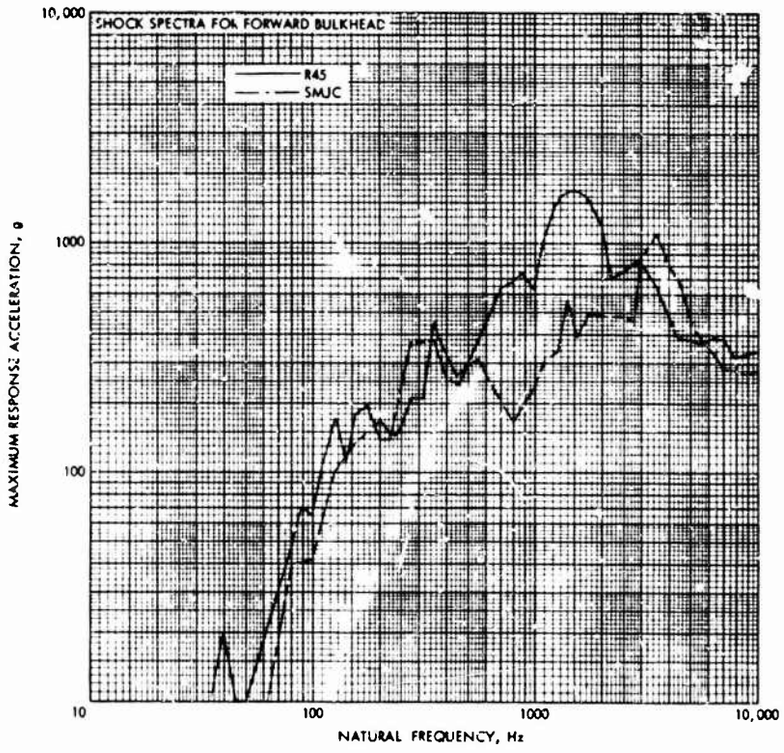

Fig. 28. Shock spectra for forward bulkhead

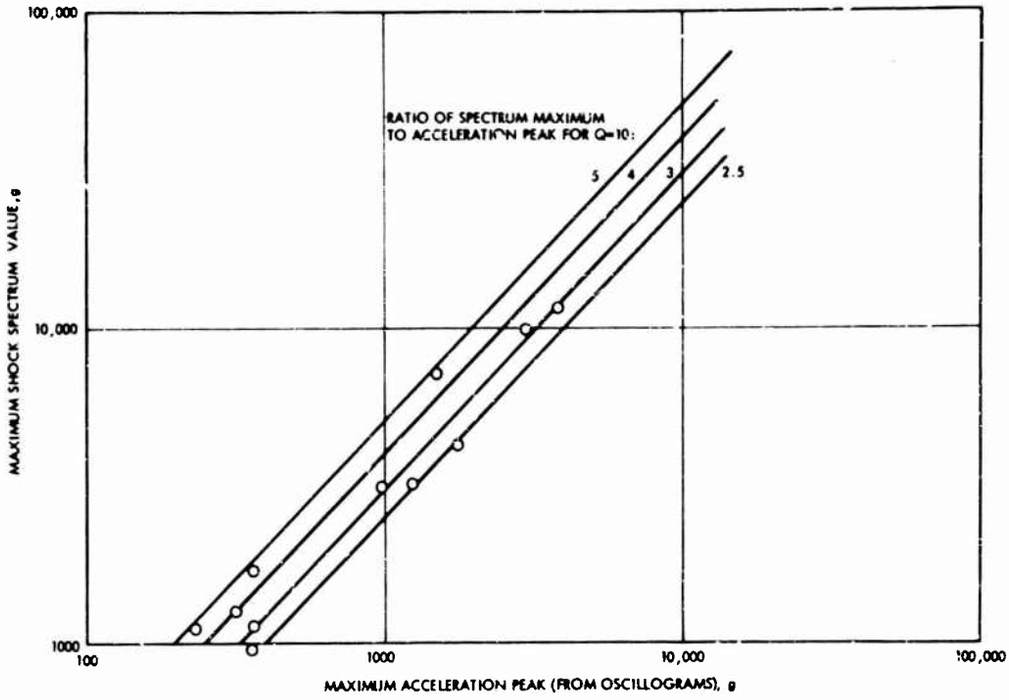

Fig. 29. Correlation between maximum values of shock spectra and maximum peaks from acceleration histories

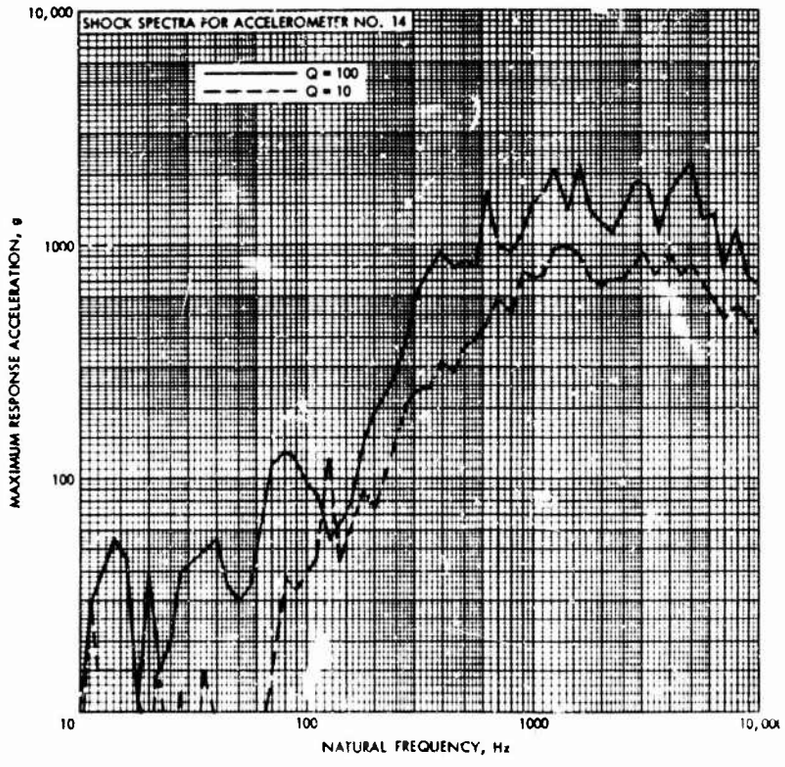

Fig. 30. Comparison of shock spectra for q = 10 and q = 100

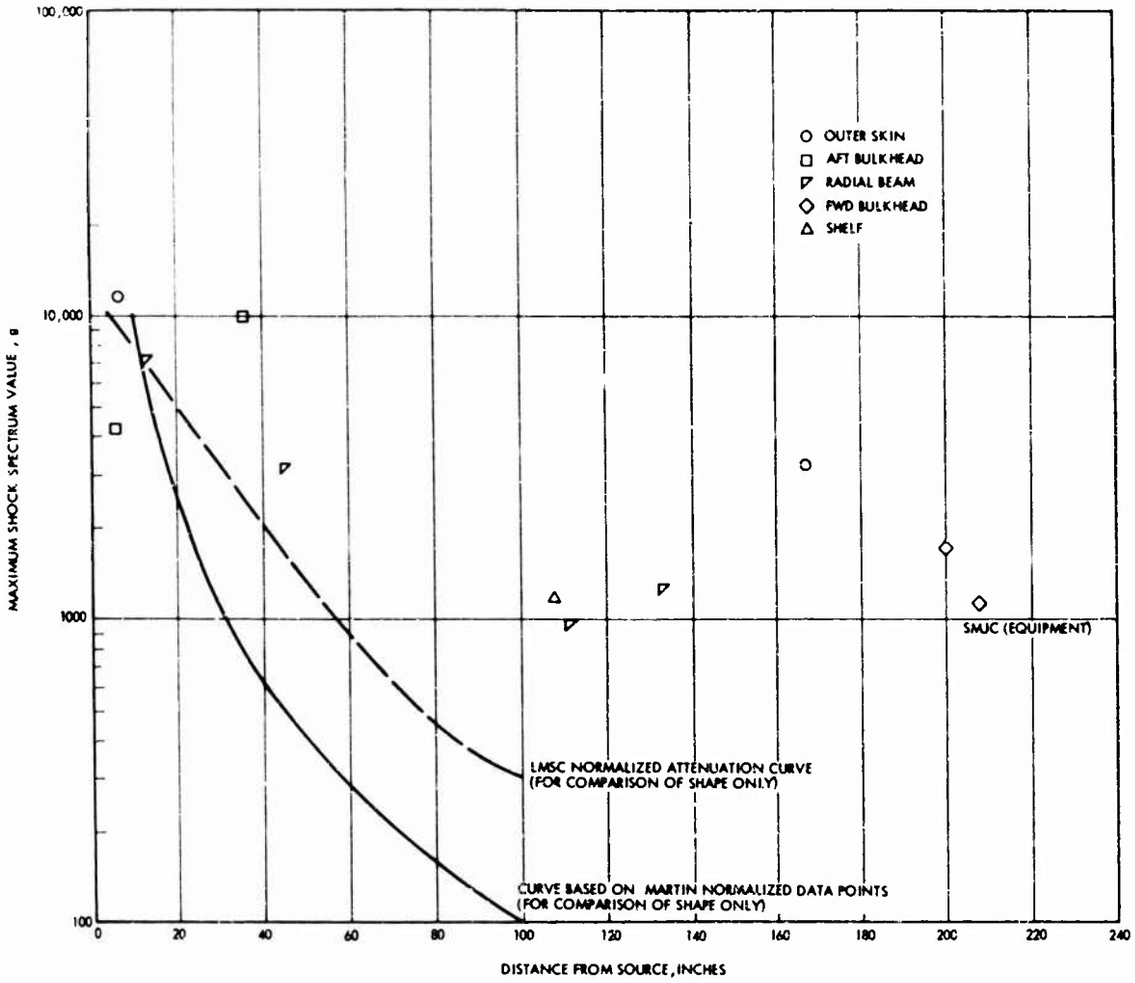

Fig. 31. Pyrotechnic shock attenuation data based on shock spectra

Figure 32 is another type of attenuation plot obtained by using maximum peak accelerations from each oscillogram. The same LMSC curve used in Fig. 31 has also been added to this figure, along with individual data points from a Douglas Aircraft Company test [4].

These plots show that shock levels were not greatly attenuated by distance during the SM test. In particular, the maximum value of the shock spectrum for the outer panel was reduced by a factor of only 3 for a distance of 13 ft. In addition, these plots show increases, rather than attenuation, with distance on the aft bulkhead. It is possible that this results from focusing (in time) of the waves from the semicircular source. Referring to Fig. 9, the R22 location is most nearly equidistant from the entire length of the source, and would experience the most concentrated excitation. Besides the potential time-focusing effect, it may be noted that the geometric center (c.g.) of the source is actually at about R33. Therefore, the inner locations are actually at shorter mean distances from the distributed source. One reason that the conception of mean distance was not used in plotting the data is that this would imply that each increment of the source has an equal effect at a given location. Thus, a mean distance conception would amount to assuming no attenuation with distance.

CONCLUSIONS

The accelerometer data from this shock test are significant because of the type of structure involved. No other pyrotechnic shock data

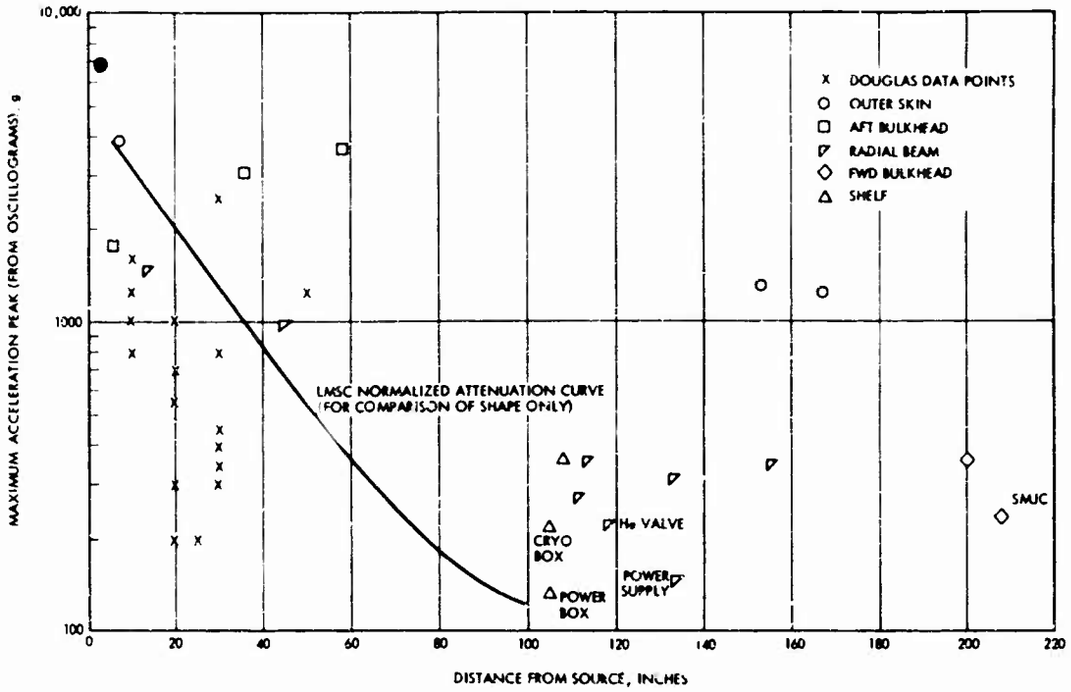

Fig. 32. Pyrotechnic shock attenuation data based on acceleration history

have been published for honeycomb structure. There was a marked lack of attenuation of the shock with distance for both the honeycomb structure and the chem-milled radial beams, in contrast to attenuations reported for other structures. However, levels on equipment items were reduced considerably.

It may be concluded that previously reported attenuation data for other structures should not be generalized to apply to this type of structure. The basic reason for this is not clear, and may not necessarily be the type of structure. Unfortunately, no analysis of honeycomb under high-intensity, high-frequency shock has been reported. Mathematical modeling of the individual cells, rather than substituting an equivalent shell layer, may be necessary because possible cell resonances may be excited by the very high frequencies associated with the shock. The limited amount of data from the Apollo service module indicates that joints and mass loading (from equipment) are the most important causes of attenuation.

ACKNOWLEDGMENT

The authors gratefully acknowledge the assistance of W. R. Wood, G. M. Hill, and G. L. Travis of North American Rockwell in the acquisition of the shock data and R. W. Budd of Hughes Aircraft in the data reduction.

REFERENCES

1. J. M. Otera, "Spacecraft Shock Environment Induced by Nose Fairing Separation Pyrotechnics," STL Rept. 2411-6001-RU-0000, Apr. 1963

2. V. R. Paul, "Mechanical Shock from Frangible Joints," Shock and Vibration Bull. No. 33, Part 4, pp. 63-71, March 1964

3. H. J. Roberge and J. Rybachi, "Shock Environments Generated by Pyrotechnic Devices," Shock and Vibration Bull. No 33, Part 4, pp. 73-81, March 1964

4. D. E. Hines, "Generation and Propagation of Stage Separation Shocks in Missiles and Space Vehicles," Proc. IES, 681-689, (1964)

5. R. E. Blake, "Problems of Simulating High-Frequency Mechanical Shocks," Proc. IES, 145-151, (1964)

6. G. Dominguez and S. Rubin, "Survey of In-flight Separation Systems," Aerospace Corp. TOR-269 (4106-01)-15, Oct. 1964

7. D. A. Heydon and W. W. Aichroth, "Spacecraft Shocks Induced by Electro-Explosive Devices," Shock and Vibration Bull. No. 34, Part 3, pp. 259-266, December 1964

8. A. L. Ikola, "Simulation of the Pyrotechnic Shock Environment," Shock and Vibration Bull. No. 34, Part 3, pp. 267-274, December 1964

9. A. L. Ikola and M. D. Wherry, "LMSC Pyrotechnic Shock Experience," SAE Paper 660717, Oct. 1966

10. W. K. Britton and G. K. Jones, "Pyrotechnic Shock Testing of a Full-Scale Re-entry Vehicle," Shock and Vibration Bull. No. 36, Part 2, pp. 71-81, January 1967

11. E. Aten, T. Jacobi, and D. White, "High Intensity Pyrotechnic Shock Testing of Titan III Airborne Inertial Guidance Equipment," Proc. IES, 243-255 (1966)

* * *

SIMPLE STRENGTH CONCEPT FOR DEFINING PRACTICAL HIGH-FREQUENCY LIMITS OF SHOCK SPECTRUM ANALYSIS*

M. Gertel and R. Holland
Allied Research Associates
Concord, Massachusetts

Simple analyses have been conducted to define the shock spectrum equivalent static accelerations necessary to produce yield stress in idealized cantilever and pin-ended beam structures as a function of their normal mode frequencies and deflections. The accelerations to produce yielding failure are based upon a superposition of the maximum stresses at a common point for all modes, including correction for modal participation factors. Simple summary plots defining the "failure acceleration" required for yielding are presented for families of uniform cantilever and simply supported beams as a function of material, dimensions, and modal frequencies. It is seen from these plots that beams with high natural frequencies are inherently stronger than low-frequency beams and require proportionately greater acceleration to cause yielding failure. A concept for utilizing these plots in conjunction with the peak acceleration of a given shock motion is presented for defining the upper frequency limit of shock spectrum analysis.

INTRODUCTION

At the present state of the art, analysis of measured environmental transient data for shock spectrum characteristics up to 2000 cps and frequently higher is commonly required. In view of the great amount of preparation detail, time, and cost associated with performing precision high-frequency analyses, it is appropriate to determine a practical upper frequency limit based on the possible utilization of these data. The concept which is presented here for defining the upper frequency limit of a shock spectrum analysis takes cognizance of the inherently greater strength of high-frequency structures and considers the utilization of either a cantilever or a simply supported beam as a reference structural element. The frequency range of interest is defined as the highest beam natural frequency at which the acceleration required to produce failure exceeds the expected peak acceleration of the shock spectrum.

DEVELOPMENT OF THE BEAM FAILURE-FREQUENCY CONCEPT

The shock response for an elementary structure, such as a cantilever beam, is depicted in Fig. 1. The completely generalized response is considered to be the superposition of the separate responses at each of the normal mode frequencies of the structure. Modal response and frequency analyses for a variety of cantilever and simple beam structures which are of possible interest here are presented in Appendixes A, B, and C for convenient reference. The principal results of the analyses in the appendixes are equations relating beam dimensional parameters, e.g., thickness and length, to the modal natural frequencies of the beams and also the equivalent static acceleration to produce yielding failure. The beam frequency equation is as follows:

$$\frac{h}{\ell^2} \propto \frac{f_n}{C_n} \qquad (1)$$

*The study reported herein was performed for the Frankford Arsenal under contract DA36-038 AMC-4295 (A). This program was conducted under the overall cognizance of David Marcus and James Wiland of the Environmental Laboratory of the Test and Evaluation Division of Frankford Arsenal.

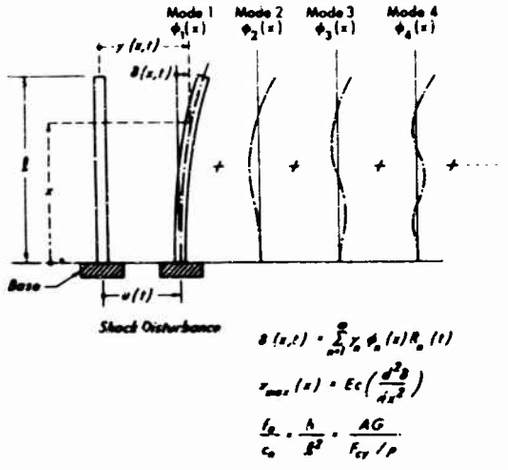

Fig. 1. Transient response of cantilever depicted as summation of separate modal responses

where

C_n = coefficient for the nth mode frequency of a given beam

f_n = natural frequency for the nth mode (cps)

h = thickness of beam (in.)

ℓ = length of beam (in.).

The beam failure equation is as follows:

$$\frac{h}{\ell^2} = \frac{AG}{F_{ty}/\rho} \qquad (2)$$

where

A = constant based on summation of stress produced at a given point by an infinite number of normal modes assumed to exist simultaneously

F_{ty} = yield stress for the material (psi)

G = equivalent static acceleration to produce yield stress (number times g)

ρ = density of the beam material (lb/in.^{3}).

Figures 2 and 3 are plots of the equivalent static "failure" acceleration from Eq. (2) for cantilever and simply supported beams of various materials as a function of the dimensional parameter h/ℓ^2. For the case of the cantilever beam, the stress constant $A = 3$ from Appendix B. For the case of the simply supported beam, the stress constant $A = 0.814$ from Appendix C. Superimposed as alternative abscissas in Figs. 2 and 3 are nomographic scales identifying the first three modal frequencies for direct correspondence with the beam dimensional parameter h/ℓ^2, in accordance with Eq. (1). Also noted for reference in Figs. 2 and 3 are the cumulative percentage contribution of the first three modes to the maximum stress produced by superposition of an infinite number of modes with the same equivalent static acceleration but adjusted for modal participation factor. The derivation of these percentage stress contributions is presented in detail in Appendixes B and C.

Equating Eqs. (1) and (2) and solving for the equivalent static acceleration to produce yielding failure, we obtain:

$$G = \frac{(F_{ty}/\rho)\, f_n}{AC_n} . \qquad (3)$$

Thus, the failure acceleration is directly proportional to natural frequency, and high-frequency systems will inherently exhibit greater strength than low-frequency systems. This may also be noted by inspection of Figs. 2 and 3 wherein the region above each curve defines failure conditions.

An approach to defining the highest frequency of practical interest from a structural failure point of view may now be conceived by superimposing a beam failure-frequency curve on a generalized shock spectrum representative of all transient environments. Figure 4 shows a beam failure-frequency curve superimposed on a completely general four-coordinate shock spectrum curve represented by constant asymptotes of displacement, velocity, and acceleration. Note that the superimposed beam failure-frequency curve plots parallel to lines of constant sinusoidal velocity. This occurs because the failure acceleration, as indicated by Eq. (3), is equal to a constant multiplied by the frequency. The failure-frequency curve intersects and exceeds the constant displacement asymptote at low frequencies and the constant acceleration asymptote at high frequencies. For purposes of the present discussion, the low-frequency intersection is of no practical interest. The high-frequency intersection, however, can serve to define the highest critical frequency from a failure point of view. Above this frequency, the beam "strength" exceeds the shock spectrum value representative of the input transient; hence no failure will occur.

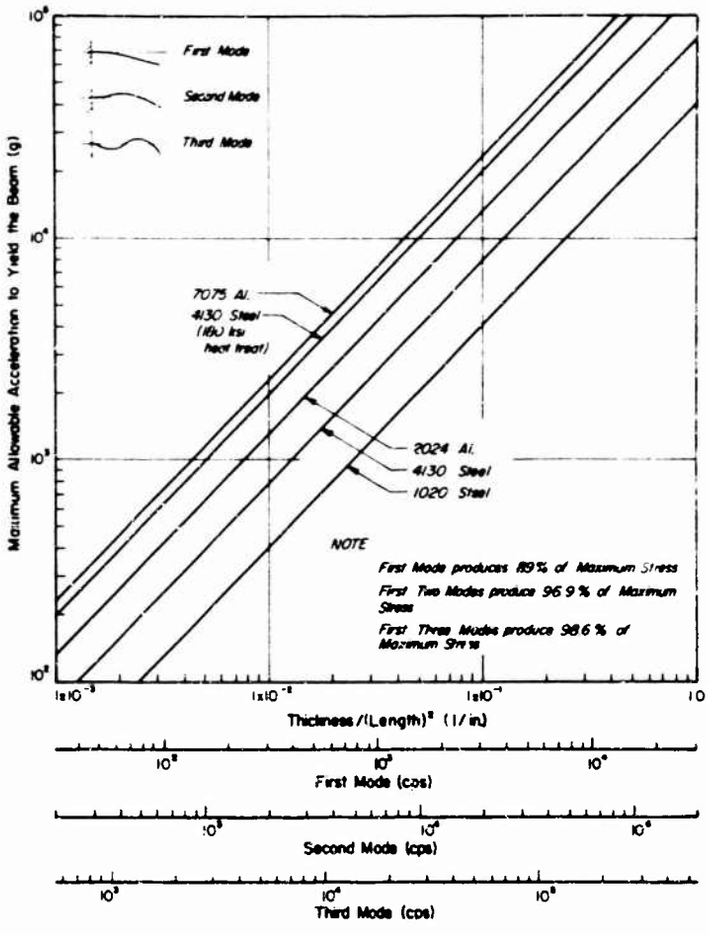

Fig. 2. Failure acceleration for uniform cantilever beams as a function of dimensions and corresponding modal frequencies

The failure-frequency concept can be adapted for application to both simple shock pulses and complex vibratory transients, as depicted in Fig. 4. In the case of a simple shock pulse, the high-frequency asymptote of the shock spectrum will correspond to the peak acceleration of the shock pulse. In the case of a complex vibratory type of shock motion where the peak acceleration may be magnified by a short-term "transient resonance" condition, the shock spectrum constant acceleration asymptote at high frequencies should be increased to account for this. A transient resonant amplification, or Q, of from 3 to 5 is suggested as appropriate for most conditions.

APPLICATION AND DISCUSSION OF CONCEPT

For purposes of illustrating the application of the beam failure-frequency concept, consider the complex shock motion with a peak acceleration of 300 g as reproduced from Ref. 1 in Fig. 5. The computed shock spectrum for this transient is reproduced in Fig. 6. Beam failure-frequency curves respectively defined by each of the first three mode frequencies for a 2024 aluminum cantilever beam have been superimposed for reference on the shock spectrum in Fig. 6. Preliminary observations relative to the application of the beam failure-frequency concept are offered below.

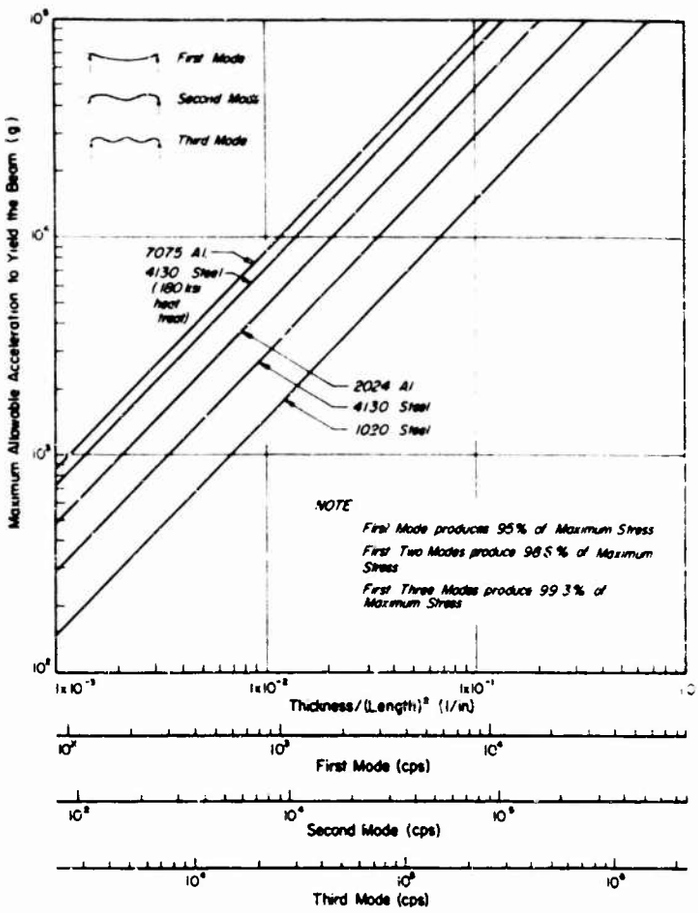

Fig. 3. Failure acceleration for uniform simply supported beams as a function of dimensions and corresponding modal frequencies

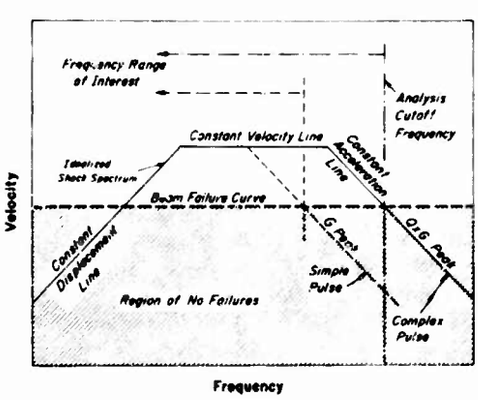

Fig. 4. Idealized representation of beam failure curve superimposed on shock spectrum

The first mode failure curve intersects and passes above the undamped shock spectrum at approximately 200 cps and 900 g. Inasmuch as the peak shock input acceleration was 300 g, it is evident that a transient resonance condition exists in the vicinity of 200 cps. Thus, if we assume that the present reference 2024 aluminum cantilever adequately represents the failure strength of systems we are concerned with, then we can infer a transient resonance magnification factor of 3 for application to the peak shock input to determine a shock spectrum analysis cutoff frequency. In other words, prior to computing the shock spectrum for the shock motion of Fig. 5, we could have multiplied its peak acceleration by a factor of 3 and then entered Fig. 3 directly with an allowable failure acceleration of 900 g. In Fig. 3 we would then

Fig. 5. Sample complex shock transient

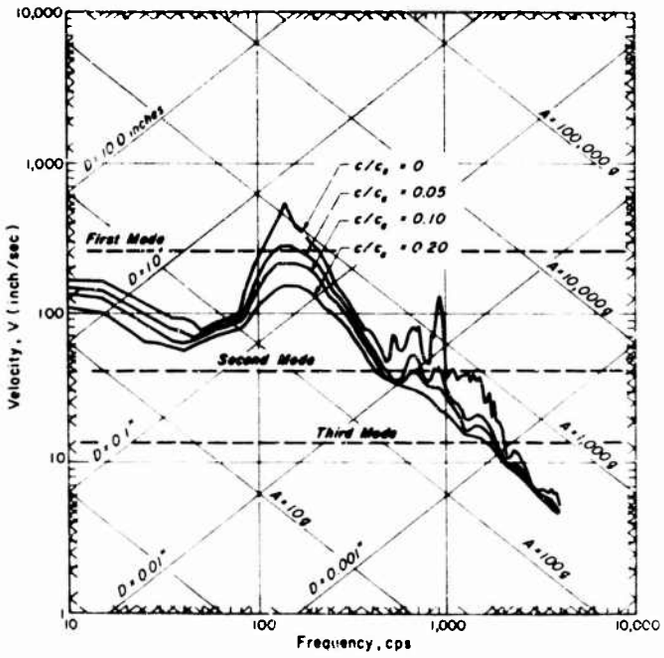

Fig. 6. Shock spectra for sample complex shock transient with superimposed aluminum cantilever beam failure curves

read a first mode frequency of 210 cps. Since the beam failure curve includes stress contributions from all modes, and the major stress contribution is from the first mode, the 210-cps frequency represents a practical upper frequency limit for shock spectrum analysis.

Alternatively, if we assume that the shock motion contains frequency components in excess of the 210-cps first mode, we could also have read 1300 cps and 4000 cps, respectively, for the corresponding second and third mode failure frequencies in Fig. 3. It can be seen that the 900-g allowable failure acceleration at both of these frequencies exceeds the failure curve intersection indicated in Fig. 6 at approximately 800 g and 1000 cps for the second mode, and 400 g and 2000 cps for the third mode. Accordingly, on the basis of these trial observations is appears reasonable to use a transient resonant magnification factor of 3 to define an allowable failure acceleration corresponding to

the reference beam's first three modal frequencies. The selection of which modal frequency should be used to define the shock spectrum analysis cutoff frequency now becomes a matter of judgment with consideration of the relative contribution to the failure stress by each modal frequency.

SUMMARY

A concept is presented for defining an upper cutoff frequency for shock spectrum analyses based on expressing the strength of simple reference beams in terms of the equivalent static acceleration to produce yielding failure. This concept has been presented for information and discussion purposes only.

Appendix A

RESPONSE OF DISTRIBUTED MASS SYSTEM TO A BASE MOTION

From Ref. 2, the relative displacement response δ of a distributed mass system, such as shown in Fig. 1, is equal to the sum of the separate modal responses as follows:

$$\delta(x,t) = \sum_{n=1}^{\infty} \gamma_n \phi_n(x) R_n(t) \quad (\text{in.}) \qquad \text{(A-1)}$$

where

n is the natural mode number of the vibration response

$\phi_n(x)$ is the nth mode shape deflection of the structure as a function of length dimension (x)

R_n is the Duhamel's Integral

$$= -\frac{1}{\omega_n}\int_0^t \ddot{u}(\tau)\sin\omega_n(t-\tau)d\tau \quad (\text{in.})$$

γ_n is the nth modal participation factor

$$= \frac{\int_0^{\ell} \mu\phi_n \, dx}{\int_0^{\ell} \mu\phi_n^2 \, dx}$$

μ is the mass per unit length.

From basic texts on elementary strength of materials, such as Refs. 3 and 4, the maximum bending stress σ is as follows:

$$\sigma_{max}(x) = \frac{M(x)c}{I} \quad (\text{psi}) \qquad \text{(A-2)}$$

where

M is the bending moment (in.-lb)

c is the distance from the neutral axis to the most remote element (in.)

I is the area moment of inertia (in.^{4}).

The differential equation of the elastic curve of a beam, from Ref. 5, is:

$$EI\frac{d^2\delta}{dx^2} = M(x) \quad (\text{in.-lb}) \qquad \text{(A-3)}$$

where E is the modulus of elasticity (psi).

By substitution of Eq. (A-3) in (A-2) we obtain:

$$\sigma_{max}(x) = \left(EI\frac{d^2\delta}{dx^2}\right)\frac{c}{I} = Ec\frac{d^2\delta}{dx^2} \quad (\text{psi}). \qquad \text{(A-4)}$$

When Eq. (A-1) is substituted into Eq. (A-4), it becomes

$$\sigma_{max}(x,t) = Ec\frac{\partial^2}{\partial x^2}\left\{\sum_{n=1}^{\infty}\gamma_n\phi_n(x)R_n(t)\right\} \quad (\text{psi}). \qquad \text{(A-5)}$$

By differentiating Eq. (A-5) twice with respect to x, we obtain:

$$\sigma_{max}(x,t) = Ec\sum_{n=1}^{\infty}\gamma_n\frac{d^2\phi_n(x)}{dx^2}R_n(t) \quad (\text{psi}). \qquad \text{(A-6)}$$

By definition the shock spectrum relative displacement d is defined as the maximum absolute value of the undamped response as follows:

$$d_n = |R_n(t)|_{max} \quad (\text{in.}). \qquad \text{(A-7)}$$

The shock spectrum acceleration a commonly called the equivalent static acceleration, is defined as:

$$a_n = \omega_n^2 d_n = |\omega_n^2 R_n(t)|_{max} \text{ (in./sec}^2\text{)}. \quad \text{(A-8)}$$

By substitution of $|R_n(t)|_{max} = a_n/\omega_n^2$ into Eq. (A-6), it becomes

$$\sigma_{max}(x) = Ec \sum_{n=1}^{\infty} \gamma_n \frac{d^2\phi_n(x)}{dx^2} \cdot \frac{a_n}{\omega_n^2} \text{ (psi)}. \quad \text{(A-9)}$$

The quantity $d^2\phi_n(x)/dx^2$ can be expressed as a dimensionless quantity $\Phi_n''(x)$. From Ref. 6, we obtain the following two relationships for beam-type structures:

$$\Phi_n''(x) = \frac{I}{\beta_n^2} \frac{d^2\phi_n(x)}{dx^2} \quad \text{(A-10)}$$

$$\omega_n = (\beta_n \ell)^2 \sqrt{\frac{EI}{\mu \ell^4}} \text{ (rad/sec)}. \quad \text{(A-11)}$$

By substituting

$$\frac{d^2\phi_n(x)}{dx^2} = \beta_n^2 \Phi_n''(x)$$

and

$$\omega_n^2 = (\beta_n \ell)^4 \frac{EI}{\mu \ell^4}$$

into Eq. (A-9), we obtain

$$\sigma_{max}(x) = \frac{Ec}{EI/\mu\ell^4} \sum_{n=1}^{\infty} \gamma_n \beta_n^2 \Phi_n''(x) \frac{a_n}{(\beta_n \ell)^4}$$

$$= \frac{c\mu\ell^2}{I} \sum_{n=1}^{\infty} \gamma_n \Phi_n''(x) \frac{a_n}{(\beta_n \ell)^2} \text{(psi)}. \quad \text{(A-12)}$$

The quantities γ_n and $(\beta_n \ell)$ are not a function of x and can be summed from n = 1 to ∞ for simple beam structures. The quantity $\Phi_n''(x)$ can be selected to correspond to the location on the beam of the maximum bending stress. Therefore, for any specific beam:

$$\sum_{n=1}^{\infty} \frac{\gamma_n \Phi_n''(x)}{(\beta_n \ell)^2} = \text{constant} \quad \text{(A-13)}$$

Equation (A-12) becomes for any one specific beam configuration:

$$\sigma_{max} = \bar{A} \sum_{n=1}^{\infty} a_n \text{ (psi)} \quad \text{(A-14)}$$

where

$$\bar{A} = \frac{c\mu \ell^2}{I} \sum_{n=1}^{\infty} \frac{\gamma_n \Phi_n''(x)}{(\beta_n \ell)^2}.$$

At high frequencies the shock spectrum equivalent static acceleration a of Eq. (A-14) will become asymptotically equal to the peak acceleration of the shock time history G_g. This is commonly referred to as the structural system acting like an accelerometer at high frequencies. Therefore, to facilitate the beam failure analysis, it will be assumed here that the shock spectrum equivalent static acceleration is constant and equal to the peak acceleration of the shock time history, as follows:

$$a_n = G_g \quad \text{for} \quad n = 1, 2, 3, \ldots \infty \quad \text{(A-15)}$$

where G is the peak acceleration (g), and g is the gravitational constant (386.4 in./sec^2). (This is true for simple pulses. It is necessary to multiply the peak acceleration input G_g by a "transient resonant magnification" factor when the shock record is complex and contains many frequencies.)

Substituting Eq. (A-15) into Eq. (A-14) we obtain:

$$\sigma_{max} = \frac{c\mu \ell^2 G_g}{I} \sum_{n=1}^{\infty} \frac{\gamma_n \Phi_n''(x)}{(\beta_n \ell)^2} \text{ (psi)}. \quad \text{(A-16)}$$

For a beam with a rectangular cross section

$$c = \frac{h}{2}$$

$$I = \frac{bh^3}{12} \quad \text{(A-17)}$$

$$\mu = \frac{\rho bh}{g}$$

where

h is the thickness of the beam (in.)

b is the width of the beam (in.)

ρ is the weight density of the beam (lb/in.^{3}).

Therefore, for a rectangular cross section

$$\frac{c\mu}{I} = \frac{h}{2} \frac{2\rho bh}{bh^3} \frac{g}{12} = \frac{6\rho}{gh^2} \quad \text{(A-18)}$$

and Eq. (A-16) becomes

$$\sigma_{max} = \frac{5\rho \ell^2 G}{h} \sum_{n=1}^{\infty} \frac{\gamma_n \Phi_n''(x)}{(\beta_n \ell)^2} \quad (psi). \quad \text{(A-19)}$$

By equating the maximum bending stress σ to the allowable yield stress of the beam material F_{ty}, Eq. (A-19) is rewritten as follows:

$$\frac{h}{\ell^2} = \frac{6 \sum_{n=1}^{\infty} \frac{\gamma_n \Phi_n''(x)}{(\beta_n \ell)^2}}{F_{ty}/\rho} G = A \frac{G}{F_{ty}/\rho} \ (1/in.) \quad \text{(A-20)}$$

where

F_{ty}/ρ is the material strength to weight ratio

A is

$$6 \sum_{n=1}^{\infty} \frac{\gamma_n \Phi_n''(x)}{(\beta_n \ell)^2}$$

and is constant for a given beam structure.

A relationship exists between h/ℓ^2 and the modal frequencies of beam structures as presented in Ref. 5, and is derived as follows, from Eq. (A-11):

$$\omega_n = (\beta_n \ell)^2 \sqrt{\frac{EI}{\mu \ell^4}} \quad (rad/sec). \quad \text{(A-21)}$$

For a rectangular cross section the square root in Eq. (A-21) is:

$$\sqrt{\frac{EI}{\mu \ell^4}} = \frac{1}{\ell^2} \sqrt{\frac{E\, bh^3/12}{\rho\, bh/g}} = \frac{h}{\ell^2} \sqrt{\frac{g}{12}} \sqrt{\frac{E}{\rho}} . \quad \text{(A-22)}$$

For most structural materials $E/\rho = 10^8$; therefore, Eq. (A-22) becomes

$$\sqrt{\frac{EI}{\mu \ell^4}} = 5.6745 \times 10^4 \frac{h}{\ell^2} . \quad \text{(A-23)}$$

Substituting Eq. (A-23) into Eq. (A-21), we obtain

$$\omega_n = 5.6745 \times 10^4 (\beta_n \ell)^2 \frac{h}{\ell^2} \quad (rad/sec). \quad \text{(A-24)}$$

Since

$$f_n = \frac{\omega_n}{2\pi} \quad (cps), \quad \text{(A-25)}$$

Eq. (A-24) becomes

$$f_n = C_n \frac{h}{\ell^2} \quad (cps) \quad \text{(A-26)}$$

where

$$C_n = 9031 (\beta_n \ell)^2$$

and is constant for each mode of vibration of a beam.

Equations (A-20) and (A-26) are equated to provide a relationship between modal frequencies of a beam structure and the peak acceleration of a shock time history that will yield the beam. The relationship is as follows:

$$f_n = C_n \cdot A \cdot \frac{1}{F_{ty}/\rho} \cdot G \quad (cps). \quad \text{(A-27)}$$

Appendix B

FAILURE AND FREQUENCY ANALYSES FOR A UNIFORM CANTILEVER BEAM WITH AND WITHOUT A POINT MASS AT THE FREE END

Appendix B is a continuation of Appendix A for a uniform cantilever beam with and without a point mass at the free end. Two equations derived in Appendix A that are utilized in this appendix are Eqs. (A-20) and (A-26) as follows:

$$\frac{h}{\ell^2} = A \frac{G}{F_{ty}/\rho} \ (1/in.) \quad \text{(B-1)}$$

where

$$A = 6 \sum_{n=1}^{\infty} \frac{\gamma_n \Phi_n''(x)}{(\beta_n \ell)^2}$$

and

$$f_n = C_n \frac{h}{\ell^2} . \quad \text{(B-2)}$$

where

$$C_n = 9031\ (\beta_n \ell)^2 .$$

The coefficients A and C_n are evaluated for a cantilever beam with and without an end mass.

From Ref. 6 the characteristic function ϕ is as follows:

$$\phi_n(x) = \cosh \beta_n x - \cos \beta_n x - \sigma_n(\sinh \beta_n x - \sin \beta_n x) . \quad \text{(B-3)}$$

The characteristic function has been normalized so that

$$\int_0^{\ell} \phi^2 dx = \ell(\text{in.}) \quad \text{for} \quad n = 1, 2, 3, \ldots \infty. \quad \text{(B-4)}$$

From Ref. 6 the quantity $\Phi_n''(x)$ from Eq. (B-1) is maximum at $x/\ell = 0$ for all modes and equals 2.0. This beam location corresponds to the maximum stress at the root of the cantilever beam. The quantity $\beta_n \ell$ is tabulated below for the first five modes of a uniform cantilever beam, and was obtained from Ref. 4. The modal participation factor is also presented and was obtained from Ref. 6.

Mode	$\beta_n \ell$	γ_n
1	1.8751	0.7830
2	4.6941	0.4339
3	7.8548	0.2544
4	10.9955	0.1819
5	14.1372	0.1415

The summation of the infinite series of Eq. (B-1) is as follows:

$$\sum_{n=1}^{\infty} \frac{\gamma_n \Phi_n''}{(\beta_n \ell)^2} = 2.0 \left\{ \frac{0.7830}{(1.8751)^2} + \frac{0.4339}{(4.6941)^2} + \frac{0.2544}{(7.8548)^2} + \frac{0.1819}{(10.9955)^2} + \frac{0.1415}{(14.1372)^2} \right\}$$

$$+ 2.0 \sum_{n=5}^{\infty} \frac{\gamma_n}{(\beta_n \ell)^2} = 0.49745 + 2 \sum_{n=6}^{\infty} \frac{\gamma_n}{(\beta_n \ell)^2} . \quad \text{(B-5)}$$

For $n > 5$,

$$\beta_n \ell \doteq (2n - 1)\frac{\pi}{2} \quad \text{and} \quad \gamma_n \doteq \frac{4}{\pi(2n-1)} ,$$

from Refs. 6 and 7; therefore the summation of Eq. (B-5) becomes:

$$\sum_{n=6}^{\infty} \frac{\gamma_n}{(\beta_n \ell)^2} = \sum_{n=6}^{\infty} \left[\frac{4}{\pi(2n-1)}\right] \Big/ \left[(2n-1)^2 \frac{\pi^2}{4}\right]$$

$$= \frac{16}{\pi^3} \sum_{n=6}^{\infty} \frac{1}{(2n-1)^3} . \quad \text{(B-6)}$$

The upper and lower bounds for an infinite series can be obtained from Ref. 8, as follows:

$$\int_N^{\infty} f(x)\, dx \le \sum_{n=N}^{\infty} u_n \le \int_{N-1}^{\infty} f(x)\, dx \quad \text{(B-7)}$$

where

$$f(n) = u_n .$$

The integration of the upper and lower bounds of the series of Eq. (B-6) yields:

$$\text{upper bound:} \quad \int_5^{\infty} \frac{dx}{(2x-1)^3} = \frac{1}{4(9)^2} = \frac{1}{324} \quad \text{(B-8)}$$

$$\text{lower bound:} \quad \int_6^{\infty} \frac{dx}{(2x-1)^3} = \frac{1}{4(11)^2} = \frac{1}{484} . \quad \text{(B-9)}$$

Therefore, the upper and lower bounds of Eq. (B-5) are 0.50063 and 0.49958, respectively. The average value is 0.50011, with a maximum possible variation of ±0.00053 or ±0.1 percent. Therefore, for engineering purposes, Eq. (B-5) is as follows:

$$\sum_{n=1}^{\infty} \frac{\gamma_n \Phi_n''}{(\beta_n \ell)^2} = 0.50011 \quad \text{(B-10)}$$

Substituting this value of the summation into Eq. (B-1), we obtain:

$$\frac{h}{\ell^2} = 6(0.500)\frac{G}{F_{ty}/\rho} = \frac{3G}{F_{ty}/\rho} . \quad \text{(B-11)}$$

The effect of using higher modes to compute the maximum bending stress at the root of a cantilever beam is indicated by Eq. (A-19) of Appendix A, as follows:

$$\sigma_{max} = \frac{6\rho \ell^2 G}{h} \sum_{n=1}^{\infty} \frac{\gamma_n \Phi_n''(x)}{(\beta_n \ell)^2} \quad \text{(psi)} . \quad \text{(B-12)}$$

The summation from n = 1 to ∞ is given in Eq. (B-10) as 0.50011. The values of the quantities γ_n and $\beta_n \ell$ are tabulated above, and $\Phi_n''(x)$ has been shown to equal 2.0. Table B-1 presents the amount which the modes of vibration

TABLE B-1
Effect of Higher Modes on Accuracy of Computing the Maximum Stress at the Root of a Cantilever Beam

Mode (N)	$\frac{\gamma_n \Phi_n''}{(\beta_n \ell)^2}$	Percent Contributed by Mode	$\sum_{n=1}^{N} \frac{\gamma_n \Phi_n''}{(\beta_n \ell)^2}$	Accumulative Percentage of Maximum Stress
1	0.44539	89.06	0.44539	89.06
2	0.03938	7.88	0.48477	96.94
3	0.00825	1.65	0.49302	98.59
4	0.00301	0.60	0.49603	99.19
5	0.00142	0.28	0.49745	99.47
$5 \rightarrow \infty$	0.00266	0.53	0.50011	100.00

contribute to the maximum stress at the root of the uniform cantilever beam subjected to a constant acceleration shock spectrum. Obtaining $\beta_n \ell$ from the tabulation above, Eq. (B-2), for the first three bending modes, is:

$$f_n^{I} = 9031\ (1.8751)^2 \left(\frac{h}{\ell^2}\right) = 31,753\ \frac{h}{\ell^2}\ \text{(cps)}$$

$$f_n^{II} = 9031\ (4.6941)^2 \left(\frac{h}{\ell^2}\right) = 198,993\ \frac{h}{\ell^2}\ \text{(cps)}$$

$$f_n^{III} = 9031\ (7.8548)^2 \left(\frac{h}{\ell^2}\right) = 557,183\ \frac{h}{\ell^2}\ \text{(cps)}. \qquad \text{(B-13)}$$

We now extend the investigation of the uniform cantilever beam to include the case of a point mass at the free end. The effective mass of the beam to be added to the point mass is shown in Ref. 9 to be

$$m_e = 0.24267\ m_b\ \text{(lb-sec}^2\text{/in.)} \qquad \text{(B-14)}$$

where

m_e is the effective mass of the beam assumed to act at the free end (lb-sec^2/in.)

m_b is the mass of the beam (lb-sec^2/in.).

Equation (B-14) is obtained in Ref. 9 by equating the maximum kinetic energy of a massless cantilever beam with an end mass to a uniform distributed mass cantilever beam with no end mass.

The single-degree-of-freedom natural frequency of the massless beam with an end mass is:

$$f_n = \frac{1}{2\pi}\sqrt{\frac{k}{m}}\ \text{(cps)} \qquad \text{(B-15)}$$

where, for a cantilever beam,

$k = 3EI/\ell^3$ (lb/in.)

$m = (N + 0.24267)\, m_b$ (lb-sec^2/in.)

N = end mass weight/beam weight.

The mass m is equal to the end mass plus the effective mass of the beam. For convenience the end mass is represented as N times the mass of the beam. For a rectangular cross section, we obtain the following:

$$I = \frac{bh^3}{12}\ \text{(in.}^4\text{)}$$

$$m_b = \frac{\rho bh\ell}{g}\ \text{(lb-sec}^2\text{/in.)}.$$

Therefore, Eq. (B-15) becomes:

$$f_n = \frac{1}{2\pi}\sqrt{\frac{3EI}{\ell^3}\,\frac{g}{(N + 0.24267)\,\rho bh\ell}}$$

$$= \frac{1}{2\pi}\,\frac{h\sqrt{g}}{2\ell^2}\sqrt{\frac{E}{\rho}}\,\frac{1}{\sqrt{N + 0.24267}}\ \text{(cps)}. \qquad \text{(B-16)}$$

Since $\sqrt{E/\rho} = 10^4$ for structural materials, Eq. (B-16) becomes

$$f_n = \frac{15,643}{\sqrt{N + 0.24267}}\,\frac{h}{\ell^2}\ \text{(cps)}. \qquad \text{(B-17)}$$

The maximum bending stress of the massless cantilever beam with an end mass is now equated to the maximum bending stress at the root of the uniform cantilever beam. The maximum bending stress of the uniform cantilever beam is found by summing the infinite series for all normal modes of vibration. The root stress of the massless beam with an end mass is due to the first mode only.

The maximum bending stress for a rectangular cross section is

$$\sigma_{max} = \frac{6M}{bh^2} \quad (psi) \qquad (B\text{-}18)$$

where

M is the bending moment (in.-lb)

b and h are the width and thickness of the rectangular cross section.

The bending moment at the root of the massless cantilever beam with an end mass is

$$M = (W_m \ell \quad W_b \ell_e) G \quad (in.-lb) \qquad (B\text{-}19)$$

where

W_m is the weight of the end mass (lb)

W_b is the weight of the beam (lb)

ℓ is the length of the cantilever beam (in.)

ℓ_e is the effective length of the beam to equate the maximum bending stresses (in.).

The effective length ℓ_e of the beam is found to be equal to $(1/2)\ell$ by equating Eq. (B-18) with zero end mass to Eq. (B-12). Equation (B-18) with zero end mass is

$$\sigma_{max} = \frac{6}{bh^2} W_b \ell_e G \quad (psi). \qquad (B\text{-}20)$$

Since $W_b = \rho bh\ell$, Eq. (B-20) becomes

$$\sigma_{max} = \frac{6\rho\ell\ell_e G}{h} \quad (psi). \qquad (B\text{-}21)$$

Equation (B-12) is rewritten, with the value of the infinite summation of 0.500 as obtained in Eq. (B-10), as follows:

$$\sigma_{max} \quad \frac{6\rho\ell^2 G}{h} (0.500) = \frac{3\rho\ell^2 G}{h} \quad (psi). \qquad (B\text{-}22)$$

By comparing Eqs. (B-21) and (B-22), it is seen that $\ell_e = (1/2)\ell$.

By substituting $\ell_e = (1/2)\ell$ into Eq. (B-19), we obtain

$$M = \ell\left(W_m + \frac{1}{2} W_b\right) G \quad (in.-lb). \qquad (B\text{-}23)$$

Since $W_m = NW_b$, we can rewrite Eq. (B-23) as

$$M = \ell W_b \left(N + \frac{1}{2}\right) G \quad (in.-lb) \qquad (B\text{-}24)$$

By substituting the equation for the weight of the beam, and Eq. (B-24) into Eq. (B-18), we obtain

$$\sigma_{max} = \frac{6\ell(\rho bh\ell)\left(N + \frac{1}{2}\right)G}{bh^2} = \frac{6\ell^2 \rho G}{h}\left(N + \frac{1}{2}\right) \quad (psi). \qquad (B\text{-}25)$$

By letting the maximum bending stress equal the allowable yield stress F_{ty}, we can rewrite Eq. (B-25) as follows:

$$\frac{h}{\ell^2} = \frac{6\left(N + \frac{1}{2}\right)}{F_{ty}/\rho} G \quad (1/in.) \qquad (B\text{-}26)$$

Equations (B-17) and (B-26) are the two equations relating the frequency to the peak acceleration of the shock time history. By substituting Eq. (B-26) in Eq. (B-17), we obtain

$$f_n = \frac{15.643}{\sqrt{N + 0.24267}} \frac{6\left(N + \frac{1}{2}\right)}{F_{ty}/\rho} G = \frac{93.858}{F_{ty}/\rho} \frac{N + \frac{1}{2}}{\sqrt{N + 0.24267}} G \quad (psi), \qquad (B\text{-}27)$$

which is the cutoff frequency for data analysis as a function of the peak acceleration of the time history.

Appendix C

FAILURE AND FREQUENCY ANALYSES OF A UNIFORM SIMPLY SUPPORTED BEAM WITH AND WITHOUT A POINT MASS AT THE MIDLENGTH

Appendix C is a continuation of Appendix A for a uniform simply supported beam with and without a point mass at the midlength. Two equations derived in Appendix A that are utilized in this appendix are Eqs. (A-20) and (A-26), as follows:

$$\frac{h}{\ell^2} \quad A \frac{G}{F_{ty}/\rho} \quad (1/in.) \qquad (C\text{-}1)$$

where

$$A \quad 6 \sum_{n=1}^{\infty} \frac{\gamma_n \Phi_n^*(x)}{(\beta_n \ell)^2} \quad , \quad f_n \quad C_n \frac{h}{\ell^2} \quad (cps) \qquad (C\text{-}2)$$

where

$$C_n = 9031\ (\beta_n \ell)^2 .$$

The coefficients A and C_n are evaluated for a simply supported beam with and without a center mass.

From Ref. 10, the characteristic function ϕ is as follows:

$$\phi_n(x) = \sin \beta_n x \qquad \text{(C-3)}$$

where

$$\beta_n \ell = n\pi \quad \text{for} \quad n = 1,3,5,7,\ldots \infty .$$

The characteristic function has been normalized so that

$$\phi_{n_{max}} = 1.0 \quad \text{for} \quad n = 1,2,3,\ldots \infty . \qquad \text{(C-4)}$$

The modal participation factor is obtained as follows:

$$\gamma_n = \frac{\int_0^{\ell} \mu \phi_n(x)\, dx}{\int_0^{\ell} \mu \phi_n^2(x)\, dx} = \frac{2}{n\pi}\left[1 - (-1)^n\right]$$

$$= \frac{4}{n\pi} \text{ for } n = 1,3,5,7,\ldots \infty \qquad \text{(C-5)}$$

where

$$\phi_n(x) = \sin \frac{n\pi}{\ell} x .$$

The quantity $\Phi_n^*(x)$ is equal to 1.0 at $x = \ell/2$, and alternates in sign. Since the shock response method of Refs. 2 and 11 is a summation of the absolute values, the sign change presents no problem. The summation of the infinite series of Eq. (C-1) is as follows:

$$\sum_{\substack{n=1 \\ 3,5}}^{\infty} \frac{\gamma_n \Phi_n^*}{(\beta_n \ell)^2} = \sum_{\substack{n=1, \\ 3,5}}^{\infty} \frac{\frac{4}{n\pi}(1.0)}{(n\pi)^2}$$

$$= \frac{4}{\pi^3} \sum_{\substack{n=1, \\ 3,5}}^{\infty} \frac{1}{n^3} . \qquad \text{(C-6)}$$

By using the same method utilized in Appendix B to evaluate the infinite series, we obtain

$$\sum_{\substack{n=1 \\ 3,5}}^{\infty} \frac{1}{n^3} = 1.05204 \qquad \text{(C-7)}$$

which has a maximum possible variation of ± 0.001 or ± 0.1 percent. Therefore, Eq. (C-6) becomes

$$\sum_{\substack{n=1, \\ 3,5}}^{\infty} \frac{\gamma_n \Phi_n^*}{(\beta_n \ell)^2} = \frac{4}{\pi^3}(1.052) = 0.13572 . \qquad \text{(C-8)}$$

By substituting Eq. (C-8) into Eq. (C-1), we obtain

$$\frac{h}{\ell^2} = 6(0.13572)\frac{G}{F_{ty}/\rho} = 0.8143\ \frac{G}{F_{ty}/\rho} . \qquad \text{(C-9)}$$

The effect of using higher modes to compute the maximum bending stress at the midlength of a simply supported beam is seen by inspecting Eq. (A-19), which is

$$\sigma_{max} = \frac{6\rho \ell^2 G}{h} \sum_{\substack{n=1, \\ 3,5}}^{\infty} \frac{\gamma_n \Phi_n^*}{(\beta_n \ell)^2} \quad \text{(psi)}. \qquad \text{(C-10)}$$

The summation of the infinite series in Eq. (C-10) from $n = 1,3,5,7,\ldots \infty$ is given in Eq. (C-8) as 0.13572. Table C-1 presents the amount which the modes of vibration contribute to the maximum stress at the midlength of the uniform simply supported beam subjected to a constant acceleration shock spectrum. From the second part of Eq. (C-3), Eq. (C-2) is, for the first three bending modes, as follows:

$$f_n^{I} = 9031\ (\pi)^2 \left(\frac{h}{\ell^2}\right) = 89.135\ \frac{h}{\ell^2} \quad \text{(cps)}$$

$$f_n^{II} = 9031\ (3\pi)^2 \left(\frac{h}{\ell^2}\right) = 802.215\ \frac{h}{\ell^2} \quad \text{(cps)}$$

$$f_n^{III} = 9031\ (5\pi)^2 \left(\frac{h}{\ell^2}\right) = 2,228.375\ \frac{h}{\ell^2} \quad \text{(cps)} \qquad \text{(C-11)}$$

We now extend the investigation of the uniform simply supported beam to include the case of a point mass at the midlength. The effective mass of the beam to be added to the point mass is shown in Ref. 9 to be

$$m_e = 0.4928\ m_b \quad (\text{lb-sec}^2/\text{in.}) \qquad \text{(C-12)}$$

where

TABLE C-1
Effect of Higher Modes on Accuracy of Computing the Maximum Stress at the Midlength of a Simply Supported Beam

Mode (n)	$\frac{\gamma_n \Phi_n^*}{(\beta_n \ell)^2}$	Percentage Contributed by Mode	$\sum_{n=1,3,5}^{2N-1} \frac{\gamma_n \Phi_n^*}{(\beta_n \ell)^2}$	Accumulative Percentage of Maximum Stress
1	0.12901	95.06	0.12901	95.06
2	0.00478	3.52	0.13379	98.58
3	0.00103	0.76	0.13482	99.34
4	0.00090	0.66	0.13572	100.00

m_e is the effective mass of the beam assumed to act at the midlength (lb-sec^2/in.)

m_b is the mass of the beam (lb-sec^2/in.).

Equation (C-12) is obtained in Ref. 9 by equating the maximum kinetic energy of a massless simply supported beam with a center mass, to a uniform cantilever beam with no center mass.

The single-degree-of-freedom natural frequency of the massless beam with a center mass is

$$f_n = \frac{1}{2\pi}\sqrt{\frac{k}{m}} \quad (\text{cps}). \qquad \text{(C-13)}$$

where, for a simply supported beam,

$k = 48\,EI/\ell^3$ (lb/in.)

$m = (N + 0.4928)\, m_b$

N = center mass weight/beam weight.

The mass m is equal to the center mass plus the effective mass of the beam. For convenience, the center mass is represented as N times the mass of the beam. For a rectangular cross section, we obtain the following

$$I = \frac{bh^3}{12} \quad (\text{in.}^4)$$

$$m_b = \frac{\rho bh\ell}{g} \quad (\text{lb-sec}^2/\text{in.}).$$

Therefore, Eq. (C-13) becomes

$$f_n = \frac{1}{2\pi}\sqrt{\frac{48EI}{\ell^3 (N + 0.4928)\frac{\rho bh\ell}{g}}}$$

$$= \frac{1}{\pi}\,\frac{h\sqrt{g}}{\ell^2}\sqrt{\frac{E}{\rho}}\,\frac{1}{\sqrt{N + 0.4928}} \qquad \text{(C-14)}$$

Since $\sqrt{E/\rho} = 10^4$ for structural materials, Eq. (C-14) becomes

$$f_n = \frac{62.571}{\sqrt{N + 0.4928}}\,\frac{h}{\ell^2} \quad (\text{cps}). \qquad \text{(C-15)}$$

The maximum bending stress of the massless simply supported beam with a center mass is now equated to the maximum bending stress at the midlength of the uniform simply supported beam. The maximum bending stress of the uniform simply supported beam is found by summing the infinite series for all normal modes of vibration. The midlength stress of the massless beam with a center is due to the first mode only.

The maximum bending stress for a rectangular cross section is

$$\sigma_{max} = \frac{6M}{bh^2} \quad (\text{psi}) \qquad \text{(C-16)}$$

where

M is the bending moment (in.-lb)

b and h are the width and thickness of the rectangular cross section.

The bending moment at the midlength of the massless simply supported beam with a center mass is

$$M = \frac{1}{4}(W_m \ell + W_b \ell_e)\,G \quad (\text{in.-lb}) \qquad \text{(C-17)}$$

where

W_m is the weight of the mass (lb)

W_b is the weight of the beam (lb)

ℓ is the length of the beam (in.)

l_e is the effective length of the beam to equate the maximum bending stress (in.).

The effective length l_e of the beam is found to be equal to $0.5428\,l$ by equating Eq. (C-16) with zero center mass to Eq. (C-10). Equation (C-16) with zero center mass is

$$\sigma_{max} = \frac{6}{bh^2}\left(\frac{1}{4} W_b l_c\right) G \quad (psi). \qquad (C\text{-}18)$$

Since $W_b = \rho bhl$, Eq. (C-18) becomes

$$\sigma_{max} = \frac{1.5\rho l l_c G}{h} \quad (psi). \qquad (C\text{-}19)$$

Equation (C-10) is rewritten, with the value of the infinite summation of 0.13572 as obtained in Eq. (C-8), as follows:

$$\sigma_{max} = \frac{6\rho l^2 G}{h}(0.13572) = \frac{0.81432\rho l^2 G}{h} \quad (psi). \qquad (C\text{-}20)$$

By comparing Eqs. (C-19) and (C-20), it is seen that $l_e = 0.54288\,l$.

By substituting $l_e = 0.54288\,l$ into Eq. (C-17), we obtain

$$M = \frac{1}{4} l (W_m + 0.54288\, W_b) G \quad (in.\text{-}lb). \qquad (C\text{-}21)$$

Since $W_m = NW_b$, we can rewrite Eq. (C-21) as

$$M = \frac{l W_b}{4}(N + 0.54288) G \quad (in.\text{-}lb). \qquad (C\text{-}22)$$

By substituting the equation for the weight of the beam, and Eq. (C-22) into Eq. (C-16), we obtain

$$\sigma_{max} = \frac{6l\,(\rho bhl)(N + 0.54288) G}{4bh^2}$$

$$= \frac{1.5 l^2 \rho G}{h}(N + 0.54288) \quad (psi). \qquad (C\text{-}23)$$

By letting the maximum bending stress equal the allowable yield stress F_{ty}, we can rewrite Eq. (C-23) as follows:

$$\frac{h}{l^2} = \frac{1.5\,(N + 0.54288)}{F_{ty}/\rho} G \quad (1/in.). \qquad (C\text{-}24)$$

Equations (C-15) and (C-24) are the two equations relating the frequency to the peak acceleration of the shock time history. By substituting Eq. (C-24) in Eq. (C-15), we obtain

$$f_n = \frac{62.571}{\sqrt{N + 0.4928}} \frac{1.5\,(N + 0.54288)}{F_{ty}/\rho} G$$

$$= \frac{93,856.5}{F_{ty}/\rho} \frac{N + 0.54288}{\sqrt{N + 0.4928}} G \quad (cps). \qquad (C\text{-}25)$$

which is the cutoff frequency for data analysis as a function of the peak acceleration of the time history.

REFERENCES

1. M. Gertel and R. Holland, "Effect of Digitizing Detail on Shock and Fourier Spectrum Computation of Field Data," Shock and Vibration Bull., 36 (Part 6):1-19 (1967)
2. Dana Young, "Response of Structural Systems to Ground Shock," Shock and Structural Response. M. V. Barton (Ed.) (American Society of Mechanical Engineers, New York) (1960)
3. F. L. Singer, Strength of Materials (Harper, New York), 1951
4. A. S. Niles and J. S. Newell, Airplane Structures, Vol. 1 (Wiley, New York), 1954
5. J. N. Macduff and R. P. Felgar, "Vibration Design Charts," paper presented at the annual meeting of the American Society of Mechanical Engineers, New York, Nov. 1956
6. Dana Young and R. P. Felgar, "Table of Characteristic Functions Representing Normal Modes of Vibration of a Beam," Univ. of Texas Publ. 4913, July 1949
7. C. E. Crede, "Failure Resulting From Vibration," Random Vibration, Vol. 2, S. H. Crandall (Ed.) (MIT Press, Cambridge, Mass.), 1963
8. A. E. Taylor, Advanced Calculus (Blaisdell, New York), 1955
9. L. S. Jacobsen and R. S. Ayre, Engineering Vibrations (McGraw-Hill, New York), 1958
10. R. E. D. Bishop and D. C. Johnson, The Mechanics of Vibration (Cambridge University Press, N.Y.), 1960
11. R. O. Belsheim and G. J. O'Hara, "Shock Design of Shipboard Equipment Part I - Dynamic Design - Analysis Method," NAVSHIPS 250-432-30, May 1961

DISCUSSION

Mr. Koehler (Orenda, Ltd.): On the last curve you extended the spectrum at the high end. It seems to be asymptotic. What was the instrumentation threshold level for that curve?

Mr. Gertel: These records were obtained by environmental engineers at Frankford Arsenal. I believe the capabilities of the instrumentation extended to approximately 2 kc. We carried our spectral analyses out to about 4 kc just to get beyond the instrumentation limitation.

Mr. Koehler: It is not so much the frequency limitation I was concerned with, but the amplitude limitation across the full frequency band. Presumably there is a threshold of noise which would be irrelevant as far as the test is concerned. Where would this line be?

Mr. Gertel: The shock spectrum line was asymptotic to approximately 300 g, which represents the peak acceleration measured near the beginning of that particular transient. The peak was certainly well above the noise threshold.

Mr. Angelopulos (Lockheed Missiles & Space Co.): In your paper you discuss a simple shock transient. It has been my experience that there is more than one type of shock transient. How do you treat these different types of shock transients? Do you segregate them? Do you average them?

Mr. Gertel: I'm afraid I am not familiar with that problem. We digitized the transient record without consideration as to what it was. We did not make any attempt to separate different types of transients.

* * *

TRANSIENT VIBRATION SIMULATION

Thomas E. Fitzgerald and Louis C. Kula
The Boeing Company
New Orleans, Louisiana

The sinusoidal sweep test normally used to simulate transient-vibration conditions was replaced by a short-duration, high-intensity shaped random-vibration test devised by the Structural Dynamics Group of The Boeing Company, Aerospace Division, Launch Systems Branch, New Orleans, Louisiana.

During the reliability test program of the S-IC stage of the Saturn V vehicle, certain critical system components were subjected to simulation of the transient vibrations that occur during the engine shutdown phase of static firings. Originally, the simulation consisted of a rapidly scanned sinusoidal sweep. It became apparent that the sinusoidal sweep did not truly simulate the engine shutdown phenomena, since overly destructive resonance response levels were attained during the scan. Consequently, the random-type transient simulation method was devised.

With pertinent vibration data obtained during the static firings of the test vehicles, octave band analyses of the acceleration levels in the frequency range of 25 to 2000 Hz produced appropriate acceleration levels for each octave band. Then, the power spectral density levels of a random equalizer-analyzer were adjusted so that the same acceleration levels could be obtained, in the various octave bands, that were obtained in the analysis of the static firing data. The test specimen was then subjected to the resulting vibration spectrum for a time approximating the duration of the transient engine shutdown.

INTRODUCTION

Vibration response data obtained during captive firings of the S-IC stage, first stage of the Saturn V vehicle, form the basis for conducting the vibration portion of the reliability test program. The acceleration data are divided into two parts, the main stage condition and engine cutoff condition (see Fig. 1). The vibration resulting from main stage operation is essentially random in nature, is of constant intensity, and is simulated in the laboratory by a constant rms acceleration (g_{rms}) random-vibration test.

The vibration resulting from engine cutoff is of high intensity and transient in nature. Simulation of engine cutoff vibration was accomplished originally by conducting a rapidly scanned sinusoidal sweep test. It was found that the sinusoidal sweep test was too severe in simulating the engine cutoff. A duct, located on the S-IC stage, had repeated failures during the sinusoidal tests, although an identical duct survived several captive firings. For this reason a new short-duration, high-intensity shaped random-vibration test was devised to replace the sinusoidal sweep test.

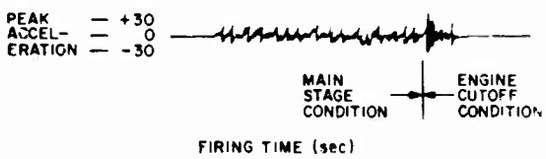

Fig. 1. Vibration response data obtained during captive firings of the S-IC stage

VEHICLE VIBRATION ENVIRONMENT

The reliability test program of the S-IC stage required certain critical system components to be tested to assure a reliability goal of 95 percent. The program was designed to prevent the failure of critical components which would prevent the S-IC stage or Saturn V vehicle from completing its assigned mission.

Vibration is one of the environments which the S-IC stage must survive. It is of particular importance because of the high loading condition imposed on many of the critical system components. The evidence to date indicates that two primary stimulants of damaging vibration to the S-IC stage are:

1. The sound field of the rocket engine;

2. The direct vibration transmission from the rocket engines.

The vibration response data taken during the captive firings of the S-IC stage are divided into two parts:

1. Steady-state random vibration occurring during main stage operation.

2. High-level transient vibration occurring at engine cutoff. The transient condition is caused by an explosion of fuel and oxidizer which accumulates after the engines are shut off.

Main Stage Condition

An analysis of response data obtained from the primary structure during static firing of the S-IC stage provided the basis by which the components' input vibration environments were developed for the reliability test program. Data from the main stage condition were analyzed as shown in Fig. 2. The rms acceleration remained constant during the main stage condition. An envelope of the analyzed vibration data from the main stage condition was constructed to provide the requirements for the simulation in the laboratory. The enveloped spectrum is also shown in Fig. 2.

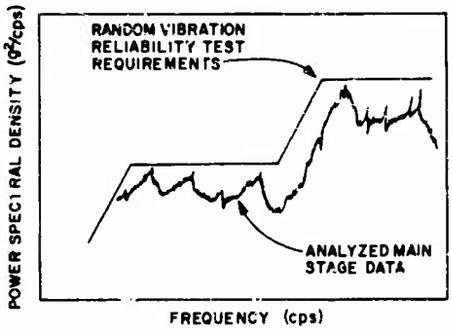

Fig. 2. Analysis of data from main stage condition

Cutoff Condition

The measured response vibration data obtained during the engine cutoff condition were analyzed by filtering the data over octave frequency bands and measuring the peak acceleration levels within each of the bands (see Fig. 3 and Table 1). The peak acceleration levels were enveloped (Fig. 4) to provide a sinusoidal sweep test to simulate the engine cutoff condition in the laboratory. The sweep rate was set at 10 octaves per minute because of the short duration (0.2-1.0 sec) of the cutoff condition. It would have been desirable to sweep at a faster rate, but maintaining the input vibration at the desired levels is difficult because of laboratory test equipment limitations.

TABLE 1
Engine-Cutoff Transient Analysis

Frequency Range (cps)	Peak Acceleration Measurements (g)				
	(1)	(2)	(3)	(4)	(5)
25-50	44	54	56	31	35
50-100	40	39	41	24	23
100-200	47	81	51	28	39
200-400	19	34	58	20	13
400-800	15	69	44	11	12
800-1600	17	65	27	8	20

SIMULATED CUTOFF CONDITION; SINUSOIDAL SWEEP TEST

Historically the sinusoidal sweep test has been used to simulate high-level random-vibration environments such as the engine cutoff condition. This has been done when the simulation of high-level random-vibration environments is unattainable by random-vibration tests because of laboratory equipment power limitations. During the sinusoidal sweep test, power is required only at a single frequency and consequently higher levels may be obtained.

The sinusoidal sweep test simulating the high-level cutoff condition was used during the early stages of the reliability test program. Midway in the test program, repeated fatigue failures occurred during the sinusoidal sweep tests of a particular duct. A reevaluation of the sinusoidal sweep test as an adequate simulation of the cutoff condition was undertaken. This was done especially since the same type of duct had survived engine cutoff during captive firing. The reevaluation resulted in the following conclusions:

1. The sinusoidal sweep test did not simulate the short-duration cutoff conditions.

2. The response acceleration of the test specimen attained during the sinusoidal sweep

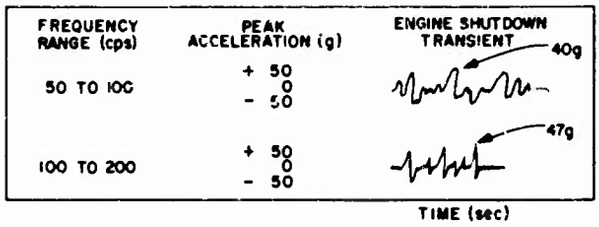

Fig. 3. Analysis of data from cutoff transient condition (measurement 1)

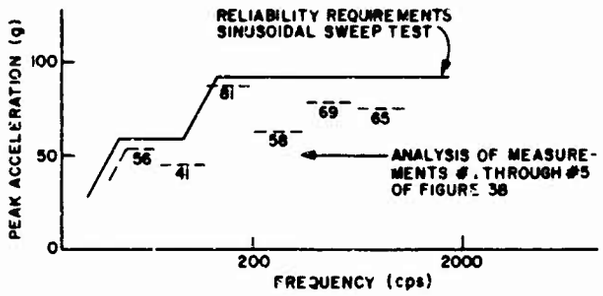

Fig. 4. Analysis of data from cutoff transient condition

test was far greater than during the cutoff condition. The degree of difference would depend on a number of conditions, namely, the mounting conditions of the specimen, specimen configuration, stiffness properties, and damping devices.

3. The ratio of high-acceleration fatigue cycles experienced during the sinusoidal sweep test to those during the actual engine shutdown condition was on the order of 200 to 1.

IMPROVED TEST SIMULATION

The conclusion noted above required the development of an improved method of simulating the cutoff condition. The improved method was devised after determining that the motion behavior of the vibrational stimulants and of the complex motion system of the laboratory possessed statistical properties similar to a Gaussian density function. Because of the Gaussian properties, the probability of peak acceleration levels occurring at the 3-σ level is only 0.27 percent. The cutoff condition is reasonably duplicated because these high-level peaks occur for such a small percentage of the time. In addition to the input, the response is also properly simulated, providing the main reason for acceptance of the improved simulation of the cutoff condition. For this reason, the improved test simulation was formulated The method consisted of specifying a peak acceleration at each octave band for a random-vibration requirement. It is believed to be a new approach to high-level, random-vibration simulation.

The peak acceleration requirements for conducting an improved simulation of the engine cutoff are given in Table 2. They are derived in a manner similar to that used to derive the sinusoidal test requirements. Applicable S-IC structure response measurements were analyzed and provided the peak acceleration of each octave band for the specimens input requirement.

Because the complex motion vibration system does provide a probability density function that is reasonably Gaussian, the system will produce peak accelerations which are at least three times the overall rms acceleration. This fact was incorporated in setting up the random spectrum. An example of the final levels of a shaped random spectrum, as derived from the peak acceleration requirements, is shown in Tables 2 and 3.

TABLE 2
Input Specification for Cutoff Condition

Octave Band (cps)	Maximum Peak Acceleration (g)
25-50	28
50-100	20
100-200	13
200-400	14
400-800	34
800-1600	32
1600-2000	32

TABLE 3
Corresponding Random-Vibration Spectrum for Data Presented in Table 2

Octave Band (cps)	Power Spectral Density (g^2/cps)	Overall Level (g_{rms})
25-50	+9 db/oct[a]	9.5
50	7.5	
50-100	0.8	6.5
100-200	0.2	4.5
200-400	0.12	4.5
400-800	0.32	10.3
800-1600	0.18	9.5
1600-2000	0.19	9.5

[a]Peak g's for various frequencies within the 25-50 band occurred in a manner to provide the +9 db/octave slope. This was verified after reviewing the results of experimental data vs engine cutoff data.

The time required for testing was obtained by measuring the elapsed time of the actual cutoff condition. Because the transient condition is a response of basic structure, the time varied from 0.2 to 1.0 sec depending upon the location of the response measurement. A number of test runs were conducted to determine an acceptable length of time in which to obtain the required peak acceleration levels. This time was determined to be a minimum of 0.8 sec. Tests in the laboratory are conducted for 1.0 sec with a tolerance of -0.2 sec, +1.0 sec. The maximum tolerance of +1.0 sec was specified because of human response time. It should be noted that the required time specified for the test is conservative. Electrical circuitry has now been provided to control the length of test time to within 0.1 sec.

Although the maximum peak acceleration level found in the data samples was specified as the required test level, a tolerance requirement was statistically determined to be ±50 percent. By taking three standard deviations on either side of the mean (required test level), 99.73 percent of the possible peak occurrences of the Gaussian distribution would be taken into account and therefore provide the ±50 percent tolerance. Each frequency band was analyzed for several input requirements and the ±50 percent tolerance held true within practical limits. The tolerance therefore became a standard for the remaining tests of the reliability test program.

LABORATORY PROCEDURES FOR THE NEW SIMULATION

To perform the new random transient simulation with a standard random-vibration control console, it is necessary to convert from a specification of peak acceleration per octave band to a specification of constant power spectral density level for that particular octave band. Assuming that 3-σ peak accelerations occur in each octave band, the overall rms acceleration level was computed for that band. Then, assuming the spectrum to be flat within each band, the power spectral density level for the band was computed. Once the desired power spectral density levels were known, individual filter adjustments of a standard multichannel equalizer were made and the required levels attained. In practice a 9-db/octave roll-off was used below 50 cps. The following procedure was subsequently followed. Prior to performing the test a closed loop plot of the programmed input to the exciter was made. This plot was made by feeding the output of the random equalizer into its corresponding analyzer. A plot of analyzer output in terms of power spectral density vs frequency was obtained.

The power spectral density levels of the closed loop plot had to conform with the computed levels. The closed loop plot, also, served as a reference for subsequent testing.

The initial test run was then made and an octave-band analysis of the input acceleration data performed. This analysis, which was in the form of peak acceleration vs time, was reviewed before further transient simulation tests were performed. If the octave band analysis revealed out-of-tolerance conditions, the

appropriate changes were made in the specified power spectral density spectrum.

Experience indicates that a tolerance of ±25 percent of the specified peak acceleration level could be held 60 percent of the time, although a ±50 percent tolerance was used for the S-IC reliability test program.

CONCLUSION

The short-duration, high-intensity shaped random-vibration test should be used to replace the sinusoidal sweep test where applicable, because of the relative simplicity of the test and the many advantages. Two primary benefits realized were:

1. The simulated random environment closely duplicated the true environment because vibration motion was fundamentally of a Gaussian nature. This provided a reasonably similar amplification of the test specimen response and a realistic number high-energy fatigue cycles.

2. The overdesign of a specimen, normally needed to meet requirements of the sinusoidal sweep test, would be unnecessary.

BIBLIOGRAPHY

R. L. Rich and J. A. Roberts, "S-IC Reliability Program From Structural Life Viewpoint," Shock and Vibration Bull. 36 (Part 7): 19 (1967)

DISCUSSION

Mr. Painter: Did you consider the use of a short duration pulse for your test rather than using the random burst. If so, why did you choose to take a short burst of random signal and shape it in the spectral sense?

Mr. Kula: I believe you are referring to some type of shock pulse. Our required time was one second in length, and therefore a simple shock pulse would not apply. There was more of a random type condition.

Mr. Painter: I wasn't really referring to a simple pulse, but to what you get when you apply a simple pulse to an array of bandpass filters. This gives a ringing type of vibration that is probably rather similar to what you obtained with your random input.

Mr. Kula: Another condition that we are trying to simulate is the number of high energy fatigue cycles that the specimen would receive. With a pulse we wouldn't get this distribution of a number of peaks occurring within this time limit.

PREDICTING MECHANICAL SHOCK TRANSMISSION

Jerome E. Manning and Kyung Lee
Bolt Beranek and Newman Inc.
Cambridge, Massachusetts

Classic methods of shock transmission analysis, which take into account only a few modes of a structure, are inadequate for many problems. Because of the broad frequency content of the shock, many, often hundreds, of modes will be excited. A promising energy-flow method of analysis has been developed. The method yields a time history of the vibratory energy in various regions of a structure. The energy stored in a region of a structure can be used to estimate the average vibration level in that region.

The method has been used to obtain predictions for an aerospace vehicle subjected to a pyrotechnic shock. The agreement between theory and experiment is satisfactory.

INTRODUCTION

This paper describes an energy-flow method of analysis to study mechanical shock transmission. The method allows treatment of cases where shock loading establishes resonant, high-frequency ringing. These cases cannot be analyzed adequately by existing methods. The normal mode approach accurately predicts the response of the first few modes of the structure. Wave propagation methods provide analysis of the primary phase of the shock, which results from direct transmission of the source shock, without reflections in the structure. Our method is suggested as a complement to these classic approaches.

The method has yet to be developed with full mathematical rigor, and some of our procedures are left unsupported. It evolved from a physical understanding of shock transmission.

The fundamental idea of our analysis is to divide a complex structure into a set of coupled subsystems. These may consist of either continuous or discrete elements. A time history of the vibratory energy in each subsystem results, if we equate the net vibratory-power input to the subsystem with the rate of change of its stored energy.

The major problem in such an analysis is to calculate the coupling factors which govern the rate of energy flow between subsystems. We have used steady-state coupling factors. A number of references give calculations of steady-state coupling factors between basic structural elements, e.g., beams, plates, cylinders, etc. [1-5]. The use of steady-state parameters to study shock transmission seems valid for quasi-steady vibrations, where the resonant ringing of the subsystems occurs with a slowly varying envelope. The commonly accepted experimental technique (e.g., Ref. 3, section III-C) of estimating steady-state coupling factors and damping factors by decay-rate measurements further supports this approach.

MECHANICAL SHOCK

Mechanical shock may be produced by a number of different sources such as pyrotechnic devices, missile staging, explosions, and aircraft landings. The shock loading at the impact point is characterized by short-rise-time, high-intensity forces. These forces cause correspondingly short-rise-time, high-amplitude accelerations at the loading point. Vibratory energy of the source shock propagates throughout the structure in the form of compressional, shear, and bending waves in the structural elements.

At each discontinuity in the structure, some of the incident energy is reflected and the remainder transmitted. After several discontinuities, most of the energy from the primary shock pulse has been reflected. The reflected energy sets up a ringing in the structural elements, which persists until it is damped out.

A typical shock at an equipment mounting point, separated from a pyrotechnic device by a beam-plate junction, is shown in Fig. 1. This type of shock, with which we are specifically concerned, can be described as a fluctuating signal with a slowly varying envelope.

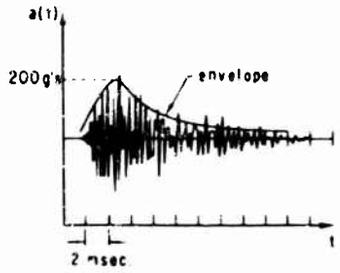

Fig. 1. Typical acceleration time history

DIVISION OF COMPLEX STRUCTURES INTO SUBSYSTEMS

The first step of our procedure is to divide the structure into subsystems. This division is somewhat arbitrary, and should be guided by both our ability to calculate coupling factors and the required detail of the solutions

To explain more fully, our procedure leads to the energy in each subsystem. But it does not lead to the distribution of energy in the subsystem. In general, a detailed modal analysis is required to gain this information. If, however, the subsystem is reasonably homogeneous, and many modes contribute to its response, the energy will be distributed uniformly in the subsystem. Plates, shells, and beams qualify as homogeneous subsystems. Ribbed plates and shells may or may not qualify. It depends on whether or not uniformity of the energy field applies.

Coupling factors have been calculated, with some approximations, for a number of idealized cases: coupled beams, plates, cylinders, lumped masses, and mass-spring oscillators. Application of the analysis with different elements, or for different types of coupling, requires calculation of the coupling factors.

Our conclusion is that a structure should be subdivided into a set of coupled beams, plates, shells, and simple lumped-parameter systems. An idealized two-subsystem structure is shown in Fig. 2. This structure consists of a beam (subsystem 1) joined to a plate (subsystem 2).

POWER BALANCE EQUATIONS

Consider a structure, such as that shown in Fig. 2, which can be divided into two subsystems. The division is shown schematically in Fig. 3. For these subsystems we can identify the stored energy (E) in each subsystem, the power dissipated by each subsystem, the power input to each subsystem, and the power transferred between the subsystems. A simple power balance on each subsystem results in the following equations:

$$\Pi_1^{in} - \Pi_{12}^{trans} - \Pi_1^{diss} = \frac{dE_1}{dT} \qquad (1a)$$

and

$$\Pi_{12}^{trans} - \Pi_2^{diss} = \frac{dE_2}{dT} \qquad (1b)$$

The next step of the analysis is to relate the power flows to the stored energies through the steady-state coupling factors. For the steady state, the power flow in a frequency band is

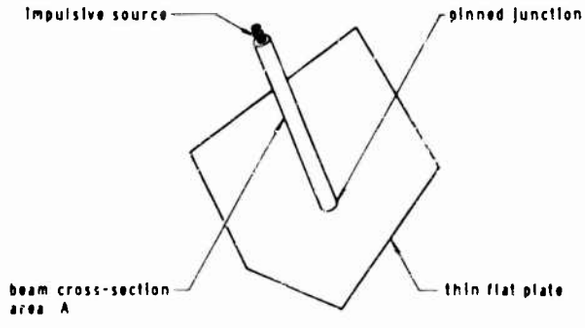

Fig. 2. Beam-plate structure

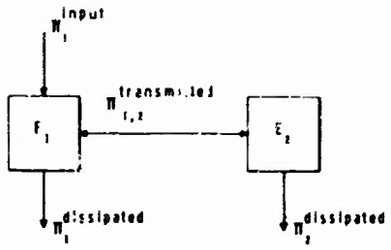

Fig. 3. Power-flow diagram

proportional to the difference in modal energy of the two subsystems:

$$\Pi_{12}^{trans}(\omega) = \omega \eta_{12} n_1 \left[\frac{E_1(\omega)}{n_1} - \frac{E_2(\omega)}{n_2} \right], \qquad (2)$$

where η_{12} is the coupling loss factor between subsystems 1 and 2, n_1 is the modal density of subsystem 1, and E_1 is the energy of subsystem 1 in the frequency band. To write this equation, we must assume that the response of each subsystem is a result of resonant response of the modes.

At this point we make an assumption, which allows us to use the steady-state coupling factors to predict transient response. The assumption is that the transient response is a result of modal resonances; i.e., each mode responds at its resonance frequency. This implies that the modal energy in one band does not contribute to the response of modes with resonances in other bands. If we let $E(\omega,T)\Delta\omega$ be the average energy at time T of all modes with resonances $\Delta\omega$, power flow between subsystems in the frequency band $\Delta\omega$ can be written as

$$\Pi_{12}^{trans}(\omega,T) = \omega \eta_{12} n_1 \left[\frac{E_1(\omega,T)}{n_1} - \frac{E_2(\omega,T)}{n_2} \right], \qquad (3)$$

where ω is the center frequency of the band, η_{12} is the steady-state coupling parameter, and n_1 is the modal density of element 1. The power dissipated in the frequency band $\Delta\omega$ is

$$\Pi_1^{diss}(\omega,T) = \omega \eta_1 n_1 \frac{E_1(\omega,T)}{n_1} \qquad (4)$$

Equations (3) and (4), in the power-flow equations, result in the following two equations:

$$\frac{\partial}{\partial T} E_1(\omega,T) + \omega \left[\eta_{12} + \eta_1 \right] E_1(\omega,T) - \omega \eta_{12} \frac{n_1}{n_2} E_2(\omega,T) = \Pi_1^{in}(\omega,T) \qquad (5a)$$

and

$$\frac{\partial}{\partial T} E_2(\omega,T) + \omega \left[\frac{n_1}{n_2} \eta_{12} + \eta_2 \right] E_2(\omega,T) - \omega \eta_{12} E_1(\omega,T) = 0. \qquad (5b)$$

We can now solve for the stored energy in subsystem 1, $E_1(\omega,T)$, and stored energy in subsystem 2, $E_2(\omega,T)$. The vibration amplitude relates to the stored energy, since for resonant response the time-average kinetic energy equals the time-average potential energy:

$$M_1 \langle v_1^2 \rangle_{x,t} = E_1. \qquad (6)$$

where M_1 is the total mass of the subsystem, and $\langle v^2 \rangle_{x,t}$ is its squared velocity averaged over a cycle of vibration and over the spatial extent of the subsystem.

BEAM-PLATE STRUCTURE

As an example of the analytic procedure introduced in this paper, consider the beam-plate structure shown in Fig. 2. This structure is a model of the reentry vehicle sketched in Fig. 4. It consists of a beam pinned to a thin flat plate. Structural parameters are:

L = beam length = 2 ft

A_{beam} = beam cross-section area = 2 $in.^2$

ρ_{beam} = beam material volume density = 0.1 lb/$in.^3$

c_{beam} = beam compressional wavespeed = 17,000 ft/sec

A_{plate} = plate surface area = 40 ft^2

t = plate thickness = 0.375 in.

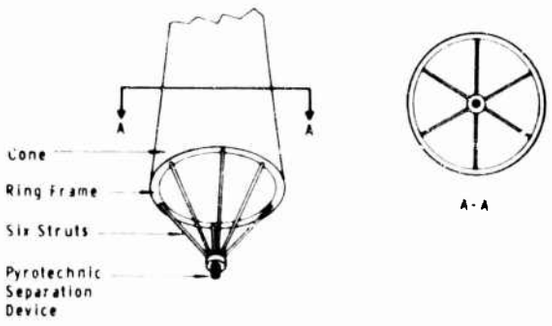

Fig. 4. Structural model of a reentry vehicle

c_{plate} = plate compressional wavespeed = 17,000 ft/sec

$F_{source}(t) = F_0 \sin 2\pi t/T$ for $0 < t < T$

F_0 = 5000 lb

T = 0.2 msec.

An impulsive source is located at one end of the beam. We will calculate the vibration envelope time history at an average point on the plate. Bending of the beam is uncoupled to bending of the plate because of the pinned joint. Therefore, only compressional modes of the beam need to be considered. The first compressional beam mode is at 4000 Hz. This predicted frequency is not exact because of the end condition at the plate junction. We have taken the resonant frequency of a free-free beam. Our calculations will be restricted to interactions between the first mode of the beam and the plate.

We can make three approximations for the beam-plate structure that will simplify the required calculations. First, the beam dissipation loss factor can be taken to be much less than the coupling loss factor between the beam and the plate: $\eta_1 \ll \eta_{21}$. Then we can take the modal density of the beam to be much less than that of the plate, since we are considering interactions involving only the first mode of the beam. This allows the approximation $\eta_1\eta_{12} \ll \eta_2\eta_2$, which amounts to neglecting the power flow from the plate back into the beam. Finally, the source-shock time duration can be taken short enough for the power into the beam to be impulsive:

$$\Pi_1^{in}(\omega_0,T) = E_0\delta(T) . \qquad (7)$$

The power-flow equations, Eqs. (5a) and (5b), can be simplified to the equations below:

$$\frac{\partial}{\partial T} E_1(\omega_0,T) + \omega_0 \eta_{12} E_1(\omega_0,T) = E_0 \delta(T) \quad (8a)$$

and

$$\frac{\partial}{\partial T} E_2(\omega_0,T) + \omega_0\eta_2 E_1(\omega_0,T) = \omega_0\eta_{12} E_1(\omega_0,T), \quad (8b)$$

where ω_0 is the resonance frequency of the first mode. These equations yield the following solutions:

$$E_1(\omega_0,T) = E_0 e^{-\omega_0\eta_{12}T} \qquad (9a)$$

and

$$E_2(\omega_0,T) = E_0 \frac{\eta_{12}}{\eta_{12}-\eta_2}\left\{e^{-\omega\eta_2 T} - e^{-\omega\eta_{12}T}\right\} . \qquad (9b)$$

where $\eta_{12} - \eta_2$ has been assumed to be nonzero. For cases in which $\eta_{12} = \eta_2$, a different form of solution will be obtained.

To complete our example, we must calculate the coupling loss factor η_{21}, the plate dissipation loss factor η_2, and the input energy E_0.

To calculate η_{12}, we consider the interaction between the beam and an infinite plate. For this case, the power input to the plate is given as

$$\Pi_{12}(\omega_0,T) = \omega_0 \eta_{12} E_1(\omega_0,T) . \qquad (10)$$

where E_1 is the energy of the first mode of the beam. Because of the impedance mismatch between the beam and the plate, we will assume that the beam acts as a velocity source. Then, the mean-square velocity at the beam-plate junction will be twice the spatial-average mean-square velocity of the beam. The power into the infinite plate becomes

$$\Pi_{12}(\omega_0,T) = \frac{2 I_{infinite\ plate}}{M_{beam}} M_{beam} \langle v^2\rangle_{x,t} \qquad (11)$$

where $I_{infinite\ plate}$ is the point input impedance of the infinite plate, M_{beam} is the total mass of the beam, and $M_{beam}\langle v^2\rangle_{x,t}$ is the total energy of the beam in its first mode. It follows that the coupling loss factor is

$$\eta_{12} = \frac{2 I_{infinite\ plate}}{\omega_0 M_{beam}} = \frac{4.6\,\rho_{plate}\, t^2 c_\ell}{\omega_0 M_{beam}} . \qquad (12)$$

The dissipation loss factor of the plate η_2 cannot be calculated theoretically. We must rely on an empirical prediction that $\eta_2 = 0.025$.

We will assume for this example that the duration of the source shock is less than 0.25 msec, which is the time for compressional waves to travel twice the length of the beam. For such a short-duration force input, the velocity in the beam can be given as

$$v(x,t) = \frac{F(t - x/c_\ell)}{I_{infinite\ beam}} , \qquad (13)$$

where $I_{infinite\ beam}$ is the input impedance of an infinite beam

$$I_{infinite\ beam} = \rho_{beam} c_\ell A . \qquad (14)$$

After the source shock the energy in the first mode of the beam can be given as

$$E_0 = M_{beam}\left\{\frac{1}{\rho_{beam} c_\ell A}\int_0^{2T} F\left(T - \frac{x}{c_\ell}\right)\psi_1(x)\,dx\right\}^2 . \qquad (15)$$

where T is the shock duration and where $\psi_1(x)$ is the mode shape

$$\psi_1(x) = \sqrt{\frac{2}{L}} \cos \frac{\pi x}{L} . \qquad (16)$$

The parameters η_{12}, η_2, and E_0 have been calculated numerically for the beam-plate system. Calculated values are:

$\omega_0 = 2\pi f_0$ = fundamental beam resonance frequency = 25,000 Hz

η_{12} = coupling loss factor = 0.1

η_1 = beam dissipation loss factor ≈ 0

η_2 = plate dissipation loss factor = 0.025

E_0 = 2.3 ft-lb.

The numerical solution of Eq. (9b) using these values is shown in Fig. 5. The envelope of the vibration has a rapid rise followed by a slow exponential decay. The rise is a result of energy flowing into the plate from the beam, while the decay is the result of energy being dissipated in the plate.

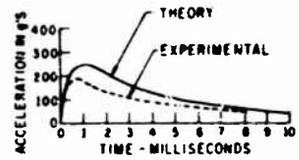

Fig. 5. Response acceleration envelope

EXPERIMENTAL RESULTS

We have conducted experiments on a structural model of a reentry vehicle, sketched in Fig. 4. The impulsive source in this vehicle is a pyrotechnic separation nut. The force generated by this device can be approximately described as one cycle of a sine wave with an amplitude of 10,000 lb. (The input force for the model has been reduced to 5000 lb because the relative angle between the beam and cone in the actual vehicle is 45 deg.) Sensitive electronic components are located on the cone of the vehicle. An experimental program was conducted in which accelerometers were located at various points on the cone, and the resulting shock from the pyrotechnic separation nut measured. The envelope of an acceleration time history for a typical point on the cone is shown in Fig. 5 and can be compared with our theoretical calculations for the beam-plate model of this vehicle. The comparison is quite good and indicates that our method of analysis is promising.

REFERENCES

1. R. H. Lyon and G. Maidanik, "Statistical Methods in Vibration Analysis," AIAA J., 2 (6): (1964)
2. R. H. Lyon and E. Eichler, "Random Vibration of Connected Structures," J. Acoust. Soc. Amer., 36 (7):1344 (1964)
3. R. H. Lyon and T. C. Scharton, "Vibrational Energy Transmission in a Three-Element Structure," J. Acoust. Soc. Amer., 38 (2):253 (1965)
4. R. H. Lyon, Random Noise and Vibration in Space Vehicles, Shock and Vibration Information Center, U.S. Department of Defense, Washington, D.C., 1967
5. J. E. Manning et al., "The Transmission of Sound and Vibration to a Shroud-Enclosed Spacecraft," BBN Rept. 1431 (submitted Oct. 1966 to NASA Goddard Space Flight Center, to be issued as Contractor's Report)

DISCUSSION

Mr. Mustain (McDonnell-Douglas Corp.): I've been working on a shock monograph with Dr. Ayre of the University of Colorado. Dr. Sheldon Rubin, Harry Himelblau, Ralph Blake, and several others were on the review board. In our conclusions we indicated that, for a low-frequency type of shock, an analysis of a mathematical model could be made by techniques that are available. On the other hand, we have definitely taken the stand that there is no analysis possible for the explosive type of shock. We find it very difficult to establish the impedances of a structure: you have to build the structure and make impedance measurements. You have hinted that an analysis may be possible.

Mr. Manning: We use the impedances of infinite systems to model the impedances of actual finite systems. This is valid for high-frequency vibrations. In the problem that I described, we evaluated the force output of the pyrotechnic device and got a rough idea of the

input impedance, which we used to calculate the power into the system. Knowing the power into the system, one can proceed with the type of analysis I have outlined. I think that the answers would be fairly accurate, perhaps within 25 percent of the peak level or a little better.

Mr. Holland (Allied Research Assoc.): How did you obtain the experimental values of the response accelerations on the plate? Did you use strain gages or accelerometers?

Mr. Manning: Accelerometers.

Mr. Holland: At how many points?

Mr. Manning: We used a recording at one point. We made recordings at many points, and they were all similar.

Mr. Holland: Were they also similar for many different pyrotechnic explosions?

Mr. Manning: We did only two explosions, and they were similar.

Mr. Holland: Did you vary your explosion to see if the accelerometer read differently?

Mr. Manning: I make no great claims about the experiment that was done. I hesitated somewhat to present this paper because the work is quite recent; I think a better experiment and a more detailed analysis is called for. I am only trying to get across rough ideas here.

Mr. Holland: I bring this up because, in the experimental work on complex structures, you get focusing and nodes with reverberation. From one shot to another you can get many different readings. As we saw before, shock spectra seem to be constant, independent of the pyrotechnic and the clamping on other spacecraft structures.

Mr. Manning: For our device, the frequencies were very high. Hundreds of modes interact; and I think you could make a strong argument that the vibration field, since it is a result of so many modes, would be fairly uniform on the plate involved. In the first drawing that I presented, there was a predominant frequency. This was the first resonant frequency of the beam in the system. At that frequency, the plate had many, many modes.

Mr. Kapur (Aerospace Corp.). How did you obtain the dissipation load factor and the coupling loss factor? They are obviously difficult to calculate.

Mr. Manning: It would be desirable to measure them. However, I estimated the dissipation loss factor and used a simplified theoretical analysis for the coupling loss factors. To calculate the coupling loss factors, you assume that the beam in the system and the plate are both infinite. Then you know the driving point impedances of the plate and the source impedance of the beam, since it is infinite. Any of the work done on statistical energy analysis involves calculating these coupling loss factors.

Mr. Painter (Lockheed-California Co.): In the literature on the energy method, there are some indications that one can, with circuit diagrams and the use of reactive elements across the dissipators, use that type of analogy for transient work. Have you looked into this?

Mr. Manning: The circuit diagrams that have been drawn are equivalent circuits in which the elements represent rather complex impedances. The reason that you can use the lumped-parameter diagrams is that the impedances of the infinite systems are fairly simple. I know the diagrams are used mainly to calculate the coupling loss factors.

* * *

SHOCK DAMAGE MECHANISM OF A SIMPLE STRUCTURE*

Lowell T. Butt
Naval Ship Research and Development Center
Portsmouth, Virginia

Two sets of four cantilever beams loaded with tip masses were mounted on the floating shock platform and shock tested by underwater explosions. These simple mechanical models were designed to undergo appreciable plastic deformations. Three analytical approaches to predict shock damage were applied to these beam-mass models: (a) one considering elastic, perfectly plastic mode response; (b) another considering an energy balance to predict displacement bounds; and (c) the third considering an inelastic deformation mode approximation. The displacement bound and mode approximation methods were applied considering both elastic, perfectly plastic and rigid, perfectly plastic deformations. The analytical results were compared with experimental data. The elastic, perfectly plastic analysis shows good agreement with experiment up to the initial peak displacement. Computed elastic-plastic bounds and inelastic mode approximations also provide good estimations of the initial displacements.

INTRODUCTION

The shock design of shipboard equipment is based on elastic response analysis. However, a large class of ductile metal structures, when subjected to shock loadings from explosions, may undergo considerable plastic deformations before their performance is seriously degraded. Elastic response analysis methods cannot allow for this. Shock design methods which could take advantage of permissible plastic deformations should result in greater shock resistance of naval vessels, lighter shipboard installations, and reduced space requirements.

Development of a design method for dynamic plastic deformations is extremely difficult; first, a good understanding of the damage mechanism is required. Brown University recently developed under Navy contract a number of approximate procedures in the theory of plasticity that offered promise for a theoretical analysis of the dynamic plastic deformation of structures [1,2,3]. Consequently, as the initial phase of an investigation into shock damage mechanisms, simple mechanical models consisting of cantilever beams with tip masses were designed to undergo appreciable plastic deformations when subjected to the underwater explosion shock loading on the floating shock platform (FSP). Three plastic deformation prediction methods, which are described here, were applied to the experimental behavior of the beam-mass models.

EXPERIMENT

The beams for these models were standard 3 I 5.7 beams machined to give uniform dimensions throughout, as shown in Fig. 1. The tip masses were assembled from lead blocks and bolted to the beams. Four pairs of models with cantilever lengths between 29 and 11 in. and frequencies between 18 and 139 Hz were tested. Figure 2 is a schematic of the test array, and Fig. 3 shows a typical velocity history at the base of the cantilever. The input has been idealized to make it more amenable to mathematics. The duration time of the input motion is about 52 msec.

The relative displacement history of a beam-mass model measured at its tip mass is shown in Fig. 4. The displacement is relative to the FSP inner bottom. Starting from zero, the tip mass moves toward the FSP inner bottom. The elastic limit deflection is reached at point 1 of Fig. 4. The tip mass continues on, deforming the beam plastically until it reaches

*This paper presents the results of one phase of research conducted under Web Task 11.066, Sub Project S-F013 10 01, Task 2960, sponsored jointly by the Defense Atomic Support Agency and Naval Ship Engineering Center.

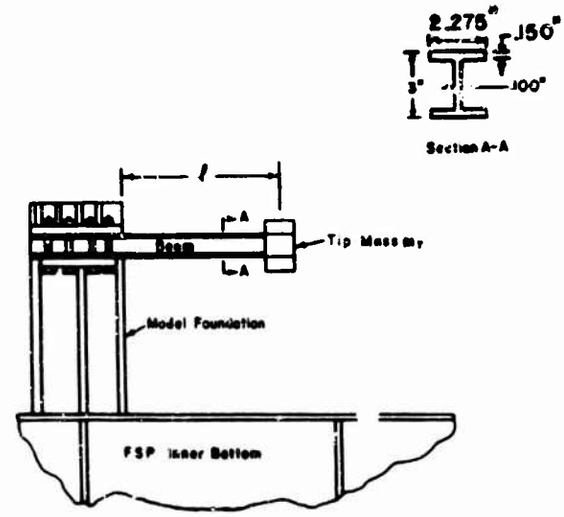

Fig. 1. Beam-mass model design

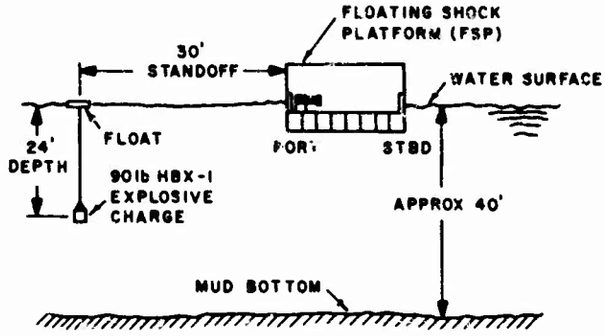

Fig. 2. Test array

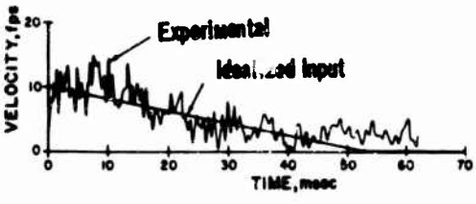

Fig. 3. Base velocity history

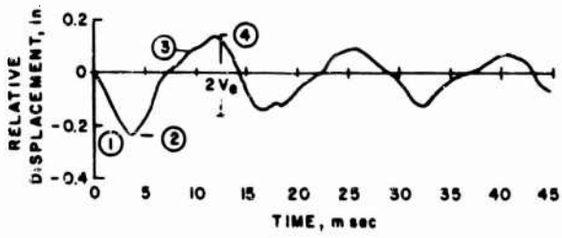

Fig. 4. Deflection history

point 2. From this peak, the tip mass begins to move away from the FSP inner bottom elastically, locking in a permanent deformation in the beam. The tip mass can continue elastically a distance twice the elastic limit deflection, which is reached at point 3; moving on from point 3, the beam is being deformed plastically. This deformation is in reverse to that locked in at point 2. The reverse plastic deformation continues until the tip mass reaches point 4, at which time elastic response begins and continues. At no later time does the peak-to-peak response exceed twice the elastic limit deflection. The total response shown occurs within the duration of the input.

THEORY

Three methods have been used in this study to predict the maximum deflection of the tip masses.

Elastic, Perfectly Plastic Mode Response

This method was derived from the complete solution of the equations of motion of a single-degree-of-freedom system subjected to a base motion which represents the idealized input velocity. To investigate this mechanism, a mathematical model with notation as shown in Fig. 5 was used. A typical force-deflection curve of the characteristics of the spring for this model is shown in Fig. 6. Here, F_e is the maximum force developed and is reached at the limiting elastic deflection Y_e. If after exceeding Y_e the displacement direction is reversed, the system remains elastic up to a change in deflection magnitude of $2Y_e$. The single mass-spring system is subjected to a base input motion consisting of an instantaneous initial velocity rise $\bar{V}$, which is followed by a linear drop to zero over a time T, as shown in Fig. 7.

The response of this idealized system to the idealized input velocity is briefly discussed here solely on the basis of energy considerations. (The appendix of Ref. 4 discusses the system in detail and presents curves for determining permanent sets.) By transferring to a set of coordinates attached to the base of the system, one obtains an equivalent system (one with the same relative displacements) by applying an initial velocity $-\bar{V}$ and a force $m\bar{V}/T$ to the mass. The force acts from the initiation of motion up to time T. Thus the energy input to the system may be divided into two parts: (a) the initial kinetic energy $m\bar{V}^2/2$, and (b) the work $(m\bar{V}/T)Y$ done by the decelerating force

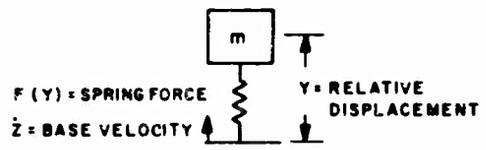

Fig. 5. Single mass-spring model

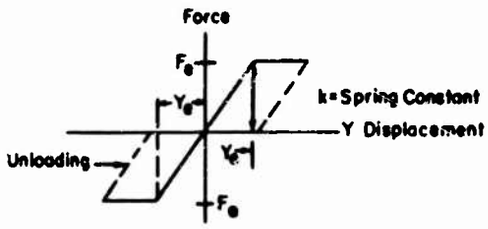

Fig. 6. Force-deflection relationship

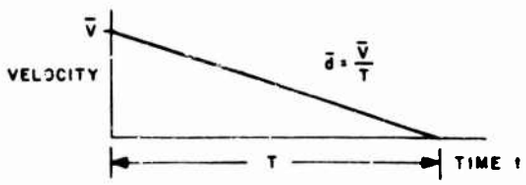

Fig. 7. Idealized velocity input

$m\bar{V}/T$ acting through the relative displacement Y of the mass. The description of the motion is characterized by two sets of solutions, each valid over a different interval of time, namely, for $0 < t < T$ and $t > T$. The differential equations valid over these time intervals are

$$\ddot{Y} + \frac{F(Y)}{m} = -\ddot{Z} = +\bar{d} \quad \text{for} \quad 0 < t < T \qquad (1)$$

$$\ddot{Y} + \frac{F(Y)}{m} = -\ddot{Z} = 0 \quad \text{for} \quad t > T \qquad (2)$$

where $F(Y) = kY$ for $0 < Y < Y_e$ and $F(Y) = F_e$ for $Y > Y_e$. The type of deformation depends on the magnitude of the initial velocity and the magnitude and duration of the force. Up to the first displacement extremum Y_1, which occurs at time t_1, the force extracts energy from the system. However, after time t_1 the force puts energy into the system so that the second displacement extremum Y_2, at time t_2, will exceed Y_1 in magnitude if $Y_1 < -Y_e$, and will exceed $Y_1 + 2Y_e$ if $Y_1 < -Y_e$. After t_2, the force again extracts energy from the system so that at no later time can the energy in the system exceed that at t_2; therefore, the system

moves elastically for $t > t_2$. Thus we are led to three deformation categories: (a) elastic response (no permanent deformation), (b) single plastic phase, and (c) reverse plastic phase. The elastic response occurs in systems where the input energy is not great enough to cause permanent deformation. An elementary momentum consideration will show that, for any system, t_1 is less than T. The total momentum of the equivalent system is composed of the initial momentum $-m\bar{V}$, the change in momentum produced by the deceleration $(m\bar{d})t$, and the momentum produced by the spring

$$\int_0^t F\,dt\ .$$

Since F is greater than zero for $t \leq t_1$ and the total momentum is zero at $t = t_1$, it follows that $\min(T, t_1)m\bar{d} - m\bar{V} < 0$ or $\min(T, t_1) < T$, and $t_1 < T$. Therefore the system energy is always greater near t_2 than near t_1. This means that if only one plastic phase occurs, it always occurs near t_2. For reverse plasticity we have both $Y_1 < -Y_e$ and $Y_2 > Y_1 + 2Y_e$. On the basis of energy considerations, the necessary and sufficient condition for reverse plasticity is

$$\frac{1}{2}kY_e^2 < \frac{1}{2}m\bar{V}^2 - m\frac{\bar{V}}{T}Y_e\ .$$

The minimum and maximum values of Y are given by

$$\left.\begin{aligned} &-F_e\left(Y_1 + \tfrac{1}{2}Y_e\right) = \tfrac{1}{2}m\bar{V}^2 + m\bar{d}Y_1 \\ &\text{or} \\ &-Y_1 = \frac{1}{2}\frac{(m\bar{V}^2 + F_eY_e)}{(F_e + m\bar{d})} \end{aligned}\right\} \text{for all } T \qquad (3)$$

$$\left.\begin{aligned} &F_e(Y_2 - Y_1 - 2Y_e) = m\bar{d}(Y_2 - Y_1) \\ &\text{or} \\ &Y_2 = Y_1 + \frac{2F_eY_e}{F_e - m\bar{d}} \end{aligned}\right\} \text{for } T \geq t_2\ . \qquad (4)$$

No simple relation can be obtained for $T < t_2$; however, curves have been derived for obtaining approximate values [4].

The method is applied to the models of this study by considering the cantilever fundamental mode and allowing the formation of a plastic hinge at its base. The effective m in the fundamental mode was determined from the formula of Ref. 5

$$m = m_T + 0.236\,\bar{m}\ell \qquad (5)$$

where m_T is the tip load mass and $\bar{m}$ is the mass per unit length along the beam length ℓ.

Displacement Bounds

The rigid-plastic bound method may be described as an energy balance between the initial kinetic energy, the work done by the forces acting during the response, and the plastic work. Early studies in the rigid, perfectly plastic approach were limited to impulsively loaded structures, which can be characterized as problems in which initial velocities are given at each point in the structure; thereafter, no external forces do work on the structure. Recently, this work was extended by Martin [1,2] and Olen and Martin [3] to include time-dependent body and surface forces acting on the structure. Upper bounds for displacements were established, and a mode approximation method was developed for estimating the deflections. Martin [1] proved that for a rigid-plastic structure,

$$\int_V \frac{\rho}{2}(v, v)\,dV \geq \int_A (P, u^f)\,dA \qquad (6)$$

where v is the initial velocity vector, ρ is the mass density, u^f is the final displacement vector, dV is differential volume, and A is surface area; P is a time-independent force vector function. In addition, there must exist at all times a stress field which is everywhere in equilibrium with the forces acting on the body — P plus actual surface and body forces — and is everywhere at or below the yield. To obtain a rigid-plastic displacement bound at a given point, we need only select $P = 0$ everywhere else and take the maximum P, consistent with the stress limitation, at the point in question. For an elastic-plastic material, one need only add a term which represents elastic strain energy to Eq. (6) to obtain

$$\int_V \frac{\rho}{2}(v, v)\,dV + \int_V \left(\int_0^{\sigma^s} \cdot\, d\sigma\right) dV \geq \int_A (P, u^f)\,dA \qquad (7)$$

where σ^s is the stress field previously mentioned [3]. The elastic-plastic bound is obtained in a manner similar to that for the rigid-plastic bound.

For the models in this study, the initial kinetic energy and the forces acting were derived from the idealized representation of the base velocity history. The resulting equivalent system is shown in Fig. 8. Here $\bar{d}$ is the

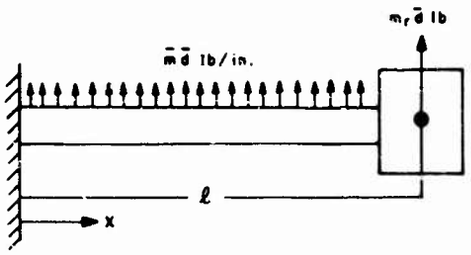

Fig. 8. External loading of model

uniform deceleration of the idealized input velocity; the vertical force P is placed at the mass for this study. Equating the initial kinetic energy to the work done by these forces plus the plastic work results in the rigid-plastic bound. For an elastic-plastic material, one need only add an elastic strain energy term to the initial kinetic energy.

Inelastic Mode Approximation

In the mode approximation method for a rigid-plastic structure, we may use the same system of Fig. 8; however, a velocity mode shape during deformation is assumed to be a product of a single space vector function ϕ and a time function $S(t)$; $v^* = S(t)\phi$. An equation of the energy difference $\Delta(t)$ is defined as

$$\Delta(t) = \int_V \frac{\rho}{2} [(v - v^*), (v - v^*)] dV \qquad (8)$$

where v is the actual velocity. It is also shown that Δ is a monotonically decreasing function of time, so that if $\Delta(0)$ is small (compared to the initial kinetic energy) then the mode is a good approximation. To make $\Delta(0)$ as small as possible for the assumed mode, it is required that

$$S(0) = \frac{\int_V \rho (v, \phi) dV}{\int_V \rho (\phi, \phi) dV} . \qquad (9)$$

Furthermore, the time of duration of the motion is less for the approximate mode than for the actual motion. The solution of the equation of motion can be interpreted in terms of simple energy relationships in the assumed mode. The solution may be very lengthy except for time-independent loads. For this mode approximation to hold with a reasonable degree of accuracy, it is necessary that the energy input be large compared with the elastic strain energy the system is capable of absorbing. For the models described in this report, the elastic strain energy accounts for a significant portion of the energy dissipated and, therefore, must be considered. There is no rigorous extension of this method to elastic-plastic structures; hence, an approximate extension is devised to predict the maximum deflection.

The force-deflection relationship of an elastic, perfectly plastic system in a given deflection mode may be represented as shown in Fig. 9, where F_e is the maximum resisting force of the system and Y_e is the elastic limit deflection. The internal strain energy is equal to the area under the force-deflection curve. At $Y = Y_1$ the energy is:

$$U_1 = \frac{1}{2} F_e Y_e + (Y_1 - Y_e) F_e$$

$$U_1 = Y_1 F_e - \frac{1}{2} F_e Y_e .$$

The force-deflection relationship for a similar rigid, perfectly plastic system may be represented as shown in Fig. 10, where F_e is the maximum resisting force of the system. The internal strain energy at $Y = Y_1^*$ is:

$$U_2 = F_e Y_1^* .$$

To determine the effect of the elastic portion of the response, the two energies are equated:

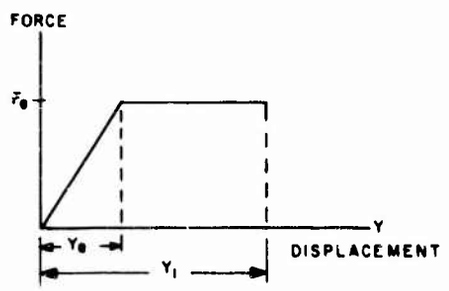

Fig. 9. Elastic–perfectly plastic force-deflection relationship

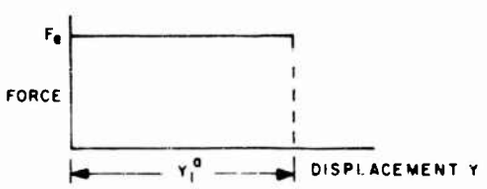

Fig. 10. Rigid–perfectly plastic force-deflection relationship

$$U_1 = U_2$$

$$Y_1 F_e - \frac{1}{2} F_e Y_e = F_e Y_1^*$$

$$Y_1 = Y_1^* + \frac{1}{2} Y_e$$

Thus it is seen that the peak displacement of an elastic, perfectly plastic single-degree-of-freedom system will be greater than that for a rigid, perfectly plastic system. However, the permanent deformation will be less. For the system under consideration, the peak displacement will be greater by at least one half of the elastic limit deflection for equal amounts of energy absorbed. This procedure is very similar to the rigorous procedure of Martin [2] for the displacement bound for elastic-plastic systems. Therefore, we expect that the elastic deflection system should be compatible with the assumed plastic mode; i.e., the maximum stresses should occur at the hinges of the rigid-plastic system, and the stresses should be in equilibrium with the forces acting. Since Y_1 includes the elastic limit deflection Y_e, the plastic deformation which we will call δ is $Y_1 - Y_e$.

To apply the rigid-plastic mode approximation to the cantilever beams, a simple linear velocity distribution is assumed with a plastic hinge at the base, as shown in Fig. 11. The initial amplitude of the mode, $S(0) = \alpha$, is obtained from Eq. (9):

$$\alpha = \frac{\int_0^\ell \bar{m}\bar{V}\left(\frac{x}{\ell}\right) dx + m_T \bar{V}}{\int_0^\ell \bar{m}\left(\frac{x}{\ell}\right)^2 dx + m_T} = \frac{3}{2}\bar{V}\left(\frac{\bar{m}\ell + 2m_T}{\bar{m}\ell + 3m_T}\right). \quad (10)$$

Equating initial energy to energy of decelerating force plus energy dissipated at plastic hinge, all in the assumed mode, leads to

$$Y_1^* = \frac{3\ell\bar{V}^2}{4} \frac{(\bar{m}\ell + 2m_T)^2}{(\bar{m}\ell + 3m_T)\left[2M_0 + d(\bar{m}\ell^2 + 2m_T\ell)\right]} \quad (11)$$

The correction for the elastic strain energy to obtain the elastic-plastic mode approximation is then made.

EVALUATION AND CONCLUSIONS

The elastic-plastic mode response accurately predicts the response of a single-degree-of-freedom system through the initial

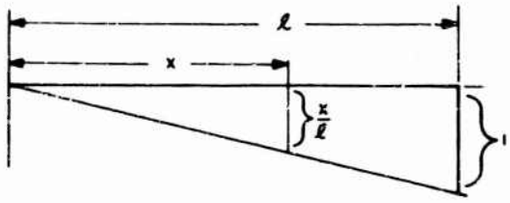

Fig. 11. Velocity mode shape

displacement extremum for the input assumed. The prediction becomes poor in time, as shown in Fig. 12. By the time of the second extremum, the correlation is only qualitative. Considered the most accurate of the methods studied, this method provides an excellent basis for evaluating the simpler approximate methods. The solution obtained through the second displacement provides insight into the secondary damage, and thus allows a sound basis for neglecting the secondary damage in cases where the initial set is of the order of at least three or four times the elastic limit deflection Y_e. All of the methods predicted the initial elastic-plastic displacement extremum equally well. The initial sets derived from these displacements agree within 0.4 Y_e and are within 0.9 Y_e of the final set. The computed results of each method and the measured result for one model follow:

Method	Initial Set Deflection (δ_1/Y_e)
Measured	-0.72
Elastic–perfectly plastic mode response	-0.97
Elastic–perfectly plastic bound	-1.02
Elastic–perfectly plastic mode approximation	-0.99

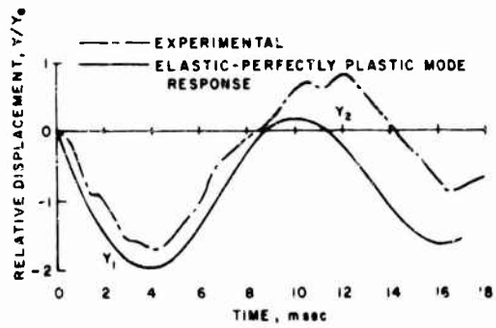

Fig. 12. Response correlation

The rigid plastic solutions also predict permanent set deflection adequately for many applications; however, they will generally predict about 0.5 Y_e greater set deflection than their elastic-plastic counterparts.

While the elastic-plastic mode response for a single-degree-of-freedom system serves very well in this study, obtaining a similar solution for a system of more than one degree of freedom would be extremely difficult. The inelastic mode approximation method has promise of application to more complex structures with the requirement of proper mode choice. The effect of mode choice on results can be evaluated only by further studies into more complex structures. The displacement bound is also applicable to a wide variety of structures. It may be expected that the displacement bound method will consistently give bounds in almost all cases, at least on the order of magnitude of the displacement at any point. By judicious application, much greater accuracies should be obtained. The acceptability of the accuracy of the displacement bound method also must be evaluated using more complex structures.

The intent of this study was to initiate an investigation of shock damage mechanisms. The methods presented here are by no means directly applicable as a shock design method, but they do supply fundamental conceptions. This study provides considerable insight into damage mechanisms and provides promise for plastic design. Further studies of more complex structures should furnish the basic tools required for the development of a plastic shock design method.

REFERENCES

1. J. B. Martin, "Bound Theorems for Rigid Plastic Continua Subjected to Certain Classes of Dynamic Loading," Brown University Report No. BU/DTMB/1, July 1963
2. J. B. Martin, "A Displacement Bound Principle for an Elastic Continuum Subjected to Certain Classes of Dynamic Loading," Brown Unitersity Report No. BU/DTMB/3, September 1963
3. M. A. Olen and J. B. Martin, "Approximate Methods for Rigid Plastic Structures Subjected to Dynamic Loading," Brown University Report No. BU/DTMB/7, August 1965
4. L. T. Butt, et al., "Shock Damage Mechanism of a Simple Structure," DTMB Report No. 2191, March 1967
5. Lord Rayleigh, "The Theory of Sound," First American Edition, Dover Publications, New York, 1945

DISCUSSION

R. J. Fitch (General Electric Co.): What was the material used for the cantilever beam?

Mr. Butt: The material was a medium structural steel. This is a standard I-beam with a yield strength of about 42,000 psi.

Mr. Fitch: Normally, when a material has yielded in one direction the yield strength in the opposite direction changes. This is called a Bauchinger effect. Do you find that the Bauchinger effect may have been important in affecting the later response, not the first peak but the shakedown effect?

Mr. Butt: We suspected that this might happen, and we had accelerometers attached to the tip masters so that we could measure the force throughout the response. However, the lead blocks flowed considerably during the shock, causing a lot of slop. We lost the accelerometer records and could not determine exactly what the Bauchinger effect would have been.

* * *

GENERAL MOTORS ENERGY-ABSORBING STEERING COLUMN AS A COMPONENT OF SHIPBOARD PERSONNEL PROTECTION*

Jackson T. Hawkins and Arthur E. Hirsch
Naval Ship Research and Development Center
Washington, D.C.

The energy-absorbing elements from General Motors collapsable steering columns has been tested and evaluated for application to force limiting devices for protection of shipboard personnel during underwater explosion attack.

INTRODUCTION

Shipboard personnel are vulnerable to the violent upward deck motions associated with underwater explosions. Man's tolerance to such short-duration shock motion is limited to accelerations of about 15 to 20 g [1]. Effective protection must therefore limit the force transmitted to the man to values below those corresponding to his injury level. For example, a seated man weighing 180 lb can endure momentary forces no greater than about 15 times his own weight, or 2700 lb.

The Personnel Protection Branch of the Navy Ship Research and Development Center (NSRDC) has been developing various systems which will reduce these shock motions to tolerable levels within the space restrictions imposed by shipboard applications. The General Motors energy-absorbing steering column shows great promise for application in some of these systems. This report evaluates the force-limiting capabilities of the crushable element of the GM steering columns under shock loading similar to that on board ships subjected to underwater explosion attack.

BACKGROUND

In the design of a system of shipboard personnel protection against underwater explosion shock motion, three main requirements must be considered: (a) the force transmitted to the man must be within his tolerance levels; (b) the thickness of the protection must be kept to a minimum; and (c) the protection must be durable enough to meet service requirements.

The tolerance of seated and standing man to short-duration shock motion is shown in Fig. 1. It can be seen that man's tolerance to shock is dependent upon the duration of the loading. If the load is applied for less than 20 msec he is sensitive to the velocity change and can tolerate any acceleration so long as the Δv is not greater than 15 fps. If the duration is greater than 20 msec and not greater than about 100 msec, then he can tolerate any Δv so long as the acceleration does not exceed about 15 to 20 g.

Full-scale shock tests have shown that during underwater attack, shipboard personnel can be subjected to velocity changes, occurring in the 1- to 20-sec range, in excess of man's 15-fps tolerance limit. One method of protection would be to increase the time of application of the shock load to man so that he can attain the high velocity of the deck without experiencing injurious accelerations.

This maximum acceleration, about 15 g, corresponds to a transmitted force of 15 times the weight of the protected man. The 1st to 99th percentile variation in man's weight is from about 120 to 220 lb [2]. The maximum allowable force that can safely be transmitted by the protection therefore varies from about 1800 to 3300 lb. In the design of a single system the lower value, 1800 lb, must be the criterion if most men are to be protected. This corresponds to accelerations of 15 g for the first and about 8 g for the 99th percentile weights. The

*This project was sponsored and funded by NAVSEC and NAVSHIP under SF 0150404 Task 1917. Permission to use human subjects in this study was granted by the Secretary of the Navy with the endorsement of the Bureau of Personnel and the Bureau of Medicine and Surgery.

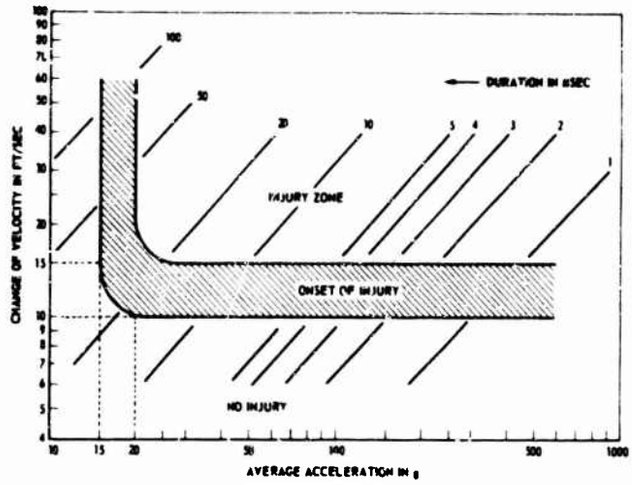

Fig. 1. Man's tolerance to short-duration shock motion

50th percentile, 168-lb man, would experience about 11 g.

However this attenuation is accomplished (e.g., mechanically, pneumatically, hydraulically, by plastic deformation, etc.), it is necessarily accompanied by a relative displacement between the deck and the upper surface of the device. The more nearly the useful force-limiting stroke approaches the initial thickness of the device, the greater the available protection for any given thickness restriction. The highest such stroke-thickness ratio for any of the protection systems previously investigated [3] has been about 0.75 for paper honeycomb.

For a force-limiting device to be of practical value for shipboard application, it must be able to withstand the same rough service use as the deck of the ship itself without compromise of its protective capabilities. Its shock-attenuating characteristics must be virtually unaffected by adverse climate, rough handling, and frequent shock loading at levels below the design yield strength. Low cost, ease of installation, and infrequent maintenance are additional requirements.

No shock protection device has been found that will completely satisfy all of these requirements. A very effective and durable hydraulic shock isolation pedestal has been developed for seated personnel; however, this device is heavy and relatively expensive, and has a stroke-thickness ratio of less than 0.5. Paper honeycomb deck modules for standing man, described in Ref. [3], are inexpensive and effective, and have a stroke-thickness ratio of about 0.75; but they are unable to withstand normal service climate and wear. The problem of shock protection for shipboard personnel is of such importance and urgency that despite their deficiencies, each of these two systems has found some degree of Navy application.

GENERAL MOTORS STEERING COLUMN

The GM steering column was developed as protection against chest crushing or chest penetration sometimes caused by rigid steering columns in automobile accidents in which the driver is impelled forward. Figure 2 shows the energy-absorbing portion of the commercially mass-produced steering column element designed for installation in many 1967 automobiles. Its undeformed length, including 1/4 in. on each end to allow for welding in pedestal fabrication, is 10-1/4 in., and its major and minor diameters are 2-7/16 and 2-3/16 in., respectively.

Energy is absorbed during axial loading by the plastic bending of the diamond-perforated sections. The average yield strength of these columns can be controlled in the manufacturing process by the selection of materials, dimensions, and the degree of annealing. The force transmitted by a protection pedestal composed of the columns is therefore not necessarily restricted to the integral multiples of the force determined herein for the strength of the production model [4]. The column is relatively inexpensive, durable under subyield strength

Fig. 2. The GM energy-absorbing steering column

loading, and easily fabricated into practical modules.

TEST AND RESULTS

A series of tests was conducted to evaluate the potential of the steering columns for application in a system of protection for shipboard personnel subjected to underwater explosion attack. The object of the tests was to determine the force-transmitting characteristics of the columns, both singly and in multicolumn configurations, during shock loading similar to that which might be experienced at shipboard duty stations.

Test modules consisted of from one to five columns mounted between parallel face plates as shown in Fig. 3. The NSRDC ship shock simulator, described in Ref. [5], was used to generate realistic input shock motion to the lower plates; steel weights were used to provide resistant forces on the upper plates. Figure 4 shows the test arrangement and the action of the columns under shock loading. The mass of the steel weights and both the rise times and peak velocities of the input motion were varied to simulate shipboard shock conditions.

Velocity time records of both the lower plate (input) and the upper plate (output) were taken during the shock loading. Records of several tests are reproduced in Fig. 5. The consistency of the velocity-time slopes, or accelerations, of the outputs in Fig. 5 indicate that the force transmitted by the modules remained virtually constant throughout dynamic compression. The value of this transmitted force was obtained as the product of the output acceleration and the mass of the resisting steel

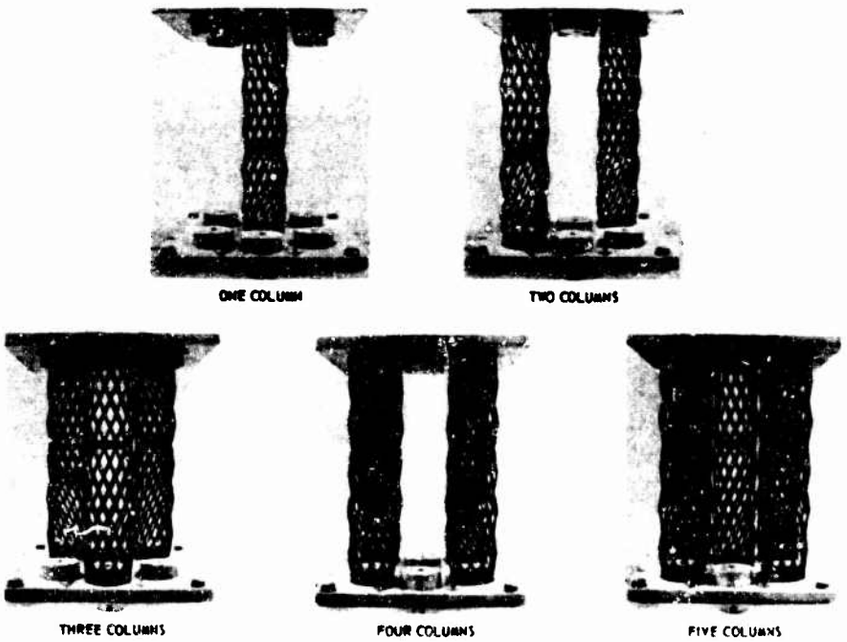

Fig. 3. Steering column test pedestals

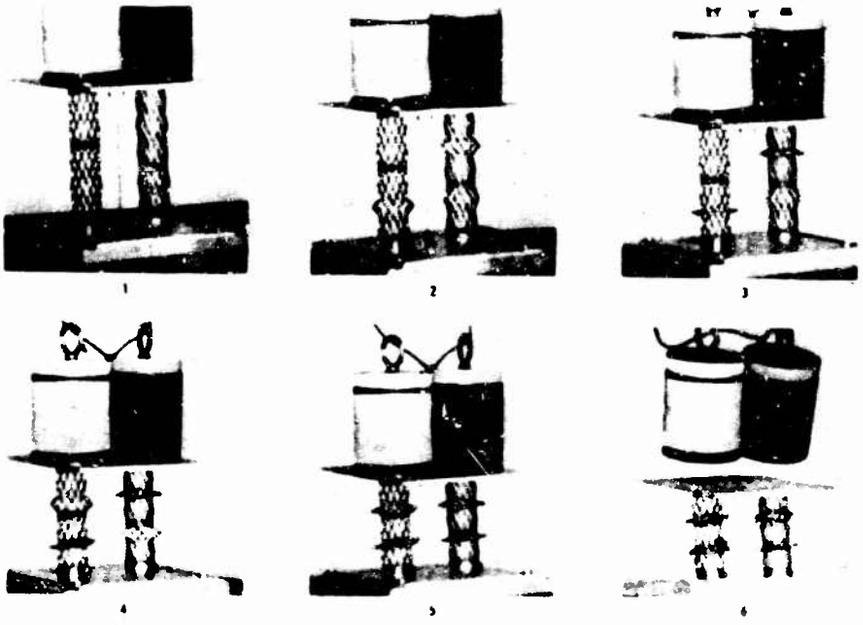

Fig. 4. Crushing action of two-column pedestal under shock loading

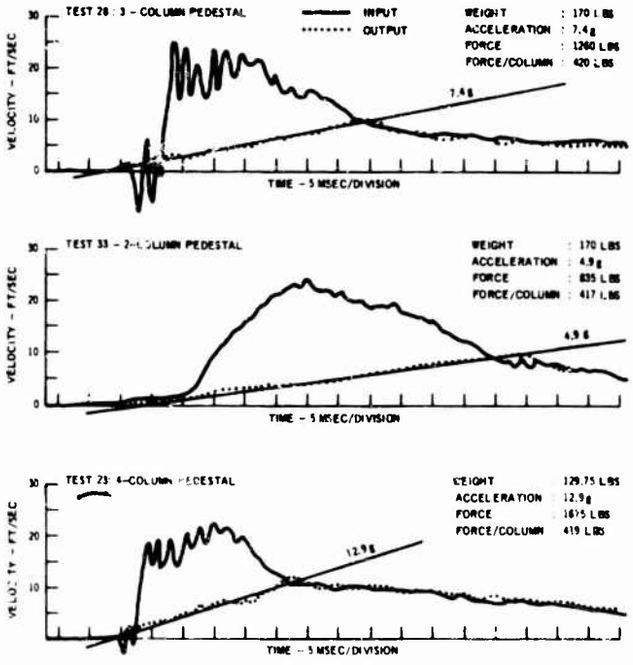

Fig. 5. Shock motion measured during typical steering column pedestal tests

weight. Figure 6 shows the corresponding stress-strain relationship as developed from test velocity time records.

Table 1 summarizes the test conditions and results. The values of the transmitted force per column are consistent within the range of about 430 lb ±15 percent, and the useful stroke of the columns is about 7-3/4 in., or about 75 percent of the undeformed length. These results indicated that a pedestal consisting of four columns would most nearly approximate the design transmitted load of 1800 lb, the criterion for one-man personnel protection devices.

CONCLUSIONS

1. Pedestals composed of integral numbers of the collapsable section of GM energy-absorbing steering columns have force-limiting capabilities which meet protection requirements of personnel subjected to ship shock motions from underwater explosion attack.

2. The high stroke-thickness ratio of this device permits its effective application for protection in low head-room areas. In this respect it is the most efficient device yet investigated.

3. Ease of procurement, low cost, simplicity, durability, and consistent and desirable shock-absorbing characteristics make this a most attractive device for incorporation into personnel shock protection equipment.

ACKNOWLEDGMENTS

The authors wish to acknowledge Frank I. Whitten for first recognizing the potential of the GM steering column for personnel protection application, and Edward V. Pickford and Mr. Whitten for developing the fabrication and testing techniques. Sincere thanks must also be extended to General Motors Corporation for its cooperation in this project.

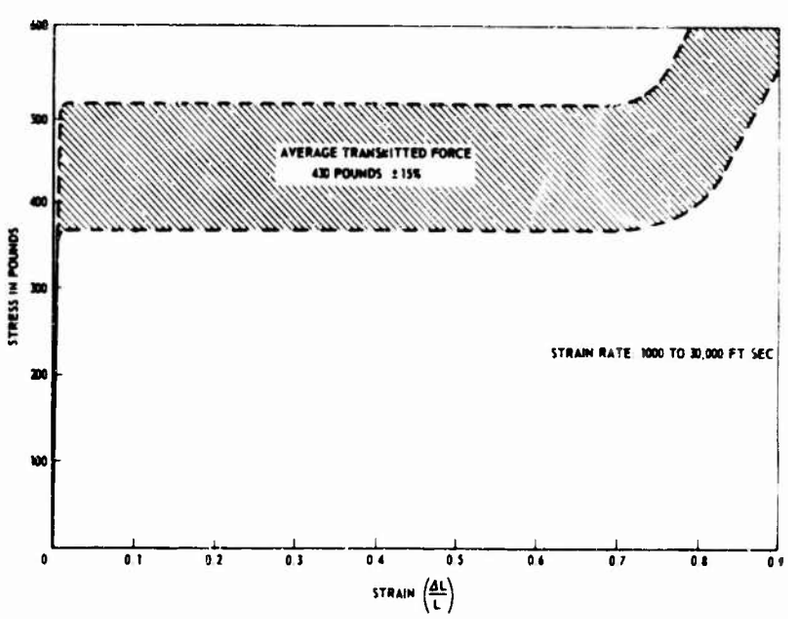

Fig. 6. Stress-strain relationship for GM steering columns corresponding to dynamic test data

REFERENCES

1. A. E. Hirsch, "Man's Response to Shock Motions," David Taylor Model Basin Rept. 1797, Jan. 1964

2. NASA Life Sciences Data Book (1st ed.) (Webb Associates, Yellow Springs, Ohio), 1962

TABLE 1
Summary of Test Conditions and Results

Test	Number of Columns	Resisting Weight (lb)	Input		Output		
			Peak Velocity (ft/sec)	Rise Time (msec)	Transmitted Acceleration (g)	Transmitted Force (lb)	Transmitted Force per Column (lb)
1	1	69.75	14	10	6.3	440	440
2	1	69.75	22	10	7.1	495	495
3	1	69.75	29	10	7.2	500	500
4	1	69.75	23	20	7.3	510	510
5	1	69.75	28	20	6.5	450	450
6	1	69.75	14	15	6.5	450	450
7	1	69.75	23	15	7.1	495	495
8	1	69.75	28	15	6.8	470	470
9	2	129.75	15	15	7.2	935	467
10	2	129.75	23	15	7.8	1010	505
11	2	129.75	27	15	7.6	990	495
12	3	170.00	23	20	7.9	1340	447
13	5	170.00	22	20	12.7	2160	432
14	4	170.00	21	20	8.6	1460	366
15	2	129.75	24	20	6.2	805	402
16	1	129.75	25	20	3.7	480	480
17	2	170.00	24	20	4.9	830	415
18	3	129.75	23	20	9.7	1260	420
19	3	129.75	24	1	9.9	1285	428
20	4	170.00	23	20	9.0	1530	382
21	1	170.00	20	1	2.5	425	425
22	3	129.75	24	1	10.7	1390	463
23	4	129.75	22	1	12.9	1675	419
24	5	170.00	23	20	11.2	1905	381
25	1	129.75	26	1	3.9	505	505
26	4	170.00	22	1	9.4	1600	400
27	5	170.0	21	1	11.5	1950	390
28	3	170.00	25	1	7.4	1260	420
29	2	170.00	30	1	5.2	885	442
30	5	170.00	20	20	11.6	1970	394
31	4	170.00	21	20	10.2	1730	432
32	3	170.00	22	20	8.0	1360	453
33	2	170.00	23	20	4.9	835	417

3. J. T. Hawkins, and A. E. Hirsch, "Protection for Minesweeper Personnel: The Shock Attenuating Deck Pad (U)," David Taylor Model Basin Rep.. C-2265, Oct. 1966 (confidential)

4. P. C. Skeels, "The General Motors Energy-Absorbing Steering Column," Proc. 10th Stapp Car Crash Conf., Nov. 1966

5. R. M. Mahone, "Man's Response to Ship Shock Motions," David Taylor Model Basin Rept. 2135, Jan. 1966

* * *

DESIGN OF HEAVY WEIGHT SHOCK TEST FACILITIES

Carl G. Schrader
San Francisco Bay Naval Shipyard
San Francisco, California

Heavy (6000 to 60,000 lb) Naval shipboard equipment is shock tested on board a floating platform by an underwater explosion. Design objectives and criteria for fixtures and test results are presented. The results suggest that in simple cases the fixture (or foundation) can be designed to be an effective shock reducer.

Naval shipboard equipment that requires shock testing but which weighs less than 6000 lb is usually tested on impact shock machines. Heavier equipment (6000 to 60,000 lb) is shock tested by mounting the unit on a Floating Shock Platform (FSP) and subjecting the platform to a series of underwater explosions. This test procedure, described in military specification MIL-S-901C, was developed by the Underwater Explosions Research Division of the Naval Ship Research and Development Center (formerly David Taylor Model Basin) [1]. Two commercial facilities, one at Electric Boat Division, General Dynamics Corporation, Groton, Connecticut, and the other at Western Gear Company, Everett, Washington have recently started conducting FSP tests. The Underwater Explosions Research Division does similar testing, but their emphasis is more on research problems. Regular qualification and developmental shock tests of the Navy shock test program are conducted at the West Coast Shock Facility. Since 1963 a few practical things have been learned which may be of help to those who will have their equipment tested on FSP's.

The FSP deck is 3 ft above the bottom of the hull and is made of 1/2 in. thick HY 80 steel. This, in turn, is supported by a grid of transverse and longitudinal plates on 3-ft centers which connects to the bottom of the hull. A supporting fixture (or foundation) that will simulate the shipboard foundation is needed to install the equipment to be tested. Although this equipment is very heavy, it may be installed anywhere on a ship from the hull beams up to the main deck. This creates the problem of how best to mount the equipment on the FSP to simulate the shipboard environment as realistically as possible. To simulate the hull frames, the equipment is mounted directly to the deck of the FSP which has similar stiffness and frequency. For equipment which is mounted above the hull frames, the hull fixture design becomes more difficult: the frequency of the supporting structure becomes lower as the equipment is placed higher in the ship, because of the additive effect of the springiness of the intervening structures [2]. In addition to designing to the same frequency as the shipboard foundation, the fixture must maintain a low center of gravity, have adequate strength and low weight, and fit within the limited space of the FSP.

The fixture should have the same frequency as that of the shipboard foundation. Figure 1 shows the ability of a fixture to modify the deck response of the FSP as "seen" by the equipment. The upper velocity-time curve shows a typical shock on the deck of the FSP with a quickly rising ramp-shaped wave. The lower curve shows the response as modified by the fixture to a low-frequency wave which almost approaches a half sine wave. This means that most of the shock energy has been converted to relatively low-frequency energy. This frequency usually corresponds to the fundamental vertical frequency of the fixture, since most of the shock energy of a surface ship is in the vertical direction. Many types of controls and structures used in typical machinery have a low-frequency resonance and therefore are excited by this low-frequency energy. A resonant frequency vibration can cause large amplitudes and stresses. In a similar manner resonant shock excitation will cause large motions, although to a lesser degree. If we placed all the equipment on deck, as directly as feasible, and with a short, stiff foundation, we would not have the low-frequency excitation as found in many shipboard foundations. Instead, the impact loading would consist mainly of high-frequency excitation not representative of the expected shipboard shock and

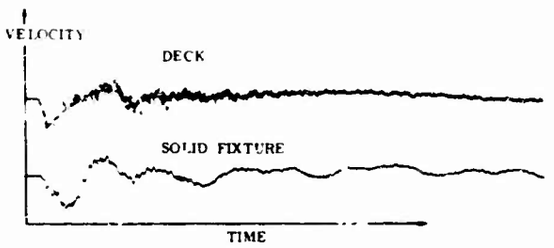

Fig. 1. Deck vs fixture response

conducive to failures of a nature entirely different from that which the normal shipboard installation could expect. In such a case the test could not be realistic. Although it costs more to build a low-frequency fixture, the large number of low-frequency structures and control failures we have encountered justifies the expense.

In designing the fixture, we need to determine the required frequency. If the equipment is already installed on a ship, we can measure the frequency by mechanical impedance techniques; but in most cases we have to calculate the frequency from the plans of the shipboard foundation. In our calculations we usually assume that the equipment acts as a single mass. To determine what strength level we should design to, we have used the surface ships input curves of the dynamic data analysis method [3,4].

To design the very low frequency fixtures that simulate equipment mounted several decks above the bottom of a ship, the design may require pin joints and alloy steel frames to keep the large displacements within the elastic range of the material. Figure 2 shows a pin-jointed fixture designed by one shipbuilder to simulate a certain deck on an aircraft carrier which has a vertical frequency of 13 cps. Figure 3 shows a solid type of fixture with about a 50-cps response. Figure 4 shows the oscillograph velocity-time traces of a solid fixture and a pin-jointed fixture. The solid fixture shows a heavily damped wave which was probably caused by the friction of many bolted joints. The pin-jointed fixture oscillated with a rather lightly damped sine wave motion for several cycles. In Fig. 5, the velocity-time response of a shipboard and a floating platform solid-fixture shock test of a turbogenerator indicated that the solid fixture very closely approximated the ship's response. The pin-jointed fixture with its low damping and resultant many cycles has a greater damage potential when equipment or parts which have slightly differing frequencies get out of phase after several cycles and the parts collide with doubled velocity. Since this low damping does not occur on many ship structures that support heavy equipment, it is believed that these

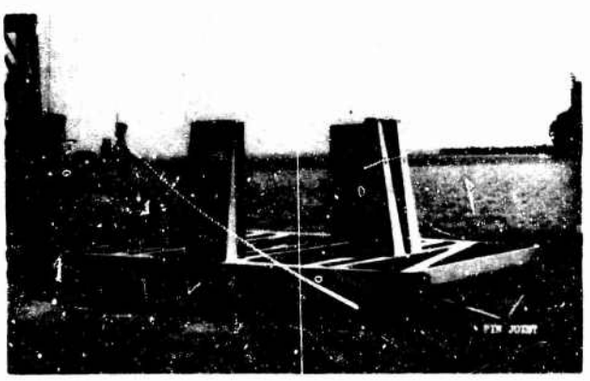

Fig. 2. Pin-jointed fixture simulating aircraft carrier deck with vertical frequency of 13 cps

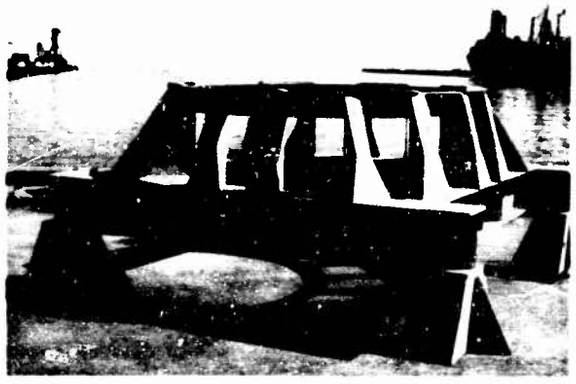

Fig. 3. Solid fixture with 50-cps response

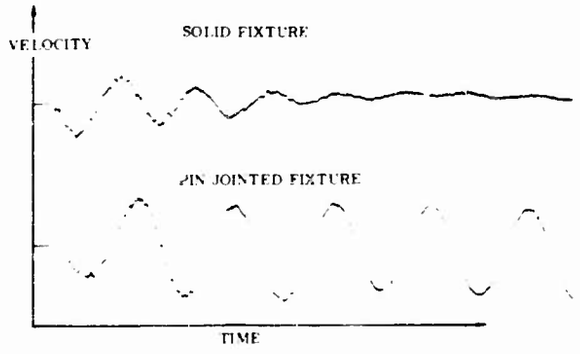

Fig. 4. Solid vs pin-jointed fixture response

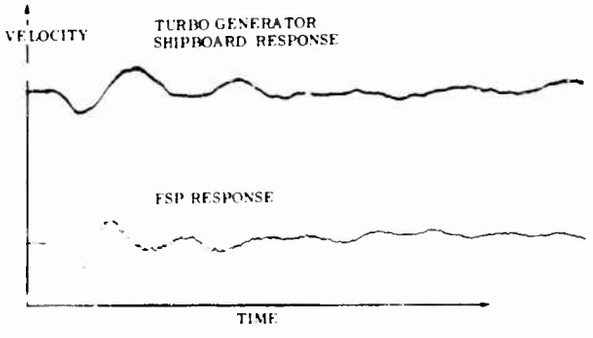

Fig. 5. FSP vs shipboard response

pin-jointed fixtures could be improved by providing friction damping.

The question of g-loads on equipment tested on the FSP is frequently raised. As shown by Table 1, these g loads vary over a considerable range and depend on the frequency of the FSP fixture. Table 1 does not show all the equipment that we have tested, but it shows a range of frequencies and g loads encountered and the effect that the fixture frequency can have upon the same type and weight of equipment. These frequencies range from 13 to 210 cps, which, in turn, have resulted in accelerations ranging

TABLE 1
Results of FSP Shock Tests

Equipment	Type of Fixture[a]	Natural Frequency, Vertical (cps)	Average Acceleration (g)	Peak Velocity (fps)
Filter	P	13	11	7.8
Towing reel	P	19	16.5	12.3
Filter	P	23	28	16
Diesel generator	R	25	32	14
Gas turbine generator	R	27	40	15
Deaerating tank	R	50	43	14
Turbogenerator	R	33	39	11
Turbogenerator	R	210	220	10

[a]P = pin jointed, R = rigid joint.

from 11 to 220 g respectively. Figure 6 shows our method of measuring acceleration. We take the long time slope of the velocity curve and use this for a basis of our g measurement. We do not consider the high frequency peak g loads that are of very short duration, for our experience indicates that the low-frequency parts involved in most machinery are damaged by the longer time energy.

cases, however, for some machinery must stay in very close alignment, or its position in the ship may be so close to the main frames that it is not practical to interpose a flexible foundation.

CONCLUSIONS

We have been fairly successful in designing the desired frequency into our fixtures; if we

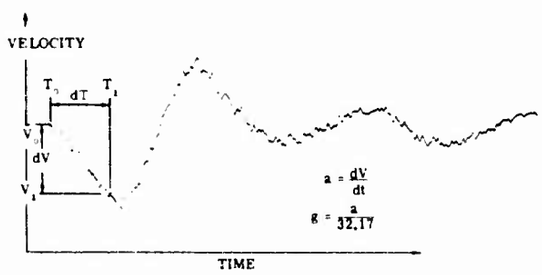

Fig. 6. Method of reading accelerations

As a by-product of this fixture study, we can see in Table 1 that the accelerations experienced by similar equipment may vary as much as 5 to 1, because of the stiffness or flexibility of the foundation. Examination of foundation plans indicated that cost difference between a flexible and a very stiff foundation was nominal. Since a 5 to 1 load factor may make a large cost difference in manufacture of an equipment, it is recommended that in simple cases, the shipbuilder design flexible foundations and pass his design criteria to the equipment manufacturer who, in turn, may design adequate shock strength at a minimum cost. This cannot be done in all

err, we prefer to be on the higher frequency side, because this, in turn, will produce higher g loads instead of lower ones. The resultant g loads have not always been as close as predicted, but they have given us safe design values for our fixtures and fastenings. It must be remembered these g loads are those of our fixture. Designing to these particular levels will not guarantee that everything else on the equipment will survive, because certain high-frequency parts of the equipment will feel higher g levels. The wave shape of the motion of our solid fixtures has been very close to shipboard motions. To improve

pin-jointed fixtures, we will try to provide friction damping so that the wave shape and duration will come closer to that of the ship's foundation.

REFERENCES

1. "The Floating Shock Platform for Shock Testing Equipment up to 30,000 Pounds," UERD Rept. 7-61, May 1961
2. A. H. Keil, "The Response of Ships to Underwater Explosions," DTMB Rept. 1576, Nov. 1961
3. R. O. Belsheim, and G. J. O'Hara, "Shock Design of Shipboard Equipment. Dynamic-Design Analysis Method," NAVSHIPS 250-423-30, May 1961
4. R. O. Belsheim, and G. J. O'Hara, "Shock Design of Shipboard Equipment. Interim Design Inputs for Submarine and Surface Ship Equipment," NAVSHIPS 250-423-31, Oct 1961

DISCUSSION

Paul Duffy (KAPL, General Electric Co.): Was any attempt made to simulate vertical and lateral stiffnesses of the foundation simultaneously?

Mr. Schrader. Most all this effort was on the vertical, since the horizontal shock load is about 50 percent of the vertical load on the floating shock platform. The horizontal stiffness in foundations varies a great deal from shipbuilder to shipbuilder, in that some will tie them directly into the side of the ship and for others the foundation will be fairly well pivotted on the bottom frames. It is rather difficult to have any real consistency here.

Mr. Bort (Naval Research Lab.): I notice that most of the accelerations seem to be numerically equal to the frequencies. Is this perhaps good enough to use as a rule for anything?

Mr. Schrader: No, I don't think it is good to use as a rule. I tried fitting this to various curves and formulas with little success. I want to caution everyone that these levels are what our fixture and the bolting see. There are higher g loads on parts of the equipment than our fixture sees. So do not use these data as a guide for overall design.

* * *

DERIVATION AND IMPLICATIONS OF THE NAVY SHOCK ANALYSIS METHOD

F. J. Heymann
Westinghouse Electric Corporation
Lester, Pennsylvania

The working equations of the Belsheim-O'Hara dynamic analysis method are developed nonrigorously, with a minimum of mathematics, on the basis of physical and logical reasoning.

The expressions for modal equivalent (or effective) mass, equivalent displacement, and shock response of system masses are derived here using no postulates other than (a) a definition of dynamic equivalence between vibratory modes of different systems, (b) the assumption that system modes of equal frequencies and equal equivalent masses will respond to the same shock condition at levels consistent with dynamic equivalence, and (c) the requirement that the responses of arbitrary single-degree-of-freedom systems be known, as from test data. The concept of equivalent displacement ratios is preferred to that of the more commonly used participation factors; the former are shown to be fixed quantities for a given system mode, whereas the latter are not.

This approach reveals clearly that the method is not predicated upon any particular shape or nature of the shock input to the system (such as a step velocity input) and can yield no information about the initial phase relationships between the various modes.

Since in a real system the responses also decay rapidly, it follows that there is an inherent difficulty, in this method, of summing the effects of the various modes without being overly conservative.

INTRODUCTION

In the analysis of complex structures subjected to shock excitation, particularly in naval shipboard equipment, the so-called dynamic analysis method of Belsheim and O'Hara [1] must often be used. The procedure involves, as a first step, reducing the actual structure to a lumped-parameter model of a finite number of degrees of freedom and calculating by any appropriate method the normal modes of vibration of this system, as represented by their frequencies and mode shapes (normalized displacements of the masses). From this information two suitably defined quantities, equivalent mass M_e and participation factor P, must be computed for each mode. Next, a shock velocity input V_s, the design spectrum value, is prescribed for each mode and is a function of modal frequency f and equivalent mass M_e. These inputs are empirical values which have been deduced from the observed responses of single-degree-of-freedom oscillators of various masses and frequencies, placed in actual vessels subjected to shock tests.

The final expression for the equivalent static force on mass k, in the particular mode, can be stated as follows:

$$F_k = M_k X_k P V_s \qquad (1)$$

This expression is not derived in Ref. [1], although undoubtedly rigorous derivations can be found elsewhere.

This paper shows how Eq. (1) can be developed nonrigorously, using a minimum of mathematics and a maximum of physical-logical reasoning, with the thought that this may help to clarify what assumptions are implicit in the method and what the physical significance is of some of the terms involved.

PHYSICAL ASSUMPTIONS AND LOGICAL ARGUMENT

In the more usual rigorous approach to a normal-mode analysis, the complete response of a multi-degree-of-freedom system is analyzed for some assumed complete base motion or excitation. Then that response is broken down into normal modes, and the modal equivalent mass is deduced by noting the similarity between the form of the modal response equation and the single-degree-of-freedom equation. In this nonrigorous approach, we shall regard

each mode as an entirely independent entity from the beginning. We shall make no assumptions concerning the total system excitation, but merely assume that each mode responds analogously to a dynamically equivalent single-degree-of-freedom system subjected to the same shock environment.

First let us consider two systems in steady-state vibration. We shall define as "dynamically equivalent" two systems vibrating at the same frequency, if the net momentum and the total energy of the two systems are the same. Since this statement is quite general, each system may represent a multi-degree-of-freedom system vibrating in a particular mode, or a single-degree-of-freedom system vibrating at its natural frequency. (The equality of net momentums also implies that the two systems apply equal forces to the "fixed base" at their points of attachment.) We shall show that, if one of the systems is indeed a single-mass-spring oscillator, then dynamic equivalence requires a definite relationship between the mass of the latter, which we can now refer to as equivalent mass M_e, and the masses and mode shape of the other system. We shall also show that dynamic equivalence requires a definite relationship between the vibratory displacement amplitude of the single-mass system, which we can now refer to as equivalent displacement X_e, and the masses, mode shape, and excitation level of the other system.

It should be clearly noted — though one would hardly expect anything otherwise — that the equivalent mass is independent of the excitation level of the multimass system, whereas the equivalent displacement is proportional to the excitation level of the multimass system. This implies, however, that the ratio of the displacement of any one of the masses in the multimass system to the equivalent displacement is once again independent of the excitation level, and, like the equivalent mass, can be considered a property of the given system vibrating in the given mode. Let us call such ratios equivalent displacement ratios.

To apply the foregoing to shock analysis, we must make the physical assumption that if two systems of the same natural frequency and the same equivalent mass are subjected to the same transient disturbance at their base, their steady-state responses will be such that they are dynamically equivalent as defined previously. Hence, the vibratory amplitudes of the two systems can be related to each other by means of the equivalent displacement ratios.

Furthermore, we assume that the total response of a multi-degree-of-freedom system to a shock input is a superposition of the independent responses in each normal mode and that the response of each mode can be computed by means of the previous argument from the response of a single-mass oscillator of the same frequency and equivalent mass. The responses of single-degree-of-freedom oscillators to typical shock inputs, as a function of their mass and frequency, are assumed known from empirical data.

Note what assumptions do not have to be made; in particular, the nature of the shock disturbance, i.e., the displacement-time history of the base, is not prescribed or defined in any way, and, therefore, it also follows that no phase relationships can be adduced for the responses in the various modes. Furthermore, in real systems with damping the responses represent maximum rather than steady-state vibratory amplitudes.

MATHEMATICAL DERIVATION

Consider a unidirectional, multi-degree-of-freedom system vibrating in one of its normal modes, the angular frequency of which is ω_a. All displacements are assumed to occur in the x direction. The subscript a identifies the particular mode under consideration; the subscript i identifies the particular mass.

The net or algebraic momentum K_a associated with a mode of harmonic oscillation in a multi-degree-of-freedom system is

$$K_a = \omega_a \sum_i M_i X_{ia} . \tag{2}$$

The corresponding kinetic energy is

$$E_a = \frac{1}{2} \omega_a^2 \sum_i M_i X_{ia}^2 . \tag{3}$$

The X_{ia} values here represent any arbitrary set of displacement amplitudes. Their relative magnitudes are of course determined by the mode shape or eigenvector of the mode under consideration.

If the mass and displacement, respectively, of the dynamically equivalent single-degree-of-freedom system are M_{ea} and X_{ea}, its momentum and energy are expressed by

$$K_{ea} = \omega_a M_{ea} X_{ea} \tag{4}$$

and

$$E_{ea} = \frac{1}{2} \omega_a^2 M_{ea} X_{ea}^2 \tag{5}$$

Since by "dynamic equivalence" we mean that $K_{ea} = K_a$ and $E_{ea} = E_a$, we can equate Eqs. (2) with (4), and (3) with (5) to obtain

$$M_{ea} X_{ea} = \sum_i M_i X_{ia} \tag{6}$$

and

$$M_{ea} X_{ea}^2 = \sum_i M_i X_{ia}^2 \tag{7}$$

Dividing Eq. (7) by (6) we obtain the equivalent displacement, i.e., the displacement amplitude of the dynamically equivalent system:

$$X_{ea} = \frac{\sum_i M_i X_{ia}^2}{\sum_i M_i X_{ia}} \tag{8}$$

Substituting Eq. (8) back into (6) results in the expression for the equivalent mass:

$$M_{ea} = \frac{\left[\sum_i M_i X_{ia}\right]^2}{\sum_i M_i X_{ia}^2} \tag{9}$$

It is important now to note that equivalent mass M_{ea} is independent of the absolute values of the X_{ia}'s, as long as they bear the proper relationships to one another as prescribed by the mode shape of the mode considered. Any arbitrary or arbitrarily normalized set of displacement amplitudes describing that mode can be used to compute M_{ea}. On the other hand, equivalent displacement X_{ea} does depend on the excitation level; if all X_{ia}'s are multiplied by some given factor, the corresponding X_{ea} is also multiplied by that factor. This means, simply, that if the amplitudes of a multi-degree-of-freedom system are, say, doubled, then the amplitude required for dynamic equivalence, in the equivalent-mass single-degree system, is also doubled.

We can now draw our attention to any particular mass k in the system, and define its equivalent displacement ratio R_{ka} as follows:

$$R_{ka} = \frac{X_{ka}}{X_{ea}} = \frac{X_{ka} \sum_i M_i X_{ia}}{\sum_i M_i X_{ia}^2} \tag{10}$$

The R_{ka} values, which represent the ratios of the displacements of the individual masses in the multimass system to the displacement of the dynamically equivalent single-mass system, are once again functions of the masses and mode shape only and can be computed from arbitrarily normalized X_{ia} values.

We are now ready to make use of the foregoing relationships to deduce the response of our multimass system under a typical shock environment. We suppose that enough single-degree systems have been observed under typical shock environments to predict from these measurements the displacement response of any single-degree-of-freedom system of arbitrary mass and frequency.

Therefore, for each normal mode a, we can compute the frequency ω_a and equivalent mass M_{ea}, and then from the empirical data predict what actual shock displacement would be recorded by a single-mass system of that frequency and mass. Let this be denoted by X_{eas}. We then assert that the response of the multimass system under the same environment would be such as to satisfy the complete conditions of dynamic equivalence as previously defined. This implies that ratios of the shock displacements of the multimass system to that of the equivalent single-mass system would once again be given by the values R_{ka} which have been computed. Thus, the shock displacement for mass k, in mode a, is given by:

$$X_{kas} = R_{ka} X_{eas} \tag{11}$$

The inertia force on mass k, which we intend to use as an equivalent static loading in the computation of shock stresses, is

$$F_{ka} = M_k X_{kas} \omega_a^2 = M_k R_{ka} X_{eas} \omega_a^2 \tag{12}$$

If the shock response of the equivalent system is specified in terms of the velocity amplitude V_{eas} rather than displacement X_{eas}, we can substitute the relationship $X_{eas} = V_{eas}/\omega_a$ to obtain

$$F_{ka} = M_k R_{ka} V_{eas} \omega_a \tag{13}$$

The physical significance of Eq. (13) is evident: the force is the product of the mass (M_k) being considered, the shock acceleration of the equivalent single-mass system ($V_{eas}\omega_a$), and the ratio R_{ka} which relates the acceleration, velocity, or displacement of mass k to that of the dynamically equivalent single-mass system. Equation (13) can be shown to be identical to Eq. (1), and it will be seen that Belsheim and O'Hara's participation factor P_a is nothing more than the reciprocal of our equivalent displacement. Hence $R_{ka} = X_{ka} P_a$, from Eq. (10). The writer feels that the ratios R_{ka}, which are invariants for a given system and mode, are more meaningful than a participation factor whose magnitude depends on how the displacement values have been normalized. In fact, the R_{ka} values could be regarded as rationally

normalized displacements for the particular system and mode. Note that the equivalent mass can be expressed in terms of the R_{ka} values simply as follows:

$$M_{ea} = \sum_i M_i R_{ia} \qquad (14)$$

This can readily be seen by comparing Eqs. (9) and (10).

The physical arguments which we have advanced make it easy to see how the equations must be modified when a multidirectional system (one which, when shock excited in a given direction, will exhibit responses in all directions) is considered. Due attention must then be given to the fact that momentum is a vector quantity whereas energy is scalar. The component of momentum which is significant is that in the shock direction; therefore, in carrying out the summation of Eq. (2), only the displacements in the shock direction should be included. On the other hand, in computing the system energy by Eq. (3), the total energy as determined by all response directions must be included.

SUMMARY AND CONCLUSIONS

The expressions for modal equivalent (or effective) mass, participation factor, and shock response of system masses have been derived here using two postulates other than (a) a definition of dynamic equivalence between vibratory modes of different modes of different systems, (b) the assumption that system modes of equal frequencies and equal equivalent masses will respond to the same shock condition at levels consistent with dynamic equivalence, and (c) the requirement that the responses of single-degree systems are known, as from test data. The concept of equivalent displacement ratios is preferred to that of participation factors. Implicit in this approach is the assumption that the modes considered are uncoupled and the response of each is completely unaffected by the existence of other modes.

The term "starting velocity" is sometimes used; this can lead to the erroneous inference that this method is somehow based on the physical assumption of step velocity inputs. This approach shows that the method makes no allegations about the shape or nature of the shock input to the system or to the ship as a whole, or about the initial phase relationship of the modal vibrations.

The prescribed design spectrum values are based on the maximum measured responses of certain instrumented equipment in full-scale and model tests [1, pp. 26-27]. How and when the buildup to the maximum response level occurs will differ for different modes, depending on the relationship of the frequency of vibration to the velocity-time profile of the shock input at the hull or foundation, and on the time required for propagation of the shock or stress waves through the system. The latter is not an insignificant effect, since the duration of the shock pulse is on the order of milliseconds, and in a millisecond a stress wave in steel travels only 16 ft. Thus, design spectrum values obtained from compact equipment close to the hull may not be valid for more extensive or distant systems where the time delay and attenuation inherent in the propagation process would be expected to reduce the maximum response in a given mode. The damping in a complex system could be expected to be greater than in a simple mass-spring oscillator.

There still follows the question of how the effects (i.e., stresses or loads) of the various modes are to be combined, which is one of the outstanding problems in the application of this procedure. Some of the remarks above, together with the known fact that shock-induced vibrations decay rather rapidly from their peak values, will suggest why phase coincidence of many modes at their peak values is most unlikely. Yet the normal-mode method is inherently incapable of deriving, on a theoretical basis, anything but the very conservative upper bound obtained by direct superposition of the maximum loadings in all modes. This is one of its most serious deficiencies. To obtain hopefully more realistic "rules" for combining modes and predicting maximum stresses, recourse must be had to empirical data once again, or, perhaps, in systems with very many degrees of freedom, to statistical methods. Also, it will be found that the predicted maximum stresses can be very sensitive to the manner in which the structure is broken down into discrete masses and flexibilities to form the analytic model. The guidelines proposed to date for dealing with these problems have seemed rather arbitrary, and more work, or more englightenment, in this area is to be encouraged.

REFERENCE

1. R. O. Belsheim and G. J. O'Hara, "Shock Design of Shipboard Equipment - Part I: Dynamic Analysis Method," Bureau of Ships, Navy Department, NAVSHIPS 250-423-30, May 1961.

DISCUSSION

Voice: Could this method apply to all systems? Could it be extended to very large systems?

Mr. Heymann: The method is no different from the DDAM. It is just one way of seeing how the equations are arrived at. This method does specify the velocity input and frequency for any mode of a large system and equivalent mass. You are making the analogy between one mode of a large system and the response of a single degree of freedom system. I think what I am trying to show is that you can't tell from this analysis what the maximum response is going to be when you superimpose modes. It can't tell you anything about the time interval between the arrival of a shock front at the hull and the maximum response for different single degree of freedom systems. You don't know what the phase relationship is going to be, so you have to look elsewhere for the rationale of some of the modes.

Mr. Forkois (Naval Research Lab.): How do you determine the equivalent rotational modes of vibration from that single mass? You show a three mass system which obviously has some unbalance. How do you determine the equivalent modes on a single mass?

Mr. Heymann: In this case I don't. This is simply a one-dimensional model to show the principle. I have indicated in my paper that the analysis can be extended to three dimensions. I don't know about rotation. If the dynamic equivalence is defined in terms of the energies and momenta, when you have response in three directions, you would only take the sum of the momenta in the shock direction. Since energy is a scalar quantity you would take the energies involved in all three response directions. I think maybe that you could extend that to include rotational response, but I really haven't thought it out.

* * *

DYNAMIC ANALYSIS OF A TYPICAL ELECTRONIC EQUIPMENT CABINET SUBJECTED TO NUCLEAR-WEAPON-INDUCED SHOCK

John H. Putukian
Kaman AviDyne
Burlington, Massachusetts

The response to nuclear weapon effects of sensitive electronic components housed in equipment cabinets on the third floor of a steel-framed structure was analytically determined.

The objective of the investigation was to generate a structural design criterion for the electronic components. Computer storage capability was the controlling consideration in generating the mathematical models. The analysis had to be done in steps: (a) going from the ground for ground shock, and the roof for air blast, to the third floor column lines; (b) going from the column lines to the "black boxes" considered as rigid bodies; and finally (c) going from the response of the black boxes to the components. It is shown that this approximate analysis using the modal superposition method gives satisfactory results. The parametric considerations affecting this analysis are discussed.

INTRODUCTION

This paper outlines the analytic effort of generating the structural design criterion for the electronic components of equipment cabinets resting on the third floor of a steel-framed structure and subjected to nuclear-weapon-induced ground shock and air blast.

This investigation consisted of the following:

1. A typical bay at the third floor level was represented by its mathematical model. The eight cabinets in the typical bay were idealized as single masses, with their weights acting at their centers of gravity and having the same fundamental frequencies in the three major coordinate axes as the original cabinets. Using the shock spectra as input and the modal method of analysis, the response at the cabinet center of gravity was determined.

2. A typical cabinet was represented by its mathematical model. The cabinet was visualized as a multimass stable space frame with the mass lumped at the joints. Using the shock spectra and the modal method of analysis, the response at the cabinet joints was determined in the same manner as a cabinet mounted at the ground level with an infinitely rigid base (i.e., no intermediate framing effect). The ratio of the average acceleration of a cabinet to the acceleration of the c.g. of the cabinet obtained in step 1 above gave us the "feedback factor" representing the floor-cabinet interaction.

3. The design criterion to be used for the electronic components was discussed. This phase of the investigation is of prime interest to the component designer. In this investigation, we used the response values from the modal method of analysis at the black box, represented by a joint on the cabinet space-frame idealization, as our new shock input to determine the response of the components. It was shown that this approximate analysis gave satisfactory results, thus eliminating the need for the time-consuming exact analysis.

NUCLEAR WEAPON ENVIRONMENT

A structure subjected to a nuclear weapon environment is affected by two shock pulses as shown in Fig. 1. The first pulse is the ground shock, which resembles an earthquake-caused disturbance and is characterized by its low-frequency oscillatory motion. The duration of the pulse is enough to excite substantially all the lower frequencies of the structure. The second pulse is the air blast, which has a greater energy content and usually controls the design.

The ground shock effect on the overall preliminary structure showed that the structure

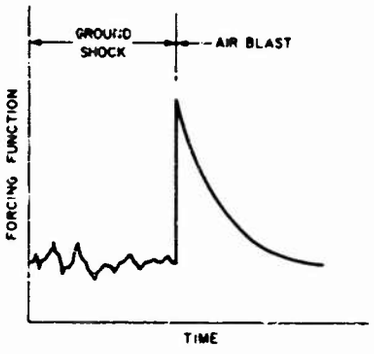

Fig. 1. Representation of nuclear weapon environment

had a low fundamental frequency and the ground shock environment was causing an amplification of about 8 times the peak input acceleration values. The structure was subsequently stiffened, changing the fundamental frequency from about 2 to 7 cps, and this caused the amplification factor to drop to below 1. This modification made the ground shock effect negligible compared with the air blast effect.

For the air blast effect, the overpressure functions, obtained by shock tube measurements on a simulated module, were resolved to force functions by two operations. First, the overpressures were converted to forces by multiplying by a load factor, using equal energy technique, and an approximate area (the module roof area). Second, the instantaneous rise times of the overpressure functions were converted to finite rise times. The rise time of each function corresponds to the time required for a sharp-front blast wave to sweep over the roof area of the analytic module.

The air-blast forcing function was used as input in the equations of motion of the mathematical model of the structure, and the time history of the response at various locations in the structure was computed. The air blast response was found to be the controlling design factor.

DETERMINING RESPONSE OF CABINET WITH NO INTERMEDIATE FLOOR FRAMING EFFECT

A typical equipment cabinet is represented by a three-dimensional structure composed of welded structural members forming the basic skeleton of the cabinet with shear panels on three of the vertical sides and on the top and bottom. One of the vertical sides is generally an open framework which is covered by a nonstructural door.

Figure 2 is the mathematical model of a typical cabinet weighing about 4460 lb, with the mass distributed at the joints. The diagonal members simulated the shear webs by using the Hrennikoff method [1]. In determining the response at the joints, the modal method of analysis for a multidegree system was used [2,3]. Using the shock spectrum as input and the eigenvalues and eigenvectors obtained from the computer program [4], one proceeds to compute the response accelerations at the joints. These results are presented in Table 1.

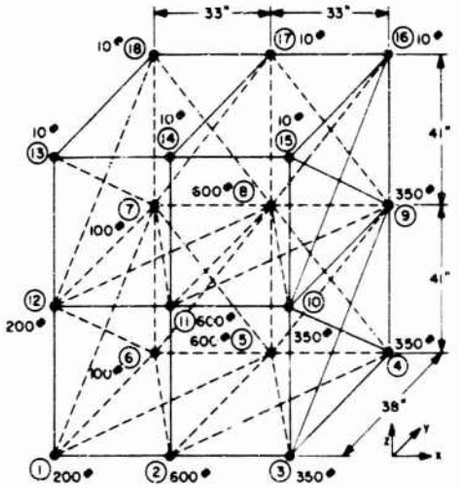

Fig. 2. Mathematical model of cabinet

TABLE 1
Response of Cabinet to Shock Spectra Input

Joint	Acceleration[a] (g)		
	a_x	a_y	a_z
1	2.77	2.14	6.71
2	2.93	2.15	3.87
3	3.05	2.95	6.49
4	3.50	2.57	4.21
5	3.49	2.16	5.04
6	3.41	2.11	4.33
7	2.60	1.67	2.50
8	2.63	2.34	2.81
9	2.71	3.27	2.62
10	2.26	3.44	3.99
11	2.12	2.37	2.57
12	2.03	1.69	4.09

[a]Average acceleration $\bar{a}_i = \sum M_j a_{ij} / \sum M_j$ (i = x, y, z; j = 1, 2 ... 12). $\bar{a}_x$ = 2.79, $\bar{a}_y$ = 2.46, $\bar{a}_z$ = 3.97.

DETERMINING RESPONSE OF CABINETS INCLUDING EFFECT OF INTERMEDIATE FLOOR FRAMING

Figure 3 is the structural floor plan of a typical bay at the third floor level of the steel-framed structure. The floor slabs were made of steel grating.

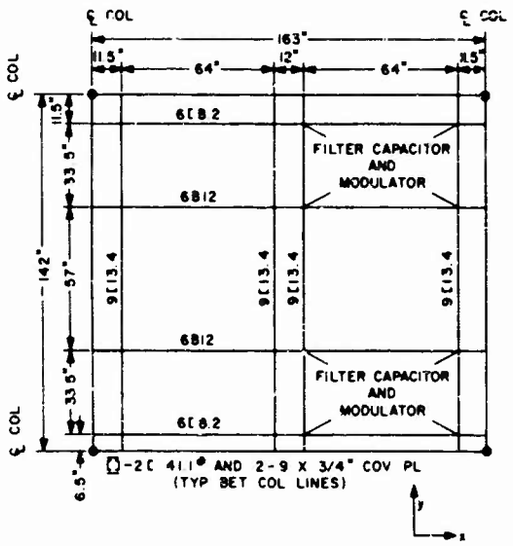

Fig. 3. Typical bay floor framing

Figure 4 is the mathematical model of this same typical bay. The computer program [4] restricted the system being analyzed to no more than 123 degrees of freedom. This restriction has been met in Fig. 4 by replacing each cabinet by one single mass having the same fundamental frequency in the three major coordinate axes as the cabinet, and by modifying the floor framing.

In deriving the mathematical model for the floor framing, it was necessary to relate the torsional rigidity of the actual floor framing to the torsional rigidity of the representative members in Fig. 4. For example, member 2-9 of Fig. 4 replaces two members spaced 64 in. apart as shown in Fig. 3. By investigating the relative bending stiffnesses of members 2-9 and 6-11, it was possible to compute the percentage of the load at joint 14 carried by member 2-9. This load was applied, in turn, as a horizontal static force on the cabinet to compute the associated reaction forces on the actual floor members replaced by member 2-9. Knowing the deflections in the actual floor

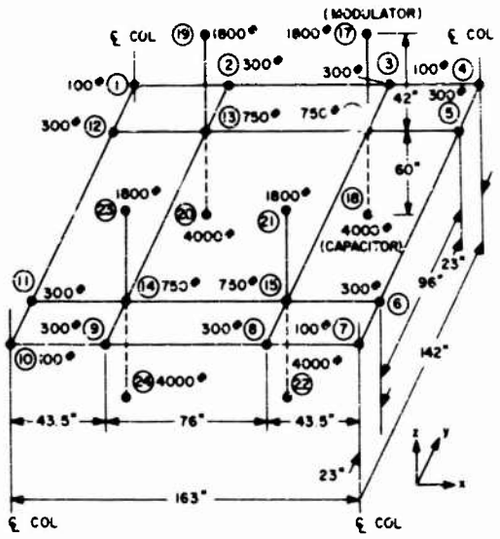

Fig. 4. Mathematical model of typical bay

members, it was then possible to compute the angle of twist, and hence the necessary torsional rigidity, of member 2-9. For member 2-9, the torsional rigidity was computed to be 199 in.^{4}

To allow for the effect of adjacent bays, the moments of inertia of the members joining the column lines were reduced by half along their horizontal axes.

Response values at various points of the typical bay are presented in Table 2.

EVALUATING EFFECT OF INTERMEDIATE FRAMING

The fundamental frequencies of the modulator and capacitor shown in Fig. 4 were 8.9 and 14.3 cps, respectively. The first six frequencies for the complete mathematical model of the typical bay shown in Fig. 4 were 8.9, 10.5, 14.3, 18.5, 19.5, and 25.5 cps, respectively.

Note that the shock spectra do not include feedback. Feedback occurs when the reaction force of a spring-mass combination affects the motion of its supporting mass or floor. This, of course, is what always happens to some extent. However, it is felt that any appreciable feedback effect would occur only if a large single mass was spring mounted and had an uncoupled natural frequency near the primary frequency of the floor's response. In this investigation, with the masses of the cabinets

TABLE 2
Response of Cabinets Including Effect of Intermediate Floor Framing to Shock Spectra Input

Joint	Acceleration (g)		
	a_x	a_y	a_z
2[a]	0.46	—	3.97
3[a]	0.67	—	4.06
5	1.86	0.51	2.97
6	1.86	0.04	2.97
8	0.69	4.58	4.06
9	0.50	3.91	3.91
11	2.28	0.27	2.97
12	4.14	0.55	2.97
13	3.41	4.40	4.14
14	2.30	4.70	4.14
15	2.30	3.75	4.16
16	2.29	1.28	4.17
17	1.21	1.11	3.32[b]
19	1.21	1.11	3.27[b]
21	1.21	1.11	3.32[b]
23	1.21	1.11	3.27[b]
18	1.19	1.34	3.20[c]
20	1.19	1.34	3.15[c]
22	1.19	1.34	3.20[c]
24	1.19	1.34	3.14[c]

[a]Restraints in the y direction.
[b]Modulator.
[c]Filter capacitor.

greater than that of the floor, it was not surprising to see an appreciable amount of feedback, which has the effect of reducing the response of the cabinets. Our results substantiated the above argument. For example, the average response of the filter capacitor cabinet to the shock in the x direction was found to be 2.79 g (see Table 1), whereas the response at the center of gravity for the same cabinet including the cabinet-floor interaction was found to be 1.19 g (see Table 2).

DESIGN CRITERIA FOR ELECTRONIC COMPONENTS

Assume that one of the black boxes containing sensitive electronic components is located at joint 1 (see Fig. 2). Table 3 shows the response of this black box to the shock input without feedback effects (no cabinet-floor interaction effect) to be 2.67 g. Note that only the first 10 frequencies of the cabinet are listed; the computer response for all the frequencies was 2.77 g.

Here we make some important observations:

1. Consider the black box as the primary structure and the sensitive component inside it as the secondary structure. Because the mass of the component is much less than the mass of the black box, it follows that the response of the component follows very closely the response of the black box.

2. The time history of the response of the black box as a rigid body to the air blast approaches that of an oscillatory motion which builds up to a peak and then decays more or less sinusoidally to zero, all within about 1.0 sec. This time history is our forcing function

TABLE 3
Sample Computation for Filter Capacitor at Joint 1 in X Direction

f_i	g_i[a]	ψ_i[b]	ϕ_{1i}	$\lvert g_i \psi_i \phi_{1i} \rvert$	$(g_i \psi_i \phi_{1i})^2$
14.3	1.19	1.42	0.998	1.69	2.86
18.6	1.34	-4.41	-0.317	1.88	3.52
34.0	2.0	-221.4	-0.0007	0.31	0.10
36.5	2.08	1.25	0.131	0.34	0.12
40.9	2.2	0.67	0.415	0.61	0.37
48.9	2.23	-2.24	0.062	0.31	0.10
84.3	2.35	-1.64	0.024	0.09	—
86.9	2.36	-183.1	-0.0004	0.17	0.03
88.4	2.36	1.14	0.052	0.14	0.02
100.7	2.4	1.19	0.002	—	—
					Total: 7.12

Note.--Response of joint 1 = $(7.12)^{1/2}$ = 2.67 g.
[a]g_i = Acceleration value.
[b]Participation factor $\psi_i = \sum_j \frac{m_j \phi_{ji}}{m_j (\phi_{ji})^2}$; ϕ_{ji} = mode shape at joint j resulting from normal mode i (normalized to the largest component in that mode).

for the component, and the relatively long duration of this time history will induce quasi-steady-state vibration in the component.

On the basis of these observations, the design criterion for the component contained in this black box was specified as being equal to the absolute value of $g_i \psi_i \phi_{1i}$ of Table 3 multiplied by the feedback coefficient of 1.19/2.77 for this cabinet and by the appropriate vibration amplification factor, i.e., the transmissibility ratio of the classic steady-state vibration response. Assuming a critical damping value of 0.05, this transmissibility ratio has an upper limit of 10 when the frequency of the component approaches one of the frequencies of the exciting forcing function shown in Table 3.

CONCLUSION

This paper presents one aspect of a complex problem: the design criterion for the components of a cabinet subjected to nuclear-weapon-induced shock. It is hoped that advances in computer technology will enable the analyst to attack the problem as a whole and thus determine the response of the component to a nuclear-weapon-induced shock directly. Meanwhile, the analyst is limited to the approximate step-by-step method described here.

REFERENCES

1. A. Hrennikoff, "Solution of Problems of Elasticity by the Framework Method," J. Appl. Mech., 8:A169 (1941)
2. J. M. Biggs, "Introduction to Structural Dynamics" (McGraw-Hill, New York), p. 246
3. Dana Young, "Response of Structural Systems to Ground Shock," paper presented at the meeting of the American Society of Mechanical Engineers, Nov. 1960
4. B. K. Wada, "Stiffness Matrix Structural Analysis," Jet Propulsion Lab. Tech. Rept. 32-774, Oct. 1965

DISCUSSION

Mr. Pakstys, GD/Electric Boat: You mentioned that this was a shock spectrum type of analysis and I assume that you have to combine the modes in some manner. How did you combine the modal responses to get your expected value at each joint?

Mr. Putukian: I used the modal superposition technique.

* * *

DEVELOPMENT OF A ZERO-G COAST PHASE AIR GUN*

Stanley Rodkin
General Electric Company
Philadelphia, Pennsylvania

The distance-measuring switch for a missile required testing in accordance with a unique acceleration-time profile followed by a zero-g coast phase. An air gun was designed and built specifically to carry out these tests. The gun provided variable performance parameters, making it useful also as an accelerator. Although the air gun was designed as a test tool, it serves also for calibrating all distance-measuring switches received, since there is no other known facility for calibrating this type of device.

INTRODUCTION

To provide adequate simulation in testing a distance-measuring device to be used in a missile, a unique acceleration-time profile was required. The rates of acceleration rise and decay were extremely high, and a zero-g coast phase was required. An operating mechanism within the component lent additional restraint to the solution of the testing problem.

Fundamentals of the distance-measuring switch exerted a great deal of influence on selection of a test method. Basically, the switch consists of a case, wheel, and lead screw. An acceleration applied to the case causes the wheel to move along the lead screw in a direction opposite to the applied acceleration. The total energy, rotational energy, and translational energy acquired by the wheel during the acceleration phase causes the wheel to continue its travel during the coast phase. Electrical contacts are closed by the wheel at the end of its travel. The distance traversed by the unit from onset of acceleration to contact closure was of particular interest.

Among test methods considered and discarded were conventional and unconventional centrifugal testing methods. It was decided that test results obtained with any type of centrifugal testing would be obscure and inaccurate because of gyroscopic forces, Coriolis-induced side loads, and unwanted variations in the intensity of the acceleration vector.

Another undesirable feature is that true distance measurements could not be obtained. The running time of the wheel is the only parameter that can be measured. This then would have to be analytically converted to distance. As in all analytical work, some assumptions would have to be made, and this would lead to a lessening of confidence in the results. Determination of the accuracy of the unit was of prime importance; consequently, it was decided that linear acceleration was required.

When the required coast distance was added to the distance represented by the acceleration-time curve, it became apparent that the overall distance was too great for even a modified shock machine of the Hyge type. The problem became one of locating or designing and constructing a linear actuator, such as an air gun, having the required performance parameters. A survey of known operating air guns disclosed that, although some could meet the rise-time requirement, none could meet the decay-time or zero-g coast requirement.

An on-site inspection of several air guns at the Naval Ordnance Laboratory (NOL), Silver Spring, Maryland, revealed that braking on the NOL air guns is achieved by sealing the muzzle and allowing the piston to pressurize the volume forward of it as it progresses. This causes the force system acting on the piston to change gradually from an accelerating system to a decelerating system. The resulting general acceleration-time curve is shown in Fig. 1.

DECISION TO BUILD

Since no suitable air gun could be located, it was decided to design and build a new air gun

*Work performed while the author was employed by Martin Co., Orlando, Florida.

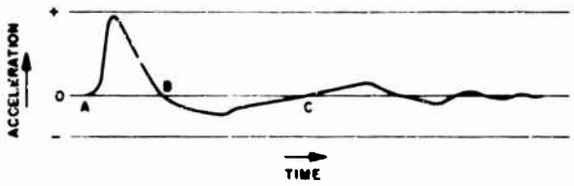

Fig. 1. Acceleration-time curve

to meet the specific acceleration-time profile of immediate interest and to make it flexible enough to provide general usefulness as an accelerator.

The first step in the predesign process was to determine the cylinder diameter. To insure that the air gun would be generally useful to the program, a survey was made of the size of some of the black boxes planned for the system. Overall dimensions of 10 to 12 in. and even larger were found to be not uncommon. It was decided that the cylinder diameter should be at least 16 in., and larger if possible.

Commercially available piping of the type used in gas transmission lines was investigated, but two problems were evident. First, the internal diameter is neither closely controlled nor highly surface finished; this would cause piston sealing and cocking problems. Second, it would be costly and time consuming to weld and machine the flanges to maintain the required alignment between sections.

A large number of surplus slotted steam catapult cylinder sections were discovered at the Naval Engineering Laboratory of the Philadelphia Naval Base. These sections were designed with a working pressure several times the anticipated air gun pressure. Their inside diameter is 18 in. The flanges were designed to maintain adequate alignment for piston velocities higher than the expected velocity and to maintain this alignment while the vessel in which they are mounted is underway in rough seas. Inspection of these cylinder sections indicated that, although they were badly worn and considered to be unfit for further use by the Navy, they were well suited to the intended purpose. A set of two worn catapult pistons was also inspected, and 11 cylinder sections and two pistons were secured.

Figure 2 shows the material upon arrival at the construction site, which is in the remote testing area of Martin Company's Orlando facility. Figure 3 shows the completed air gun.

Fig. 2. Construction site

Fig. 3. Completed air gun

DESIGN AND CONSTRUCTION

Two problems were approached simultaneously: accelerating the piston (which was to contain the test item) and decelerating it. No valve could be used to transfer gas from an accumulator to the cylinder, because the valve, with its associated operating gear and a power source, would be too costly. It was decided simply to restrain the piston at some intermediate position along the cylinder while the cylinder volume behind the piston was pressurized. When the desired cylinder pressure was obtained, the piston would be released and accelerated by the expanding gas. Here a tradeoff was necessary. Expansion of the fixed volume of gas provides a pressure-vs-volume curve, hence an acceleration vs stroke curve, having the shape of an adiabatic or an isothermal expansion curve. In this application, the curve probably approaches an adiabatic because of the extremely short time for release of energy. Although this type of acceleration curve is not desirable, it was judged acceptable if sufficient initial volume was available to prevent too great a decay of pressure. The velocity was to be the controlling factor; that is, when the velocity of the air gun piston (and the test item) equals the peak pop-up velocity of the missile, the inertia wheel in the test item will have received the proper energy input.

The acceleration achieved with the air gun peaked earlier than the missile acceleration; however, the velocity vs time and displacement vs time curves for the air gun were almost exact duplicates of those curves for the missile.

A holdback and release mechanism (Fig. 4) was designed, which performed quite effectively. Control of the piston is possible for something less than one half of the diameter of the pin or approximately 1/2 in. This provides a higher than desired acceleration rise rate. The higher rise rate was considered acceptable since the wheel of the test item would be in, or very close to, its "home" or safest position when the peak acceleration occurred.

After complete release of the piston by the holdback mechanism, the piston is accelerated in the cylinder by the expanding gas behind it. As discussed earlier, no gas is added to the cylinder. The initial volume of gas merely expands to lower pressures as the total volume behind the piston increases. The approximate point at which the required piston velocity would be obtained was calculated. Two large ports were cut into the cylinder at this point to vent the pressure as rapidly as possible. The cylinder slot was sealed in the three 12-ft sections used to form the accumulator. It was also sealed in additional sections to provide for the power stroke. Beyond the power stroke the slot was left open to prevent buildup of pressure forward of the piston. The final sizing of the ports was done experimentally. The pressure (acceleration) decay ultimately obtained closely approximates that of the tactical unit.

After porting, the piston travels at essentially constant velocity. The dynamic pressure, Q, which acts on the forward face of the piston to produce negative acceleration was quite small for the anticipated velocity. The followup pressure acting on the rear face of the piston to produce positive acceleration was assumed to be equal to or slightly greater than Q. The other force considered at this time was the frictional force. Taking 0.1 as the coefficient of friction, the frictional force expressed in gravitational units was 0.1 g. The sum of these theoretical and assumed forces is seen to be trivial. Experimental results proved that the sum of these forces is actually trivial.

The test item was to be used in a vertically launched missile. Since the proposed air gun was too long to be erected vertically, the tradeoff between horizontal and vertical operation showed that a very subtle difference exists in the operation of the test item depending upon whether it is constrained to move vertically or

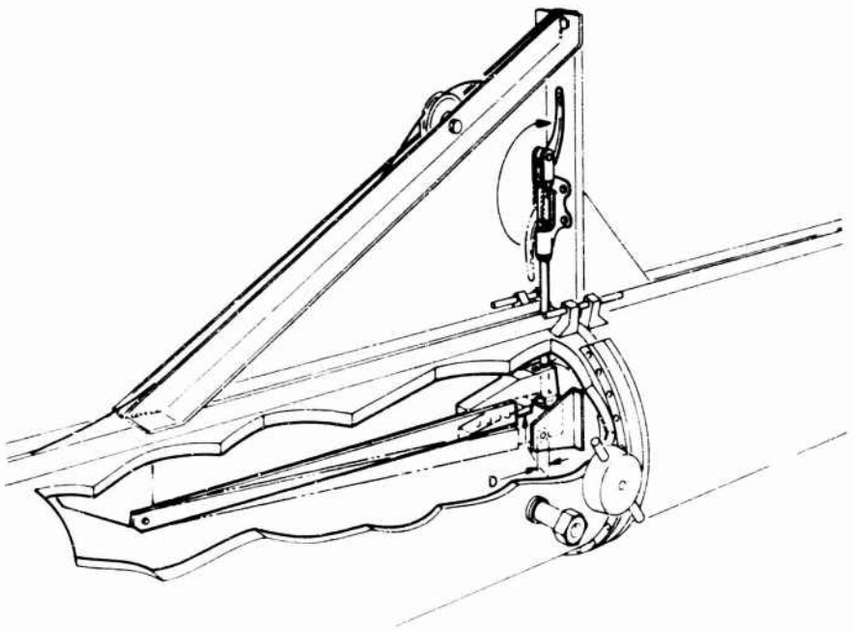

Fig. 4. Holdback and release mechanism

horizontally. The inaccuracy induced by horizontal rather than vertical travel was insignificant and, furthermore, immeasurable.

BRAKING

The braking device is the most interesting aspect of the air gun system. The acceleration-time curve for an air gun using gas compression braking is shown in Fig. 1. The portion of the curve between points B and C may be brought up to zero by ports located forward of the piston. Porting, then, could provide a coast phase for an air-retarded piston, but rebound is not eliminated. Rebound could be reduced by relief valves that dump some of the pressurized gas, but this becomes a difficult problem since the pressure builds relatively slowly until the piston approaches the end of the cylinder. At this point, the time available for gas egress is small, and the valve must be large in order to be effective; if it is large, its response time will be slow. In addition, the danger of releasing too much gas and allowing the leading edge of the piston to impact the end of the cylinder is always present.

A braking method other than compression of air or gas was desired. Various means of absorbing kinetic energy from the piston or of causing its mass to be increased were considered. The simplest and most direct solution is to align the cylinder with a 1/2-deg forward pitch. Water is then placed in the cylinder (Fig. 5). The water depth at the forward end controls the aftermost reach of the water and, consequently, the point where deceleration begins. This point can be readily varied to meet other braking requirements. With the deceleration point 56 ft from the forward end of the cylinder, the water depth at the forward end is approximately 1 ft. There is no danger of the piston impacting the end plate.

Another desirable feature of the catapult cylinder sections functioned in the design and operation of the water braking system. This feature is the slot in the top of the cylinders (Fig. 6). The slot permits some of the water scooped up by the piston to escape to the rear when the piston velocity is high. This reduces peak deceleration since the water which escapes rearward does not undergo as large a change in momentum as that which remains with the piston.

INSTRUMENTATION

Instrumentation was provided to monitor the piston's longitudinal and lateral acceleration and the performance of the test item. The instrumentation cable is attached to the front of the piston and brought out through the slot (Fig. 7). The bungee is used to provide tension on the cable until the piston passes the ports, thus

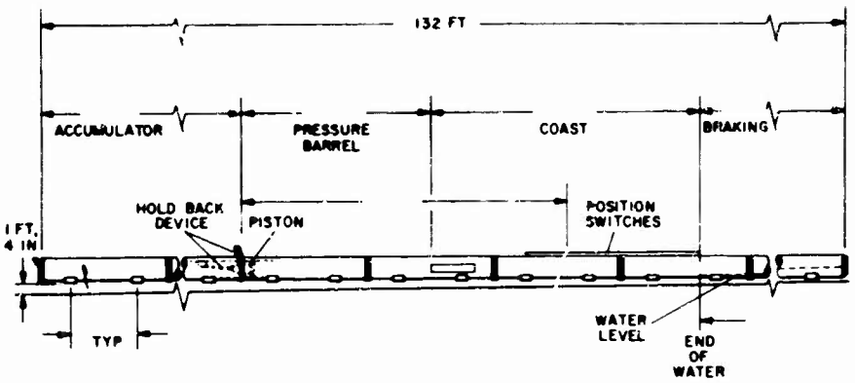

Fig. 5. Side view showing water brake

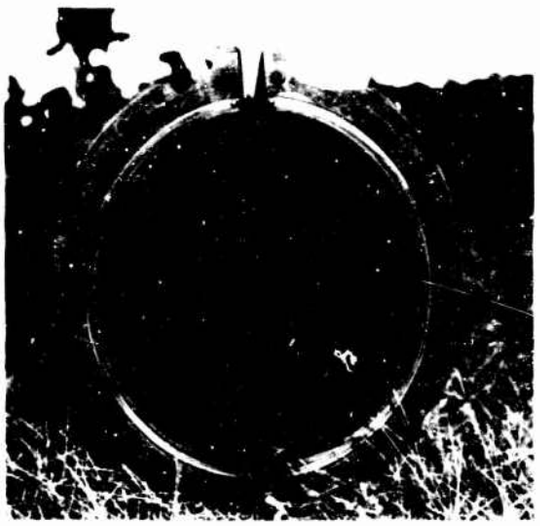

Fig. 6. Slot in cylinder

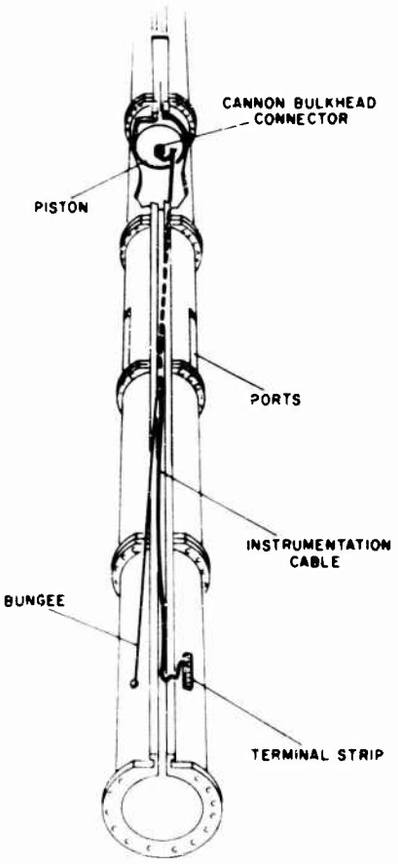

Fig. 7. Instrumentation cable

keeping a loop or kink from flying out through the ports and being cut off as the piston passes. When the cable becomes slack because of the advance of the piston, the piston simply gathers the cable before it and pushes it down the cylinder. A small protruding lip or scoop around the outside diameter of the piston is provided for this purpose. This system has been quite effective, and one cable can be used 10 times before it becomes damaged.

It would have been quite time consuming to integrate each acceleration trace to obtain velocity as a check on the energy imparted to the piston and as a check on the constancy of velocity during coast. The velocity curve would also have had to be integrated to obtain distance. This would have been a costly effort, and the overall accuracy of the system might have been compromised by the data reduction process. Consequently, it was desirable to have a means of comparing piston position with time. The oscillographic recorder provides the time reference,

and breakwires are a convenient method of establishing position, provided they do not break prematurely. Of course, if position and time are known, average velocity is immediately known. An effective breakwire, or contact-wire system, was devised and built from bits and pieces available in the instrumentation laboratory. The system is cheap, accurate, and foolproof. A sketch of one element is shown in Fig. 8, and a wiring diagram in Fig. 9. The wires, which protrude through the cylinder wall, are insulated from it. A potential of 6 v is applied across the recorder. When the piston passes, the wires are bent over against the cylinder wall, closing the circuit and allowing current to flow through the recorder. Each element in the system is accurately located with reference to the battery position of the piston. The velocity is determined by the time between circuit closures. The overall time to pass all breakwires is used to determine average piston velocity. Velocity is quite nearly constant throughout the interval. The precise point at which test item actuation occurs also can be determined. Actuation of the test item results in a change in voltage across the recorder. The velocity in the 2-ft interval preceding actuation is determined, and the elapsed time between passage of the preceding breakwire and test item actuation is read from the oscillograph. Since the exact distance to any breakwire is known, and since the velocity remains constant across the breakwire system interval, it is a simple matter to determine the distance at which test item actuation occurred. This may be stated mathematically as $S = S_1 + Vt$.

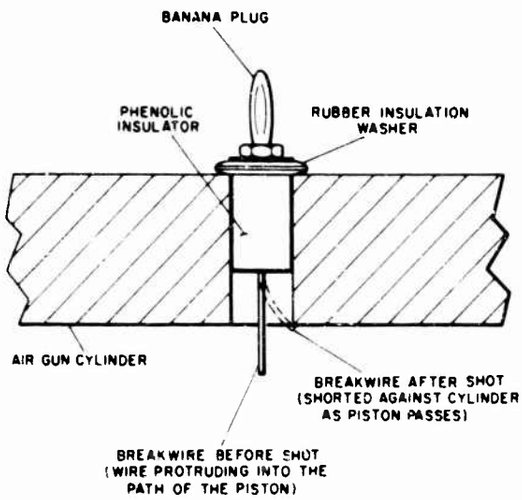

Fig. 8. Breakwire

TEST BED

The test bed is simply a shelf mounted inside a watertight chamber. The chamber-shelf assembly is mounted inside the piston. The piston in the air gun is a worn catapult piston acquired with the cylinders. It has a length/diameter ratio of approximately 0.66. Perhaps the largest single risk concerned with development of the air gun was in firing this relatively short piston down the cylinder. In the original steam catapult application, the piston merely provides the pressure area for an assembly 8 to 10 ft long. This assembly consists mainly of the piston, a relatively long barrel, a forward guide, and a brake spear.

The short piston has performed well; accelerometers mounted within it have shown that it has no tendency to cock and jam in the cylinder. The vertical accelerometer has indicated a transient response equal in amplitude to approximately 20 percent of the longitudinal acceleration. This response is due to the release mechanism. The response dies out after one cycle, and no vertical motion is detected again until the water entry phase.

The piston incorporates what is believed to be a unique application of an O-ring (Fig. 10). The O-ring is placed at position A before the piston is retracted into the battery position, and sealing is accomplished while accumulator pressure is increased to the desired level. When the piston is released and forward motion takes place, the O-ring drops to position B, where it is free of the cylinder walls. Gas leakage is considered negligible because of the short time involved. Relatively little wear takes place with this arrangement, and the O-ring needs to be changed only when deterioration due to exposure to the elements takes place.

CONCLUSION

The air gun has performed very well and has been utilized much more than was originally anticipated. Upwards of 400 shots have been made. Although initially designed as a test tool, it was subsequently used for calibrating all the distance-measuring switches received, since there is no other known facility where true distance calibration can be done. In addition, the air gun was used to investigate to what degree the acceleration intensity applied to the test item could be reduced before the unit would fail to actuate.

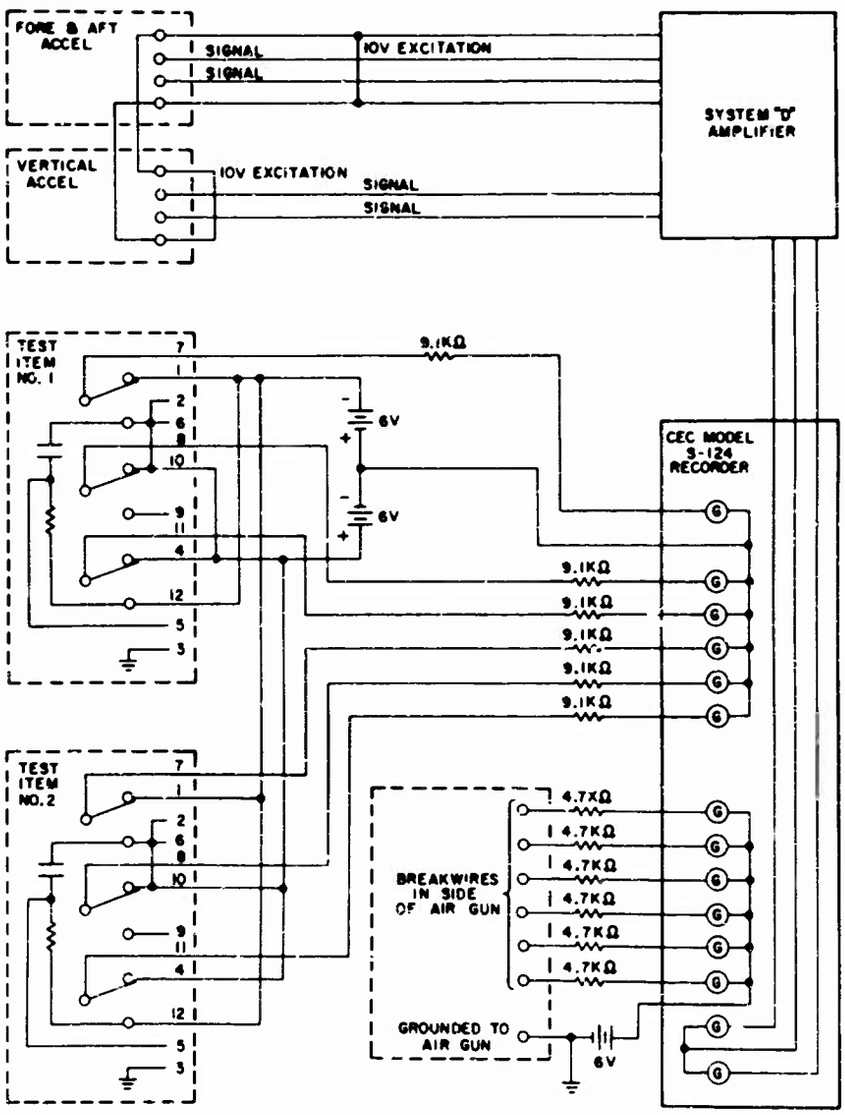

Fig. 9. Wiring diagram

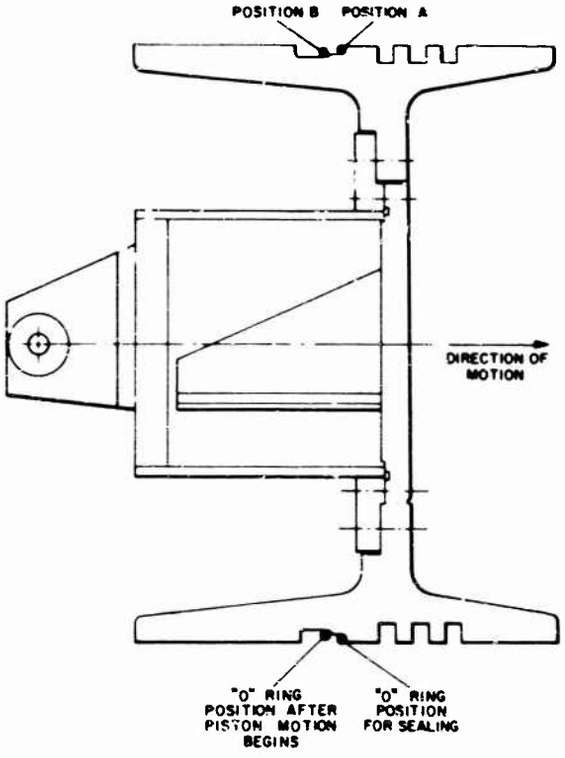

Fig. 10. Piston showing O-ring arrangement

ACKNOWLEDGMENTS

The author thanks Val Dvost of the NOL for providing information on various aspects of piston sealing and braking. He also acknowledges the O-ring innovation provided by William E. Dickson of Martin's Engineering Prototype Laboratory.

* * *

DEVELOPMENT OF A MISSILE LAUNCH SHOCK TEST FACILITY FOR SHILLELAGH

Richard W. Stevens
Martin-Marietta Corporation
Orlando, Florida

The facility described was developed to test Shillelagh antitank missile components in a unique shock and acceleration environment. It is a 96-ft-long launch tube made from aircraft carrier catapult sections. Test samples, or complete missiles, are mounted in a carrier piston which has hard-wire provisions for electrical power, signals from a guidance simulator, and monitoring of subsystem or missile responses to guidance command during the simulated launch shock tests. The carrier piston is accelerated by high-pressure nitrogen which is released by a specially designed valve which is described in detail. During a 50-msec pulse time (10-msec rise and 40-msec decay), longitudinal acceleration loads greater than 250 g are attained. (The facility has a 600-g capacity.) Terminal velocity for a 250-g shot is 240 fps. A water brake is used to absorb approximately 300,000 ft-lb of kinetic energy from the piston.

The facility has been used successfully since the beginning of the year in Shillelagh pilot lot and reliability confidence tests. Test conditions are repeatable within the limits of accuracy of pressure instrumentation. Recycle time for tests is as low as 30 min.

INTRODUCTION

The Army's Shillelagh missile is a ground-to ground, command guided, solid propellant weapon designed as main armament for armored combat vehicles. It is launched from a 152-mm combination gun-launcher on the Sheridan and the M-60 AIEI tanks. The missile is 45 in. long, 6 in. in diameter, and weighs approximately 62 lb. The missile is controlled in flight by a gas-generator-powered jet reactor thrust system. When the missile is launched from the gun-launcher it develops a launch shock profile of approximately 250 g during the initial part of the boost phase. This long pulse shock profile is unique to the Shillelagh missile and requires a unique test facility. The development of a launch shock test machine to test the Shillelagh missile and its components is discussed here.

TEST REQUIREMENTS

The limitations and constraints imposed upon this program presented a challenge. They required a vehicle to shock the test specimens, to provide a watertight container, to record test parameters, and finally to stop the vehicle with a uniform braking force. Testing of live ordnance missiles and gas generators was also required. Both time and funds for development of the facility were very limited.

Two basic types of test programs were conducted, the first being qualification testing, commonly called pilot lot acceptance. This required shock testing at the 250-g level. The second type was reliability confidence testing. A number of components of each type were subjected to increasing shock levels to determine failure levels. The components were first shock tested at the 250-g level and then at levels increasing to 600 g or the point of failure.

By specification the shock pulse was defined as a skewed half-sine shape, with a 10-msec rise time to a peak acceleration of 250 g, then a decay to 25 g for another 40 msec. The total pulse length was to be 50 msec. The shock pulse length for levels up to 600 g was shortened to 30 msec (the shock pulse profile is shown in Fig. 1).

Operational performance of the electrical components during each shock exposure required continuous electrical monitoring during the boost and glide phase or for approximately

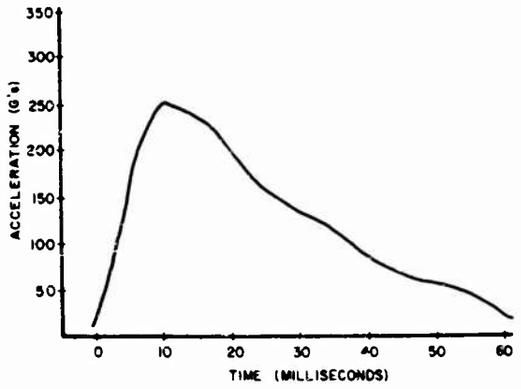

Fig. 1. Launch shock profile

20 sec. Besides monitoring, it was necessary to supply ac and dc voltages to the test components and high-frequency modulated command signals, some of which required separate shielded conductor cables.

DESIGN APPROACH

Existing System

We had an air gun system composed of 11 Navy surplus catapult tubes, each 12 ft long, with a 100-g capability. The tubes had a bore diameter of 18 in. and a 1.5-in slot at the top. Three sections welded shut provided a 63-cu-ft accumulator tank. The other 8 tubes joined in line provided a 96-ft run for the carrier piston. Test items were fastened to a flat plate inside the carrier piston. The piston was mechanically restrained between the accumulator sections and the launch way with a hook and lug device. Mecharical release was effected when the hook was pulled up, disengaging it from the lug. The unrestrained piston was accelerated down the tube by the expanding compressed air. The acceleration level was controlled by the gas pressure. The pulse length was controlled by the location of the exhaust ports cut through the side of the tube. Braking was accomplished when the piston encountered water in the lower end of the tube. The piston came to rest near the end of the tube. The acceleration pulse was recorded through a hard-wire system which was severed during each shot.

Although the existing system was available, it was operationally limited to shock profiles of approximately 100-g acceleration. The restraining release mechanism and the accumulator sections were the limiting factors because they were structurally critical above the 100-g level of operation. It was determined that a new method of release or valving was required to meet the Shillelagh requirements for a 600-g system.

An investigation of cost and lead time revealed that it was not feasible to buy suitable test equipment. Equipment of this type and size would require special design and manufacturing. In addition it would be necessary to build a new test site. Both phases would require considerable time and expense above that available. Therefore a decision was made to modify the existing air gun.

Analytical and empirical data were instrumental in developing an approach to a design for the new launch shock valve. On the basis of mass and acceleration the operating pressure or force could be calculated. Pressure and volume at the end of the power stroke along with the energy equation were used to determine the size of the accumulator. Integrating the area under the velocity curve produced the length of the power stroke and thus the location of the exhaust ports.

The New Valve

A number of valving and restraining methods were investigated. The first approach was to "beef up" the existing system. The massiveness of the restraining mechanism would have imposed a large weight penalty. Also the required rise time of 10 msec would be difficult to obtain with the necessary large hook and lug design, to say nothing of the friction problem.

Another conception which was investigated consisted of a pilot-valve-operated sliding cylinder. The cylinder contained large orifices which allowed the gas to flow into the plenum behind the carrier piston. The pilot valve was electrically controlled and hydraulically powered. A large storage tank was to supply the air pressure through a large pipe. Cylinder opening time was found to be 30 msec at best. Mass flow calculations proved this valving method to yield only 50 percent of the required pressure-volume necessary to accelerate the piston in the prescribed 10 msec. In addition the cost and time for manufacturing this type of custom hardware was excessive.

It was decided to use a mechanically released, pressure-actuated vent valve with one 9-in-diam valve (Fig. 2). The valve opens into the plenum behind the carrier piston. Accumulator pressure behind the valve drives it

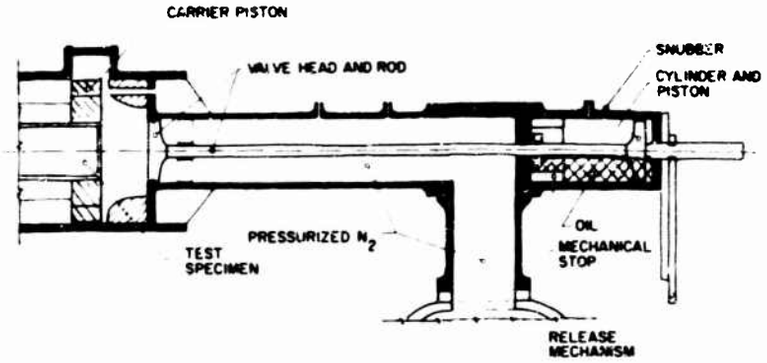

Fig. 2. Valve cross section

open when the valve rod is mechanically released. By use of a small, 8-in. valve rather than an 18-in. piston, workable loads and stresses are handled more efficiently. The valve operates with a varied reaction time because of the snubber system. The stroke of the valve and opening at the throat can also be adjusted by this same snubber provision. The plenum at the rear of the carrier piston was streamlined with a liner to improve the valve efficiency. It was anticipated that the time delay for the gas to expand into the plenum would provide the 10-msec rise time required. This was verified later during tests.

Prior to firing, the rod is restrained by a scissor clamp operated by an over-center linkage. When the lanyard is mechanically pulled, the scissor clamp opens. Once the scissor has released the rod, the valve pops open, allowing the high-pressure nitrogen to flow into the plenum and drive the carrier piston down the catapult tube.

A method of preventing the valve from striking the carrier piston and regulating its opening characteristics was provided with the snubber arrangement at the rear of the valve rod. The snubber consisted of a piston which traveled in a closed steel cylinder containing oil and a mechanical stop. Metering holes in the piston head were added during test to regulate the oil flow. Adjustment of this flow was necessary to cushion the impact of the valve during its short stroke of 4 to 5 in. After a number of test shots, the proper metering and oil level was determined. The snubber piston was threaded to the rod to allow longitudinal adjustment. As stated above, by adjustment of the snubber piston, the oil level, and the mechanical stop, the stroke could be regulated and the valve throat opening changed. The flow rate and the rise time could also be adjusted.

The release mechanism was built in the same principle as a pair of wire cutters or pliers (Fig. 3). The handle applied a large mechanical advantage to the clamping surface. An over-center linkage was designed to hold the scissor handles apart and close the clamp on the valve rod. When the lanyard is pulled, the handles close, the clamp opens, and the rod slides free between the grips. During tests the contact angle between the rod and scissor grips was increased to near 45 deg before the mechanism would release properly. At first the friction in the contact plane exceeded the force on the rod.

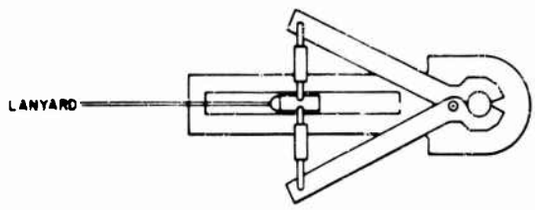

Fig. 3. Release mechanism

The accumulator volume was determined by the following expression:

$$V_0P_0 \quad V_1P_1 + \frac{1}{2}Mv^2 + K$$

where K = valve efficiency approximately 80 percent, V_0P_0 = initial value or total requirement, and V_1P_1 = duration of the power stroke. This expression combines Boyles gas law for static-state gases with the energy equation. The accumulator volume could be regulated by the addition of water in the bottom of the tank. This technique was planned for shaping the pulse.

The Piston

The carrier vehicle consisted of an aluminum cylindrical piston 18 in. in diameter and 24 in. long. The piston was designed around an aluminum tube slightly larger than the missile diameter. Test specimens slide into the watertight tube from an access plate in the front. The piston rides on bronze shoes which are mounted at each end. The design of the piston was governed mostly by weight. Previous aluminum pistons of a similar design weighed three times as much, requiring a correspondingly higher operating pressure.

A longer piston, 50 in. in length, was built to accommodate testing of the whole missile. A three-piece collar clamp fixture secures the missile inside the carrier piston tube.

BRAKING

Another factor important to this test system was the braking. At peak velocity, the carrier piston develops approximately 300,000 ft-lb of kinetic energy. Stopping the piston with a uniform braking force posed an interesting problem. Several types of friction-braking systems were first investigated. None of these could be adapted to the catapult tube without extensive modifications to the system. Following this, water scoop schemes were studied, and it was decided to use the existing water brake. After some test runs the data proved that the deceleration peak did not exceed the allowable 20 percent of the acceleration peak, nor did the lateral pitch acceleration exceed the 10 percent allowable. During the water scoop study the following expression was helpful based on 180-deg transfer:

$$F = \frac{\rho A v^2 \, 2}{g} .$$

where F is the decelerating force, ρ is the specific weight of water and A is the cross sectional area of the water.

The water brake system works very simply. The catapult tube, 96 ft long, is sloped down approximately 1.0 deg. With a steel plate over the end of the tube, water is filled to a point about 60 ft from the end. At peak velocity the piston contacts the shallow water first. As the piston continues, water builds up in front of the piston until it ejects vertically out the top of the tube. The piston comes to rest near the end of the tube with virtually no acceleration indicated from the data. The highest acceleration occurs when the velocity is maximum in accord with the energy expression K.E. $1/2Mv^2$.

ELECTRICAL MONITORING SYSTEM

A hard-wire system was developed to supply control voltages and to monitor electronic functions during launch shock exposure. This communication was also necessary to simulate guidance commands during operational performance. The cable penetrated the front bulkhead of the carrier piston with a pressure fitting to prevent water penetration. After a number of test shots the cable assembly and the rigging were perfected. At first the cable broke frequently.

The cable was made up of a 30-conductor Belden cable, two shielded pairs, and a steel reinforcing wire. All were covered with plastic sheathing. The cable had to be lightweight and flexible. Once this assembly was developed and the proper rigging set up to prevent cutting or breaking because of whiplash, the cable became a very reliable system.

TESTING

During the test phase a number of experimental shots were made to check out and adjust the valve. In particular, the snubber and the release mechanism were operationally tested and perfected to a point of reliable performance. Pressure, acceleration, and displacement measurements were recorded to establish the oil level and the metering to cushion the valve stroke. Acceleration vs operating pressure curves were established.

Prior to the complete assembly of the valve assembly, the accumulator and other pressure bearing components were hydrostatically proof loaded to a factor of 2.0 to verify safe performance. This was based on a peak operating pressure of 800 psig. So far the operating pressure range for 600 g has been 350 to 450 psi, depending on the piston weight.

Flight axis acceleration control and repeatability were verified to be within the reading accuracy of the Bourdon pressure gage, or less than 1 percent. Lateral acceleration (pitch or yaw) approached but did not exceed the 10 percent allowable.

From a continuous operating basis, turn around time between shots varied for different

types of tests. Some reliability tests were accomplished in less than 30 min while others required 1 hr or more.

CONCLUSION

The Shillelagh missile launch shock test facility has performed well during the last year of operation. Both of the Shillelagh test programs, pilot lot and reliability confidence, have completed a large number of tests. The system has functioned well at levels of 250 to 600 g.

ACKNOWLEDGMENTS

I should like to acknowledge the contributions of Jim Mackey and Mark Hendricks for development and testing assistance and John Cawthorn and Bill Dickson for design assistance.

* * *

USE OF EXPLODING WIRE APPARATUS FOR LABORATORY SIMULATION OF SHOCK WAVES*

Fred B. Safford†
Northrop-Nortronics
Palos Verdes Peninsula, California

and

Raymond C. Binder
University of Southern California
Los Angeles, California

The results of an investigation of the potential of the exploding wire for generating shock waves in the laboratory are reported. Previously unavailable information was obtained. Two main features are discussed: the development of apparatus and the use of this apparatus in particular experiments.

The apparatus consists of a power supply, a capacitor storage unit, an explosion chamber for electrodes, ducting for the shock wave, and a termination at the end of the duct. Shock wave velocities, sound pressure levels, and shock front curvature were measured with high intensity microphones.

The shock waveform is similar to that measured for nuclear and chemical explosions. The shock wave system has proved to be a reliable, convenient, repeatable, inexpensive, and safe laboratory tool, with the capability of expansion to higher energy yields. Prediction of peak side-on pressures for a ducted configuration can be made from system parameters.

Transmission studies were made with solid plates. The results indicate that transmission loss follows the acoustic mass law with respect to panel weight and frequency, but yields a higher loss because of the transient nature of the disturbance. Exploratory studies of screens (porous barriers) has disclosed substantial transmission loss.

While used primarily for shock waves in air, the exploding wire apparatus can also be used for shock waves in water.

INTRODUCTION

This paper reports the development of a laboratory apparatus for producing transient pressure waves by electrical discharge. Characteristics of concern in this work comprise repeatability, waveform, control, pressure range, far-field effects, growth potential, simplicity of operation, ease of maintenance, and safety.

Demonstration of this apparatus as an investigative tool is covered by studies of transient waves in transmission through solid and porous barriers.

EXPERIMENTAL APPARATUS AND INSTRUMENTATION

The blast wave system developed is schematically represented in Fig. 1. This apparatus consists of a 40-kv dc power supply, a 7-μf capacitor bank, an explosion chamber for electrodes, ducting for the blast wave, and a nonreflecting termination at the end of the duct. Transfer of stored energy to the exploding wire electrode is accomplished by a simple manual slide switch. The test station is located in the duct 5 ft from the plasma source and consists of a high-loss enclosure with one face equipped for mounting test panels for transmission and

*This paper was not presented at the Symposium.
†Now at Mechanics Research Inc., El Segundo, California.

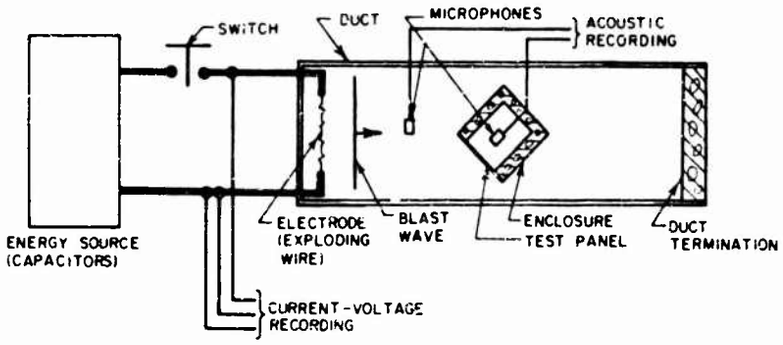

Fig. 1. Schematic arrangement of blast wave apparatus, instrumentation, and panel transmission tests

reflection studies. Figure 2 pictures the apparatus. The duct is 15 ft long and has an internal diameter of 20 in. The explosion chamber and ducting are acoustically lined.

Detailed instrumentation of the system is shown in Fig. 3. Time histories of electrical and acoustic signals are obtained from oscilloscope cameras. A chromel current shunt in the return circuit of electrodes provides for current monitoring. High intensity microphones used were Altec-Lansing type 21BR200. Netic and Conetic material was extensively used to suppress electromagnetic interference from the plasma. Shielding is routed to power ground, and electrical and acoustic signals are equipped with a separate ground.

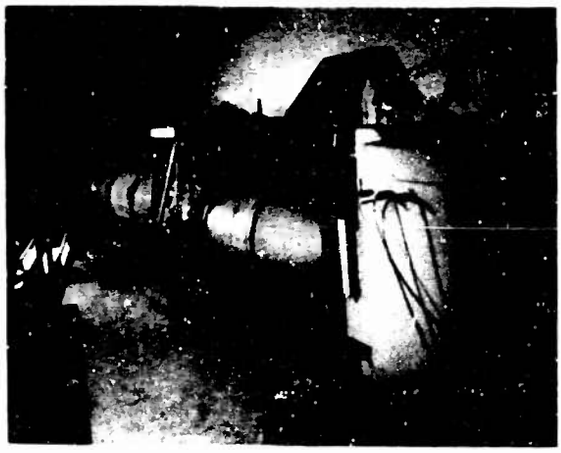

Fig. 2. Blast wave system (generating end)

SYSTEM PERFORMANCE

System control is provided by voltage charge level in the capacitor banks and by type of electrode (exploding wire) employed. Maximum energy storage of the capacitors is 5600 w-sec. Electrodes studied covered a wide variety of conducting materials, cross sections, lengths, and configurations. A 4-mil-diam copper magnet wire was eventually selected as the standard, allowing electrode length as a control variable. Electrode lengths varied from 0 to 19 in. Because of the explosion chamber configuration, straight wires up to 8.8 in. could be employed; above this length a zigzag configuration was required. Above the 19-in. length, the plasma failed to develop and the electrode exhibited a simple burnout with slight energy loss.

Discharge characteristics of the system showed a time history for voltage or current as a damped sinusoid under all control settings. Decay times for current discharge ranged from 66 μsec for a 5-in. electrode at 28 kv to 13 μsec for a 19-in. electrode at 20 kv. Oscillation frequency was quite constant over this range of voltage-electrode combinations being measured at 75 kc. Peak currents ranged from 41.6 ka for 19-in. electrode at 20 kv to 145 ka for a 5-in. electrode at 28 kv.

The characteristics of the electrical time history during discharge suggest representation of the electrical subsystem as a lumped R-L-C circuit. With an initial charge E_0 on the capacitors, the discharge current i is given as:

$$i = \frac{-E_0}{L\left[\frac{1}{LC} - \left(\frac{R}{2L}\right)^2\right]^{1/2}} e^{-R/2L} \sin \omega t , \qquad (1)$$

and

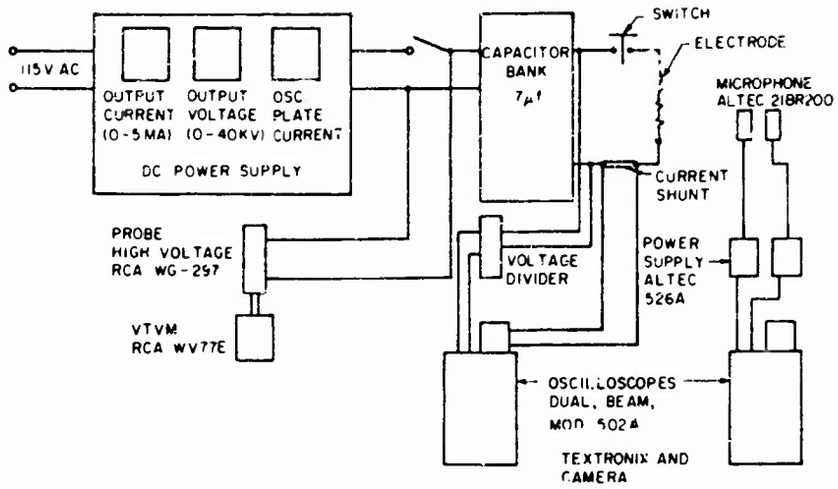

Fig. 3. Block diagram of instrumentation system

$$\omega \approx \sqrt{\frac{1}{LC}}. \qquad (2)$$

and

$$R = \left(\frac{2L}{t_2 - t_1}\right) \ln\left(\frac{L_1}{L_2}\right). \qquad (3)$$

where R = resistance, L = inductance, ω = frequency and t = time.

Measurements of current discharge from direct shorts to various lengths of electrodes over an appropriate voltage range provide values for the determination of source impedance and load impedance. These values, together with the schematic of the circuit, are shown in Fig. 4. Load impedance of the plasma is composed of a low impedance 0.06 μh which appears, within measurement resolution, to be independent of electrode length and a normalized conductance. Conductance has been normalized directly with length and inversely by the square of the voltage. Electrode configuration provides a further effect by lowering the conductance in a zigzag configuration compared to a straight wire. As is to be expected, arcing at the switch affects source resistance as a function of voltage.

Stored energy transferred to the plasma W_p is given by:

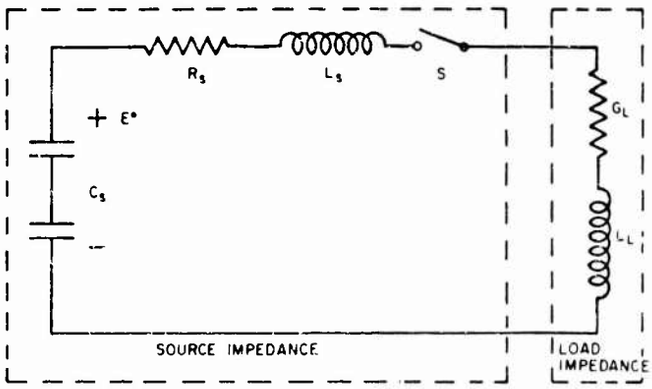

SOURCE IMPEDANCE

$C_s = 7\mu h$

$L_s = 0.59\mu h$

R_s = 30MΩ AT 28 kv; 27MΩ AT 24 kv; 21MΩ AT 20 kv

LOAD IMPEDANCE

$L_L = 0.6\mu H$

G_L = 0.190 mho - in/kv² (ZIGZAG)

0.295 mho - in/kv (STRAIGHT)

Fig. 4. Lumped parameters of electrical subsys

$$W_P = \frac{4R_L C L^2 E_0^2}{(4L - R^2 C)(R^2 + 4L^2 \omega^2)} \left[\frac{2L \omega^2}{R} (1 - e^{-RT/L}) - \left(\frac{R}{L} \sin \omega T + 2\omega \cos \omega T \right) e^{-RT/L} \sin \omega T \right] \quad (4)$$

where R_L = plasma resistance and T = decay time of current oscillation.

Output plasma energy as a function of transfer efficiency from stored energy is given in Fig. 5 for electrode length and discharge voltage. Transfer efficiency varies from a low of 49 percent for a 5-in. electrode at 28 kv to a high of 95 percent for a 19-in. electrode at 20 kv.

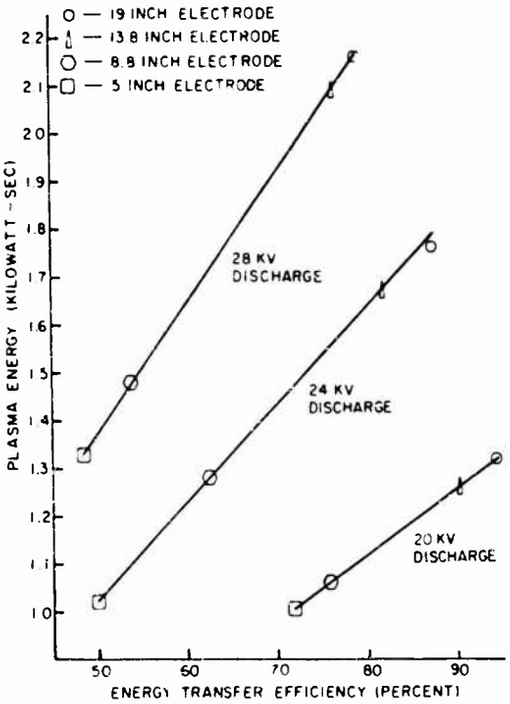

Fig. 5. Output plasma energy as a function of transfer efficiency, discharge voltage, and length of electrode

The sudden release of electrical energy into a fine wire or across an air gap creates a rapid plasma expansion, giving rise to a series of shocks in the atmosphere which radiate outward from the discharge [1,2]. At a short distance from the source, these shocks coalesce to form a steep pressure front having a generally

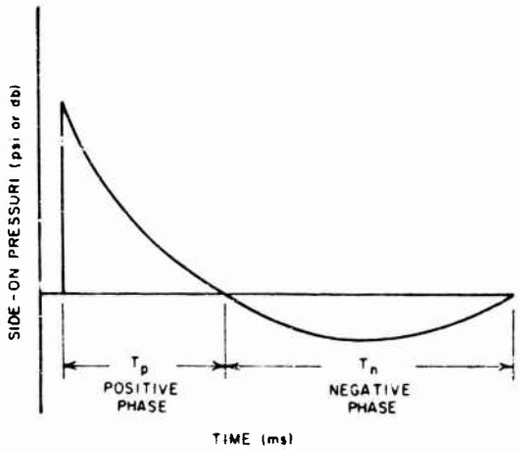

Fig. 6. Transient wave generated by system

exponential decay into a negative pressure, with subsequent return to ambient level. Figure 6 illustrates the pressure-time history of this phenomenon which is similar to waveforms encountered with nuclear and chemical explosions [3]. Absolute values of Fourier transform components of a blast wave side-on pressure are shown in Fig. 7. This display has been computed from a standardized test of a 13.8-in. electrode at 28-kv discharge with microphones located in the duct at a distance of 5 ft from the explosion source.

Peak side-on overpressures are given for control settings of voltage and electrode type in Fig. 8 for combustion chamber location and Fig. 9 for the test station 5 ft downstream in the duct. In the combustion chamber a maximum 28-psi peak side-on overpressure was measured, while at the test station the maximum peak was measured at 4.2 psi.

Conversion of plasma energy into acoustic energy in the combustion chamber ranges from 15 to 52 percent, depending upon control settings of voltage and electrode in accordance with Fig. 10. Acoustic energy W_A was determined from:

$$W_A = \frac{5AC_0 P^2 T_p}{7P_0} \left[0.216 - 0.0359 \frac{P}{P_0} + \cdots \right] \quad (5)$$

where

A = Duct cross section

C_0 = Local velocity of sound

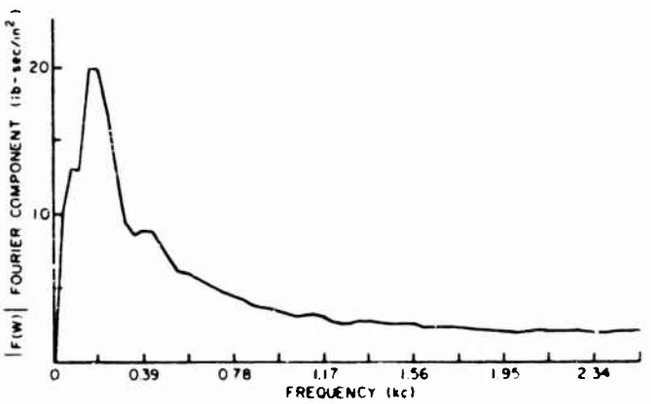

Fig. 7. Absolute values of Fourier components of blast wave side-on pressure as function of frequency (28-kv discharge using 13.8-in. electrode; microphone located at test station 60 in. from source)

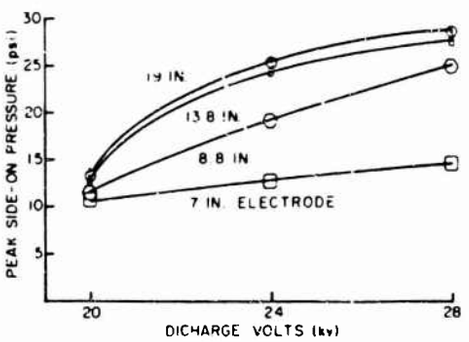

Fig. 8. Peak side-on pressure (psi) for discharge voltage and electrode in combustion chamber

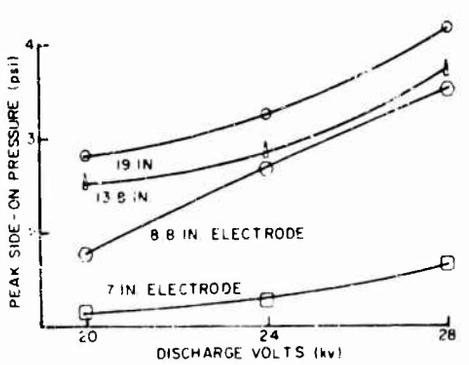

Fig. 9. Peak side-on pressure (psi) for discharge voltage and electrode at test station 60 in. from source

P = Peak side-on overpressure

P_0 = Ambient pressure

T_p = Positive phase duration.

An empirical relation between plasma energy and acoustic energy was found to give:

$$W_A \quad (4.6 \cdot 10^{-8})\, W_p^{3.16} \qquad (6)$$

Peak side-on pressure may be determined by:

$$P^2 \left(1 - 0.166 \frac{P}{P_0}\right) \quad \frac{P_0(8.6 \cdot 10^{-5})}{AC_0 T_p}$$

$$\cdot \left[\frac{R_L C L^{3.2} E_0^2}{R(4L - R^2 C)(R^2 + 4L^{2.2})}\right]^{3.16} \qquad (7)$$

From the 9-in.-diam combustion chamber, the blast wave expands through a conical horn into a 20-in.-diam duct to the test station. For a standard test of 13.8-in. electrode at 28 kv, it was found that the shock wave velocity U decayed exponentially with duct distance

$$U \quad 873e^{-0.65d} + 1127, \qquad (8)$$

where d = distance in feet. This gives a blast wave velocity of 1167 fps at the test station. Local sonic velocity at this point in the duct was measured as 1045 fps [4], such that the Mach number of the wave was 1.12.

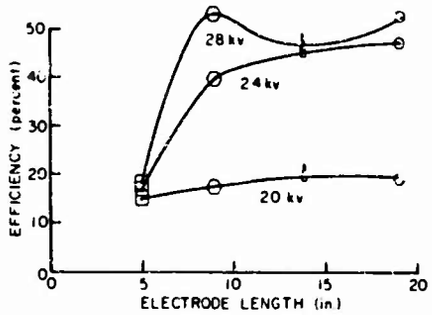

Fig. 10. Electroacoustic conversion efficiency from plasma energy in combustion chamber for electrode length and discharge voltage

Pulse duration (positive phase) varied with wave energy and ranged from 1.5 to 2.15 msec. In general, the one-third power law was followed at the same measurement location only.

Wavefront curvature was measured at various locations in the duct system using two microphones over the cross section. Within the limits of instrumentation, the wavefront was found to be essentially flat. Variation in pressure-time history over various cross sections of the duct and repeatability of the waveform for fixed microphone positions were examined by small-sample theory. Student's t distribution showed sample means were well within the process mean at the 1 percent critical level. Confidence limits for variance by distribution indicated a 96 percent confidence that deviation ranged between 5 and 10 percent of the mean [5].

Between the combustion chamber and the test station, duct losses amounted on the average to 16.5 db (re 0.0002 μbar). Spreading loss in the horn expansion accounted for 8 db in addition to 5.2 db for the horn. Loss in the 20-in. duct amounted to 3.3 db.

An electroacoustic block diagram is used to represent the system with associated matrix notation for peak values as shown in Fig. 11. Figures 12 through 15 are plots of the overall transmission matrix for plasma voltage and current to test station pressure and particle velocity [5].

TRANSMISSION TESTS

A series of aluminum plates ranging in thickness from 0.017 to 0.093 in. were tested for transmission characteristics for the

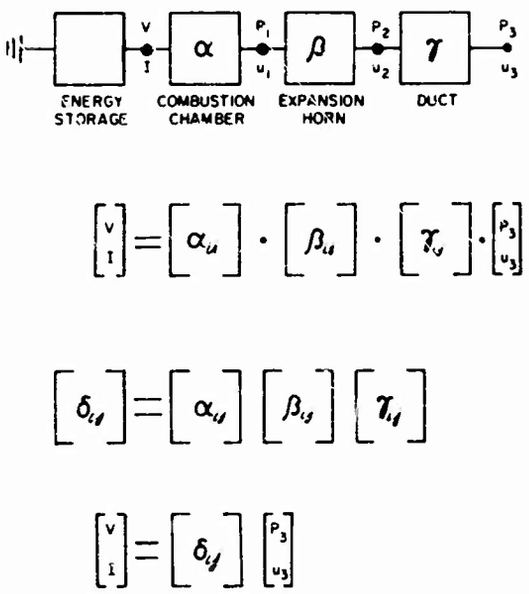

Fig. 11. Electroacoustic system block diagram and matrix representation

transient conditions of the blast wave. The panels were simply supported at only 0-deg angle of incidence of the blast wave. Partially clamped plates were used at angles of incidence ranging from 0 to 90 deg.

Pressure transfer functions for the plates indicated four general characteristics:

1. All plates exhibited a low-frequency single peak in the 0- to 60-deg range, as shown in Fig. 16.

2. Thick plates showed a partial dual-peak low-frequency characteristic in the 0- to 60-deg range.

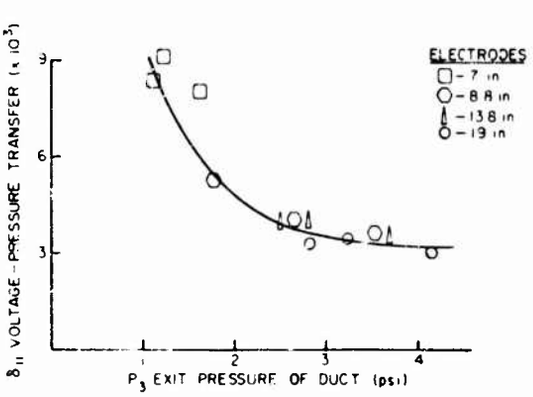

Fig. 12. Voltage-pressure transfer function for values of exit pressure from duct

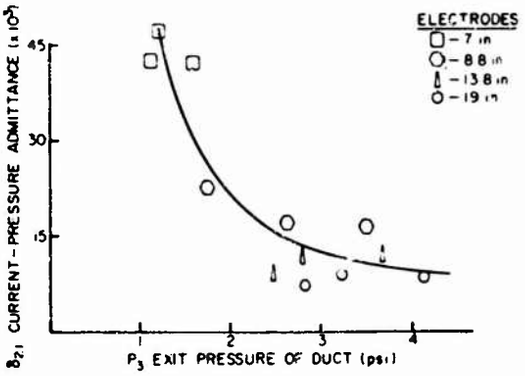

Fig. 13. Current-pressure admittance for values of exit pressure from duct

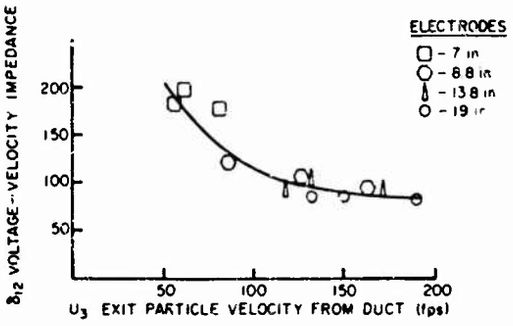

Fig. 14. Voltage-velocity impedance for values of exit particle velocity from duct

3. Thin plates exhibited multipeak characteristics above 70-deg angle of incidence.

4. Predominant high-frequency peaks with near unity transmission occurred at angles of incidence near 90 deg, suggesting coincidence effects, as shown in Fig. 17.

Fourier transform representations of plate transmission responses are shown in Fig. 18 for 0-deg angle of incidence. For these simply supported plates, there was very close agreement between blast loading function, pressure transform, and response function in profile and center frequencies of the peaks.

The effect of simply supported edges and partially clamped edges is shown in Fig. 19.

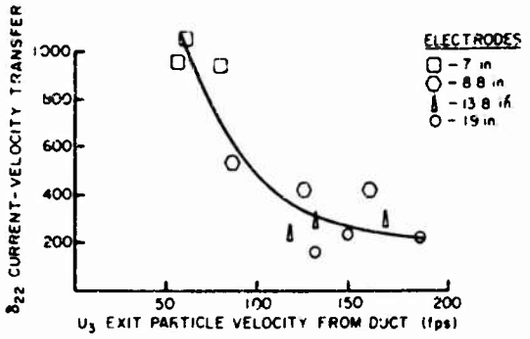

Fig. 15. Current-velocity transfer function for values of exit velocity from duct

The simply supported plates closely follow the mass law, showing a 4-db greater loss than the steady-state case. The partially clamped plates exhibited the constraints of the boundary at all angles of incidence.

Exploratory studies of a porous plate were also made for transmission characteristics. This plate, consisting of a 66 percent open area, comprised five layers of screens spaced 0.25 in. apart. Transmission loss at high angles of incidence (90 deg) amounted to 65 percent. Fourier transform presentations of the transfer function and response function are given in Figs. 20 and 21.

CONCLUSION

This paper is a summary of activities conducted to date at the Hypersonic Range Laboratory at the University of Southern California. The extensiveness of the system, together with its applications, has permitted only brief coverage in many areas. The technique for measurement of the four-pole parameters [6] was omitted, as well as the individual parameter plots of each duct element. Phase angles associated with Fourier transform displays, while available, were not included.

While expansion of the system for higher energy yields is quite feasible, extensive shielding of the capacitor banks and explosion chamber is necessary to suppress electromagnetic interference in the instrumentation system.

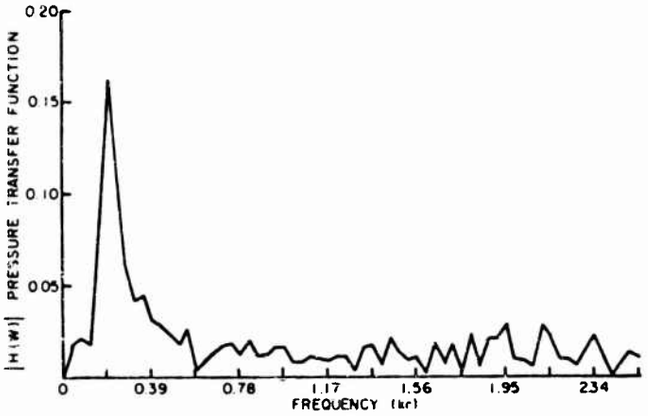

Fig. 16. Pressure transfer function for 0.062-in. plate at 30-deg blast wave incidence; except for thickest plate (0.193), single peak characteristic is typical in 0- to 60-deg incidence range

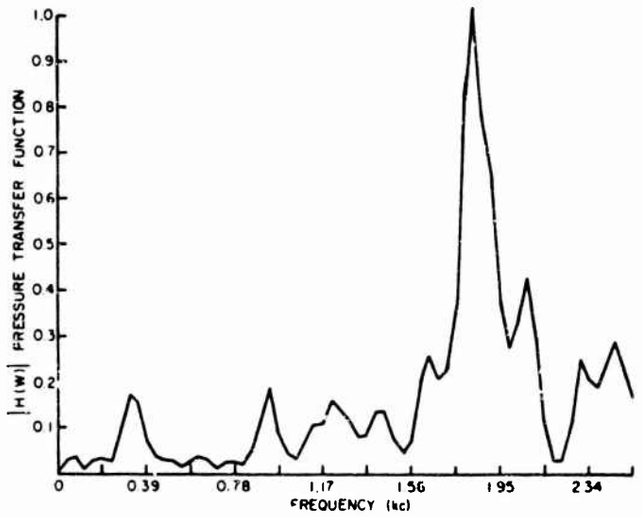

Fig. 17. Pressure transfer function for 0.127-in. plate at 90-deg blast wave incidence (high-frequency peak predominates at angles of incidence greater than 75 deg)

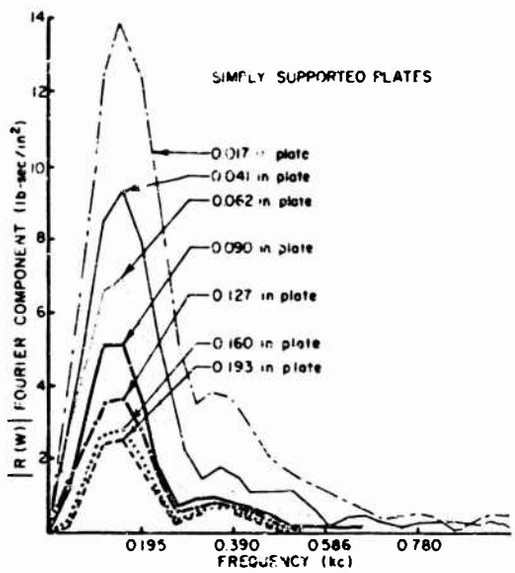

Fig. 18. Absolute values of Fourier components of response of simply supported plates to blast wave as function of frequency and for range of plate sizes (28-kv discharge using 13.8-in. electrode, 0-deg angle of incidence

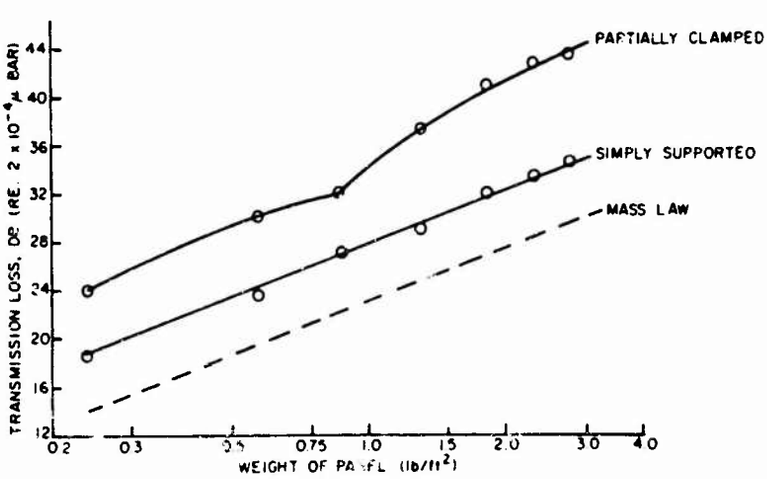

Fig. 19. Shock pulse transmission loss (db) for panel weights at 0-deg angle of incidence (comparison of partially clamped edges to simply supported edges; acoustic mass law shown for reference)

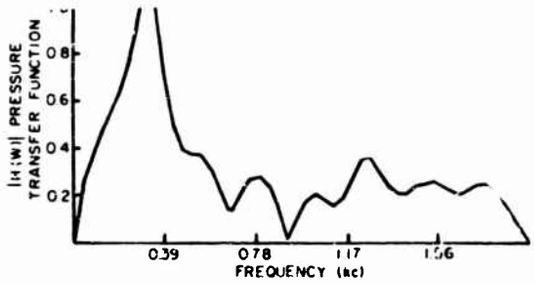

Fig. 20. Pressure transfer function for porous plate (five-layer screen) at 90-deg angle of incidence

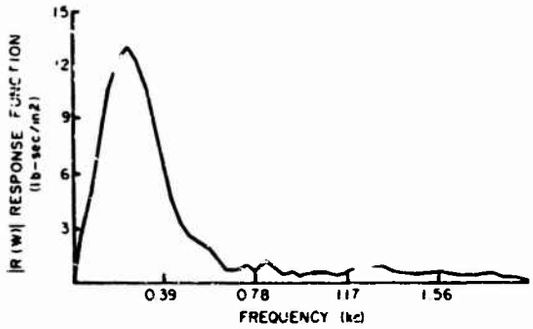

Fig. 21. Porous plate (five-layer screen) absolute values of Fourier components of response to blast wave at 90-deg angle of incidence (28-kv discharge using 13.8-in. electrode)

REFERENCES

1. W. G. Chace and H. K. Moore (Eds.), Exploding Wires, Vol. 1, Plenum Press, New York, 1959

2. W. G. Chace and H. K. Moore (Eds.) Exploding Wires, Vol. 2, Plenum Press, New York, 1962

3. S. Glasstone (Ed.), Effects of Nuclear Weapons, Government Printing Office, 1962

4. R. C. Binder, Advanced Fluid Mechanics, Vol. 1, p. 265, Prentice-Hall, Englewood Cliffs, N. J., 1958

5. P. G. Hoel, Introduction to Mathematical Statistics (2nd ed.), Wiley, New York, 1954

6. F. B. Safford, "Measurement of Four-Pole Parameters of Complex Structures," Trans. ASME Series B, Vol. of Engr. Inds., 84(1): 15

* * *

NIKE-X SHOCK TUBE FACILITY

Richard G. Donaghy and John J. Healy
Office of the Chief of Engineers
Department of the Army
Washington, D.C.

A new compressed air shock tube facility is being built by the Office of the Chief of Engineers at Aberdeen Proving Ground, Maryland, to test operating prime movers under simulated air blast conditions. The testing to be performed is in support of the development of power systems for the NIKE-X Anti-Ballistic Missile System. Two shock tubes are provided, one 5.5 ft in diameter and 610 ft long and the other 8.0 ft in diameter and 500 ft long. The performance characteristics of the facility are discussed, along with consideration of the special design problems encountered in the areas of dynamic reactions and stresses, traveling waves in the tube shells, fatigue, and brittle fracture. A summary of the testing to be performed is included.

INTRODUCTION

The Office of the Chief of Engineers (OCE), Department of the Army, has under construction a new compressed air shock tube facility designed to test the performance of diesel engines and gas turbines under conditions of air shock loading. The facility, designed by Black and Veatch, Kansas City, Missouri, is being built at the U.S. Army Ballistic Research Laboratories (BRL), Aberdeen Proving Ground, Maryland. The testing to be conducted at the facility is part of the OCE research and development program leading to the design and construction of power systems for the NIKE-X Anti-Ballistic Missile System.

The powerplants for the various types of NIKE-X sites will range in size from 7 to 68 Mw. Very precise control of voltage and frequency must be maintained at all times, including those periods when under attack. To meet the large power demand, prime movers up to 25,000 hp are being considered to drive the generators. The shock tube facility has been designed to test prime movers up to the maximum size.

The duration of the environmental disturbance for the worst-case attack condition postulated for the NIKE-X system is long enough to preclude isolating the prime-mover air inlet and exhaust ducts from the atmosphere. Analyses have been made which indicate that existing diesel engines and gas turbines can perform satisfactorily when air shock is imposed on their air inlet and exhaust systems. Figure 1 shows typical output speed response, the major area of concern, when the diesel engine and gas turbine are subjected to air shock.

The analytical programs which have been developed to analyze prime-mover performance are unique in that there has been no previous detailed effort in this area. There is, also, no test data with which to verify the analyses. Studies were made to determine the best means of verification, and the result was the development of a test program which will be performed at the shock tube facility. This test program has two coequal purposes: (a) to verify the methods of analysis used, and (b) to obtain actual hardware experience on large prime movers under scaled test conditions.

THE SHOCK TUBE FACILITY

Configuration

Figure 2 shows the major features of the facility. The two parallel shock tubes are shown with ducts leading to the prime-mover intake and exhaust stacks. A control center and a building for diaphragm change and compressors provide support spaces for the test operations.

Shock Tubes

The air blast wave moving over the tactical powerplant structure will produce a simultaneous overpressure load on the intake and exhaust

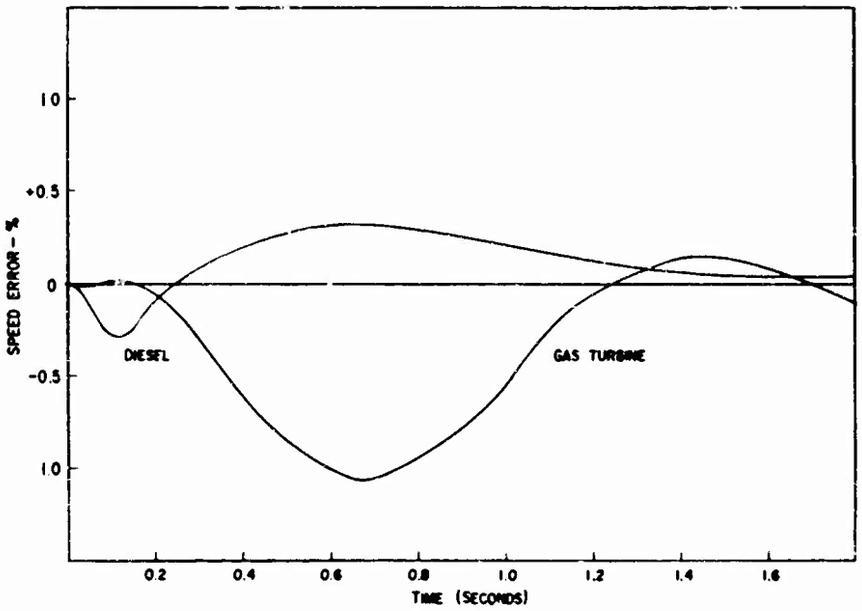

Fig. 1. Output shaft speed response; simultaneous air shock, maximum overpressure

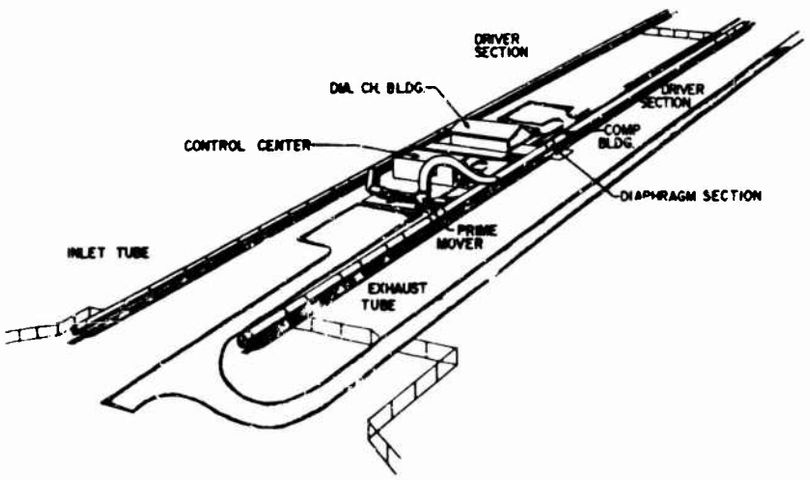

Fig. 2. Shock tube installation

stacks of the prime mover. The problem of reproducing the duality of this load in the test facility, when coupled with breathing and temperature problems under normal operating conditions, dictated the conception of two parallel shock tubes. The need for uncontaminated air behind the shock wave ruled out an explosively driven shock tube. The compressed-air-driven tube, therefore, was adopted as the operational mode. A thin metallic diaphragm is used to contain compressed air in the driver chamber. The air shock wave is produced by rupturing the diaphragm with a Primacord cutting charge. The intake shock tube has a diameter of 5 ft 6 in. and is 610 ft long. The exhaust air shock tube is 8 ft in diameter and 500 ft long. The tubes are supported by carriages on crane rails. Figure 3 shows the principal components of the tubes. The driver section is restrained by a reaction section. A diaphragm retaining section

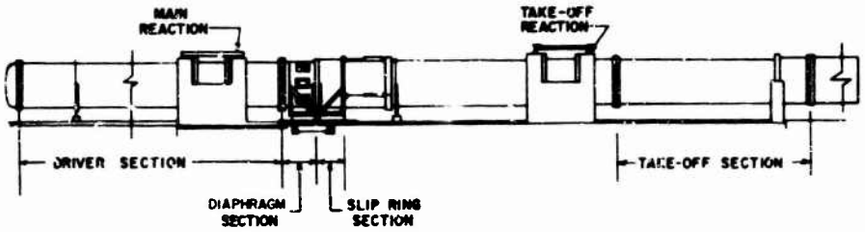

Fig. 3. NIKE-X shock tube

is bolted to the driver section on the downstream side of the reaction section. A clamping ring for the diaphragm is bolted to the retaining section flange at the end of the driver. To facilitate diaphragm changes, a slipring section is moved downstream by pneumatic cylinders to disengage the diaphragm section. Provision is made to install a branch takeoff in the expansion chamber to connect to the intake or exhaust stacks of the prime mover. The driver section of the intake shock tube has externally mounted heating elements and is sheathed with rigid insulation. The reaction section shown in Fig. 4 is restrained by a pier-supported truss at the top and by anchor plates at the sides and bottom. The longitudinal reaction force is transferred to the truss and anchor plates by large wide-flange ring beams. A similar reaction section is provided at the branch takeoff to handle the lateral thrust induced by the branch takeoff.

Foundation

A reaction block with shear keys as shown in Fig. 5 extends from the main reaction section to the downstream side of the branch takeoff section. The reaction forces are transferred to the soil by shear at the base of the shear keys. Because of a high water table in a fine-grained silty soil, a subdrain system has been

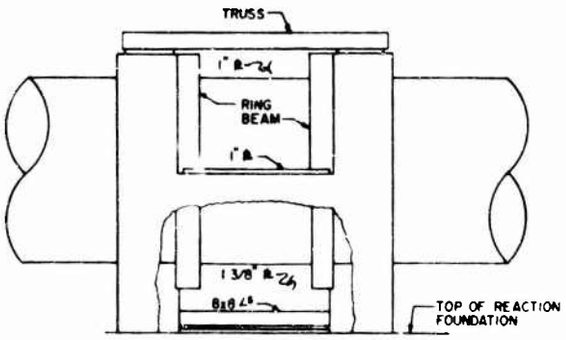

Fig. 4. Driver reaction support

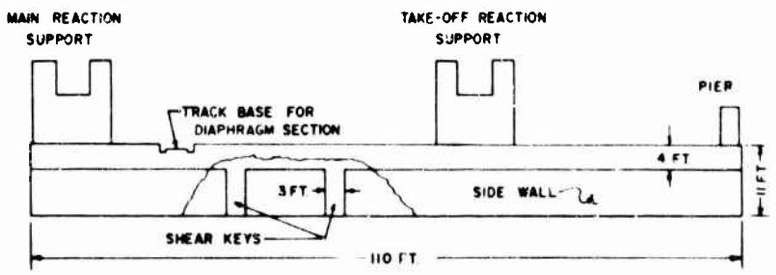

Fig. 5. Reaction foundation

located below the bottom of the shear keys to preclude liquefaction in the soil and loss of shear strength for load transfer.

Control Building

The control building is a reinforced-concrete single-story structure designed to resist the blast effects of a driver-section tube rupture. The design overpressure was determined by considering the release of the energy stored in the driver section by a rupture to produce a point source detonation of an equivalent quantity of TNT. This energy release was assumed to be located at the center of the driver chamber and calculated to have a 10 percent energy loss because of work on the tube shell. The energy stored in a 20-ft section of the driver chamber located at the diaphragm was also evaluated as an equivalent TNT detonation. The two detonations would produce the same overpressure at the control building. The control building contains all the instrumentation recording equipment and an operational control station. It does not have windows and is fitted with blast doors.

Diaphragm Change Building

The diaphragm change building is a light prefabricated structure providing covered space for replacing diaphragms. The air compressors for charging the shock tubes are also located in this building. It is unoccupied during the shock tube charging and firing cycle. The diaphragm section is moved to the diaphragm change building on a crane rail track by special carriage, thus making it unnecessary to lift the diaphragm section during the change process.

Prime-Mover Foundation

The prime movers under test will be located on a foundation between the shock tubes and connected by takeoff ducts. Combustion air and exhaust flow preshock will be provided through the open ends of the shock tubes. Electric generators and load banks will be used to load the prime movers. The resistive load banks and prime-mover auxiliary equipment will be located adjacent to the tubes.

SHOCK TUBE PERFORMANCE CHARACTERISTICS

Pressure

Classical linear, one-dimensional, unsteady-flow wave theory was used to establish the shock characteristics of the shock tubes. Using equations for conservation of mass, momentum, and energy, flow equations were determined in the time and distance domain and in the velocity-density domain. When the temperatures of the driver chamber and expansion chambers are equal, the required driver-chamber pressure can be obtained from:

$$\frac{P_1}{P_4} = \frac{P_1}{P_2}\left\{1 - \frac{\left(\frac{P_2}{P_1}\right) - 1}{\left[12\left(\frac{P_2}{P_1}\right) + 7\right]^{1/2}}\right\}^7 \qquad (1)$$

where P_1 = expansion chamber pressure, P_2 = shock wave pressure, and P_4 = driver chamber pressure. After diaphragm rupture, an expansion wave proceeds toward the head of the driver section. This expansion wave was divided into a number of pressure regions over which conditions were averaged. The progress of the expansion wave was computed by a time step process using the flow equations. When the expansion wave reaches the closed end of the driver chamber, it is reflected as a second expansion wave and interacts with the original expansion wave. An air shock wave moves toward the open end of the expansion chamber after rupture of the diaphragm. The shock wave also reflects as an expansion wave at the open end of the tube and interacts with the shock wave. A third interaction process occurs when the expansion wave reflected by the driver chamber head meets the expansion wave reflected by the open end. An analysis of this type was used to obtain a pressure-time history as shown in Fig. 6. The dotted portion of this pressure-time history shows the effect of flow loss in the takeoff duct.

Duration

The positive pressure phase, required to provide an adequate simulation, was determined by study of predicted prime-mover performance and the pressure decay curves for the range of weapons being considered. It was concluded that the shock tubes must deliver a good simulation of the largest weapon for periods long enough to generate the maximum speed excursion in the prime mover. The flat top characteristic of the pressure wave is the critical portion for the simulation. The duration of the flat-top portion of the shock wave is a function of the overpressure level and the respective lengths of the driver and expansion chambers. Each overpressure level has its own optimized tube length characteristics to obtain maximum duration of the flat-top wave. A compromise was necessary to obtain suitable durations for a selected range of overpressures. Typical

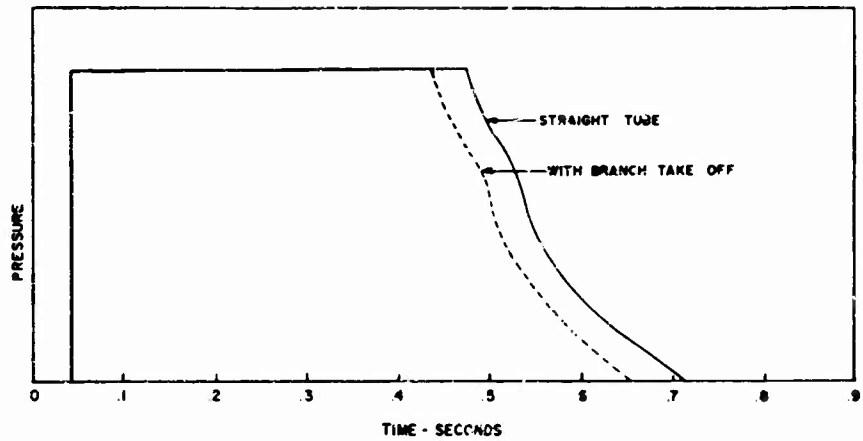

Fig. 6. Pressure-time history, intake tube

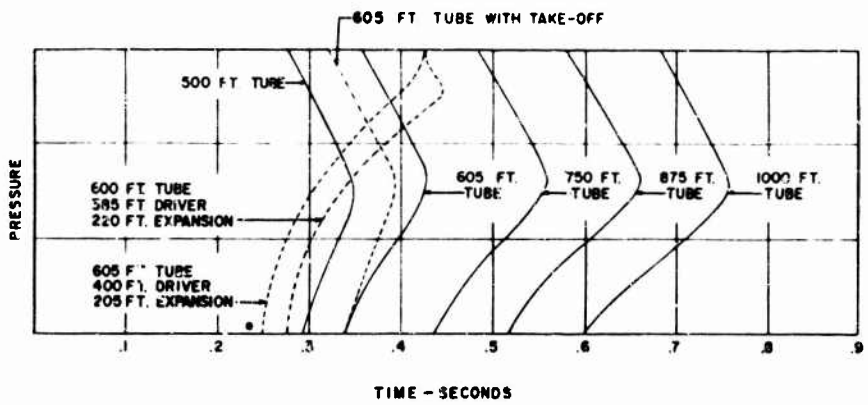

Fig. 7. Flat-top pressure duration, intake tube

results of an analysis of duration derived from the flow relationships discussed above are shown in Fig. 7. Lengths for the intake and exhaust tubes were selected so as to produce similar durations over a range of overpressures.

Heating

The air behind the shock wave formed after rupture of the diaphragm will have a significantly lower temperature than that of the driver chamber. This manifests itself as a contact surface discontinuity behind the shock front. Because this temperature-density discontinuity at the contact surface can affect combustion in the prime mover, it represents a phenomenon which is not desired as a simulation of the real air blast environment. The discontinuity is eliminated by heating the air in the driver chamber to offset the temperature loss experienced during shock formation. When the temperatures of the driver and expansion chambers differ, the driver pressure is modified by the ratios of specific heat and speed of sound in both the driver chamber and in the region ahead of the shock wave. The interrelationship between shock pressure, open-tube pressure, and pressure in the driver section is shown in Fig. 8. The curves shown are for various ratios of expansion-chamber temperature to driver-chamber temperature. From these considerations a driver pressure/temperature relationship was selected.

STRUCTURAL DESIGN

Dynamic Analysis of the Driver Section

Stresses in the tube shell of the driver section and reaction loads to be transferred to

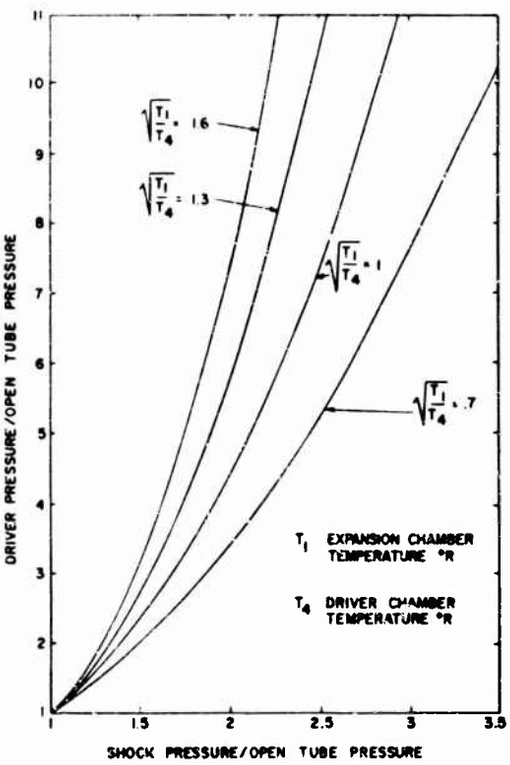

Fig. 8. Driver pressure ratio vs shock pressure ratio

the foundation were obtained from a dynamic analysis. The driver section was modeled as a stiff rod or spring restrained from translation by the reaction block as shown in Fig. 9. A step pulse was applied to the free end of the spring. The pulse was equal in magnitude to the pressure force applied to the driver head.

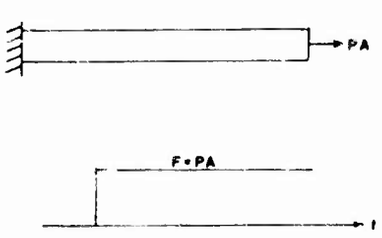

Fig. 9. Dynamic model

The equation of motion [1] is:

$$\frac{E}{\rho}\frac{\partial^2 u}{\partial x^2} - \frac{\partial^2 u}{\partial t^2} = 0 \qquad (2)$$

where E = Young's modulus, ρ = density, and u = displacement.

The boundary conditions are:

$$u(0,t) = 0,$$

$$EA\frac{\partial u}{\partial x}(L,t) = P(t),$$

where A = area of shell material, L = distance from driver head to reaction, and P(t) = step pulse. A solution for this equation can be expressed as follows:

$$u(x,t) = \frac{8PuL}{\pi^2 EA}\sum_{n=1}^{\infty}\frac{(-1)^{n-1}}{(2n-1)^2}\left\{\sin\left[\left(\frac{2n-1}{2}\right)\frac{\pi x}{L}\right]\right\} \times \left\{1 - \cos\left[\left(\frac{2n-1}{2}\right)\frac{\pi c t}{L}\right]\right\} \qquad (3)$$

where

$$c^2 = \frac{E}{\rho}.$$

Using longitudinal stress in the shell expressed as:

$$s = \frac{P}{A} = \frac{uE}{L} = E\frac{\partial u}{\partial x} \qquad (4)$$

and substituting in Eq. (3) above, stress becomes:

$$s = \frac{8PL}{\pi^2 A}\sum_{n=1}^{\infty}\left\{\frac{(-1)^{n-1}}{(2n-1)^2}\right\}\left\{\left(\frac{2n-1}{2}\right)\frac{\pi}{L}\right\} \times \left\{\cos\left[\left(\frac{2n-1}{2}\right)\frac{\pi x}{L}\right]\right\}\left\{1-\cos\left[\left(\frac{2n-1}{2}\right)\frac{\pi c t}{L}\right]\right\}. \qquad (5)$$

Evaluation of this equation gave a dynamic load factor of 2 to be applied to the static load on the driver chamber head.

Traveling Wave Analysis

As the shock wave moves into the expansion section, bending stresses at the wave front must be examined. The problem is analogous to a moving load on an elastic foundation [2]. The compatibility equation for a step load moving at constant velocity is:

$$D\frac{d^4 y}{dx^4} + \frac{Eh}{R^2} = P(x) \qquad (6)$$

where $D = Eh^3/(12(1-\mu^2))$, R = radius, h = tube thickness, and μ = Poisson's ratio. Similarly, the compatibility equation for a beam on an elastic foundation is

$$EI \frac{d^4y}{dx^4} + ky = P(x) . \quad (7)$$

Thus

$$EI = D \text{ and } \frac{Eh}{R^2} = k .$$

The equation of motion for a beam of infinite length with a point load is then

$$EI \frac{\partial^4 y}{\partial x^4} + \frac{a\gamma}{g} \frac{\partial^2 y}{\partial t^2} + c \frac{\partial y}{\partial t} + ky = P_0(x,t) , \quad (8)$$

where a = cross-sectional area of the beam, γ = weight of the beam per unit volume, g = gravitational acceleration, and the critical velocity is

$$V_{cr} = \left(\frac{4k\, EI\, g^2}{a^2 \gamma^2} \right)^{1/4} . \quad (9)$$

Tang [2] has determined the bending moment for the case with no damping to be

$$M = \frac{P_0}{4\lambda} \left\{ \frac{e^{-(1-\theta^2)^{1/2} |\lambda x|}}{(1-\theta^2)^{1/2}} \right\} \times \left\{ \frac{-(1-\theta^2)^{1/2}}{(1+\theta^2)^{1/2}} \sin (1+\theta^2)^{1/2} |\lambda x| + \cos (1+\theta^2)^{1/2} \lambda x \right\} \quad (10)$$

where

$$\lambda = \left(\frac{k}{4EI} \right)^{1/4} , \quad \theta = \frac{v}{V_{cr}} .$$

This moment is a maximum at $x = 0$:

$$M_{max} = \frac{P_0}{4\lambda} \frac{1}{(1-\theta^2)^{1/2}} , \quad (11)$$

in which the dynamic load factor is

$$F = \frac{1}{(1-\theta^2)^{1/2}} .$$

For the uniformly distributed load and a large x_2 as shown in Fig. 10

$$M = -\frac{p}{4\lambda^2} \left\{ \frac{e^{-(1-\theta^2)\lambda x_1}}{(1-\theta^4)^{1/2}} \right\} \sin (1+\theta^2)^{1/2} \lambda x . \quad (12)$$

Fig. 10. Uniform load

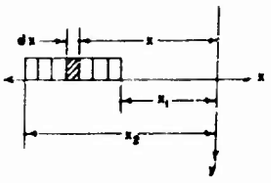

For the static case M_{max} occurs at $\tan \lambda x_1 = 1$:

$$M_{max} = \frac{p}{4\lambda^2} e^{-\pi/4} \sin \frac{\pi}{4} . \quad (13)$$

with a dynamic load amplification factor:

$$F = \frac{1}{(1+\theta^4)^{1/2}} \frac{e^{-(1-\theta^2)\lambda x_1} \sin (1+\theta^2)^{1/2} \lambda x_1}{e^{-\pi/4} \sin \frac{\pi}{4}} \quad (14)$$

θ is determined from:

$$\tan (1+\theta^2)^{1/2} \lambda x = \left(\frac{1+\theta^2}{1-\theta^2} \right)^{1/2}$$

Thermal Stresses

The transmission of heat from the sun produces an elongation of the top of the tube resulting in a longitudinal bending stress in the tube. An analysis of tube heating resulting from this solar radiation was made. A 30°F temperature gradient was calculated to produce a longitudinal bending stress of 3120 psi in the tube shell of the 8-ft tube.

Fatigue Failure

The oscillatory nature of the loading in the driver section gave cause for concern with respect to susceptibility of the shell to fatigue failure. Following the approach outlined in Section III of the ASME Boiler and Pressure Vessel Code, strain amplitude was evaluated in terms of the number of loading cycles [3] as shown in Fig. 11. An experimental stress history in a shock tube at BRL is shown in Fig. 12. Looking at the driver-section longitudinal stress in Fig. 12, a high-frequency low-amplitude oscillation is superimposed on a major low-frequency stress excursion. The major stress amplitude is approximately 1.5 times the peak positive amplitude or approximately 40,000 psi for the shock tubes. Using one half of this value in Fig. 11, fatigue failure is estimated at greater than 10^5 cycles. The magnitude of the higher frequency components is low enough to preclude

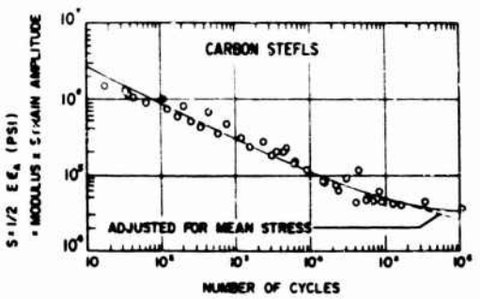

Fig. 11. Fatigue curve

any fatigue effects. It is not expected that normal shock tube operation will approach the number of cycles indicated for fatigue failure during its useful life.

Brittle Fracture

The failure mode of primary concern for the shock tube is brittle fracture. For this reason an examination of necessary properties of the shell material in terms of brittle fracture sensitivity was made. Figure 13 shows a fracture analysis diagram for typical mild steel plate [4]. It combines the influence of the nil ductility temperature (NDT), size of flaws, and temperature on the crack propagation problem. Based on this kind of analysis, a shell material with an NDT of -50°F was specified. This would allow operation of the shock tube at 10°F ambient temperature which is within the yield limit of the shell plate. The steel chosen for these properties was ASTM A-516 to which was applied the A-300 normalizing specification. Charpy V-notch tests were specified for 15 ft-lb at -50°F. The steel is thus a fully killed, fine-grained practice, normalized mild steel. The fabricator is being required to furnish test specimens for additional Charpy V-notch tests. These specimens are for the "as rolled and formed" condition with and without typical welded joints. The results of these tests will establish conclusively the safe minimum operating temperature to avoid brittle fracture.

Stress Criteria

The design problem required a definition of allowable stress levels for all conditions of loading. The large amount of energy being stored in the driver section was a principal concern in establishing stress limits.

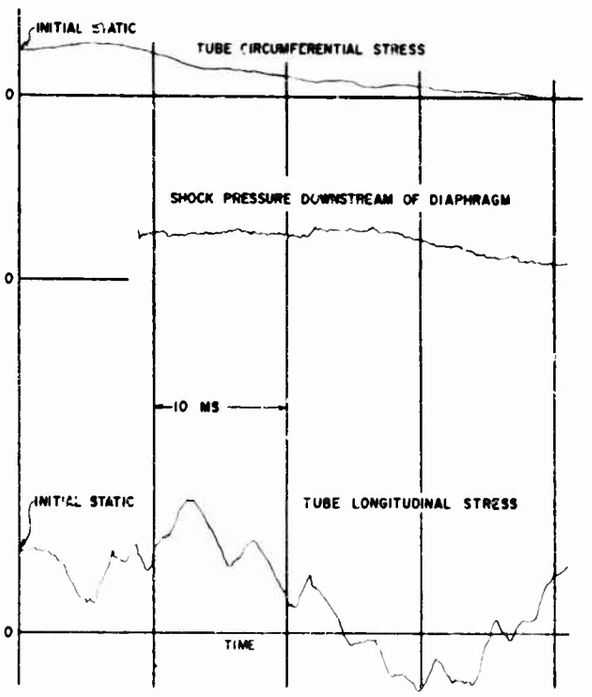

Fig. 12. Stress history, midsection of driver section (BRL test data)

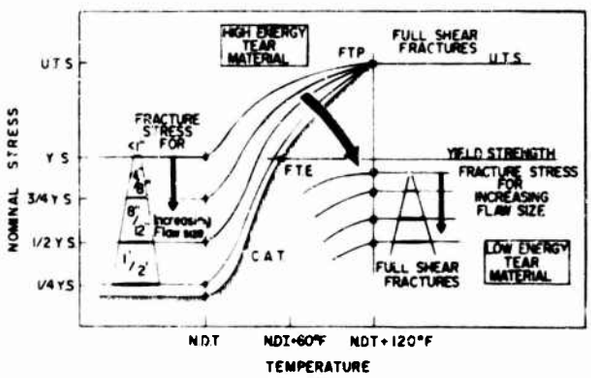

Fig. 13. Fracture analysis diagram

The ASME Boiler and Pressure Vessel Code for unfired pressure vessels provided a basis for the static design of the tube shell. The major stresses for the dynamic case were in the longitudinal direction. In addition to these longitudinal stresses produced by the reaction force and the thermal bending stress, secondary bending stresses were introduced by the reaction support ring beams and the connecting flange at the diaphragm section. The ASME Boiler Code for unfired pressure vessels permits working stresses at 25 percent of the specified minimum tensile strength or 62.5 percent of the expected yield strength for 0.2 percent offset strain. For design, we established the stress limit for the dynamic case at 1.5 times the working stress for the static case. This limits stresses to 37.5 percent of the specified tensile strength for A-516 steel having a 70,000-psi tensile strength. The stress limit for dynamic stress combinations is 26,250 psi. It should be recognized that the structure moves out from under secondary bending stress concentrations as the yield condition is approached. This results in a redistribution of stress and an adjustment toward a more stable stress condition.

TEST PROGRAM

The testing to be performed at the NIKE-X Shock Tube Facility is scheduled to begin in July 1968. Four prime movers will be tested: a 2200-hp diesel engine, a 6000-hp diesel engine, a 3150-hp gas turbine, and a 25,000-hp gas turbine. The smaller diesel engine and gas turbine will be tested with scaled shock-attenuation equipment placed between the shock tubes and the prime mover to verify the theory of attenuation being used in the design concepts. Initial shock tests will be at low overpressure levels, and will be increased gradually to slightly over the pressure which our predictions indicate is the limit of satisfactory performance. There will be no attempt to determine the pressure at which structural failure will occur. A typical test schedule is shown in Table 1.

The shock tubes will be operated and maintained by personnel of the Ballistic Research Laboratories. The operation of the prime mover and the overall test direction will be the responsibility of Arthur D. Little, Inc., under contract to OCE. The facility has been designed to complete a test cycle requiring the maximum shock pressure level within a period of 8 hr. It is anticipated that several tests per day can be made at lower pressure levels. The testing of the diesel engines is scheduled for completion in April 1969 and the gas turbine tests in May 1970.

TABLE 1
Tests to be Conducted with Prime Movers

	Electrical Load (% Rated)	Peak Overpressure	Application of Shock at Inlet and Exhaust	
			Simultaneous	Staggered
Normal Operation	50	0	–	–
	75	0	–	–
	100	0	–	–
Step Load	100-75	0	–	–
Overpressure (Without attenuators– all prime movers)	100	$1/3P_0$[a]	Yes	–
		$2/3P_0$		–
		P_0		–
		$4/3P_0$		–
		$5/3P_0$		–
	75	XP_0[b]		–
	100	XP_0	No	$(I/E)t_1$[d]
		XP_0		$(I/E)t_2$
		XP_0		$(I/E)t_3$
	–[c]	XP_0	Yes	$(E/I)t$
	75[c]	XP_0		
	100[c]	XP_0	No	$(I/E)t$
		XP_0		$(E/I)t$
Step Load	100-75[c]	0	–	–
Normal Operation	50	0	–	–
	75	0	–	–
	100	0	–	–
Overpressure (With attenuators– small prime movers only)		$1/3P_0$	Yes	–
		$2/3P_0$		–
		P_0		–
		$4/3P_0$		–
		$5/3P_0$		–
	–[c]	XP_0		

[a] Pressure levels in shock tube at duct takeoff will be those that induce overpressures in the ducting equivalent to that predicted for the condition where the free-stream peak overpressure from a nuclear blast is P_0 or a fraction thereof as indicated.
[b] XP_0 represents a fraction of P_0 to be selected on the basis of the results of preceding tests.
[c] Repeated tests.
[d] $(I/E)t_1$ – Shock applied to inlet before exhaust with a time interval of t_1; $(E/I)t$ – Shock applied to exhaust before inlet with a time interval to be selected on the basis of the results of preceding tests.

REFERENCES

1. W. Nowacki, Dynamics of Elastic Structures (Chapman and Hall, London), 1963
2. S. C. Tang, "Dynamic Response of the 6 Foot Diameter Shock Tube to a Constant Velocity Pressure Front," Air Force Special Weapons Center Rept. TR-61-60, Aug. 1961
3. E. A. Lange and A. G. Picketts, "Full-Size Pressure Vessel Testing and Its Application to Design," ASME Paper 63-WA-293
4. W. S. Pellini and P. P. Puzak, "Fracture Analysis, Diagram Procedures for the Fracture Safe Engineering Design of Steel Structures," U.S. Naval Research Laboratory Rept. 5920, Mar. 1963

* * *

DESIGN AND PERFORMANCE OF DUAL MODE SHOCK MACHINE

W. Douglas Everett
Naval Missile Center
Point Mugu, California

In response to several widely varying shock test requirements, a new shock test machine was built. This somewhat novel machine satisfied all the test requirements by incorporating the following operational features: (a) two modes of operation (drop test and hammer test), (b) portability between several test sites, and (c) flexibility in accommodating test items of widely varying configurations. The machine consists of two dynamic elements: a chain drive test table and a pneumatically powered anvil-hammer mass. This second element provides a dual test mode capability by functioning as a seismic anvil during drop tests and as an adjustable mass hammer head during hammer tests. In its first year of operation, the machine has performed a variety of Military Specification and simulated underwater shock tests on specimens as large as a 3000-lb, 14 by 3 by 2 ft shipping container. The dual mode shock machine performance has been highly satisfactory with respect to both shock pulse fidelity and operational reliability.

INTRODUCTION

The Environment Branch at the Naval Missile Center was confronted with two distinct test requirements to be met by the design and construction of a new shock machine. First, there was a general requirement for a machine that would extend the shock test capability with respect to test specimen size and resultant shock forces. Second, there was a Navy program requirement for a machine capable of testing a new missile shipping and stowage container conception to the extremes of simulated shipboard underwater explosion shocks.

Those test requirements demanded the following test machine capabilities:

1. Two modes of operation: (a) the hammer test mode, wherein the test package is set into motion by a hammer blow from beneath, to simulate shipboard shock motion; (b) the drop test mode, wherein a test item's free-fall motion is terminated by impact with an anvil, for the more conventional tests.

2. Portability from one test site to another. The machine would have to be sufficiently light, rugged, and weather resistant to withstand being moved repeatedly between several possible test sites. The test site atmospheres would include the damage potentials of ocean salt fog at an outdoor explosive hazard test site, and temperature extremes from -65°F to +160°F, generated in the sea level climatic hanger at the Environmental Laboratory.

3. Adaptability to widely varying test package configurations. The extremes of the test requirements in the immediate future included a 3000-lb shipping container to be shocked through its 14 by 3 ft base and a 1000-lb missile to be shocked through its 15-in-diam aft end.

DESIGN, CONSTRUCTION, AND OPERATION

The dual mode shock machine (Fig. 1), satisfying the aforementioned performance requirements, consists of three basic elements: (a) a pneumatically powered anvil-hammer assembly, (b) an electric-motor and roller-chain drive, table-positioning assembly, and (c) a rectangular frame structure to contain and support the anvil and table assemblies.

The pneumatic anvil-hammer assembly is basically a 4000-lb lead mass attached to the upper end of a 3-ft-stroke, 2-ft-diam piston, which is powered by a 3.5 cu ft compressed-air reservoir. Because of the anticipated extremes of test package configurations, two anvil-hammer mass elements were fabricated for initial machine test operations. One of the mass elements is an aluminum box, 9 ft long, 2 ft wide, 15 in. high, weighted with 3000 lb of lead. This long

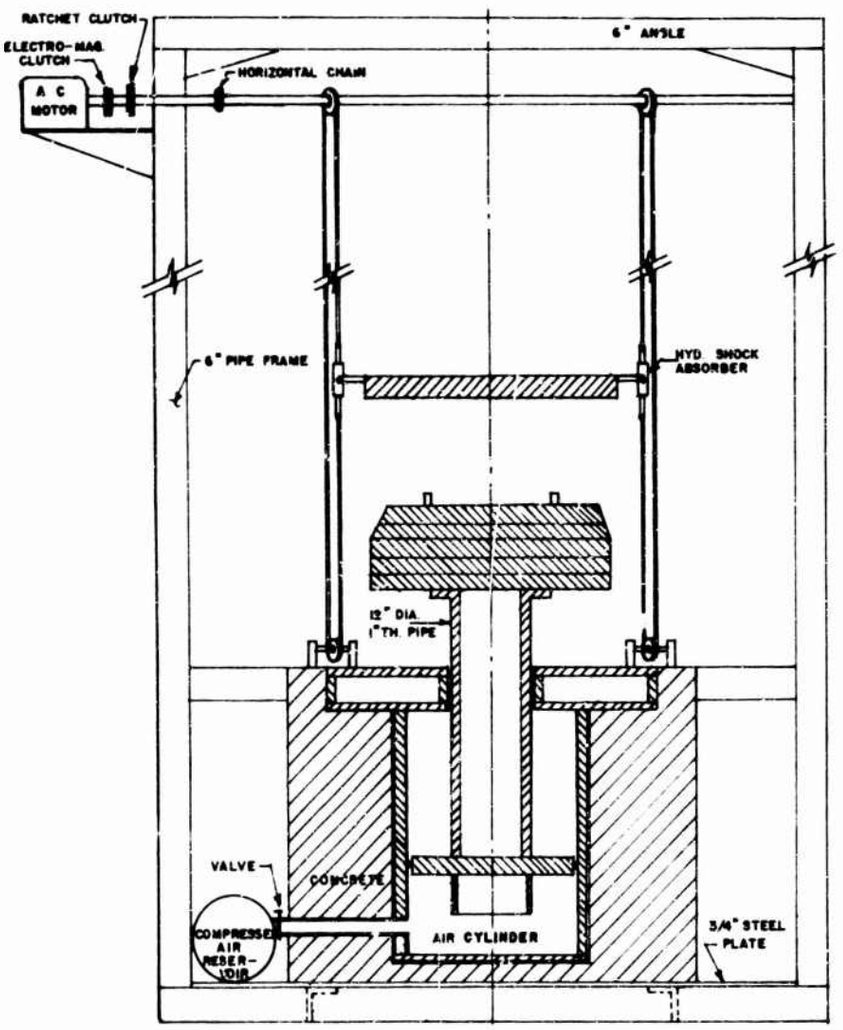

Fig. 1. Sketch of dual mode shock machine cross section

mass element is used in conjunction with the 14-ft-long, 3.5-ft-wide, 2-ft-high aluminum test table (Fig. 2) to provide for a distribution of the shock forces over the length of the table. The other mass element is a cylinder of steel and lead, 28 in. in diameter, 17.5 in. high, comprised of four 3-3/8-in.-thick lead wafers sandwiched between 2-in.-thick steel plates. This element, used in conjunction with a 30-in.-diam, cast aluminum test table (Fig. 3) can be reduced in mass by removal of one or more of the four lead wafers to accomplish high impact velocities in hammer test operations.

The test table positioning system consists of a specimen test table attached via hydraulic shock absorbers to four vertical roller-chain drive loops. These four chain loops, positioned by idler sprockets at the base, are driven by two parallel shaft and sprocket assemblies overhead. The two overhead shafts are in turn driven by a 3-hp motor, driving through an electromagnetic clutch and two mechanical ratchet-type clutches. The electromagnetic clutch in the drive system provides for the release of the table and chain drive system from the motor for free-fall drop tests. Because the four vertical chain loops and the two overhead shafts remain attached to, and are thus driven by, the falling table, the table descent rate is reduced to approximately three fourths of that of true free fall. The ratchet-type clutches, on

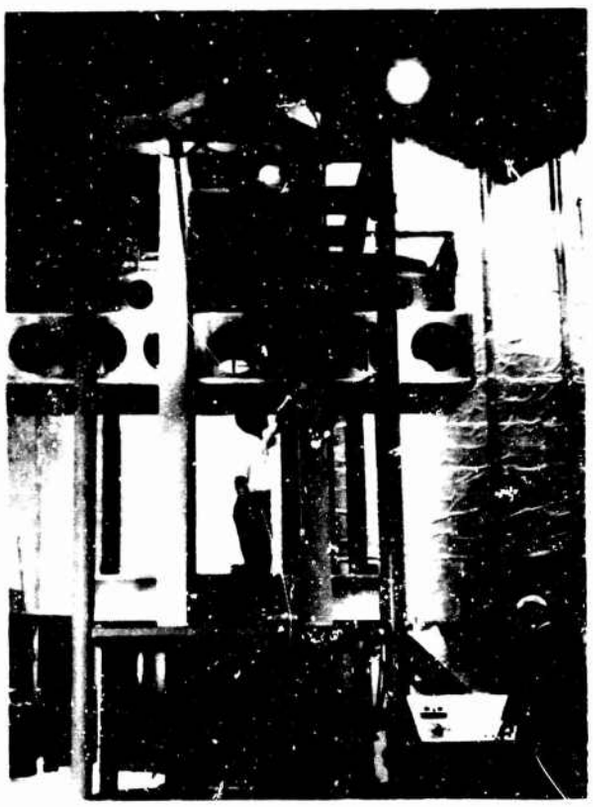

Fig. 2. Dual mode shock machine configured with rectangular test table and rectangular anvil-hammer mass

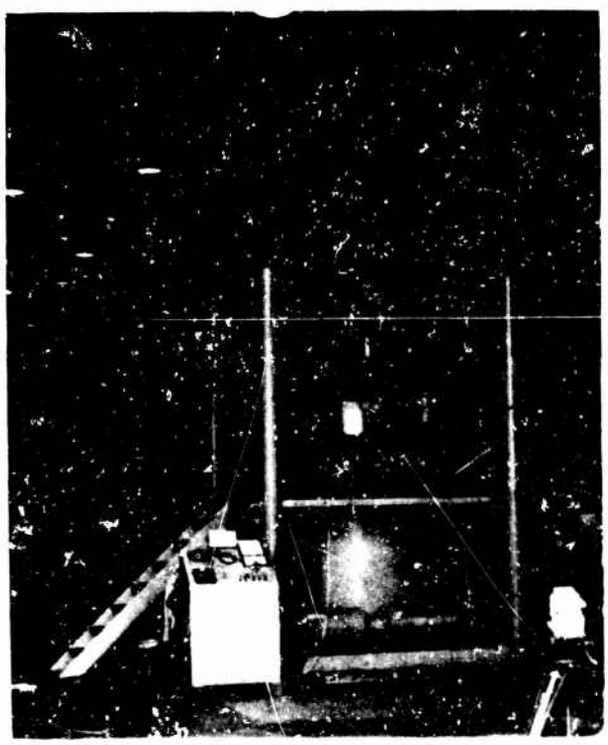

Fig. 3. Dual mode shock machine configured with cylindrical test table and cylindrical anvil-hammer mass

the two overhead drive shafts, allow the table to move upward, free of restraint from the motor drive system, following a hammer impact.

The frame supporting the two dynamic elements is an 8-ft-square, 18-ft-high structure employing a 6-in.-diam, 18-ft-long structural steel pipe at each of the four corners separating the angle iron and steel plate anvil support base from the overhead angle-iron motor drive assembly support frame. A telescoping feature of the 18-ft vertical pipe members allows the machine to be shortened to a 12-ft height to facilitate transportation between test sites.

The sequence of events required for a drop or hammer shock test involves the following operations:

1. For a drop test the table and test specimen assembly is raised via the motor and chain drive system to an appropriate free-fall height above the impact point. The anvil-hammer assembly is then raised pneumatically to approximately a 2-ft stroke of the piston. The table drive clutch is then deenergized allowing the table to fall, impacting via appropriate rubber or lead pads with the pneumatically supported anvil-hammer assembly. Then, the shock impulse reaction is transferred to the laboratory floor through the seismic motion of the anvil-hammer assembly on the approximately 1-cps air spring pneumatic cylinder.

2. For a hammer test the table and test specimen assembly are positioned at the appropriate distance (6 to 18 in.) above the retracted anvil-hammer assembly. The compressed-air reservoir is charged with air pressure appropriate for the desired anvil-hammer impact velocity. The air reservoir is then rapidly vented to the underside of the anvil-hammer piston, driving the anvil-hammer assembly into impact with the suspended table. Following impact, the table moves upward against the restraint of gravity to a point of zero velocity, whereupon the ratchet clutch in the motor drive system reengages the table, preventing downward motion. The anvil-hammer assembly is brought to rest independently of the table by the increasing pressure of the trapped air above the rising piston.

DESIGN INNOVATIONS AND TEST EXPERIENCE

It may be noted from the description of the shock machine construction and operation that two features represent rather basic departures from the conventional shock machine design. Perhaps the more significant feature is the duality of the anvil-hammer element. This moderately heavy element represents a compromise, in magnitude, between the "infinite" mass conception normally associated with drop tester anvils and the small-mass, high-velocity projectiles associated with hammer, slingshot, and air gun shock generators. Because the resultant "compromise" machine can generate the shock pulses associated with most operational vehicle environments and Military Specifications, and at the same time generate the more appropriate acceleration and velocity phase relationship of either an accelerating or decelerating shock, it is felt to be a successful compromise for our laboratory requirements.

The second feature is the absence of a conventional vertical guide rod system for vertical constraint of table motion. This function is accomplished by the four vertical chain drive loops, slightly pretensioned for a low-frequency constraining effect. Obtaining lateral restraint in this manner not only eliminated the complexity of precision vertical guide rails and bearings but resulted in a guide system more amenable to relocation for the accommodation of unusual test specimen configurations.

Test experience to this date is confirming the expediency of both the aforementioned design innovations. The following review of test experiences is offered to illustrate the machine versatility. Official use of the machine began in September 1966 with developmental testing of a 3000-lb missile shipping and stowage container, 3 by 13 ft at base and 2 ft high, evaluated under shock conditions simulating shipboard deck response to an underwater explosion. Subsequently, tests have been conducted on: SPARROW III shipping containers, tested to MIL-S-901C shock impulses in combination with high and low temperature extremes; an airborne computer mockup, tested to MIL-E-5422 shock specifications; an Aero 21A missile handling skid, tested to MIL-S-901C shock impulses; and a shipboard electronics cabinet, tested to MIL-STD-810A sawtooth shock impulse. The most recent test, involving the sawtooth shock pulse, was the most critical of machine performance, because of (a) the closely defined shock pulse tolerance limits, (b) the relatively heavy, 1000-lb test package, and (c) the potential of a sawtooth pulse to excite high-frequency resonant responses in the shock generating equipment. Unfiltered oscilloscope data from that test are presented in Fig. 4 as an index of performance for the machine.

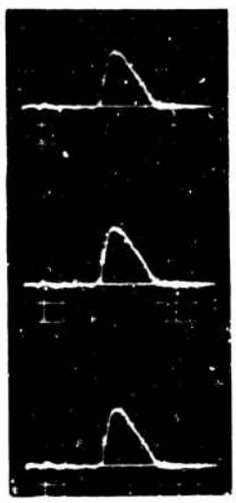

Fig. 4. Unfiltered acceleration vs time records of test table motion during three successive 50-g, 6-ms sawtooth shocks (time progressing from right to left on record)

CONCLUSIONS

The successful test experience with the dual mode shock machine can be attributed primarily to its design simplicity. The acknowledgment that shock forces are simply generated by the transfer of momentum between two masses led to the creation of a machine utilizing this principle in a very direct manner. Thus, both drop test and hammer test operations are accomplished by the transfer of momentum between an anvil-hammer mass and the test specimen mass. The incorporation of a minimum number of simple machine elements to facilitate this interaction of two masses results in a machine with inherent qualities of flexibility and reliability.

DISCUSSION

Mr. Hughes (Naval Ordnance Laboratory): What are the upper limits of frequency and acceleration reached? What sort of strains can you go to on this facility?

Mr. Everett: We pushed the facility no further than the shock test requests we have had up to this time. We have not had the opportunity to explore its limits. The most difficult test was the sawtooth test because of the potential of the sharp corners.

Mr. Hughes: What was the peak acceleration on the sawtooth?

Mr. Everett: Fifty g with a thousand-pound package.

Mr. Berkman (Litton Data Systems): You said you could simulate the Navy 901-C spec. Could you give us more details; do you have more information on it?

Mr. Everett: No, and that is probably misleading. The only way to simulate that spec is to build a machine. This is not that machine. But what we propose is to simulate the initial phase of the shock impulse with the appropriate momentum exchange between the hammer element and the table and test specimen, perhaps a little more effectively since we have built this hammer and table to work up to higher frequencies.

Mr. Hammaker (Naval Ship Engineering Center): How quickly can you open that valve to get a decent shock pulse?

Mr. Everett: The pressure buildup occurs over about 30 ms. It is not considered critical. During the early phase of the pressurization the piston is not moving. The intent is to transfer the energy in the air tank to the piston as kinetic energy.

Mr. Levin (Naval Ship Engineering Center): The summary mentioned the use of the machine combined with other environments such as heat. Perhaps humidity was included. Could you give us some idea of the variations you may have found in test results when the shock test was combined with temperature, as opposed to performing the tests on a serial basis?

Mr. Everett: The one test we ran that combined shock with temperature extremes was on

a Sparrow container. In this case the effect of the temperature was to alter the response of the rubber shear mounts in the container. The shift in resonant frequency was on the order of 10 percent—2 or 3 cycles—and somewhat of an increase, in at least the initial pulse, of the response of the missile isolated with these shear mounts.

Mr. Levin: Have you had the opportunity to compare the damage effects that might have been caused by combining testing method versus the single test method? Did you go far enough to determine anything in this direction?

Mr. Everett: No, this is the only combined environment test we ran and there was no damage. The test was conducted at ambient as well as at the two temperature extremes. There was an appreciable shift in resonances but no damage resulted during any of the tests.

Mr. Levin: You mentioned the test invoked by MIL-STD-810A in which a triangular waveform was used and implied that there was a similar shipboard requirement. Where is this requirement that the triangular pulse called out by 810A be used for shipboard environment, or was this a requirement of the individual problem?

Mr. Everett: It was a spec applied by one of our engineers. He felt that the sawtooth pulse probably would excite all frequencies that would be encountered throughout a ship, and that this cabinet might be located at any of several points within the ship. Therefore, the exciting frequencies ranged from 10 to 50 cps.

Mr. Levin: There seems to be some divergence of opinion as to which waveform produces the most damaging effect or the greatest accelerations. It has been argued that by testing with a half-sine pulse the damage potential will be maximum. In fact, there are many references in the literature stating that by using the half-sine waveform you may be, in some cases, overtesting. But in order to be safe this testing method is recommended by these same sources.

Mr. Everett: I think that is the case. In this instance the sawtooth was used as an exploratory or developmental tool. It was not intended necessarily to qualify this cabinet. The cabinet had no electronics in it.

Mr. Peete (Naval Undersea Warfare Center): What is the approximate diameter of your piston?

Mr. Everett: Two feet.

* * *

AIR BLAST AND GROUND SHOCK

INFLUENCE OF SHIP MOBILITY ON INTERNAL FORCES PRODUCED BY BLAST*

Alexander Chajes, Frederick J. Dzialo, and Merit P. White
Department of Civil Engineering, University of Massachusetts
Amherst, Massachusetts

A study of the effect of hull mobility on the dynamic behavior of an aircraft carrier subjected to blast loads is presented. Using a simplified model of the carrier, equations of motion and their solutions are derived. From these equations, natural modes, frequencies, and dynamic displacements resulting from a triangular load pulse are obtained for a numerical example. Two cases are studied: one assumes the hull to remain fixed in the water and one allows the hull to move. Comparison of the results for these two conditions indicates that inclusion of hull mobility in the analysis results in a sizable reduction of the design shears for the vertical bulkheads. Hull mobility is also shown to have a significant effect on the natural modes and frequencies.

INTRODUCTION

The purpose of the investigation is to study the effect of hull mobility on the dynamic behavior of an aircraft carrier subjected to blast loads. In an earlier investigation [1], the dynamic response of the structure above the main deck to blast loads was determined, assuming the hull below the main deck to remain fixed in the water. In the present study the hull of the carrier is assumed to move as a rigid body in the water while the structure above the hull deforms elastically as a result of the blast loads. Of special interest is the effect that hull mobility has on the shear forces for which the vertical bulkheads and frames above the main deck must be designed.

THEORY

Model

The basic structure of the carrier is depicted in Fig. 1. It consists of two main sections: (a) a flight deck supported on a series of transverse frames and bulkheads, which extend from the flight deck down to the main deck, and (b) numerous transverse bulkheads and horizontal decks below the main deck, comprising the hull of the carrier. An idealized model of this structure is shown in Fig. 2. The flight

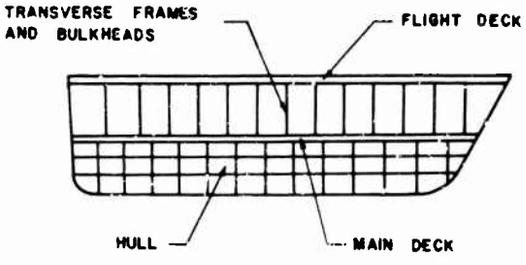

Fig. 1. Basic carrier structure

deck is approximated by n lumped masses, m_n, connected to one another by massless webs of bending stiffness EI_n. Vertical webs of stiffness k_n representing the vertical bulkheads and frames extend from the flight deck masses to the main deck. The hull, comprising all of the structure below the main deck, is assumed to be a rigid body. The mass and mass moment of inertia of the hull combined with an apparent mass of water are M and I_0, respectively. The moment of inertia, I_0, is about O-O, the longitudinal centroidal axis of the hull. The use of a lumped-mass beam, instead of a continuous one, to represent the flight deck makes it possible to account for variations in the properties of the flight deck

*This study was conducted in the course of work performed under Contract N600(i(7)65486(X)FBM between the David Taylor Model Basin and the University of Massachusetts.

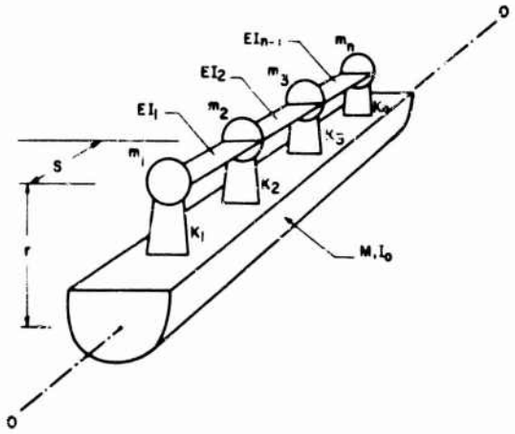

Fig. 2. Model of carrier

The dynamic loading on the ship is shown in Fig. 3. It consists of a set of forces p_n applied at the flight deck masses, and a single force P applied to the rigid hull. The forces p_n and the force P are applied at distances of r and h above the hull centroid, respectively. This loading causes a rigid body translation and rotation of the hull, and elastic deformation of the structure above the hull. Figure 3 depicts the model in a displaced configuration. The rigid body motions of the hull are x and θ, and y_n is the displacement of a mass m_n of the flight deck relative to the hull.

Equations of Motion

Setting the horizontal forces and the moments about axis 0-0, for the entire ship, equal to zero, leads to

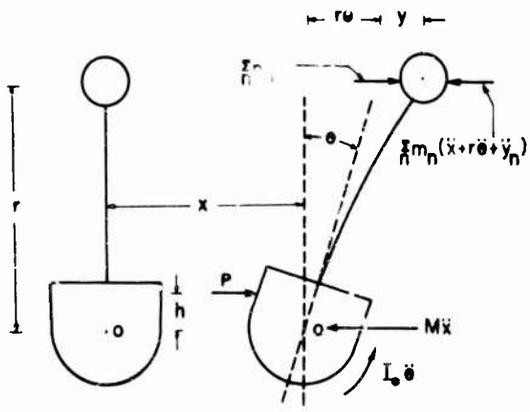

Fig. 3. Displacement of and load on model

$$\sum_n m_n(\ddot{x} + r\ddot{\theta} + \ddot{y}_n) + M\ddot{x} = P + \sum_n p_n \qquad (1)$$

and

$$\sum_n m_n(\ddot{x} + r\ddot{\theta} + \ddot{y}_n) + \frac{I_0\ddot{\theta}}{r} = \frac{Ph}{r} + \sum_n p_n . \qquad (2)$$

Another equation is obtained by setting the horizontal forces acting on a single lumped mass of the flight deck equal to zero (see Fig. 4):

$$m_n(\ddot{x} + r\ddot{\theta} + \ddot{y}_n) + ky_n + R_n = p_n . \qquad (3)$$

An expression similar to Eq. (3) can be written for each of the n masses comprising the flight deck. In Eq. (3), R_n is the net restraining force applied to mass m_n by the flight deck web. R_n is given as a function of y_n by the matrix equation

$$[R_n] = [K][y_n] \qquad (4)$$

where [K] is the stiffness matrix of the lumped-mass flight deck beam and $[R_n]$ and $[y_n]$ are column matrices.

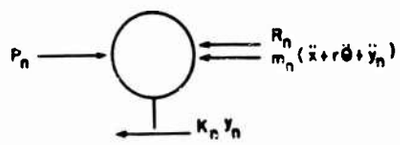

Fig. 4. Forces acting on a single mass m_n of flight deck

Equations (1) through (3) can be solved simultaneously for $x, \theta, y_1 \ldots y_n$. The solution can be simplified considerably, however, by eliminating x and θ and solving only for the y_n's. If Eqs. (1) and (2) are used to express x and θ in terms of y, and the result is substituted into Eq. (3), the following relation is obtained:

$$m_n\ddot{y}_n - \alpha m_n \sum_n m_n\ddot{y}_n + k_n y_n + R_n = p_n - \beta m_n . \qquad (5)$$

Equation (5), like Eq. (3), represents n expressions, one for each of the n lumped masses comprising the flight deck. The constants α and β, appearing in Eq. (5), are given by

$$\alpha = \frac{I_0/r^2 + M}{(I_0/r^2)\left(M + \sum_n m_n\right) + M\sum_n m_n} \qquad (6)$$

and

$$\beta = \frac{p_n(I_0/r^2 + M) + P\left(I_0/r^2 + \frac{Mh}{r}\right)}{(I_0/r^2)\left(M + \sum_n m_n\right) + M\sum_n m_n} \quad (7)$$

As $M \to \infty$, the hull becomes immobile in the water. For this case α and β are equal to zero and Eq. (5) reduces to

$$m_n\ddot{y}_n + k_n y_n + R_n = p_n . \quad (8)$$

Comparison of Eqs. (5) and (8) gives a qualitative indication of the effect that hull mobility has on the vertical bulkhead shears. If the first two terms in Eq. (5) are considered to represent an effective inertia force and last two terms an effective blast load, then comparison of Eqs. (5) and (8) indicates that hull mobility causes an apparent decrease in both inertia and loading. In both equations the maximum value of the bulkhead shear $k_n y_n$ is equal to the sum of the load and inertia minus the horizontal web restraint R_n. It can therefore be assumed that inclusion of hull mobility in the equations of motion will probably decrease the maximum bulkhead shears.

Orthogonality Conditions

The rigid body motions of the hull, obtained by solving the homogeneous parts of Eqs. (1) through (3), can be expressed in the form

$$x = x_p + x_{np} \quad (9)$$

and

$$\theta = \theta_p + \theta_{np} . \quad (10)$$

where x_p and θ_p are the periodic parts of the motion and x_{np} and θ_{np} the nonperiodic parts. Since the normal modes of vibration contain only the periodic part of the motion, the absolute displacements of the hull and flight deck masses during any of the normal modes can be expressed in the form

$$x_p = X e^{i\omega t} , \quad (11)$$

$$\theta_p = \Theta e^{i\omega t} , \quad (12)$$

and

$$z_n = (Y_n + X + r\Theta) e^{i\omega t} , \quad (13)$$

where z_n is the absolute motion of m_n.

If the principle of virtual work is applied to the system, deformed in accordance with Eqs. (11) through (13), the following orthogonality relation is obtained:

$$\sum_n m_n Z_{na} Z_{nb} + M X_a X_b + I_0 \Theta_a \Theta_b = 0 \quad (a \neq b). \quad (14)$$

Subscripts a and b refer to any two normal modes, and Z_{na}, the absolute displacement of mass m_n during the ath mode, is given by

$$Z_{na} = X_a + r\Theta_a + Y_{na} . \quad (15)$$

Y_{na} is the displacement of m_n relative to the hull during the ath mode.

If Eqs. (1) through (3) are solved simultaneously for x, θ, and the y_n's, the orthogonality condition given by Eq. (14) applies. If, on the other hand, x and θ are eliminated and Eq. (5) is used to solve for the y_n's, then an orthogonality condition free of x and θ is necessary. This relationship may be obtained by substituting expressions for X and Θ in terms of Y_n into Eq. (14).

Substitution of Eqs. (11) through (13) into expressions for the linear and angular momentum of the system during free vibrations leads to

$$X = -C_1 \sum_n (m_n Y_n) . \quad (16)$$

and

$$r\Theta = -C_2 \sum_n (m_n Y_n) . \quad (17)$$

where

$$C_1 = \frac{1}{M + \sum_n m_n \left(1 + \frac{Mr^2}{I_0}\right)} \quad (18)$$

and

$$C_2 = C_1\left(\frac{Mr^2}{I_0}\right) \quad (19)$$

If Eqs. (16) and (17) are substituted into Eq. (14), the following orthogonality condition, free of X and Θ, is obtained:

$$\sum_n m_n Y_{na} Y_{nb} - C_1\left(\sum_n m_n Y_{na}\right)\left(\sum_n m_n Y_{nb}\right) = 0 \quad (a \neq b) \quad (20)$$

For the case of an immobile hull, both Eqs. (14) and (20) reduce to

$$\sum_n m_n Y_{na} Y_{nb} = 0 \quad (a \neq b) \tag{21}$$

Equations (14) and (21) give orthogonality relations in a form usually encountered, namely, as a sum of products of mass or inertia times displacements in two modes. The somewhat unusual form, taken by the orthogonality relation in Eq. (20), is attributed to the presence of relative instead of absolute displacements in this expression.

Modal Analysis

Using normal mode theory [2], it can be shown that the dynamic displacement y_n, resulting from blast loads, is given by

$$y_n = \sum_a \frac{Y_{na}}{\omega_a} \frac{\int_0^t \sum_n Y_{na} \left[F_n f(T)\right] \sin \omega_a (t - T)\, dT}{\sum_n m_n (Y_{na})^2 - a\left(\sum_n m_n Y_{na}\right)^2}, \tag{22}$$

where ω_a and Y_{na} are the natural frequency and displacement at m_n corresponding to the ath mode. $F_n f(T)$ is the loading function at m_n. It consists of a time function $f(T)$ which must be the same for each mass and a load factor F_n which can vary with n.

Equation (13) indicates that y_n consists of the sum of n shape functions Y_{na}, each of which is multiplied by a participation factor and a dynamic load factor. If corresponding to mode a, the dynamic load factor is given by

$$(DLF)_a = \omega_a \int_0^t f(T) \sin \omega_a (t - T)\, dT \tag{23}$$

and the participation factor by

$$(PF)_a = \frac{1}{\omega_a^2} \frac{\sum_n Y_{na}}{\sum_n (m_n Y_{na}^2) - a\left(\sum_n m_n Y_{na}\right)^2}. \tag{24}$$

Then the dynamic displacement can be written in the form

$$y_n = \sum_a Y_{na} (PF)_a (DLF)_a \tag{25}$$

NUMERICAL EXAMPLE

Using a three-mass system to approximate the flight deck, the dynamic response of the carrier to blast loads has been determined. Numerical solutions for the natural frequencies, mode shapes, dynamic displacements, and vertical bulkhead shears are obtained for a fixed and mobile hull. The properties of the system and the magnitudes of the applied loads are listed in Table 1. The applied loads, P and p_n, are suddenly applied triangular load pulses, with an initial pressure p_0 and a decay time of 0.18 sec.

In the model being investigated, as in an actual carrier, m, EI, and k vary along the span of the ship. To give a clear picture of the effect of hull mobility on the natural frequencies

TABLE 1
Properties and Applied Loads for Three-Mass System

Flight Deck Mass System	m_n (lb-sec^2/ft)	k_n (lb/ft)	EI_n (lb/ft^2)	F_n (lb)
1	50×10^4	60×10^7	54×10^{13}	$174\times10^4\, p_0 f(T)$[a]
2	50×10^4	50×10^7	46×10^{13}	$174\times10^4\, p_0 f(T)$
3	40×10^4	32×10^7	—	$174\times10^4\, p_0 f(T)$

[a] $f(T) = 1 - (T/0.18)$; units of p_0 are lb/in.^{2}

Note: $M = 5\times10^6$ lb-sec^2/ft
$I_0 = 9\times10^9$ lb-sec^2-ft
$r = 60$ ft
$h = 14.6$ ft
$s = 300$ ft
$P = 522\times10^4\, p_0 f(T)$ lb

and mode shapes, these functions have been determined for a system with uniform properties as well as for the system with varying properties described in Table 1. The uniform system has the same dimensions and properties as the nonuniform one except that $m_1 = m_2 = m_3 = 50\times10^4$ lb-sec^2/ft, $k_1 = k_2 = k_3 = 50\times10^7$ lb/ft, and $EI_1 = EI_2 = 54\times10^{13}$ lb/ft^2. The properties of the uniform model were chosen to make this system as similar as possible to the nonuniform one.

Using the homogeneous part of Eq. (5), the natural frequencies and characteristic shapes were obtained for both the uniform and nonuniform system. The results of these calculations are given in Figs. 5 and 6. In both figures the solutions for the mobile hull are compared with those of the fixed hull. This is done for the model with uniform properties in Fig. 5 and for the one with nonuniform properties in Fig. 6.

The remaining calculations were carried out only for the model with variable properties. Using Eqs. (23), (24), and (25), the dynamic load factors and dynamic displacements were calculated. These quantities are listed in Tables 2 and 3. Table 4 then compares the vertical bulkhead shears $k_n y_n$ for the mobile hull with those for the fixed hull.

TABLE 2
Numerical Results for Variable-Properties Model

Mode	Dynamic Load Factor		Participation Factor (10^{-4} p_0)	
	Rigid	Mobile	Rigid	Mobile
A	1.47	1.50	-3.5	-4.9
B	1.54	1.65	26.7	12.9
C	1.58	1.58	5.4	-0.3

RESULTS

Comparison between the equation of motion for a mobile hull and the equation for a fixed

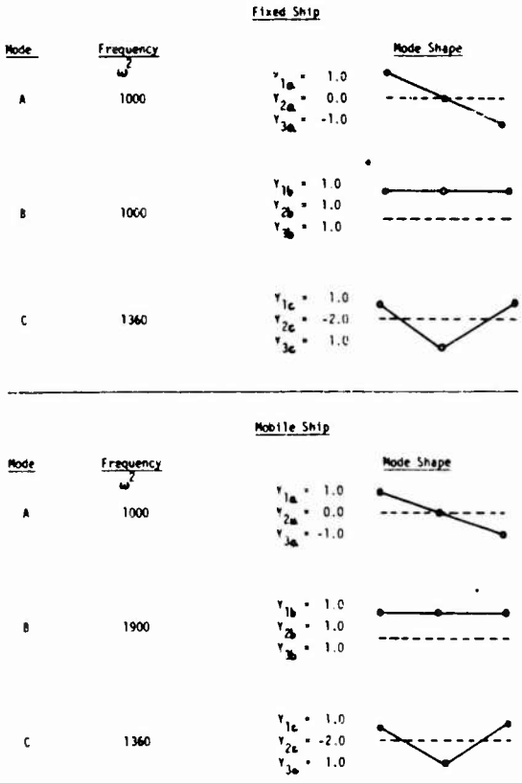

Fig. 5. Natural frequencies and mode shapes for constant m, k, EI

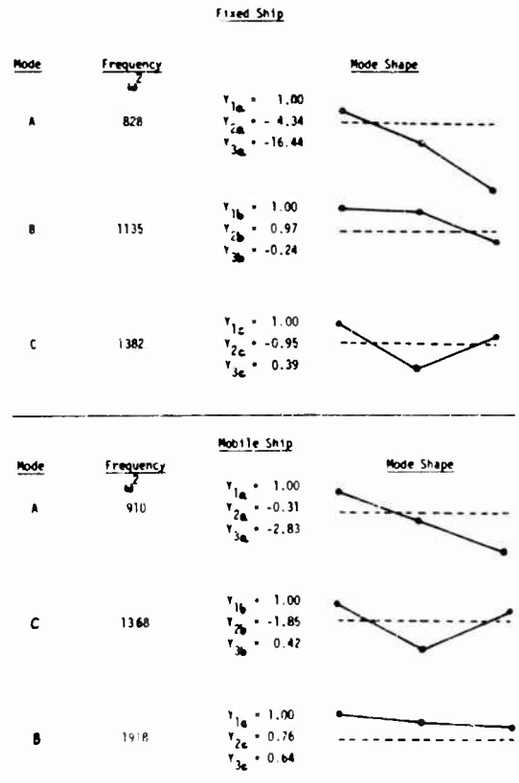

Fig. 6. Natural frequencies and mode shapes for variable m, k, EI

TABLE 3
Dynamic Displacement for Variable-Properties Model

Flight Deck Mass	Dynamic Displacement y_n (10^{-4} p_0, ft)	
	Rigid	Mobile
1	54	28
2	71	17
3	99	35

TABLE 4
Vertical Bulkhead Shears

Vertical Bulkhead	$k_n y_n$ (10^5 p_0, lb)	
	Fixed	Mobile
1	33	18
2	35	9
3	32	11

hull indicated that hull mobility would tend to reduce the shears in vertical bulkheads. This is substantiated by the numerical results given in Table 4. Comparison of the shears for the mobile hull with those for the fixed hull indicates that inclusion of hull mobility in the analysis leads to a sizable reduction in the design shears of the vertical bulkheads.

In addition to reducing the design loads, hull mobility has an important effect on the natural mode shapes and frequencies. It is apparent from Fig. 5 that for a ship with uniform properties, a change from the fixed to mobile hull has no effect on the frequencies of modes A and C but does have a marked effect on the frequency of mode B. Whereas mode B is one of the two possible fundamental modes for the fixed hull, it becomes the mode corresponding to the highest frequency for the mobile hull. The reason that the frequency of modes A and C is the same regardless of whether the hull is assumed to be fixed or mobile is that X and θ are zero for both conditions. For the fixed hull, X and θ are obviously zero for all modes. That X and θ are also zero for modes A and C of the mobile hull condition is evident from Eqs. (16) and (17). These equations indicate that the term $\sum_n m_n Y_n$ and consequently X and θ are zero for modes A and C and nonzero only for mode B. This will, of course, only be true when m_n, EI_n, and k_n do not vary with n, as in the system with uniform properties.

Equations (16) and (17) also show X and θ to be of opposite sign to Y_n. Based on this observation and the ones made in the foregoing paragraph, the vibration patterns of a single mass, m_n, for a uniform system have been sketched in Fig. 7 for both fixed and mobile hull. Figure 7a is typical of all three modes for the fixed hull and of modes A and C for the mobile hull. Figure 7b represents the vibration

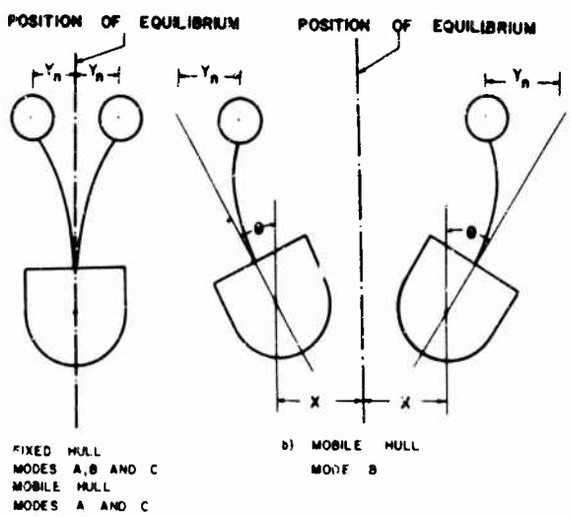

Fig. 7. Normal modes of vibration

pattern of mode B for the mobile hull. Comparison of the two vibration patterns for mode B indicates that the mobile hull condition gives rise to a shorter vertical web wavelength and consequently a higher frequency than the rigid hull condition.

When considering the vibrations depicted in Fig. 7 it is important to remember that they include only the periodic parts of X and Θ. The total hull translation and rotation due to an applied blast load will be made up of a nonperiodic displacement in addition to the above-mentioned periodic displacements.

If the properties of the system are not constant, X and Θ will be nonzero for all three modes of the mobile hull condition. As indicated in Fig. 7, changes will therefore occur in all three mode shapes in going from a fixed to a mobile hull. Comparison of Figs. 5 and 6 indicate, however, that the introduction of variable properties has not materially affected the validity of the foregoing conclusions. For the variable- as for the constant-properties model, the frequency of mode B is increased from close to the lowest to the highest of the three frequencies in going from the fixed to the movable hull condition.

The participation factors (Table 2) clearly indicate that mode B is the most important of the three principal modes in the determination of the dynamic response to a uniform lateral pressure. If a complete modal analysis, using all of the normal modes, is carried out, the correct solution will be obtained. If, however, as is often the case, one tries to approximate the solution by using only the mode corresponding to the lowest frequency, a completely erroneous result would be obtained for the mobile hull condition.

SUMMARY

The effect of hull mobility on the dynamic response of an aircraft carrier subjected to blast loads is studied. A simplified model of the carrier is used in the investigation. Equations of motion, orthogonality relations, and a solution for the dynamic displacements of the model are derived. Using the above theory, the natural modes and frequencies and the dynamic displacements are obtained for a numerical example. Both a carrier whose hull is assumed to remain fixed in the water and one whose hull is allowed to move in the water are considered. Comparison of the results for the mobile hull with those of the fixed hull indicates that inclusion of hull mobility in the analysis results in a sizable reduction of the design shears of the vertical bulkheads. Hull mobility is also shown to have an important effect on the natural modes and frequencies.

NOMENCLATURE

C_1 = Constant

C_2 = Constant

EI = Flexural stiffness of flight deck in horizontal plane

h = Vertical distance between resultant hull load P and center of gravity of hull

I_0 = Mass moment of inertia of hull with respect to centroidal axis of hull

K = Stiffness matrix of lumped-mass flight deck beam

k_n = Shear stiffness nth vertical bulkhead

M = Total mass of hull

m_n = Mass of nth flight deck mass

O = Center of gravity of hull

P = Resultant horizontal blast load on hull

p_n = Horizontal blast load on the nth mass of flight deck

R_n = Net shear force applied by flight deck web to nth flight deck mass

r = Vertical distance between flight deck mass and hull center of gravity

s = Distance between flight deck masses

X = Amplitude of hull translation

x = Hull translation function

Y_{na} = Amplitude of displacement of nth flight deck mass during ath mode relative to hull displacement

y_n = Displacement function of nth flight deck mass relative to hull

Z_{na} = Amplitude of absolute displacement of nth flight deck mass during ath mode

Z_n = Absolute displacement function of nth flight deck mass

α = Constant

β = Constant

θ = Amplitude of hull rotation

ϕ = Hull rotation function

ω_a = Frequency of ath mode

ACKNOWLEDGMENT

The assistance of Edward Habib, head of section 741 of the David Taylor Model Basin, and his staff is gratefully acknowledged.

REFERENCES

1. John O'Brian, "CVA 67 Supplementary Design Data for Nuclear Blast," BuShips Code 443, Rept. 1, Aug. 1962

2. John M. Biggs, Structural Dynamics (McGraw-Hill, New York), 1964, pp. 116-125

DISCUSSION

Mr. Hughes (Naval Ordnance Laboratory): Could you explain why you get the same frequency for two mode shapes? This is a little counter to my way of thinking.

Mr. Chajes: In this case we do have two mode shapes with the same frequency. You can say the energy in both of them is the same. There are two alternate fundamental frequencies and both mode shapes correspond to lowest frequency.

Mr. Hughes: If you have a physical structure on a vibrator this would happen. You could get a case where it would not know which mode it is going to go into.

Mr. Chajes: This is only true for constant properties, which was the case with this system where I got the same frequencies. The properties were all completely uniform. The moment the properties varied on the second side there was a differentiation of frequencies.

* * *

DYNAMIC BEHAVIOR OF SHIPBOARD ANTENNA MASTS SUBJECTED TO BLAST-GENERATED OVERPRESSURES

F. Adrian Britt and Robert H. Anderson
Mechanics Research, Inc.
El Segundo, California

A design analysis of a model shipboard antenna and support mast is presented. An overall program directed toward the derivation of a design technique for such structures subject to nuclear blast is discussed in light of the analytic results. A test program, to be performed in the spring of 1968, for the experimental verification of the analytic study is also described.

INTRODUCTION

An analytic study was performed to determine the behavior of a typical shipboard antenna support mast subjected to a field-test generated-blast environment. The objectives of the study were:

1. To determine the design methods for blast-resistant shipboard antenna mast support structures;

2. To provide a basis for a future field experiment (including the instrumentation plan), wherein one may verify the sufficiency of the design approach used and infer size and overpressure extrapolation rules.

In addition, the three masts considered were designed for the field test; the appropriate foundation required for the surface-burst ground test was included.

STATEMENT OF THE PROBLEM

The basic problem stated in its most simple terms is to provide a design technique which will enable the naval architect to evolve a simple, economical, and adequate support structure for shipboard electronic equipment such as large dish antennas. It has become increasingly apparent that equipment of this type will become more common on naval vessels of the future. Further, their size, orientation, and location are not dictated by the structures engineer. In recognition of this fact, and with the added complication of the rather severe blast-generated overpressure environment to which these structures are to be subjected, a program was initiated with the objective of providing such a design technique. The ensuing technical discussion, therefore, is concerned with:

1. The program plan for the accomplishment of this task;

2. The description of the field-test loading environment and correlation with shipboard operational environment;

3. Preliminary configuration designs of the structural masts;

4. Dynamic response analysis of the masts;

5. Specification of the field-test plan including the appropriate instrumentation system.

The actual accomplishment of the field test and the final recommendations on the appropriate design techniques must be the subjects of a future report. However, it is hoped that this paper will encourage discussion which may have a timely and positive effect on the total program.

PROGRAM PLAN

A schematic of the program plan is shown in Fig. 1. In addition, a sketch indicating the basic components of the support structure and its simulated side antenna is shown in Fig. 2. Because of the wide variation in antenna mast structure heights and orientation of the basic antennas, an attempt was made to study a representative structure that would retain the

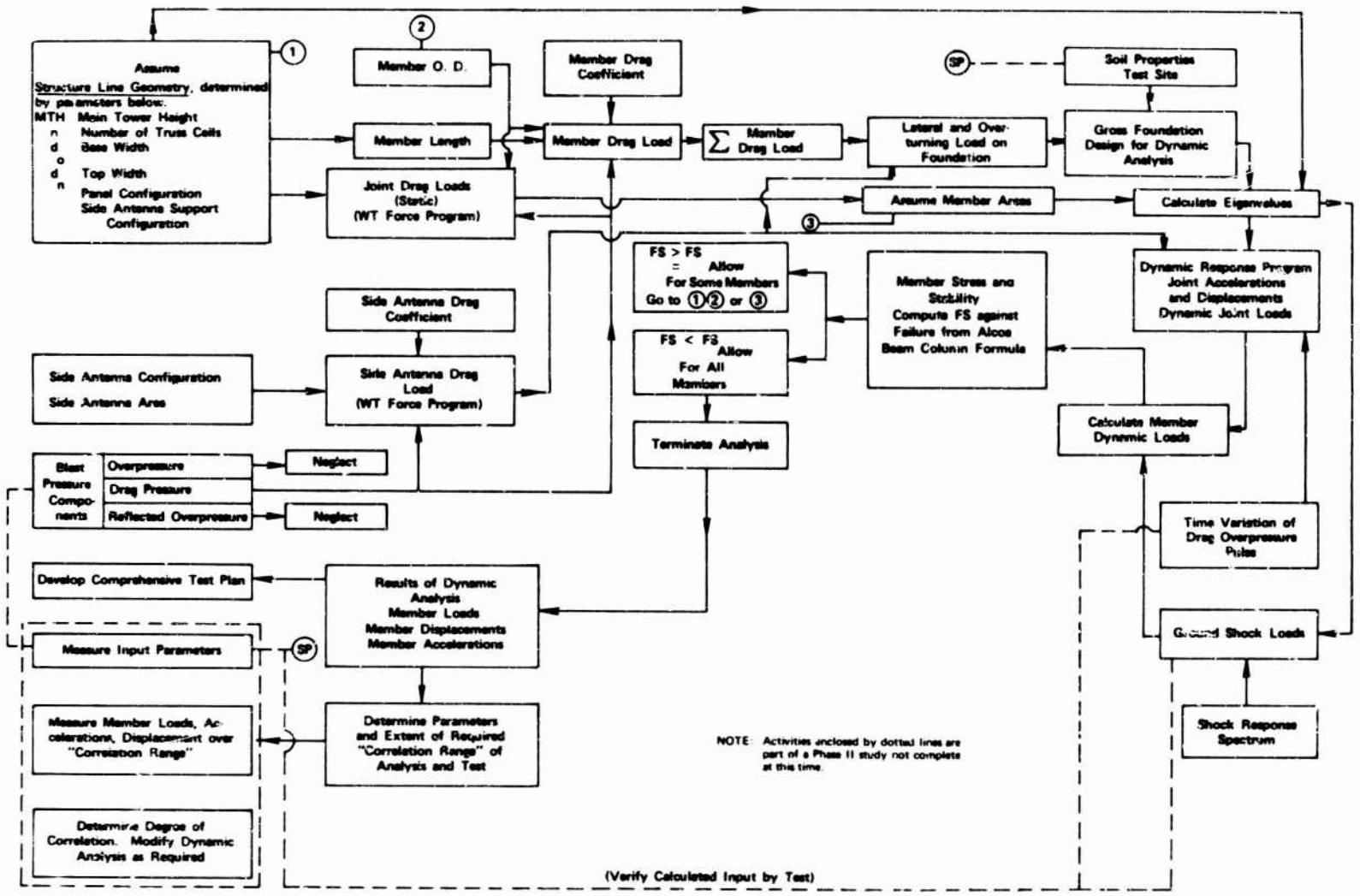

Fig. 1. Program plan

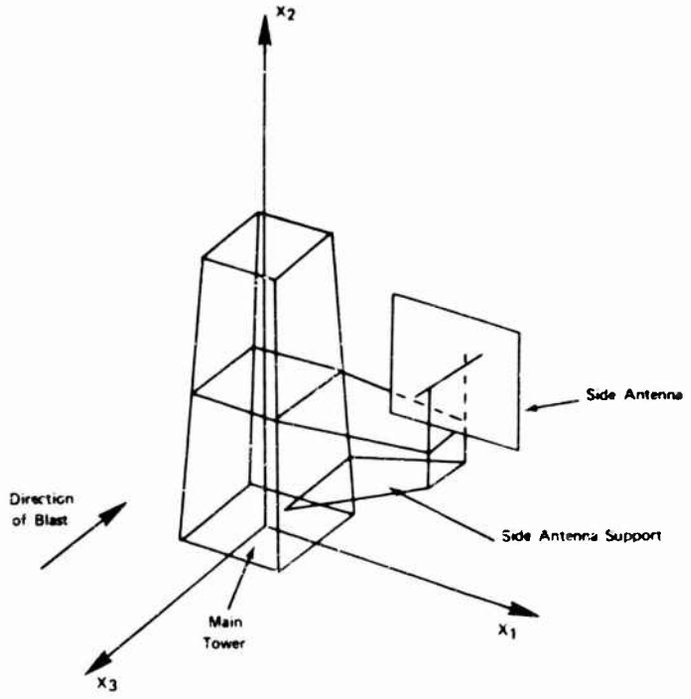

Fig. 2. Basic components of system

major dynamic characteristics of actual systems. The side antenna, side antenna support, and main tower arrangement shown in Fig. 2 closely simulate existing and future contemplated antenna mast systems.

The structure line geometry was first determined from parameters such as the main tower height, the number of truss cells, the base width, the top width, panel configuration, and the side antenna support configuration. Member lengths and diameters were assumed and external drag loads computed. The overpressure and reflected overpressure components were neglected. The justification for neglecting these components of blast loading will be discussed more fully in the section concerning the field-test environment. Using these loads and the assumed geometry, the gross lateral load and overturning moments on the foundation were calculated. A preliminary design was then generated by assuming member areas and foundation characteristics such that the appropriate mode shapes and frequencies for the total system could be calculated. A dynamic response program then generated the dynamic member loads. Consideration was also given to ground shock environment. The member stresses and factors of safety were then computed. An iterative structural design cycle then ensued, as can be seen from the upper- and right-hand portions of Fig. 1. When the factors of safety showed an allowable margin for all members, the analysis was terminated. The results of this dynamic analysis were then used to provide specifications for the test program and the structure foundation designs. The second phase of this program will include the actual test program and the eventual data analysis and correlation studies necessary to yield a satisfactory design technique.

FIELD-TEST ENVIRONMENT

The masts designed as part of this study will be subjected to a field test at Suffield Experimental Station, Ralston, Alberta, Canada, in the spring of 1968. A 500-ton TNT charge partially buried in the ground will explode, subjecting the trial masts to a 10- or 15-psi overpressure, depending on their radial placement. The radial locations are uniquely related to overpressure and are given in Table 1. The trial masts will be oriented with the X_3 axis pointing directly to ground zero. The theory of air pressure loading on aboveground structures resulting from explosive bursts is extensively covered in Refs. [1] and [2]. Only the points essential to describing the structural load will be discussed below.

TABLE 1
Blast Parameters, 500-Ton Surface Explosion

Parameter	Overpressure					
	15 psi			10 psi		
	Ref. [1]	Ref. [2]	Ref. [3]	Ref. [1]	Ref. [2]	Ref. [3]
Distance from ground zero (ft)	638	630	760	755	770	940
Drag overpressure (lb/in.^{2})	←	4.76	→	←	2.210	→
Drag positive impulse (lb-sec/in.^{2})	0.1735	0.159	–	0.112	0.087	–
Positive phase duration (sec)	0.1828	0.1825	0.200	0.2125	0.210	0.230
Arrival time (sec)	0.1905		–	0.254		–
Velocity of shock front (ft/sec)	←	1530	→	←	1408	→

In general, there are two pressure components acting: overpressure and drag pressure. An approximate expression relating these two components is:

$$q_{do} \approx \frac{5}{2}\left(\frac{p_{so}^2}{7p_0 + p_{so}}\right), \qquad (1)$$

where

q_{do} = maximum drag pressure,

p_{so} = maximum overpressure, and

p_0 = ambient pressure (see Nomenclature).

Another important parameter is the velocity of the shock front U where

$$U = c\sqrt{1 + \frac{6p_{so}}{7p_0}}, \qquad (2)$$

and c = velocity of sound in air (standard atmospheric conditions). On a closed boxlike structure, the air blast structural load results from both overpressure and drag pressure. On an open frame such as the antenna mast system considered here, only the drag pressure produces significant loads. The air blast pressure wave engulfs the open structure of the antenna mast both internally and externally. In this way, the buildup of the static pressure is canceled and the overpressure as a loading component is eliminated. Similarly, loads from reflection of the overpressure front by members of the antenna mast also will be negligible. This can be seen by considering the duration of a reflected overpressure pulse given by

$$t_c \approx \frac{D}{U}. \qquad (3)$$

D is a typical member lateral dimension (e.g., outside diameter). As such dimensions, in this case, are less than 1 ft, and $1400 < U < 1530$ fps, the resulting reflected overpressure durations are of the order of 0.001 sec. Such loads, having the shape of a pressure spike, produce no significant primary structural loads (near zero impulse). For this reason, the primary structural loads, resulting from air blast, will be based on drag overpressure only. Table 1 and Figs. 3 and 4 contain all the parameters necessary to describe the external blast-generated loading functions on the masts.

The air blast load is common to both shipboard and field-test mast installations. Ground shock, however, is peculiar to the land base field trial only. Ground motions resulting from explosions are discussed elsewhere [2, Ch. 4], and only a brief coverage is given here. There are two types of blast-induced ground motions: air-induced ground motions and directly transmitted ground motions. Directly transmitted ground motions generally travel significantly faster than the shock front. Accordingly, direct ground motion will reach the trial masts before the air-induced ground motion or air blast. The effects of direct ground motion on the mast damp quickly and are negligible by the time the air-induced ground motion arrives. This factor was checked and completely supported by Suffield Experimental Station. It is sufficient then to account for the effects of air-induced ground motion when considering the ground shock structural loads.

The seismic velocity of the highly layered test site soil is in the range of $600 < c_s < 2200$ fps in the upper 20 ft of depth. Reference [4] gives $c_s = 2200$ fps, while Ref. [5] quotes $c_s = 1100$ fps. Accordingly, the air-induced ground motion is of the subseismic-transseismic type.

When evaluating the structural load resulting from this type of ground motion, the shock

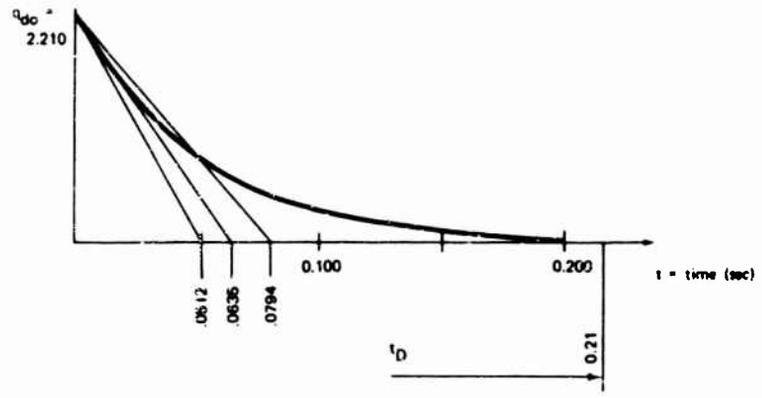

Fig. 3. Drag pressure vs time

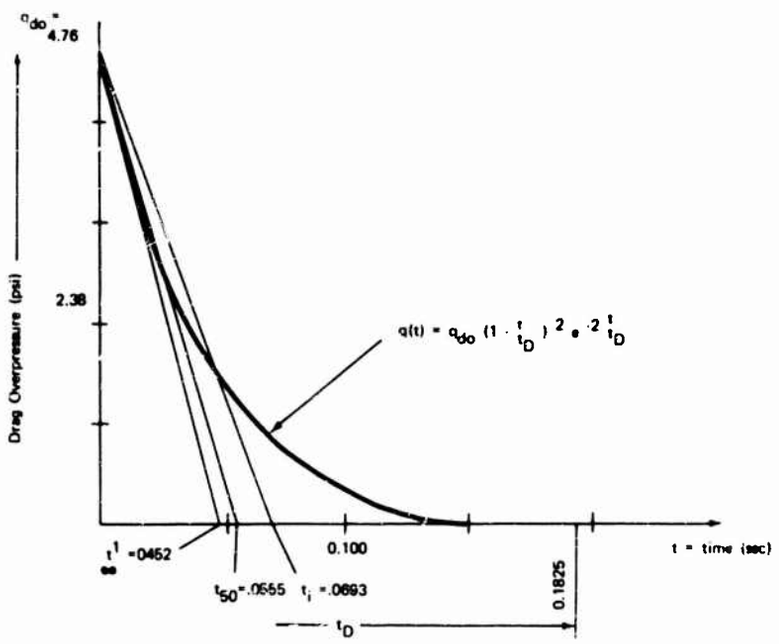

Fig. 4. Drag pressure vs time

spectrum technique is used to account for ground shock effects on structural loads. The shock response spectrum approach is used extensively in predicting the response of structures due to earthquake motions, and its use has been extended to ground shock problems arising from air blast. This technique is described elsewhere (e.g., [2, Ch. 10]).

As previously stated, only the drag overpressure need be considered in estimating the air blast effect on open mast structures. The parameters necessary to describe the drag overpressure external loading function are shown in Figs. 5 and 6, which show the time variation of the overpressure and drag pressure vs time at a fixed location. Both the pressure pulses commence at the same time (t_{ar}). The initial magnitude of the drag pressure pulse is determined by Eq. (1). The duration t_D of the drag overpressure pulse is taken equal to the positive phase of the overpressure pulse. The actual duration of the drag pressure pulse is somewhat longer than t_D because of inertia effects of the moving air; but the difference is not significant and is ignored here. The drag

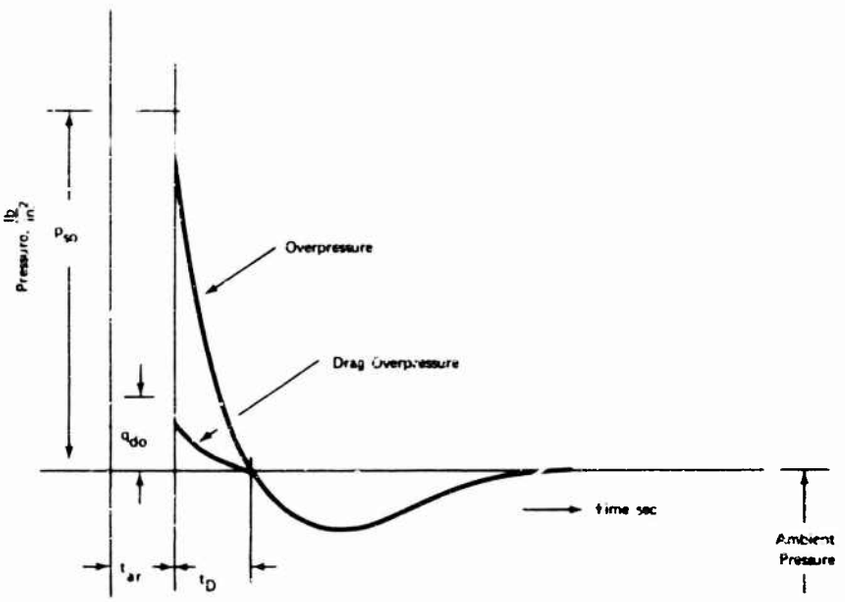

Fig 5. Overpressure and drag pressure vs time at a fixed location

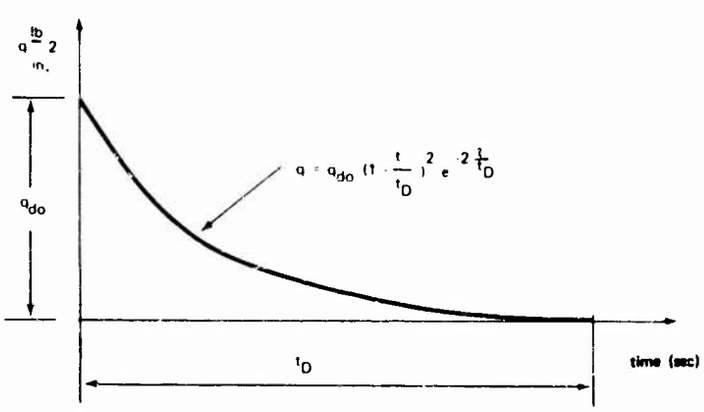

Fig. 6. Drag pressure vs time at a fixed location

overpressure pulse is described by the parameters q_{do} and t_D and an exponential time decay. The magnitude of the drag overpressure in the time interval $t_{ar} < t < (t_{ar} + t_D)$ is given by

$$q(t) = q_{do}\left(1 - \frac{t}{t_D}\right)^2 e^{-2t/t_D} \qquad (4)$$

For the present study, values for the overpressure p_{so} were established at 15 and 10 psi. The corresponding magnitudes of q_{do} calculated from Eq. (1) are 4.76 and 2.21 psi, respectively. The additional blast parameters t_D and t_{ar} and the blast impulse are calculated from Refs. [1] and [2] and are displayed in Table 1. The resulting drag overpressure pulse shapes are shown in Figs. 3 and 4. Based on the foregoing, the time-dependent member external load can be written as

$$F_M = q(t)\, C_D A_{PM} \qquad (5)$$

where A_{PM} = projected member lateral area. The member drag coefficients C_D in Eq. (5) are assumed to be constant. Dependence on Reynolds number is not considered, because of an insufficiency of data on this subject. In this respect, the recommendations of Ref. [2] are followed.

Members of the trial masts are cylindrical, and from Ref. [2]

$$C_D = 1.2 \quad \text{for} \quad 5 < p_{so} < 15 \text{ psi}$$

The total external load on the mast structure is taken as

$$F_S = \sum F_M + q(t)\, C_D A_A . \qquad (6)$$

where A_A = side antenna area. The summation in the first term of Eq. (6) is taken over all the members of the structure in the analysis. Total structural load calculated in this manner (ignoring shading effects on the leeward members) is conservative and is recommended by both Refs. [1] and [2]. The time variation of the drag overpressure pulse is assumed to be identical and simultaneous for all members of the structure and also for the side antenna drag area. Member lengths are taken to the joint intersection of the line diagram of the structure. The extra load thus introduced approximately accounts for the effect of gussets.

To construct a shock response spectrum due to ground shock, the maximum values of ground displacement, velocity, and acceleration must be estimated. The techniques of Ref. [2] (Chs. 4 and 10) were used to construct the shock spectrum corresponding to weapon yield and overpressure values previously quoted. An example of the vertical spectrum corresponding to the 15-psi overpressure level is shown in Fig. 7.

CONFIGURATION OF TRIAL MASTS

The basic components of the trial masts are the main tower, the side antenna support, and the side antenna, shown in Fig. 2. A more detailed model of the system including the corresponding nomenclature is depicted in Fig. 8. Additional numerical data on the three masts are given in Table 2. The main tower heights of 30 and 15 ft were chosen for reasons discussed below. The numerical values for critical parameters shown in Table 2 evolved in the analytic phase of the study.

As the drag load is a product of the projected area and the drag overpressure, the resulting structural load on the mast is seen to increase in proportion to the projected area of the mast itself. Accordingly, other factors being equal, there is a premium on the mast structure with the least projected area. A mast structure with a minimum number of long members and with a relatively small member outside diameter satisfies this criterion. The minimum member size is constrained as the member outside diameters, wall thicknesses, and lengths must be proportioned to preclude buckling.

In preliminary discussions, it was decided that the base configuration of the main tower would be square rather than triangular or circular. This square cross section has been used in all design and analysis. As real antennas were not available for the field test, the side antenna had to be a simulated structure. It was decided that the simulated side antenna would be of pipe frame construction essentially similar in construction to the main tower. The configuration of the simulated side antenna was arrived at by scaling an actual antenna. The antenna component drag areas such as dish frame, mesh, and pedestal were scaled from this actual structure. A representative simulated side antenna structure is shown in Fig. 9. A very important parameter in this study is the antenna drag area ratio (DAR) where:

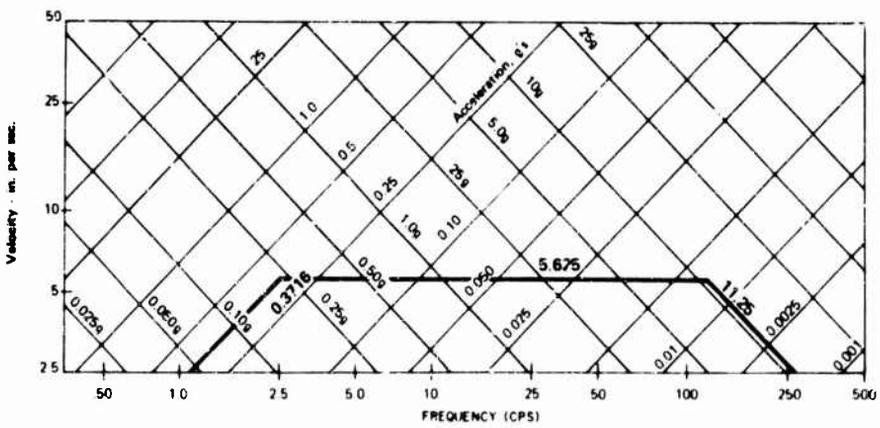

Fig. 7. Ground shock spectrum, 15-psi overpressure

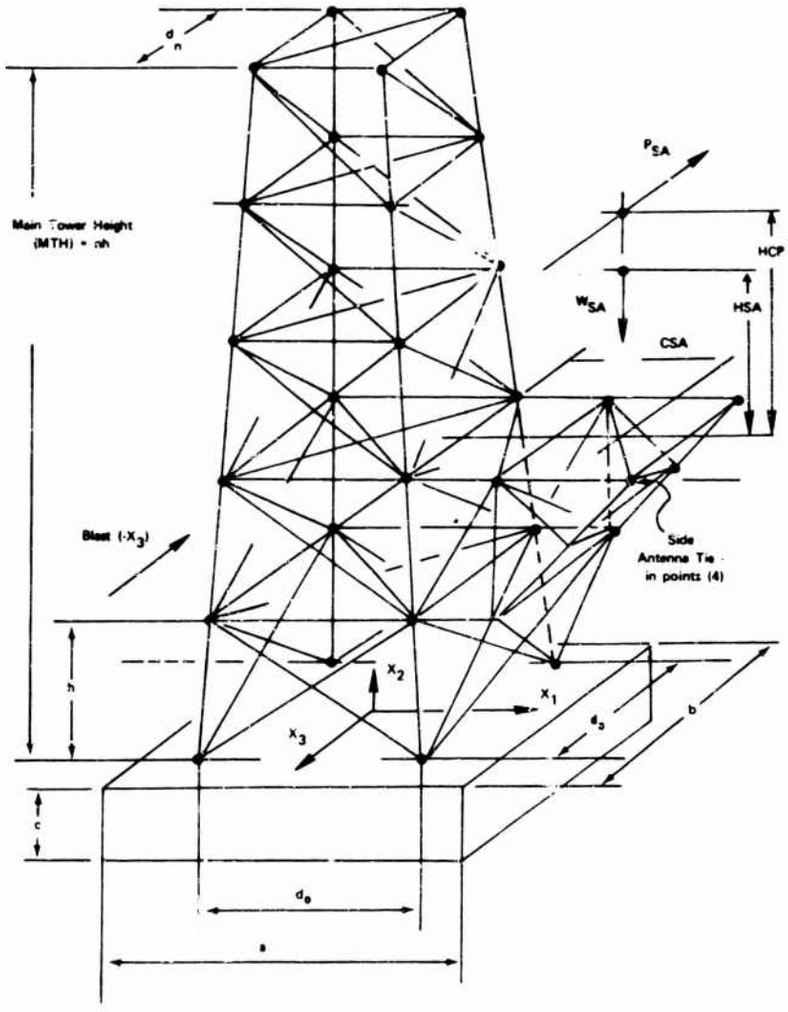

Fig. 8. Structural model

$$DAR = \frac{A_A}{\Sigma A_{PM}} ,$$

the ratio of antenna projected area to remainder structure projected area. Studies indicated that a DAR of approximately 0.3 closely matched the composite of many actual structures. To derive the maximum benefit from the test program (within economic restraints), the two major mast parameters, i.e., the external load (overpressure) and structural configuration, should extend over an appropriate range. The extent of the overpressure range was specified as between 5 and 15 psi. The design overpressure for future masts was specified as 10 psi. The height of the antenna mast was taken as the defining structural configuration parameter. Other configuration parameters can be related to the height of the antenna mast (main tower height – MTH). The range of MTH is predicated on (a) the actual height of future masts, and (b) the maximum allowable height of a mast for possible wind tunnel experimentation. Item (a) corresponds to an MTH equal to 80 ft, and item (b) points to an MTH of 6 ft. This range of 6-80 ft, however, had to be narrowed by practical considerations of the field-test environment. Clearly, a 6-ft MTH, at say 10 psi, would not present structural behavior worth investigating. A very tall mast would require extensive foundation structure. Accordingly, the study started with an MTH range of 15-45 ft. In the course of analyzing antenna masts of the type described, it was concluded that loads at 5 psi are so low compared to those at 15 or 10 psi (12 and 26

TABLE 2
Structural Model Numerical Parameters

Parameter		Mast		
Description	Symbol	A	B	C
Height of truss cell, main tower (ft)	h	5	6	6
Base width of main tower (ft)	d_0	5	8	8
Top width of main tower (ft)	d_n	3	4	4
Number of truss cells[a]	n	3	5	5
Height of center of pressure of side antenna (ft)	HCP	3.08	4.130	4.130
Area of side antenna (projected) (ft^2)	A_A	32.3	64.17	64.17
Weight of side antenna (lb)	W_{SA}	476.8	1115	1115
Height of c.g. side antenna (ft)	HSA	2.765	3.465	3.465
Center of c.g. side antenna (ft)	CSA	4.55	6.300	6.300
Width of foundation (ft)	a	15.7	—	23.6
Breadth of foundation (ft)	b	20	—	30
Depth of foundation (ft)	c	4	—	4
Radius of foundation[b] (ft)	r_0	10	—	15

[a] n = (main tower height)/h.
[b] Circular base.

percent, respectiveiy), that again the corresponding structural behavior was not worth investigating. This consideration led to the elimination of a 30-ft mast at 5 psi from a further course of study. Furthermore, as elements in the proposed design method evolved, it became clearer that this design method can be sufficiently proved out over the more limited range of MTH. The recommended sizes and locations relative to ground zero are shown in Fig. 10.

DYNAMIC RESPONSE ANALYSIS

A lumped-parameter approach was used in formulating the dynamic model of the mast, side antenna, and side antenna support structure. A gross picture of this approach may be inferred from Figs. 8 and 9.

The foundation-soil system was also included in the overall dynamic model. The method used in formulating the basic stiffness and inertial properties of the foundation-soil system is described by Funston [6]. This method describes a technique for calculating four (vertical, horizontal, rocking, and torsional) equivalent support stiffnesses for the four primary modes of motion considered. Next, mass or inertia coefficients are calculated. These coefficients take into account the effect of soil mass vibrating with the foundation slab. References [4] and [5] provided the appropriate empirical data required to provide mass and stiffness factors indigenous to the specific test site considered. The foundation-soil model then becomes just another part of the lumped mass-spring system described below for calculation of member responses.

The physical structure modeled was described in a right-handed Cartesian coordinate system. The structure is represented as a spatial array of nodes or joints which are interconnected by the "defining elements" or "elemental building blocks" of the system. The node has the following characteristics associated with it:

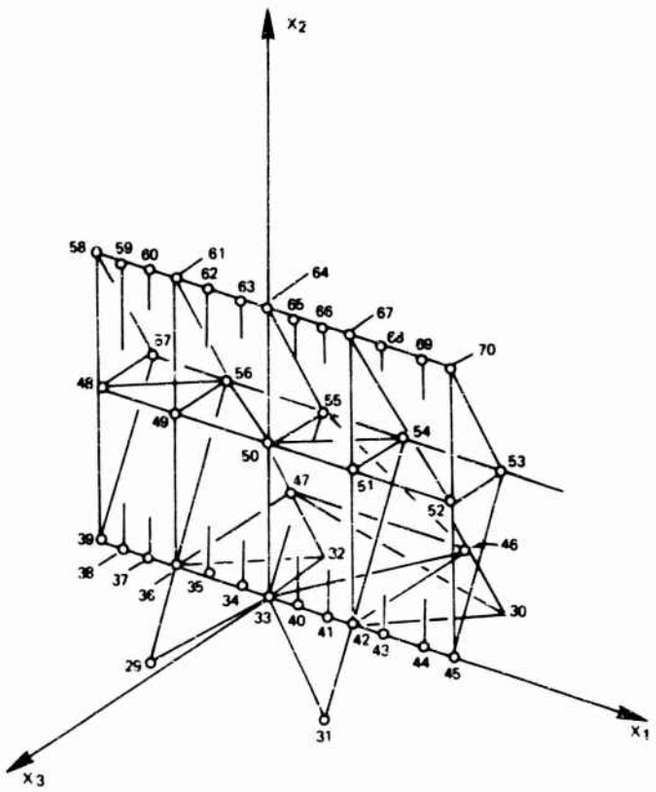

Fig. 9. Typical side antenna structure

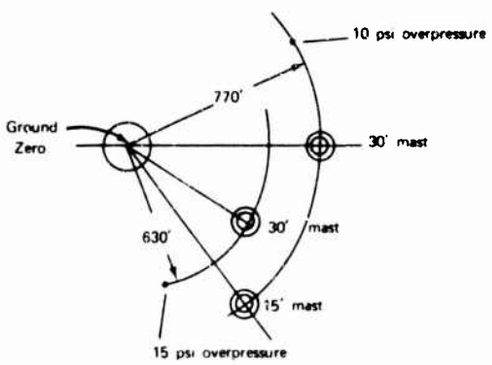

Fig. 10. Recommended arrangement of test masts

1. Position in space: the three Cartesian coordinates locate the node in the system coordinate system;

2. Movement in space: the node may translate and rotate in and about each of three directions;

3. Connectivity: node is connected to the other nodes that are joined directly by an element;

4. Mass: a mass value may be associated with each of the movements permitted by the node;

5. External forces: external forces and moments may be applied to the node in any of the permitted directions of movement.

The node is the basic parameter of the mathematical model representing the structural system. The position, displacement, mass, connectivity, loading, and restraints of the system are all defined in terms of the node point. In defining a node, it may be desired to restrain the movement of that node in one of the permitted directions of movement. Whenever a node is restrained from movement in any one direction, it can be said that a restraint has been applied to the structure.

The MRI STARDYNE and DYNRE-I computer programs were used to calculate the eigenvalues and eigenvectors and the resulting

member responses, respectively, for the mast systems considered. Bar elements were used to connect the lumped masses at the nodes, although the program has capability to include plate finite elements. The mast and antenna structure was treated as a rigid jointed structure throughout the analysis. Every joint, other than points of restraint at the ground, was allowed six degrees of freedom. With this modeling approach, member end loads of axial force, shear, and bending moment (as well as torque) are provided in the computer printout. These loads, in turn, enable the stress analysis of typical joints to be made with facility in the iterative and final design stage. An example of the time variation of dynamic loads (axial and bending moment) in a typical member is shown in Fig. 11. A description of the "normal mode" response analysis employed in achieving these results is given in the Appendix. The resulting stresses and factors of safety for representative members in the masts designed for 15 and 10 psi, respectively, are given in Table 3.

The significant conclusions drawn from a detailed review of the resulting dynamic response data were:

1. A dominant cantilever bending mode (the second mode) was found to exist in the mast structures examined. Further, the dynamic response of the mast structure can be calculated with sufficient accuracy by utilizing four modes.

2. The influence of foundation was found to lower slightly the dominant frequency of the mast without changing its character. The assumption of a rigid base will be sufficiently accurate for future dynamic analysis of field-tested antenna mast systems if appropriate attention is paid to foundation design.

3. Significant dynamic amplification of member loads was found to result from the application of the drag overpressure pulse to the mast structure.

4. Ground shock loads were found to be insignificant compared to the drag overpressure load (note: field-test environment is 500 ton – surface burst – conventional explosive).

The results of the dynamic response analysis were then used to specify:

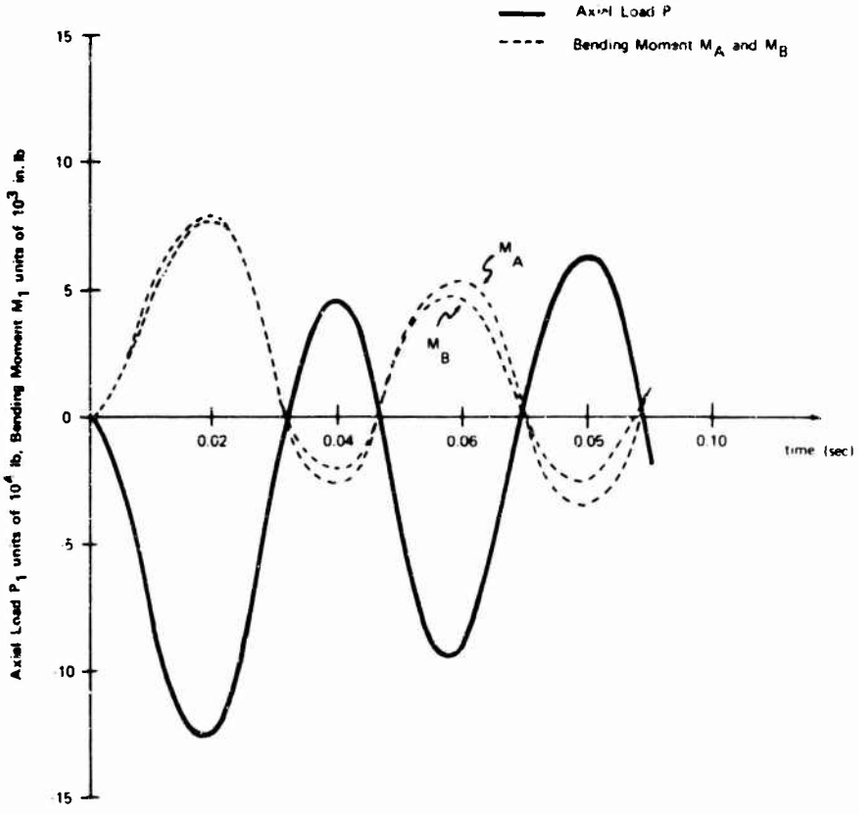

Fig. 11. Dynamic loads in member 2-4 at 15-psi overpressure pulse

TABLE 3
Member Stress and Stability

Symbol	Unit	Mast C (15-psi overpressure)		Mast A (10-psi overpressure)
		Member 4-8	Member 4-5	Member 3-23
P_{max}	lb	142,340	47,564	41,231
M_{max}	in.-lb	66,850	29,535	17,860
A	$in.^2$	9.694	9.694	6.324
Z	$in.^3$	10.830	10.830	5.905
f_{cw}	$lb/in.^2$	14,680	5,910	6,375
f_{bw}	$lb/in.^2$	6,170	2,720	3,020
f_c [a]	$lb/in.^2$	30,020	23,400	29,050
f_b [a]	$lb/in.^2$	53,330	53,330	53,430
KL r	—	41	66.1	45.75
L	in.	72.32	116.3	64.75
r	in.	1.762	1.762	1.415
FS	—	1.253	3.33	3.14

Note.--See Nomenclature.
[a] f_c and f_b are based on 6061-T6.

1. The appropriate field-test instrumentation plan;

2. Fabrication specifications for the field-test models;

3. Specifications for the foundation design and installation.

FIELD-TEST INSTRUMENTATION PLAN

The three antenna masts will be instrumented so that data can be obtained from the 500-ton surface explosion. These empirical data will be used to verify results obtained in the analytic study. The masts will be instrumented with strain gages, accelerometers, and pressure transducers. The strain gages will be placed on selected members which are on the structures. These gages will measure the strain levels resulting from the blast, and from these strain levels member stress levels will be calculated. The accelerometers will measure the vibration levels at a particular location. The displacements at a single point can be calculated from the accelerometer output data. The pressure transducers will measure the pressure profile of the blast. The exact pressure input data at the masts will be obtained so that it can be used as the forcing function input. The analytic data can be updated by using the correct forcing input for each mast.

Each mast will be instrumented with approximately 33 channels, of which 18 channels would be strain gages, 12 would be accelerometers, and 3 would be pressure transducers. Strain gages should be located on at least 10 members of the structure so that the structure's behavior will be adequately defined when subjected to the blast force loading. The members that were selected for this instrumentation were either those which were the most critically loaded or those which would best produce data that can be compared with analytical predictions regarding the dynamic response of the structure. In the lower leg members of the mast, relatively large axial and bending loads

are anticipated. Thus, these members will be instrumented for both bending and axial loading.

Other members in the lower antenna mast support that are expected to experience high combined bending and axial loads are also instrumented for both axial and bending strains. The gages that will be used to instrument the tower can be any foil strain gage, for example, Micro-Measurement series EA. These are 120-ohm gages with a gage factor of approximately 2. They will withstand temperatures up to 250°F and are self-temperature-compensating. The active gages will be placed on the members with an epoxy or other cement. The dummy gages would be placed on a compound, such as room temperature vulcanizing rubber. This compound does not transmit stress but it does transmit heat. Therefore, the dummy gages would merely act as temperature-compensating gages in the Wheatstone bridge circuit. All of the strain gages will be protected from moisture and other adverse environmental factors.

The accelerometers will be installed at the base of the mast and at the base of the antenna. Two locations will be selected at the base of the mast. Three accelerometers will be mounted in the three perpendicular axes at each location. In addition, accelerometers will be mounted at each of the four support members of the antenna. One of these four locations would consist of three accelerometers in each of the three axes, and the other three locations would consist of accelerometers mounted in the direction of the blast. The accelerometers must be able to measure vibration responses at very low frequencies. A strain-gage type of transducer must be used which has a frequency response from 0 to approximately 200 cps. Accelerometers manufactured by Statham, CEC, or Endevco can be used.

Provisions will be made on the tower base for rigidly mounting two accelerometer locations. A steel block will be embedded in the concrete, and on this block three accelerometers will be mounted. The location for the mounting blocks will be selected very carefully so that all vibration parameters of the base can be found: the average acceleration of the base in each axis and the angle of rotation of the block in each axis.

The amplitude range of the accelerometers is obtained from the analytic results. The maximum acceleration levels that were computed occur at the top of the tower, joints 17-22 and 13-16. At these joints the acceleration levels reach a maximum value of 80 g for the 15-psi overpressure level. However, these joints will not be instrumented. The maximum acceleration at the antenna base is approximately 12 g. This level occurs in the direction of the blast. The maximum vertical acceleration level is approximately 4 g. Therefore, accelerometers with a full-scale range of ±15 g will be required.

Pressure transducers will be mounted at each tower to measure the pressure from the blast. These transducers have a crystal sensing element which can respond to very high transient pressure measurement. The pressure measurement transducers are manufactured at the Suffield Experimental Station.

The sensing element would be placed in a metal disk which would be faced toward the blast so that it would cause minimum wave interference. These disks will be placed at three elevations on the side of the tower; therefore, they would not interfere with the pressure front hitting the tower. A sketch of the pressure transducer locations is shown in Fig. 12. The data acquisition system is now being chosen.

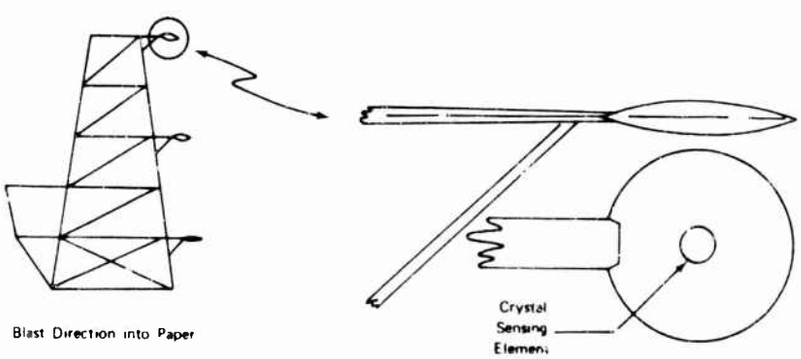

Fig. 12. Location of pressure transducers

The requirements are: (a) it must be capable of recording 33 channels of data, and (b) it must be capable of resolving frequencies up to approximately 200 cps.

An end-to-end mechanical calibration will be performed for the antenna mast structure prior to the test. This calibration will be conducted following the installation of all instrumentation and recording equipment. It is not intended that this calibration take the place of the electrical shunt calibration but that it complement the latter. The purpose of the mechanical calibration is to evaluate the strain gage installation under loading conditions, to evaluate the static load distribution in the structure, and to define the dynamic response, frequencies, and mode shapes of the antenna mast structures.

The type of calibration proposed is by use of a twang test. A static horizontal load will be applied to the structure in the direction of the blast pressure propagation. The load will be applied simultaneously to four joints near the top of the structure. The load application will be accomplished with hydraulic cylinders with wire rope slings attached to structural joints. The magnitude of load utilized will be less than 25 percent of the maximum anticipated load resulting from the blast; the load will not exceed the maximum anticipated load at each of the four joints. After the desired static load is achieved, the load will be released with a quick release mechanism located in the wire rope, allowing the tower to oscillate at its true damped natural frequency. An estimate of the fundamental mode frequency and structural damping will be obtained from this test.

SUMMARY

It is concluded that, on the basis of technical accuracy (recognizing the wide variation in structural and inertial properties of such structures), a separate three-dimensional computer study is required to verify each particular design. Further, it is shown that the field test environment should represent a reasonable operational simulation even with the presence of a more flexible foundation and the associated ground shock effects.

The final phases of this program will include the aforementioned field test; data acquisition, analysis, and correlation with the analytics; and recommendations of preliminary design rules for future structures of this type. It is felt that the successful culmination of this program should yield a significant advance in the state of the art relative to the design of open-frame-type structures subject to air blast or even wind gusts.

NOMENCLATURE

Symbol	Unit	Description
P_{so}	lb/in.^{2}	Overpressure
p_0	lb/in.^{2}	Atmospheric pressure
q_{do}	lb/in.^{2}	Drag overpressure
c	ft/sec	Sonic velocity
U	ft/sec	Velocity of shock front
t	sec	Time
D	ft or in.	Outside diameter of structural member
t_D	sec	Duration time
t_{ar}	sec	Time of arrival (measured from instant of detonation) of shock front at a given location
$q(t)$	lb/in.^{2}	Time-dependent drag overpressure
C_D	None	Member drag coefficient
A_{PM}	in.^{2} or ft^2	Member projected area
F_M	lb	Member drag load
F_S	lb	Structure drag load
P_{SA}	lb	Side antenna drag load
A_A	in.^{2} or ft^2	Projected area of side antenna
C_S	ft/sec	Seismic velocity of soil
P_{max}	lb	Maximum member axial load
M_{max}	in.-lb	Maximum member bending moment
f_{max}	lb/in.^{2}	Maximum member stress
f_{cw}	lb/in.^{2}	Maximum member compressive stress
f_{bw}	lb/in.^{2}	Maximum member bending stress

Symbol	Unit	Description
f_c	lb/in.^{2}	Member allowable compressive stress
f_b	lb/in.^{2}	Member allowable bending stress
r_c	None	f_{cw} f_c
r_b	None	f_{bw} f_b
FS	None	Member factor of safety against failure by buckling
Z	in.^{3}	Section modulus

ACKNOWLEDGMENT

Acknowledgment of the Royal Canadian Navy and Suffield Experimental Station is hereby given for the contract awarded. Acknowledgment is also given to Robert Geminder and Robert J. Bartholomew of Mechanics Research, Inc., for their technical support.

REFERENCES

1. Samuel Glasstone (Ed.), The Effects of Nuclear Weapons (United States Atomic Energy Commission, Washington), 1957
2. N. M. Newmark and J. D. Haltiwanger, "Principles and Practices for Design of Hardened Structures," Air Force Tech. Documentary Rept. AFSWC-TDR-62-138, Dec. 1962
3. Reino Niemi and Richard Rabenau, "Blast Effects on Space Vehicle Structures," NASA TN D-2945, Feb. 1966
4. C. H. H. Diehl and G. H. S. Jones, "A Preliminary Soil Survey for Distant Plain 6 and the 1968 Trial," Suffield Experimental Station SP 62, DRB Project Nos. D53-95-11-69 and D53-16-01-28, Dec. 1966
5. A. D. Ree, Zelman, and D. F. Coates, "Unlined Tunnel Failures from Ground Shock - Appendix: Soil Tests and Seismic Velocities," RCAF Experiment, Operation Snowball, Dec. 1964
6. Nelson Edward Funston, "The Vibration of Foundations with Various Types of Subgrade Support," unpublished thesis, University of Illinois, 1966

BIBLIOGRAPHY

American Society of Civil Engineers, "Design of Structures to Resist Nuclear Weapons Effects," ASCE Manual 42 (ASCE, New York), 1961

Appendix

DYNAMIC RESPONSE TECHNIQUE

The DYNRE-I program was used for calculation of dynamic responses. DYNRE-I is a digital computer program designed to analyze the time-dependent response of linear elastic structural models subjected to dynamic loadings. The normal mode method is employed to obtain the results.

The user has two options for determination of the time points for which the structural responses will be calculated:

1. He may specify the points by his own estimations.

2. He may specify a time interval and allow the program to examine the modal responses calculated over the interval and then predict the critical time points.

The dynamic loading conditions are specified as a spatial load vector and an associated time history. Several sets of load vectors and time histories may be imposed simultaneously to represent complex loadings.

The elements of the spatial load vectors must be compatible with the elements of the input modal columns. For example, if the structure has six degrees of freedom per joint represented as displacements or rotations in the x_1, x_2, x_3, θ_1, θ_2, and θ_3 directions, respectively, and the expanded eigenvectors are input, then element 1 of the load vector would

represent a force at joint 1 in the x_1 direction, element 2 a force at joint 1 in the x_2 direction, and so on.

The number of degrees of freedom allowed is 300. These may be either unrestrained or restrained, provided that 300 is not exceeded in either case. The number of unrestrained degrees of freedom is defined as (the number of modes) × (the number of degrees of freedom per mode) and the number of restrained degrees of freedom is defined as (the number of unrestrained degrees of freedom) - (the number of restraints).

The program has capacity for 150 eigenvectors (modal columns), 300 time forcing functions, and 100 time points.

Each joint or node on the structure may have six degrees of freedom: namely, linear motion in the x_1, x_2, and x_3 direction and rotations about the x_1, x_2, and x_3 axes. If each degree of freedom is considered to be a "coordinate," then the structure can be said to have (6 × number of joints) coordinates or degrees of freedom. (Note that some structure types have only three available motions per joint.) Next, consider the motions 1 through 6 of joint 1 as the first six coordinates, the motions of joint 2 as 7 through 12, and so on, thus developing the system coordinate number scheme.

The primary advantage of the normal mode method lies in the fact that the differential equations of motion are decoupled when the displacements are expressed in terms of the normal modes. Thus, the solution may be obtained by dealing with independent differential equations rather than a set of simultaneous differential equations.

For the rth normal mode, the decoupled equation of motion is:

$$\ddot{\eta}_r + 2\beta\dot{\eta}_r + \omega_r^2 \eta_r = \frac{N_r}{M_r} , \qquad \text{(A-1)}$$

where η_r, $\dot{\eta}_r$, and $\ddot{\eta}_r$ are the modal displacement, velocity, and acceleration, respectively, of the rth normal coordinate, the term 2β is the proportional damping term, ω_r is the rth natural frequency in radians per second, N_r is the rth generalized force, and M_r is the rth generalized mass.

The generalized force, N_r, may also be defined as follows:

$$N_r = \sum_k \{\varphi^r\}^T \{F_k\} f_k(t) , \qquad \text{(A-2)}$$

where $\{\varphi^r\}$ is the rth modal column (eigenvector), $\{F_k\}$ is the kth spatial load vector (loads applied at the mass points), and $f_k(t)$ is the kth time forcing function.

Substitution of Eq. (A-2) into (A-1) yields:

$$\ddot{\eta}_r + 2\beta\dot{\eta}_r + \omega_r^2 \eta_r = \sum_k \frac{\{\varphi^r\}^T \{F_k\} f_k(t)}{M_r} \qquad \text{(A-3)}$$

The solution to Eq. (A-3) for $\eta_r(t)$ takes the form:

$$\eta_r(t) = \sum_k \frac{\{\varphi^r\}^T \{F_k\} D_{rk}(t)}{\omega_r^2 M_r} , \qquad \text{(A-4)}$$

where

$$D_{rk}(t) = \int_0^t \frac{\omega_r^2}{\sqrt{\omega_r^2 - \beta^2}} e^{-\beta(t-\tau)} \times \sin\left[\sqrt{\omega_r^2 - \beta^2}\,(t-\tau)\right] f_k(\tau)\, d\tau . \qquad \text{(A-5)}$$

Equation (A-5) may be differentiated to arrive at the expressions for velocity and acceleration:

$$\dot{\eta}_r(t) = \sum_k \frac{\{\varphi^r\}^T \{F_k\}}{\omega_r^2 M_r} \left[D^*_{rk}(t) - \beta D_{rk}(t)\right] . \qquad \text{(A-6)}$$

and

$$\ddot{\eta}_r(t) = \sum_k \frac{\{\varphi^r\}^T \{F_k\}}{\omega_r^2 M_r} \left[-(\omega_r^2 - 2\beta^2) D_{rk}(t) - 2\beta D^*_{rk}(t) + \omega_r^2 f_k(t)\right] \qquad \text{(A-7)}$$

where

$$D^*_{rk}(t) = \int_0^t \omega_r^2 e^{-\beta(t-\tau)} \times \cos\left[\sqrt{\omega_r^2 - \beta^2}\,(t-\tau)\right] f_k(\tau)\, d\tau . \qquad \text{(A-8)}$$

The system coordinate responses are then computed by the following equations:

$$\{x(t)\} = \sum_r \{\varphi^r\}\, \eta_r(t) . \qquad \text{(A-9)}$$

$$\{\dot{x}(t)\} = \sum_r \{\varphi^r\}\, \dot{\eta}_r(t) . \qquad \text{(A-10)}$$

$$\{\ddot{x}(t)\} = \sum_{r} \{\phi^{r}\} F_{r}(t) \qquad \text{(A-11)}$$

The joint forces are computed using the modal acceleration technique. The force acting on the jth joint of the structure in the kth direction of motion is computed using the following equation for each specific time t:

$$P(t)(j,k) = \sum_{i=1}^{NF} F(t)(j,k) - \sum_{m=1}^{NM} m_{(j,k)} \ddot{x}(t)_{(j,k,m)} \qquad \text{(A-12)}$$

where NF is the number of forcing function components and NM is the number of modes entered.

DISCUSSION

Mr. Dzialo (University of Massachusetts): You mentioned in your paper that you carry the program to 192 degrees of freedom and you make use of normal mode theory. How reliable are your modes, let's say after the 50th or 30th? How many significant numbers do you usually use to really make the problem practical?

Mr. Anderson: That is a difficult question. We consider the zone of interest as far as major structural responses as somewhere between zero and 200 Hz. We haven't really considered that the responses outside that range are important. They may well be and maybe we'll so find from our test. We will have the ability to go back, remodel the structure, include more degrees of freedom, and possibly go to a larger extent than the mode shapes and frequencies. That is why we are testing.

Mr. McCalley (General Electric Co.): Would you comment on the various eigenvalue routines you used? Which one do you prefer and why?

Mr. Anderson: We prefer the inverse iteration technique. It is a new one. It has not been published. I will be glad to talk with you about it later.

Mr. McCalley: Could you say just a few words about it? Are you adjusting the mode shape, substituting in, or what?

Mr. Anderson: Basically we are limiting ourselves to a band of frequencies. We are guessing a mode shape and frequency and we are iterating in on that zone.

Mr. Gibbonet (Martin-Marietta Corp.): Could you comment as to what the lowest frequency was and about how many modes you used?

Mr. Anderson: We used something like 25 or 26 modes. I think the lowest frequency was about 12 or 14 Hz.

Mr. Della Rocca (Gibbs & Cox): Was any consideration given to unsymmetrical sections, such as anvils?

Mr. Anderson: No, the structure is primarily tubing using a joint technique specified by the Royal Canadian Navy. The effect of gussets and things of that nature were not accounted for, other than in the total area of the structure, in computing the total force.

Mr. Della Rocca: Did you have any platforms on the structure at all?

Mr. Anderson: The only platform we had was the one which mounts the simulated side antenna.

Mr. Schell (AF Flight Dynamics Lab.): I believe you mentioned 196 degrees of freedom and you were going to run a twang test to verify this. How many twang tests and from how many different positions do you plan on running before you will be able to verify this model?

Mr. Anderson: I think we should use a sufficient number of twang tests and I would be glad to hear any advice that you may have in that area.

Mr. Kelso (Defense Atomic Support Agency): I would like to make a few comments on the test that Mr. Anderson mentioned. It is called Operation Prairie Flat. It is being conducted by the Suffield Experimental Station, part of the Defence Research Board in Canada in August of '68. Participation by U. S. agencies is being coordinated through DASA.

* * *

ABOLUTE UPPER AND LOWER BOUNDS FOR THE CRITICAL BLAST LOADING ENVIRONMENT OF TARGET ELEMENTS AND SYSTEMS

Eugene Sevin and Walter Filkey
IIT Research Institute
Chicago, Illinois

Mathematical programming formulations are considered for the problem of determining upper and lower bounds on the loading environment capable of causing a prescribed critical response in structures and systems. The formulations will accept as constraints whatever time-varying or gross characteristics are known concerning the loading environment. Bounds on properties of loadings within this class are then ascertained so as to establish that a loading environment exhibiting certain characteristics either "will always" or "can never" generate a critical response. Specific results are prescribed for the upper and lower bounds of impulses that cause (a) a prescribed displacement in a simple viscous linear elastic system, and (b) the rigid body overturning of a block. The loadings considered are characteristic of blast wave loads.

INTRODUCTION

There are numerous situations in which a problem is not the usual one of determining the response of a system to prescribed loading; rather, the loading is sought that can generate a prescribed response. A capability that can perform this "inverse analysis" is useful in identifying post facto the loading environment that caused observed damage and in ascertaining acceptable loadings in vulnerability studies. It is this sort of capability that is considered here. Specifically, this paper deals with the problem of determining upper and lower bounds on the loading environment capable of causing a specified damage level to structures and systems.

The usual approach in the study of critical response of systems involves analyzing the system for increasing intensities of the loading environment until the desired damage level is attained. Each stage of this process requires the complete specification of the time details of the loadings. Often the response is a sensitive function of the loading details which are seldom known with the precision implied by the method of analysis.

The approach adopted here consists of first using whatever loading information is available to define a class of acceptable loading functions. The response problem then is formulated as one of mathematical programming in which the objective function is taken as some desired characteristic of the loading, while the specified damage level and properties of the loading class are introduced as constraints. By maximizing and minimizing the objective function, the upper and lower bounds are deduced for the selected loading characteristic, as are the corresponding particular members of the class of loading functions under consideration that generate the critical response. Thus, it is now known that loading functions belonging to the class and possessing a characteristic property lower than the lower bound can never produce the critical response, whereas those with one higher than the upper bound must always cause the critical response.

The method is applicable to systems described by nonlinear as well as linear equations of motion. High-order linear systems are perfectly acceptable for treatment. In the way of nonlinear systems, particular attention is directed to ones where response modes are those of combined sliding and tipping and where damage is characterized by exceeding either a given level of rotation or translation. In the examples, total impulse is selected as the load characteristic to be either minimized or maximized, according to whether the lower or upper bound is sought.

The critical loading environment problem is closely related to the min-max problem studies reported previously [1-4]. In the min-max problems for a given system, the goal is to find the extreme responses for classes of loading rather than the environment question of seeking the extremum loading characteristics for a given critical response.

THE PROBLEM

Let $\bar{x}$ denote a vector of state variables of interest, such as displacements, velocities, stresses. For example,

$$\bar{x} = \begin{bmatrix} x_1 \\ x_2 \\ x_3 \\ \vdots \\ \dot{x}_1 \\ \dot{x}_2 \\ \dot{x}_3 \\ \vdots \\ \sigma_1 \\ \sigma_2 \\ \sigma_3 \\ \vdots \end{bmatrix}$$

Assume the structure or system can be solved analytically or computationally; that is, the state vector is available as a function of the loading $\bar{q}$. Thus

$$\bar{x} = \bar{f}(\bar{q}, t), \tag{1}$$

where t represents time. Suppose the known properties of the loading function are used to define a class of loadings $\bar{g}(\bar{q}, t)$. Set the loading characteristic to be studied equal to $h(q, t)$.

The problem is twofold. First, we wish to find for all loadings in class $g(q, t)$ the upper bound of the loading characteristic $\bar{h}(q, t)$, such that one (or several) of the state variables belonging to x, say x^*, just reaches its prescribed critical level x^*_{cr}. Then it is known that any other loading within class g with a greater h must surely cause a response greater than the critical one. This can be expressed in mathematical programming terms as

maximize $\bar{h}(\bar{q}, t)$

subject to the constraints

1. $x^* = f^*(\bar{q}, t) \leq x^*_{cr}$, at some t
2. q belongs to the class $\bar{g}(q, t)$
3. other system restrictions, say $d(\bar{x}, \bar{q}, t) \leq 0$.

Second, we seek for loadings belonging to g the lower bound of the loading characteristics $\bar{h}(\bar{q}, t)$, such that certain state variables just reach the critical levels. Any other loading of the class under consideration with a loading characteristic less than the lower bound cannot possibly cause a critical response. This problem statement is identical with the previous one if $\bar{h}(\bar{q}, t)$ is minimized rather than maximized.

A discrete version of the problem will be used in the computational mathematical programming formulation. To this end let

$$\bar{x}_i = \bar{x}[(i-1)\Delta t]; \quad i = 1, 2, \ldots$$

Discrete representations of $\bar{q}, \bar{f}, \bar{h}, \bar{g}, \bar{d}$ are obtained in a similar fashion.

LOADING ENVIRONMENT

Suppose a structure or system is subjected to loading for which only limited local and/or global properties are known. Typically, a time-varying bandwidth within which the imposed loading or rise time of the disturbance must lie might be given with reasonable certainty. Similarly, the duration and upper and lower limits to the total impulse may be prescribed. Perhaps a combination of such classes of disturbances best describes the loading. Fortunately, it is usually a simple matter to derive expressions for the known characteristics of the loading. These expressions become constraints in the formulation developed here.

Consider, for example, a class of loadings defined by a time-varying band and duration (Fig. 1). Then, for some loading q of g,

$$\begin{aligned} Q_i^- \leq q_i \leq Q_i^+ \quad & i = 1, 2, \ldots, N \\ q_i = 0 \quad & i = N+1, \ldots \end{aligned} \tag{2}$$

A representative problem suitable for solution using the formulations developed here would be the determination of upper and lower bounds on total impulse for a structure that

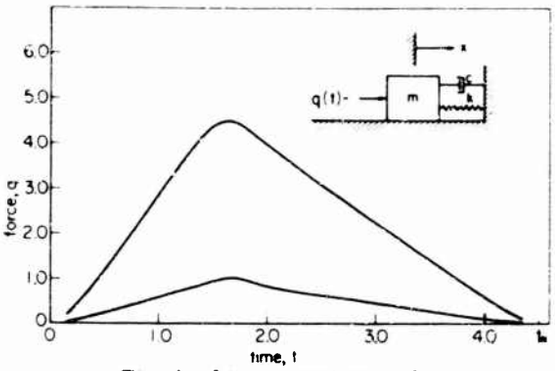

Fig. 1. Linear system and band definition of loading

reaches a critical stress level from a loading lying within a known band. Such problems as the calculation of peak forces that could generate a critical displacement in a system subject to loading with bounded rise times and of known duration and total impulse can also be solved.

COMPUTATIONAL SOLUTION FORMULATIONS

Linear and Nonlinear Programming

Linear and nonlinear programming codes can be used in an attempt to select the set of loading parameters $\bar{q}_i$ which extremize the objective function $\bar{h}(\bar{q}_i, t_i)$ subject to the constraint conditions on $\bar{x}, \bar{g}, \bar{d}$. Linear programming is particularly appropriate for the problem at hand since some codes have been developed that can successfully treat problems with several thousand constraints and variables. Thus, if the objective function and constraints can be expressed as linear functions of the parameters $\bar{q}_i$, very complex problems can be treated.

Linear and nonlinear programming formulations of the critical loading environment problem are easily established. The objective to be minimized or maximized is $\bar{h}(\bar{q}_i, t_i)$. The constraints based on $\bar{g}$ and $\bar{d}$ are clear from their definitions. However, the constraint of the response variable x_i^* reaching its critical level deserves special attention. Frequently, it is evident from the problem situation (the form of h, the type of loading $\bar{g}$) when the variables x_i^* will equal x_{cr}^*. Usually, for the maximization problem this time is of no concern since a loading function is sought that forces x_i^* to x_{cr}^*, and hence the constraint is $x_i^* \leq x_{cr}^*$ for all time (t_i, $i = 1, 2, \ldots, N$). It may be necessary to extend the t_i beyond the duration of a transient pulse to ensure that the critical response level is not violated after the loading terminates.

For the minimization problem, it is not adequate, in general, to find a $\min \bar{h}(\bar{q}_i, t_i)$ such that $x_i^* \leq x_{cr}^*$ for all time, because x_i^* may never reach x_{cr}^*. Recall that the lower bound on $\bar{h}(\bar{q}_i, t_i)$ is sought such that x_i^* just equals x_{cr}^*. In the event it is not obvious beforehand at what t_i the critical level is reached, x_i can be set equal to x_{cr}^* for some $t_i = t_k$ and $x_i^* \leq x_{cr}^*$ for all other time, and the mathematical program should be executed for all possible t_k. The minimum of the resulting set of minimum $\bar{h}$ is then the minimum possible loading characteristic. It is plausible that the critical t_k can occur after the loading is terminated. To limit the computational burden in finding the time and minimum $\bar{h}$ corresponding to x_{cr}^*, it is usually adequate to let $x^* = x_{cr}^*$ for a number of widely spaced t_k and determine the minimum $\bar{h}_{minimum}$, and then, assuming the minimum $\bar{h}$ points exhibited regular behavor, zero into the desired solution using fine increments of t_k near the previously computed minimum $\bar{h}_{minimum}$. Once the mathematical programming solution is found, the trajectories of the response variables that generated the bounding values of $\bar{h}$ can be plotted using the $\bar{q}_i$ determined in the solution.

It is important to emphasize that full-scale dynamic analyses of complicated structures and systems can be coupled to this formulation. For example, a typical response function (stress or displacement) according to normal mode theory for a linear elastic structure takes the form

$$\bar{x}(s,t) = \sum_m A_m(t)\, \bar{x}^m(s) \qquad (3)$$

where $\bar{x}^m$ are the eigenfunctions and s is a spatial coordinate. The loading $\bar{q}$ is contained in the generalized coordinate $A_i(t)$ and is readily discretized to make the problem suitable for linear programming.

In general, the mathematical program used here is not an iterative process involving repeated dynamic analyses, as it often is in the optimum synthesis of systems. In this formulation, the dynamic analysis need be performed only once.

A simple example illustrates the formulation. Assume a damped spring-mass system is subjected to a loading lying within a known band (Fig. 1). Suppose the upper and lower bounds on the total impulse are sought such that a critical displacement $x^* = x_{cr}^*$ is reached. The loading can be discretized such that the

displacement and total impulse are linear functions of the loading, and, consequently, the upper and lower bound loading environment study becomes a linear programming problem. For example, the displacement for a piecewise constant loading representation is listed in many vibrations texts, while the total impulse is given by

$$h(q,t) = \sum_{i=1}^{N} q_i \Delta t_i .$$

Computations were made, using a linear programming code, for a system with unit mass, unit spring constant, $c/c_{cr} = 0.5$, and $x^*_{cr} = 1$. The upper and lower bounds on the total impulse, in dimensions of force × time, are 3.74 and 2.44, respectively. Thus, any forcing function lying within the loading band with a total impulse greater than 3.74 must displace the system beyond the critical damage level ($x^*_{cr} = 1$), and one with a total impulse less than 2.44 can under no circumstances result in the critical displacement. A forcing function, satisfying the load definition, with a total impulse between 2.44 and 3.74 may or may not generate the critical displacement.

The extremum loading environment study was also performed for the same system in which the restriction that the force fall within the band of Fig. 1 was removed. For a nonnegative force of the same duration, the upper bound on total impulse is 31 percent greater than that for the previous force limited case and the lower bound is 24 percent less than the corresponding minimum total impulse.

The particular forcing functions that generate the upper and lower bounds on total impulse are shown in Figs. 2 and 3. The impulse for the unrestricted force of the lower bound problem (Fig. 3) is not unique in time and could have taken place at any time during the prescribed total time interval $0 \leq t \leq t_N$. The critical displacements that correspond to the forcing functions belonging to the loading class of Fig. 1 are pictured in Fig. 4.

Dynamic Programming

A problem that can be given a linear formulation should be treated by linear programming because of the availability of large-scale efficient codes. One useful approach to the solution of nonlinear problems of low order is dynamic programming. Here the response is discretized in n time-ordered states, called stages, and an optimization process is conducted at each stage.

To exemplify a dynamic programming formulation, consider an unanchored structure that is subjected to blast loading and can undergo both sliding and tipping modes of motion (Fig. 5). A host of intriguing problems with this system can be treated in this manner. We choose a simplified representation [5] of the equations of motion to render an uncomplicated illustration of a dynamic programming formulation.

Let the components of the state vector be

$$\begin{aligned} x_1 &= \theta \\ x_2 &= \dot{\theta} \\ x_3 &= x \\ x_4 &= \dot{x} . \end{aligned} \tag{4}$$

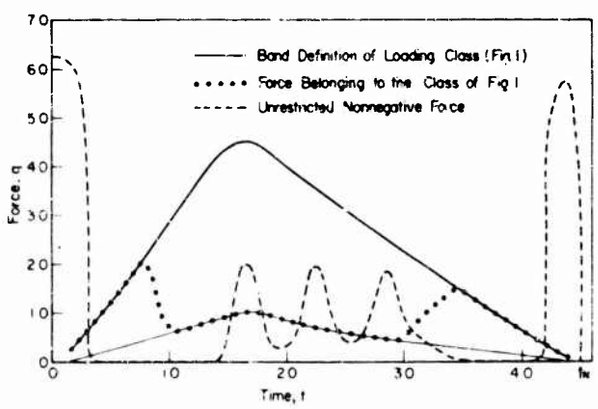

Fig. 2. Loading trajectories that generate the upper bound on total impulse

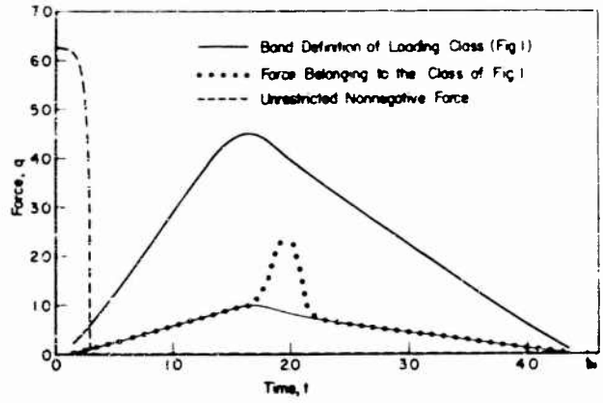

Fig. 3. Loading trajectories that generate the lower bound on total impulse

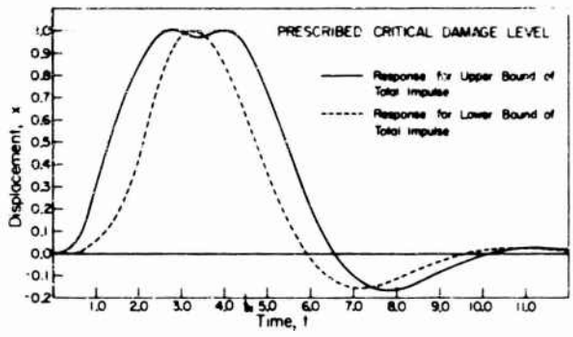

Fig. 4. Displacements corresponding to the loading functions, within the class of Fig. 1, that generated upper and lower bounds on total impulse

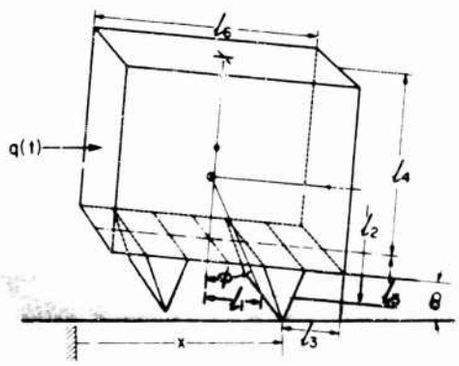

Fig. 5. Sliding and tipping structure

Then the equations of motion are given by the system of first-order differential equations

$$\begin{aligned} \dot{x}_1 &= x_2 \\ \dot{x}_2 &= (A_1A_2 - A_5)\,(A_1A_3 - A_4) \\ \dot{x}_3 &= x_4 \\ \dot{x}_4 &= (A_4A_2 - A_3A_5)\,(A_4 - A_1A_3) \end{aligned} \tag{5}$$

where

$$A_1 = r\cos(\gamma - x_1)$$

$$A_2 = r x_2^2\left[\mu\cos(\gamma - x_1) - \sin(\gamma - x_1)\right] + \frac{q(t) - \mu W}{m}$$

$$A_3 = r\cos(\gamma - x_1) + \mu r\sin(\gamma - x_1)$$

$$A_4 = J/m$$

$$A_5 = \left[q(t)A_6 - Wr\sin(\gamma - x_1)\right]/m$$

$$A_6 = \left(\frac{r_4}{2} + r_5\right)\cos x_1 + \left(\frac{r_6}{2} - r_3\right)\sin x_1$$

$$\therefore \quad \tan^{-1}\left(\frac{r_1}{r_2}\right)$$

J = moment of inertia about the pivot point

μ = coefficient of friction at the pivot

m = mass

W = weight.

Assume the upper and lower bounds are to be sought on the global loading characteristic total impulse I. Consider q(t) belonging to the class of forcing functions

$$0 \le Q^-(t) \le q(t) \le Q^+(t) \tag{6}$$

The problem then is for a loading of type (6) and of duration $T = t_N$:

1. maximize

$$I = \int_0^T q(t)\,dt \tag{7}$$

(the upper bound of I)

2. minimize

$$I = \int_0^T q(t)\,dt \tag{8}$$

(the lower bound of I)

for the critical response level. The loadings q(t) that generate the extreme impulses are also sought.

With

$$t_j = (j-1)\Delta t \quad j = 1, 2, \ldots, N \tag{9}$$

discretize the impulse as

$$I = \sum_{j=1}^{N} I_j \tag{10}$$

The problem now is to select the I_j, that are permissible relative to the constraints, that maximize or minimize I of Eq. (10). That is, find

$$\underset{\{I_j\}}{\text{extreme}} \sum_{j=1}^{N} I_j \tag{11}$$

such that loading constraints (Eq. (6)) are satisfied and the critical response level, say the block overturning or being displaced a specified distance, is just reached. Here,

$$\underset{\{I_j\}}{\text{extreme}}$$

represents

$$\max_{\{I_j\}} \text{ or } \min_{\{I_j\}},$$

and the symbology $\{I_j\}$ indicates that the extreme value of I is taken over the totality of admissible I_j, $j = 1, 2, \ldots, N$.

The essential ingredient of dynamic programming theory is the principle of optimality [6]. Application of this principle to Eq. (11) gives

$$\underset{\{I_j\}}{\text{extreme}} \sum_{j=1}^{N} I_j = \underset{\{I_j\}}{\text{extreme}} \left\{ I_1 + \underset{\{I_j\}}{\text{extreme}} \sum_{j=2}^{N} I_j \right\} \tag{12}$$

Computationally, a recursive procedure

$$\underset{\{I_j\}}{\text{extreme}} \sum_{j=k}^{N} I_j = \underset{\{I_j\}}{\text{extreme}} \left\{ I_k + \underset{\{I_j\}}{\text{extreme}} \sum_{j=k+1}^{N} I_j \right\} \tag{13}$$

is executed for $k = N, N-1, \ldots, 1$ with

$$\underset{\{I_j\}}{\text{extreme}} \sum_{j=N+1}^{N} I_j = 0 \tag{14}$$

This chronological stage-by-stage optimization must be conducted such that the forcing constraints (Eq. (6)) are not violated at each stage and such that the critical damage criterion is satisfied. The state of the system at any stage is related to the state at the previous stage by the solution of Eq. (5):

$$x_{j+1} = F(x_j, I_j) \tag{15}$$

To study in detail this dynamic programming formulation of the extremum critical loading environment problem, consider a block that can undergo only tipping. Equations (5) reduce to

$$\dot{x}_1 = x_2$$
$$\dot{x}_2 = \frac{q(t)}{J} A_6 - \frac{Wr}{J} \sin(\cdot - x_1) \quad (16)$$

that is,

$$J\ddot{\cdot} + Wr \sin(\cdot - \cdot) = q(t) A_6 \quad (17)$$

The loading can be discretized in almost any manner suggested by the nature of the class of loading functions. Choose, for simplicity, a sequence of impulse functions representation. That is,

$$q(t) = \sum_{j=1}^{N} I_j \cdot (t - t_j) \quad (18)$$

where $\cdot(t - t_j)$ is the Dirac delta function.

We wish to perform the stage-by-stage optimization indicated by Eq. (13). The admissible range of I_j is defined by Eq. (6), say

$$I_j^- \le I_j \le I_j^+ \quad (19)$$

and by the critical damage level of a given rotation, say just overturning. Values for this latter constraint can be obtained for most systems numerically from the equations of motion; in the case of the overturning block it can be found analytically. At any stage j the change in velocity because of an increment of the impulse I_j is found by integrating in time the second of Eq. (16) from t_j^- to t_j^+. Thus,

$$\int_{t_j^-}^{t_j^+} \dot{x}_2 dt = \Delta x_2 = \int_{t_j^-}^{t_j^+} \frac{q(t)}{J} A_6 dt - \int_{t_j^-}^{t_j^+} \frac{Wr}{J} \sin(\cdot - x_1) dt \quad (20)$$

Then, since $(x_1^+)_j = (x_1^-)_j$,

$$(x_2)_j^+ - (x_2)_j^- = I_j \frac{A_6(x_1)_j}{J} \quad (21)$$

or

$$\dot{\cdot}_j - \dot{\cdot}_j = \frac{I_j A_6(\cdot_j)}{J} \quad (22)$$

Certainly, it is to be expected that at a given angle of tipping there is a corresponding velocity that will just result in the block overturning from free motion. To find this velocity, integrate the homogeneous form of Eq. (16) for the interval $t_j < t \le t_{j+1}$:

$$\frac{1}{2} \dot{\cdot}^2 \Big|_{\dot{\cdot}_j}^{\dot{\cdot}_{j+1}} + \frac{Wr}{J} \cos(\cdot - \cdot) \Big|_{\cdot_j}^{\cdot_{j+1}} = 0 \quad (23)$$

or

$$(\dot{\cdot}_{j+1})^2 - (\dot{\cdot}_j)^2 = \frac{2Wr}{J} \left[\cos(\cdot - \cdot_j) - \cos(\cdot - \cdot_{j+1})\right] \quad (24)$$

Consider the critical rotation level with $\cdot_{j+1} = \cdot$ and $\dot{\cdot}_{j+1} = 0$. Then, it is clear that for any angle $\cdot_j$, the corresponding velocity must be equal to or less than

$$\sqrt{\frac{2WR}{J}\left[1 - \cos(\cdot - \cdot_j)\right]}$$

to ensure that the block does not overturn. That is,

$$\dot{\cdot}_j \le \sqrt{\frac{2Wr}{J}\left[1 - \cos(\cdot - \cdot_j)\right]} \quad (25)$$

The desired admissible values of I_j, as defined by the critical damage level criterion, are obtained from Eqs. (25) and (22) as

$$0 \le I_j \le \frac{J}{A_6(\cdot_j)} \sqrt{\frac{2Wr}{J}\left[1 - \cos(\cdot - \cdot_j)\right]} - \dot{\cdot}_j \quad (26)$$

The dynamic programming solution using Eq. (13) can now proceed in the usual fashion [3]. Care must be used in handling the constraints on I_j (Eqs. (26) and (19)): not only must a combined constraint be defined on the basis of the overlapping of these two relations, but it is possible to be faced with a poorly posed problem if the constraints do not overlap at all. In the minimization problem, the dynamic program must be written such that the block is forced to reach the critical level at some time in the response. This requirement is, of course, achieved automatically when the total impulse is maximized.

The formulation for the overturning block was programmed. The results in Fig. 6 were computed for a block, with $\cdot_1$ = 3.5 ft, $\cdot_2$ = 2.25 ft, $\cdot_3$ = 0 ft, $\cdot_4$ = 5 ft, $\cdot_5$ = 1 ft, $\cdot_6$ = 7.3 ft, W = 5000 lb, J = 3523 slug ft^2. Loading classifications considered are nonnegative forcing functions with and without prescribed bounds. Loadings belonging to these categories with total impulse greater (less) than the upper (lower bound will (will never) overturn the block.

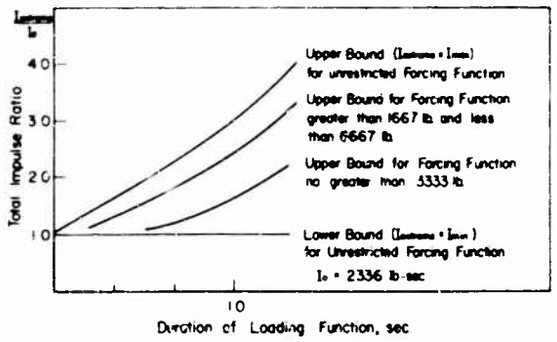

Fig. 6. Upper and lower bounds on total impulse for overturning structure

CONCLUSIONS

It is shown that the problem of determining upper and lower bounds on the critical loading environment on a structure or system can be formulated as a mathematical programming problem. The formulation begins with the definition of critical damage in terms of response variables and the selection of a class of loading functions based on available information. Upper and lower bounds on characteristics of the loadings within the class that always or never cause the critical response are found.

Systems and structures that can be studied with linear analyses are suitable for coupling to available large-scale linear programming codes. The formulation is independent of the complexity of the analysis and requires the dynamic analysis to be made only once. Thus, realistic high-order system and structural representations can be subjected to this loading environment analysis. Nonlinear systems can be treated either by nonlinear optimization codes or by dynamic programming and hence are limited in order because of computational burdens.

REFERENCES

1. E. Sevin, "Min-Max Solutions for the Linear Mass-Spring System," J. Appl. Mech., 24: 131 (1957)

2. T. Liber and E. Sevin, "Optimum Shock Isolation Synthesis," Shock and Vibration Bull., No. 35, Part 5, pp. 203-214, Feb. 1966

3. E. Sevin and W. Pilkey, "Computational Approaches to the Min-Max Response of Dynamic Systems with Incompletely Prescribed Input Functions," J. Appl. Mech., 34:87 (1967)

4. E. Sevin and W. Pilkey, "Min-Max Response Problems of Dynamic Systems and Computational Solution Techniques," Shock and Vibration Bull., No. 36, Part 5, pp. 69-76, Jan. 1967

5. C. E. Gebhart, "Effects of Sliding on the Blast Loads Required to Overturn Structures," Shock and Vibration Bull., No. 37, Part 4, Jan. 1968

6. R. E. Bellman and S. E. Dreyfus, Applied Dynamic Programming (Princeton University Press, N.J.), 1962

* * *

ELASTIC-PLASTIC COLLAPSE OF STRUCTURES SUBJECTED TO A BLAST PULSE*

Walter B. Murfin
Sandia Corporation
Albuquerque, New Mexico

A finite difference method is used to analyze the elastic-plastic, large deflection response of shell structures to blast loading. It is shown that, although the usual design methods are adequate for some conditions, they may be over-conservative under other conditions. When the shell structure is surrounded by an elastic medium, elementary design methods are grossly conservative.

INTRODUCTION

The dynamic response of shell structures subjected to blast has been frequently treated in the elastic regime. The present investigation is concerned largely with the response of such structures undergoing large plastic deflections. Also of concern is the interaction of the structure and a surrounding medium.

Forrestal and Duffey [1] have shown that the elastic response of shell structures in an elastic medium is very much reduced from the free air response. It was expected that the energy absorption in yielding would permit structures to withstand even higher blast loads.

Unfortunately, consideration of yielding and large deformation precludes a rigorous analytical method. However, Wittmer [2,3] and Balmer [4] have shown that a finite difference analysis can be applied to problems of this type.

SYMBOLS

c Sound speed (in./sec)

E Young's modulus (psi)

h Shell thickness (in.)

M_1 Meridional moment (lb-in./in.)

M_2 Circumferential moment (lb-in./in.)

N_1 Meridional stress resultant (lb/in.)

N_2 Circumferential stress resultant (lb/in.)

P Pressure (psi)

Q Shear resultant (lb/in.)

R Radius of shell (in.)

r, z Cartesian coordinates

s Length along shell

t Time (sec)

V Particle velocity (in./sec)

w Generalized displacement

Δ Geometric increment

Temporal increment

Strain

Angle of inclination of element

Density ($lb/sec^2/in.^4$)

Curvature

Stress (psi)

$_y$ Yield stress (psi)

*This work was supported by the United States Atomic Energy Commission.

SHELL ANALYSIS

Two basic types of structures have been analyzed: (a) a spherical shell, with various conditions of support and stiffening (typical of a gas storage tank); and (b) a semicylindrical shell panel with fixed longitudinal edges (typical of a quonset structure).

The analysis of the spherical shell is outlined below. The cylindrical shell, because of axial uniformity, is approximated by a ring. The analysis is similar to that for the sphere, but much simpler.

Consider the shell element shown in Fig. 1. The equilibrium equations are

$$\rho h\ddot{r} = \frac{\partial(N_1 \cos\varphi)}{\partial s} - \frac{\partial(Q \sin\varphi)}{\partial s} - \frac{N_2}{r} - P \sin\varphi ,$$

$$\rho h\ddot{z} = \frac{\partial(N_1 \sin\varphi)}{\partial s} + \frac{\partial(Q \cos\varphi)}{\partial s} + P \cos\varphi ,$$

and (ignoring rotatory inertia),

$$Qr = \frac{\partial(M_1 r)}{\partial s} - M_2 \cos\varphi .$$

Using a finite difference representation as shown in Fig. 2, where $N_{1,i}$ and Q_i are centered at $i-(1/2)$, and $N_{2,i}$ and M_i are centered at i, these equations can be replaced by a set of three algebraic equations for each mass point:

$$m_i\ddot{r}_i = N_{1,i+1}\bar{r}_{i+1}\cos\varphi_{i+1} - N_{1,i}\bar{r}_i\cos\varphi_i - Q_{i+1}\bar{r}_{i+1}\sin\varphi_{i+1} + Q_i\bar{r}_i\sin\varphi_i - N_{2,i}\Delta s - P\overline{\Delta s}\,(\sin\varphi_i + \sin\varphi_{i+1})/2 .$$

$$m_i\ddot{z} = N_{1,i+1}\bar{r}_{i+1}\sin\varphi_{i+1} - N_{1,i}\bar{r}_i\sin\varphi_i + Q_{i+1}\bar{r}_{i+1}\cos\varphi_{i+1} - Q_{\theta i}\bar{r}_i\cos\varphi_i + P\overline{\Delta s}\,(\cos\varphi_i + \cos\varphi_{i+1})/2 .$$

and

$$M_{1,i}r_{i,0} - M_{1,i-1}r_{i-1,0} = M_2\Delta s\cos\varphi_i - Q_i\bar{r}_i\Delta s_i .$$

Accelerations and displacements are centered at the end of each time interval; velocities are centered at the midpoint of each interval (Fig. 3).

The quantity Δw^j (the increment of displacement during the jth interval) is obviously:

$$\Delta w^j = \dot{w}^{j-1/2}\Delta t$$

and

$$\Delta w^{j+1} = \dot{w}^{j+1/2}\Delta t .$$

Furthermore,

$$\dot{w}^{j+1/2} = \dot{w}^{j-1/2} + \ddot{w}^j\Delta t .$$

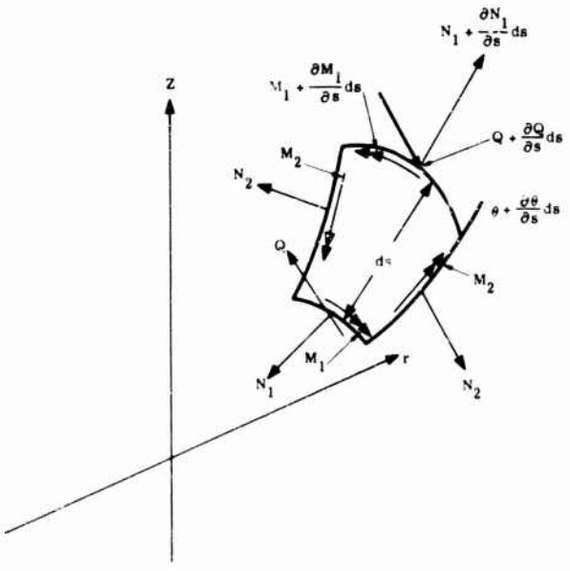

Fig. 1. Shell element

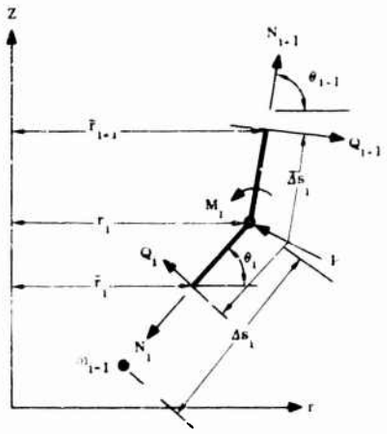

Fig. 2. Finite representation of shell element

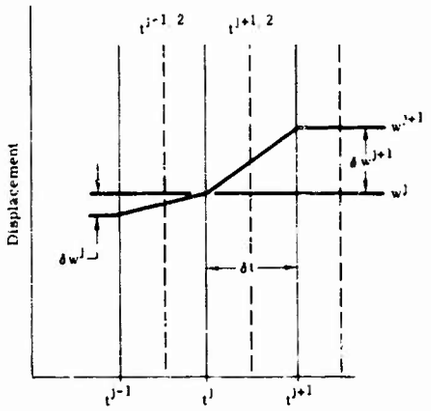

Fig. 3. Time differencing

Multiplying by Δt, we have

$$\Delta w^{j+1} = \Delta w^{j} + \ddot{w}^{j}(\Delta t)^2$$

The normal strain rates in the ith link are [5]

$$\dot{\lambda}_{1,i} = \left\{(\dot{r}_i - \dot{r}_{i-1})\cos\theta_i + (\dot{z}_i - \dot{z}_{i-1})\sin\theta_i + \dot{\theta}_i\left[-(z_i - z_{i-1})\cos\theta_i + (r_i - r_{i-1})\sin\theta_i\right]\right\}\frac{1}{\Delta s}$$

and

$$\dot{\lambda}_{2,i} = \frac{\dot{r}_i}{r_{i,0}}$$

where $r_{i,0}$ is the original radius to the ith mass point. The rates of change of curvature are

$$\dot{\lambda}_{1,i} = \frac{(\dot{\theta}_{i+1} - \dot{\theta}_i)}{\Delta s}$$

and

$$\dot{\lambda}_{2,i} = \frac{d}{dt}\left(\frac{\sin\theta_i}{r_{i,0}}\right)$$

Using these strain rates, we compute the increments of strain during the time interval: $\Delta\varepsilon = \dot{\varepsilon}\Delta t$.

The constitutive relation used is shown in Fig. 4. The stress-strain law is anisotropic, but is believed superior to the kinematically translating hardening law of Ref. [2]. The Von Mises-Hencky yield criterion, the Prandtl-Reuss flow law, and the Symonds-Ting strain-rate rule are used.

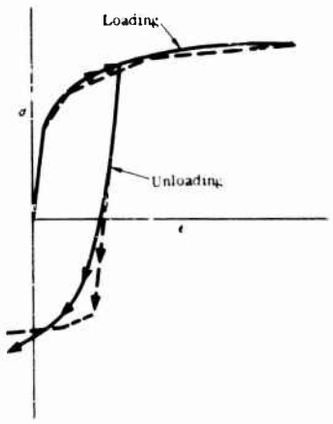

Fig. 4. Stress-strain behavior: actual (solid line) and computer model (dashed line)

BLAST MODEL

It was realized that a rather detailed model of blast interaction would be required. However, since only general effects rather than specific strength of structures was required for this analysis, the model of Glasstone [6] was used in all blast regimes. This model is not adequate for incident overpressures in excess of 25 psi, and it should be pointed out that although the general conclusions of this analysis are believed correct, the strength of specific structures is not accurately given for higher blast strengths. Recognizing that reflected pressures

decay more rapidly on a sphere than on a cylinder, the times for this decay given in Ref. [6] were shortened by a factor of 4. Whether or not this factor is correct should have little influence on the general trends shown.

ANALYSIS OF STRUCTURES

The designer of a structure intended to withstand blast is faced with a number of choices. He can design the structure for incident overpressure, which is usually unconservative. He can design for normal reflected overpressures; such a design may often be overconservative, but is more reliable than is a design based on incident pressure. Figures 5 and 6 show the required thicknesses of representative fixed cylindrical panels and free spheres vs incident overpressure, where the design is based on normal reflected overpressure uniformly applied to the structure. Elementary formulas were used for these curves. Also shown on Figs. 5 and 6 are some failure points using the finite difference analysis (failure has been defined as permanent deformation exceeding 10 percent of the radius). It is seen that the quonset structure follows the theoretical curves well, but that it is difficult to fail unsupported spheres by elastic instability. Instability often did occur during failure of the spheres, but was preceded by yielding in every case.

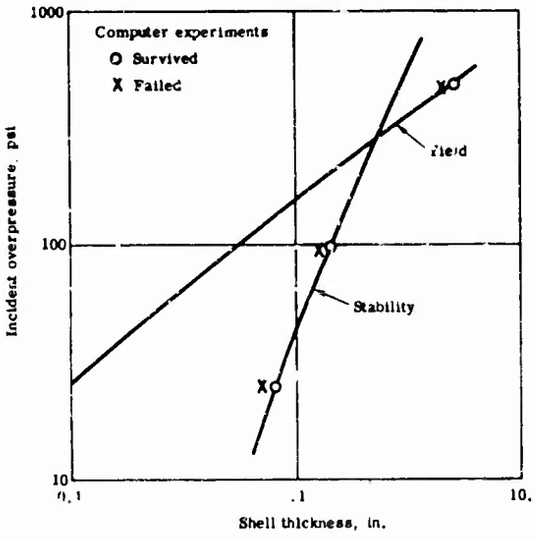

Fig. 5. Semicylindrical panel: free-air failure limits ($R = 50$, $E = 30 \times 10^6$, $\sigma_y = 4.5 \times 10^4$)

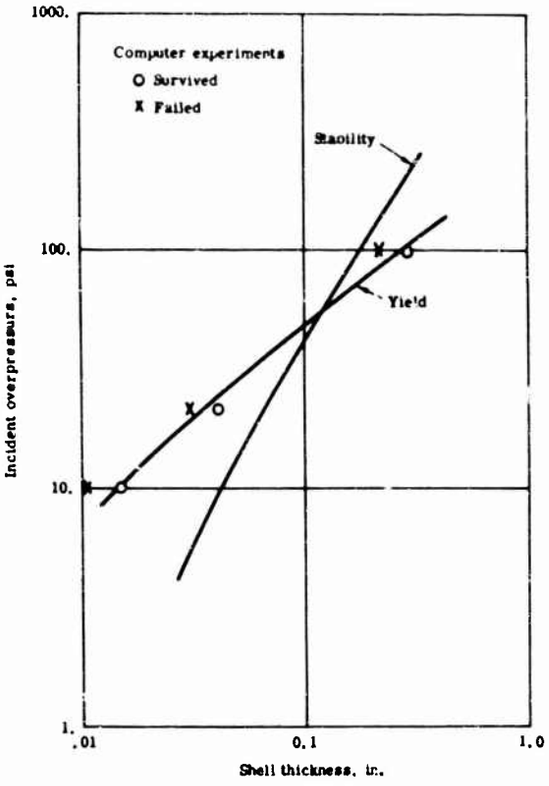

Fig. 6. Unsupported sphere: free-air failure limits ($R = 50$, $E = 30 \times 10^6$, $\sigma_y = 4.5 \times 10^4$)

EFFECTS OF SUPPORT

The failure of spheres supported as in Fig. 7 has also been computed and is shown in Fig. 8. These results show that the supported spheres fail by elastic buckling much as do the cylinders.

Additional support in the form of a very stiff ring has been added to the spheres of Fig. 9. It is seen that this type of support makes little difference in the failure curves. The buckled shape of a typical stiffened sphere is shown in Fig. 10.

Effects of Pulse Length

As might be expected, structures are much stronger for very short pulse durations than for long pulses.

Since normal reflected pressure is the predominant failure determinant, and since the duration of this pressure is determined by the

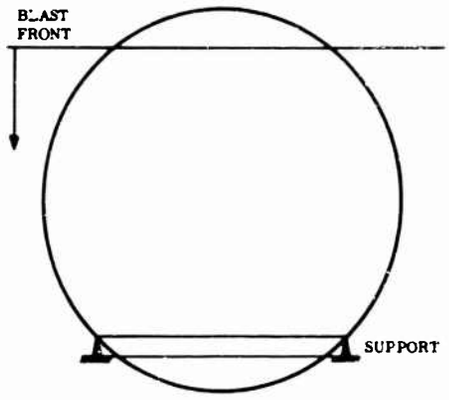

Fig. 7. Supported sphere

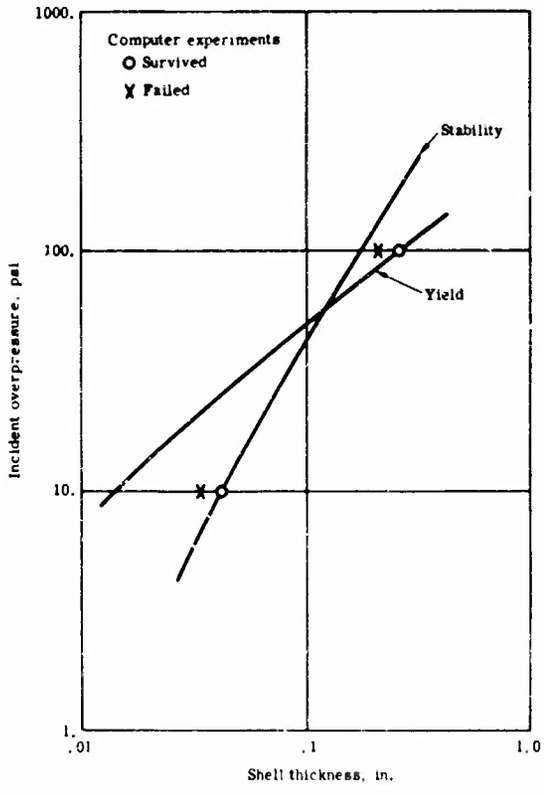

Fig. 8. Supported sphere: free-air failure limits ($R = 50$, $E = 30 \times 10^6$, $\sigma_y = 4.5 \times 10^6$)

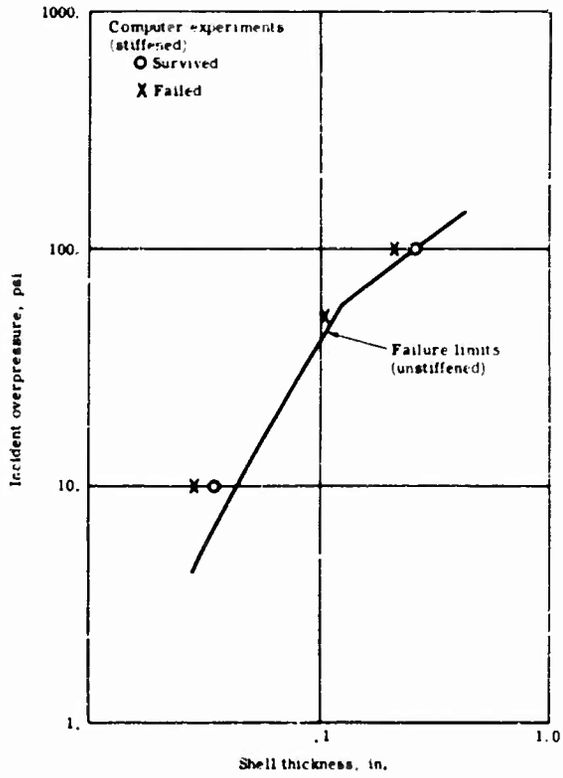

Fig. 9. Supported, stiffened sphere (curve for unstiffened spheres is redrawn from Fig. 8)

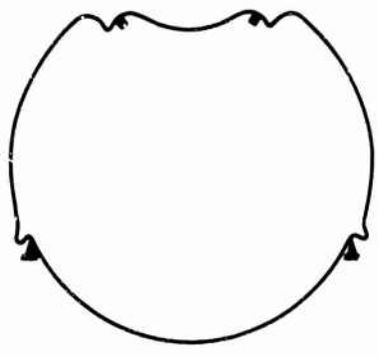

Fig. 10. Supported, stiffened sphere: typical buckled shape

ratio of radius to shock velocity, it was necessary to vary this ratio for meaningful results.

The shock velocity bears a fixed relation to the incident overpressure. However, the present analysis is principally concerned with discovering general trends. The ratio was easily varied by varying shock velocity; the trend is shown, although individual points are unrealistic. The results are indicated in Fig. 11.

In all these calculations, the accelerations of the structure have not been sought. Accelerations may be of concern if sensitive components are located within the structure or attached

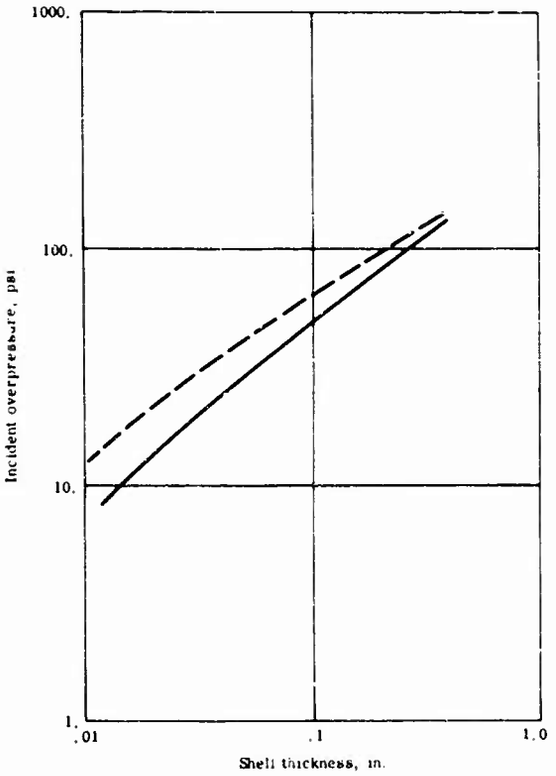

Fig. 11. Unsupported sphere: dependence of failure limit on pulse duration (duration for dashed curve are one-fifth the durations for the solid curve)

to the walls. Because the accelerations are calculated for each element, only a minor change in the computer program is required to have them printed out.

EFFECTS OF AN EXTERNAL MEDIUM

The most dramatic increase in strength has been found by surrounding the structure by a medium, through burial. The model of the medium is quite crude, and a more accurate model would no doubt show somewhat different results. However, the general conclusions are expected to be unchanged.

Measurements of underground soil pressures and particle velocities show that the rise time of an underground pulse is very slow. The pulse shape has been taken as approximating a half sine. It has been assumed that free-field soil particle velocities can be given by $V = P/\rho c$, where P is the free-field stress, ρ is the soil density, and c is the speed of sound (this is actually a function of pressure, but has been taken as constant for simplicity). It has further been assumed that the soil stress wave travels as a purely dilatational wave. Then, if the medium is in contact with the shell, pressure on the shell and local pressure in the medium are equal, and displacement of the medium is adjusted to be equal to the local displacement of the shell. When the shell separates from the medium, however, the pressure becomes zero and the particle velocity of the medium is determined by the free-field pressure and the effect of the free surface.

Three assumptions have been made concerning interactions between the structure and the medium: (a) the pressure on the shell is equal to the free-field pressure; (b) the pressure on the shell is proportional to the local relative displacements of the shell and cavity; and (c) the pressure on the shell is proportional to the local relative particle velocities of the shell and cavity.

It appears that these conditions do not greatly affect the response of the structure. One is thus led to believe that the finer detail of the medium model is of secondary importance.

A number of limitations are inherent in the model. Energy of reradiated waves, shear wave reflections at oblique boundaries, Rayleigh waves on the cavity surface, and plastic flow of the medium are all ignored.

However, subject to these limitations, it has been determined that the strength of medium-surrounded shell structures is many times the free-air strength.

The usual engineering assumption that medium pressures are hydrostatically transmitted to the structure appears to be grossly overconservative. The degree of conservatism cannot be determined without a much more sophisticated soil model (for example, using the TOODY [7] code).

EXPERIMENTAL VERIFICATION

A qualitative verification of the protective effects of a surrounding medium has been secured in a very simple experiment. This experiment was carried out during a test of 50 tons of high explosive at White Sands Missile Range.

Ordinary empty steel beverage cans were emplaced in holes bored in playa soils with and without soil coverage. The collapsing pressure of the cans was calculated to be far less than

either surface overpressures or soil pressures. As expected, all the unburied cans were destroyed (Fig. 12). None of the buried cans exhibited the slightest deformation due to the blast (Fig. 13). The can closest to ground zero should have experienced a soil pressure equal to five times its collapse pressure. Computer runs using the finite difference method for buried and unburied cylinders confirmed these results.

Fig. 12. Typical unburied can

INTERNAL PRESSURIZATION

It has been shown [8] that internal pressure, even at a relatively low value, is very effective in preventing the collapse of spherical shells under acceleration loads. This condition has not been included in the present study, although the computer programs allow its inclusion. It is to be expected that internal pressure would be similarly effective for blast loading.

Fig. 13. Typical buried can

CONCLUSIONS

1. Design of blast-resistant structures based on normal reflected pressure is conservative, especially for unsupported structures or for short pulse lengths.

2. Detailed analyses of the blast and the structure are necessary if a design is not to be overconservative.

3. The resistance of structures surrounded by an elastic medium may be many times the free-air strength, at least in regimes where medium stress is not grossly greater than medium strength.

4. A more sophisticated model of the surrounding medium is required for computation of the true strength of buried structures.

5. Ring stiffening of blast-loaded spherical shells appears to be of little value.

REFERENCES

1. M. J. Forrestal and T. A. Duffey, "Transient Response of Soil-Surrounded Tubes," Sandia Corp. SC-TM-67-565, Aug. 1967

2. E. A. Witner, et al., "Large Dynamic Deformations of Beams, Rings, Plates, and Shells," AIAA J. 1(8):1848 (1963)

3. E. A. Witmer and H. A. Balmer, "Theoretical-Experimental Correlation of Large Dynamic and Permanent Deformations of Impulsively Loaded Simple Structures," Massachusetts Institute of Technology FDL-TDR-64-108, July 1964

4. H. A. Balmer, "Improved Computer Programs-Depross 1, 2, and 3 — To Calculate the Dynamic Elastic Plastic Two-Dimensional Responses of Impulsively-Loaded Beams, Rings, Plates, and Shells of Revolution," Massachusetts Institute of Technology ASRL-TR-128-3, Aug. 1965

5. W. B. Murfin, "Computer Programs for Axisymmetric Impact of Simple Structures," Sandia Corp. SC-TM-67-213, June 1967

6. S. Glasstone (Ed.)., The Effects of Nuclear Weapons (2nd ed.) (U.S. Govt. Printing Office, Washington), 1962. pp. 190-194

7. W. Herrmann and B. J. Thorne, "TOODY, A Computer Program for Calculating Problems of Motion in Two Dimensions," Sandia Corp. SC-RR-66-602, Apr. 1967

8. W. B. Murfin, "Dynamic Collapse of Pressurized Spherical Shells in An Elastic Medium," Sandia Corp. SC-TM-67-320, May 1967

DISCUSSION

Mr. Weissman, Ammann & Whitney: In regard to the previous analysis being conservative, for the buried cylinder beer can, is the capacity greater than what you calculate if the free field loading were just applied uniformly?

Mr. Murfin: No, as a matter of fact if you were to apply the free field environment uniformly you get almost exactly the same collapse pressure. With the reflected pressure coming only on the one line, very close to the facing side, this provides you almost with a predimpling which then leads to further collapse. It turns out that the fact that there is less total load is pretty much balanced by this predimpling.

Mr. Weissman: This is, as you know, an approach that is sometimes used for so-called fully buried arches or cylinders. I was wondering whether it was still too conservative according to your results.

Mr. Murfin: I think that for fully buried arches or cylinders it is very conservative. I would really hesitate to say how much unless I could bet a better soil model.

Mr. Pakstys, GD/Electric Boat: Could you go into the analysis technique? Is this the work that was done at MIT?

Mr. Murfin: Yes, but it has been extended quite a bit.

Mr. Pakstys: Is it only applicable to axisymmetric structures?

Mr. Murfin: Yes. There is some work going on there now which should be applicable to nonaxisymmetrically loaded axisymmetric structures. The codes are quite a bit different from the originals. There are several changes that make them almost unrecognizable.

Mr. Callahan, Black & Veatch: In my experience I've seen some failed structures. I've only seen an outward acting component in the failure and I am quite surprised that your computer does not show that at all.

Mr. Murfin: If the original shapes are plotted, there is a bulge at the equator when there is a "push in" at the pole. It is rather small and does not show up here. I have run some that, instead of just dishing in on one side, are smashed flat with a big bulge at the equator.

Mr. Callahan: This is the type I have normally seen in the field.

* * *

INTERNAL LOADING OF STRUCTURES BY BLAST WAVES*

Joseph F. Melichar
Ballistic Research Laboratories
Aberdeen Proving Ground, Maryland

The internal loading of a structure, created by the impingement of a blast wave on its exterior, is discussed. The expansion of the shock wave into any chamber of the structure and the subsequent inflow of energy and mass that raise the pressure in the interior are described.

A sample structure shows how these aerodynamic processes are related to the loads on internal structural components. The following physical processes are stressed: (a) internal pressure as a pulsating phenomenon whose frequency is a function of the interior's geometry; (b) timing of the pressure pulses as a major factor in determining the loading of the interior; and (c) uneven loading of the internal components because of out-of-phase pressure pulses as a major cause of damage.

INTRODUCTION

The detonation of a large yield weapon or an accidental explosion produces an expanding pressure and flow field. The expanding field, propagated by a blast wave, creates a potentially destructive force on objects with which it interacts. Of particular interest is the interaction with a structure and the resulting loading of its exterior and interior. A structure's ability to withstand the blast environment determines its protective capability as well as its postloading usefulness. This ability to survive is dependent on the balance between internal and external loads as well as on their absolute magnitudes. Similarly, internal substructures are dependent upon the balance and magnitudes of the internal loading.

This paper discusses the internal loading of structures created by the blast wave interaction. As internal loads are dependent on external loads, a brief synopsis of external loads is made. The incident blast wave interacts with the structure to form a complex transient flow field about it. The thermodynamic and aerodynamic properties within this field vary with location; thus, the loading of the structure is a function of position as well as time. For example, a wall facing the blast wave is exposed to reflected and stagnation overpressures which are higher than the "leeward" wall's "side-on" overpressures. These and other situations are discussed in Refs. 1, 2, and 3, which relate the incident blast wave parameters, the geometry of the building, and the position of the structure to the resultant loading. These computed pressure profiles become the input for the internal loading of the structure.

AERODYNAMIC MECHANISMS

The discussion of the internal loading is in two parts; the first describes the aerodynamic processes involved using a two-dimensional room, and the second illustrates how internal loading is evolved from these processes, using a sample structure. The model two-dimensional room has a length greater than its width; its opening to the exterior is on one wall and extends the full height of the room. A step shock wave will be normally reflected from the exterior wall, creating a maximum pressure differential of 13.1 psi between the interior and the exterior. For all pressure differentials below this limit the inflow is subsonic in the opening. Under these conditions the following occur:

1. The incident shock wave expands into and through the chamber.

*Work supported by the Office of Civil Defense.

2. The pressure differential across the access opening generates an inflow into the chamber.

3. The inflow of mass and energy increases the pressure in the chamber.

Although the three mechanisms occur simultaneously, they are discussed separately before being linked together.

The incident shock wave expands after entering the chamber and forms a rarefaction wave system. The rarefaction waves spread inward from the sides of the entrance and interact at the center. As these two wave systems propagate and interact, they weaken the shock front; but as they vary in strength with time, their weakening effect at each point in the flow field varies. This factor, combined with the inflow of mass and energy behind the wave, gives the expanding shock front a variable strength over its surface at any time.

In shadowgraphs of the expansion process [4], the shock wave front appears to have a cylindrical geometry. The strength variation over the front's surface indicates that the shock wave cannot follow the laws of a cylindrical expansion. This seeming contradiction results from the near equality of the wave speeds with the sound speed ahead of the shock wave (for the limited pressure range being considered). Because of this small difference between velocities, the cylindrical approximation does provide a good method for estimating the shock front position-time history, although not its pressure amplitude. The approximation is useful even though the shock reflection process with the side walls of the chamber and can be used to determine the reflection angles, and in turn the reflection factors. The entire wave system propagates through the room, reflects from the rear wall, and propagates back toward the entrance.

An approximation method [5] for determining the position of the shock front can be based on the relationship:

$$P \quad P_0 \left(\frac{R_0}{R}\right)^n .$$

where P and R are pressure and radius, respectively, and the zero subscript represents an initial condition. From experimental results presented in Ref. 4, the exponent n varies in the range 0.7 to 2.0 for a two-dimensional expansion. The value of n is smaller where the inflow is the strongest, as well as later in the expansion after the interaction with the wall occurs. The use of this approximation technique to determine the shock strengths is discussed in Ref. 6.

With the passage of time, the transmitted wave's pressure field decays near the opening, and the pressure differential between the interior and the exterior becomes greater; thus, the inflow increases. An adiabatic expansion brings the inflow from the external pressure to that in the interior. Its momentum causes the flow to continue. The inflow weakens the rarefaction wave system, and in the limit determines the shock front's terminal strength.

The motion of the wave back and forth through the chamber is used as a basis for a stepwise mathematical model [6] for the computation of the chamber's pressure-time history. An inflow of mass and energy is allowed to occur in the mathematical model at the initial pressure differential until the step is terminated by the arrival of the reflected wave. The kinetic energy of the influent mass during the step is then transferred into potential energy, which is distributed equally through the chamber and results in a pressure increase. The new conditions within the chamber determine the inflow for the next step in the process, which produces another increase in the chamber's pressure. The process continues until the chamber pressure rises above the external pressure, at which point the mathematical model is reversed to determine the pressure-time history during the inflow. The mechanics of the motion is similar to that of a resonator; the frequency is a function of the chamber's length and the ambient sound speed.

STRUCTURAL LOADING

In the preceding section, the flow processes dealing with the propagation of blast waves into the interior of buildings were discussed. Prediction techniques based on these processes are discussed in Ref. 6 and are not dwelt upon here. The internal flow processes are used as a common ground from which to discuss how the interior of the structure will be loaded. With respect to the structural loading, only the two pressure-oriented processes, the shock expansion and the filling, are of importance. The inflow, though an integral part of the other two mechanisms, does not directly cause structural damage and hence is not considered further.

Loading is defined as the pressure differential that acts upon a structural member to produce a net force on it. Under this definition

pressure amplitude in itself is not important, but rather the difference in amplitudes opposing each other across the member. In this context the transient nature of blast loading has added significance, in that timing of opposing pressures determines the loads. Although both the shock expansion and the filling load the interior, more emphasis is placed on the higher amplitude filling process. The damage-causing potential of the filling process is enhanced by its resonant characteristics, as seen by variations in chamber frequencies, producing loading variations even though chambers are loaded similarly.

A hypothetical structure is used to discuss the filling process in terms of loading, and also illustrates the effects of chamber resonance. The structure, a multistoried building (Fig. 1), contains the three floors and the basement whose loading will be considered. For this model, the exterior loading is the same on all three above-grade floors being considered. To illustrate how interior loads are generated, the three floors are made up of different-size rooms and exterior openings.

Floor A has many openings around its exterior and no hardened interior walls. Any division of space within floor A is assumed to be of the room divider variety with little or no resistance to the flow and the filling process. Floor B has hardened walls dividing it into four rooms. The lowest floor is undivided, has no exterior openings, and has its ventilation system closed during the blast loading. The basement is undivided and has one opening. Flow is not propagated between floors through the elevator shaft.

The incident wave has a strength of 5-psi overpressure at standard atmospheric sea-level conditions and a duration of 3.3 sec. These conditions [1] occur at a range of 6.8 miles from the detonation at optimum burst height of a weapon of 1-megaton yield. This idealized wave is assumed to interact with the building to produce the pressure-time profiles for the

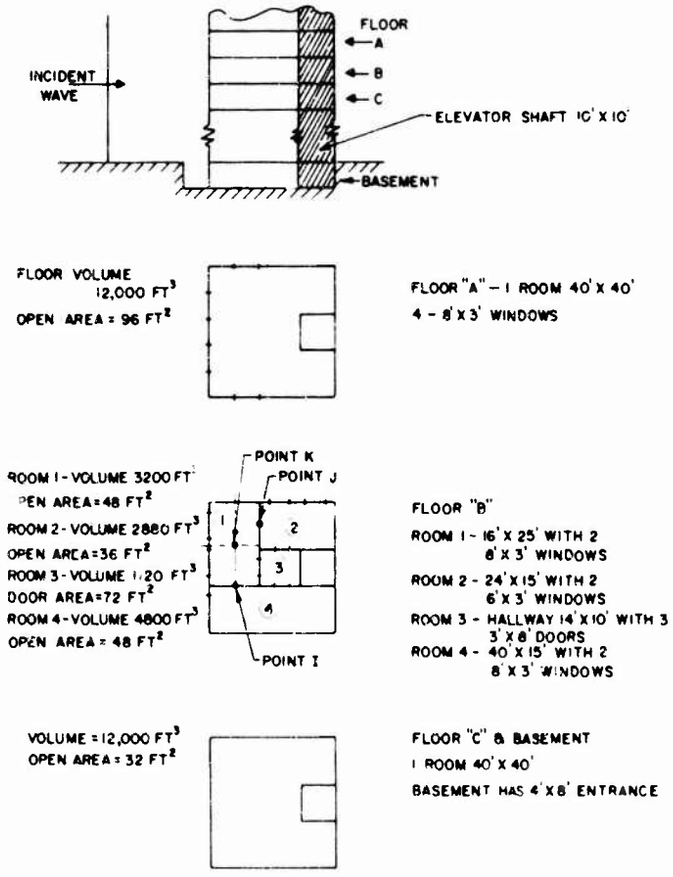

Fig. 1. Model building

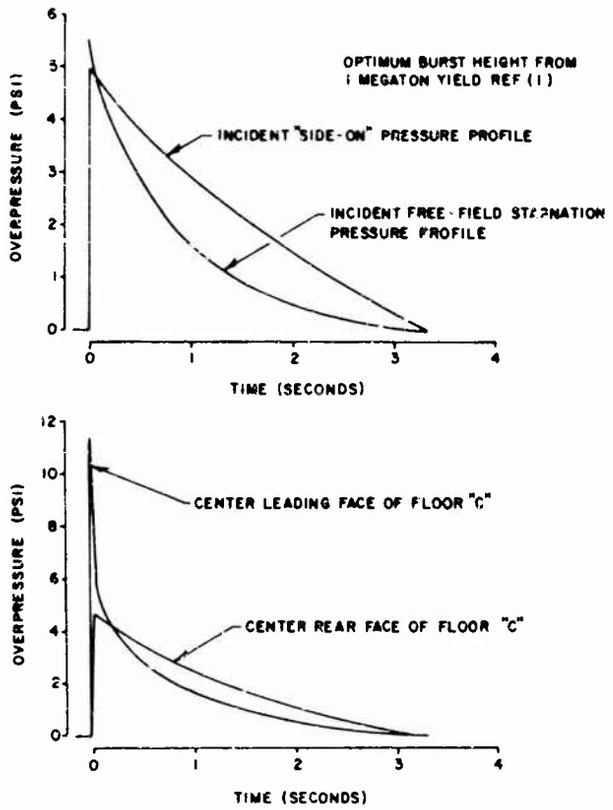

Fig. 2. Representative pressure-time profiles

points on the exterior of floor C shown in Fig. 2. These profiles are averages, and variations would occur. For example, the side-on profile would approximate the pressure profile on the side of the building; however, a slightly higher pressure would occur near the front corner and a slightly lower one near the rear corner.

These profiles are the inputs for the internal loading. In the case of the basement, the combined reflected and stagnation conditions on the front of the building produce the inflow through the entrance door. The incident shock wave passes through the door into the basement and expands two-dimensionally as the reflection process is carried out on the front wall. The expansion into the basement's large volume rapidly decreases the strength of the wave, as is indicated by the isopressure contours of Fig. 3. The shape of the contours is illustrative of the variable strength over the expanding shock wave's front surface. From the bowing, the attenuation of the wave is seen to be smallest where the inflow is the strongest. This variation in strength corresponds to the variable

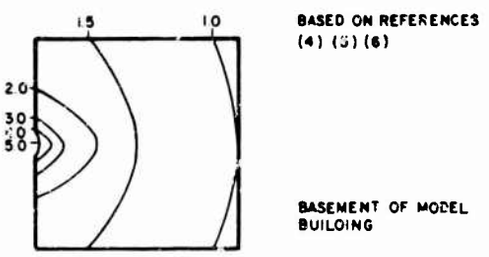

Fig. 3. Isoshock front overpressure curves

value of the exponent n in the prediction equation discussed previously.

The pressure-time history for the filling of the chamber was computed using the energy-mass balance technique (Fig. 4). The computed points are linked together in a sawtooth pattern; however, in the real case the pattern begins with a series of steps which decay to a smoother harmonic oscillation. The second pressure-tim

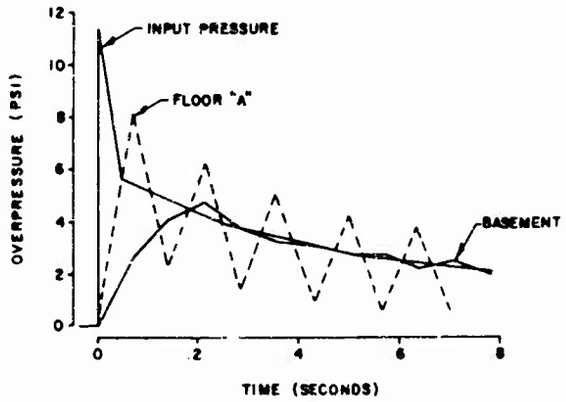

Fig. 4. Pressure-time histories on different floors

history of Fig. 4, the filling of floor A, has a more pronounced oscillation. The larger amplitude oscillations are the result of the greater open area through which an excess of mass and energy can flow prior to the arrival of the reflection from the rear wall to signal a new flow condition. The result is an interior pressure that is significantly above the exterior pressure; thus an outflow is created that removes too much mass and energy to achieve a balance. The imbalance again forms the conditions for the next step, and an oscillatory flow is established.

In the preceding example, the imbalance between the frequencies and amplitudes of the two filling processes could cause severe loads on a divider between two such chambers. To explore further how the loading results from the phenomena, point K on the dividers between floors A, B, and C was selected (Fig. 1). Using a stepped representation of the wave motion (for discussion purposes), the pressure-time loading of point K on both sides of the common divider between floors A and B is traced in Fig. 5. The differences in amplitudes and directions result in the differential pressure (loading)-time histories shown in the bottom of Fig. 5.

The histories traced in Fig. 5 were computed using the energy-mass balance and shock expansion prediction techniques of Ref. 6. These techniques were applied again to point K, but on the divider between floors A and B. The loads differ widely both in magnitude and direction because of differences in filling frequencies, which in turn are a function of the differences in the geometric subdivisions of the rooms. This differs from the comparison between the basement and the top floor, where the variation in open area was the differentiating factor. These results point out that pressure within chambers, and in turn loading of internal structural members, rely on the balance between several factors in addition to the input blast wave.

A further illustration of the loading process is made using point J on the common wall between rooms 1 and 2 of floor B. The pressure histories on either face of the wall are plotted on a common time base in Fig. 6, measured from incidence of the shock wave on the front of the structure. The pressure differential across the wall is the loading on the wall, represented by the shaded areas. Because of the longer transit time of the shock wave to point J in room 2, the major loading occurs in early times. Because the geometries of rooms 1 and 2 are similar, the end loading is nearly the same. The early imbalance would, however, create a large enough load to cause walls of most types of construction to fail. The eventual equalization of pressures on both sides of the wall would serve only to keep the translation of the broken wall to a minimum.

A second case of a common wall was selected from rooms 1 and 4 of floor B, at point I (Fig. 7). In this case, the filling at early times is nearly the same; after this period, however, the room geometries create a difference. The smaller length of room 1 creates a higher natural frequency, and hence the room fills faster. The more rapid filling produces an imbalance of pressures acting on the common wall until the slower response room comes up to pressure. This again illustrates the effect timing has in the loading of the interior of the structure.

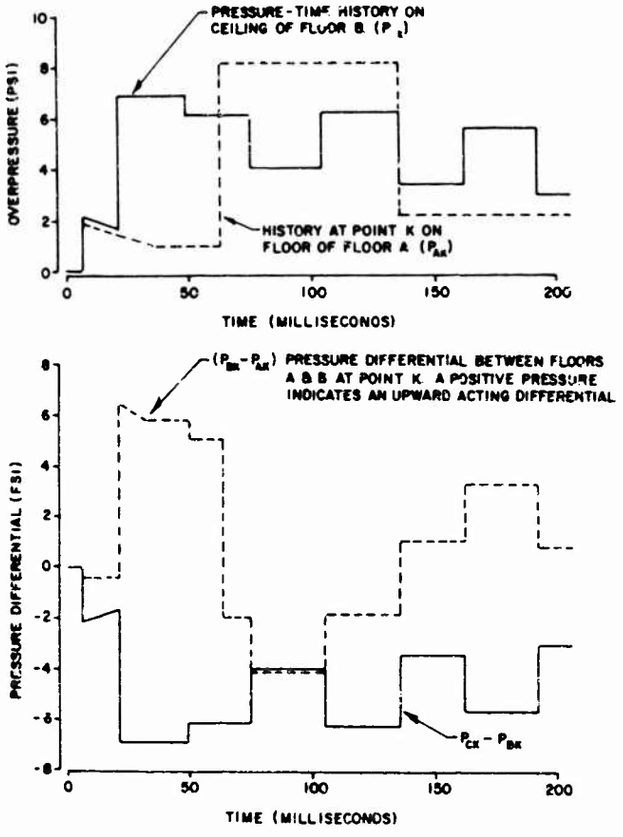

Fig. 5. Floor loading, point K

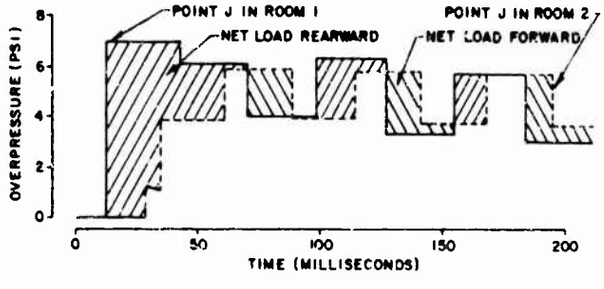

Fig. 6. Loading on common wall of rooms 1 and 2, floor B, at point J

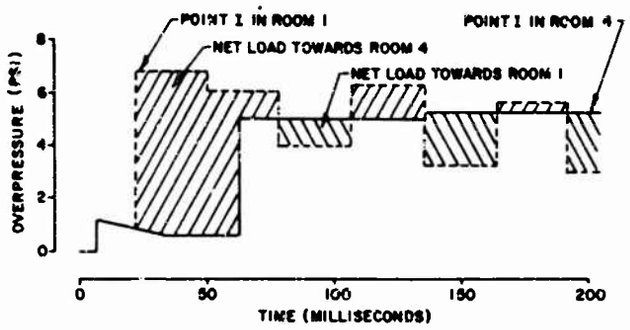

Fig. 7. Loading on common wall of rooms 1 and 4, floor B, at point I

As in the case of point J, the wall would be expected to fail, as would all dividing walls of floor B because of the uneven filling of the chambers they form. With the failure of the dividers, the filling history would begin to take the form of floor A.

SUMMARY

In summary, the factors considered to be most significant to the internal loading of a structure because of incidence of a blast wave are reviewed. Of the two load-producing processes, shock wave expansion and chamber filling, it is believed that the amplitude steps of the filling process produce the greater loads. The filling process behaves similarly to a resonator, whose pulse frequency is a function of the length of the chamber and the ambient sound speed. The natural period plus the transit time of the incident shock wave to each chamber's opening creates the pressure imbalances that load the dividing walls of adjoining chambers. In a chamber with hardened walls, i.e., those which can withstand 1- to 2-psi overpressures, it is the filling process that is the major cause of damage.

Prediction techniques have been briefly outlined; the actual methods are presented in Ref. 6 with experimental verification based on Ref. 4. Work is presently underway, sponsored by the Office of Civil Defense, to improve further the prediction techniques. Though a fairly thorough evaluation of the filling prediction method has been made for both two- and three-dimensional models in shock tubes, only limited checks are available for larger scale cases. The same holds true for the shock wave expansion into a two-dimensional room, even for scaled cases. Although additional work is needed, the methods outlined in this paper provide a good approximation of the internal loading of a structure by a blast wave.

REFERENCES

1. S. Glasstone (Ed.), "The Effects of Nuclear Weapons," Dept. of Army Pamphlet 39-3, Apr. 1962

2. K. Kaplan and C. Wiehle, "Air Blast Loading in the High Shock Strength Region (U): Part II. Prediction Methods and Examples," United Research Services Rpt. 633-3 (DASA 1460-1), Feb. 1965

3. C. K. Wiehle and W. L. Durbin, "Combined Effects of Nuclear Weapons on NFSS Type Structures," United Research Services Rpt. 658-3, June 1966

4. G. A. Coulter, "Air Shock Filling of Model Rooms," Ballistic Research Laboratories MR (in press)

5. A. Sakurai, "Blast Wave Theory," MRC Tech. Sum. Rpt. 497 (AD 608861), Sept. 1964

6. J. F. Melichar, Progress Report to Office of Civil Defense, Ballistic Research Laboratories MR (in press)

* * *

EFFECTS OF SLIDING ON BLAST LOADS REQUIRED TO OVERTURN STRUCTURES

Carlton E. Gebhart*
IIT Research Institute
Chicago, Illinois

A computer program capable of simulating the sliding and/or tipping of boxlike structures caused by nuclear blast loads is described. A sample problem demonstrates that sliding motions increase the loads required to overturn a structure.

INTRODUCTION

A typical problem in nuclear weapon vulnerability studies is the possibility of overturning an unanchored structure. Overturning implies serious damage to the contents of the structure, if not to the structure itself. Common structures of interest are mobile vehicles such as trucks, vans, trailers, generators, and personnel shelters, which often may be modeled satisfactorily as a rectangular box. A boxlike structure with a face broadside to the blast loading allows for a relatively easy description of the load time history. Since the equations of motion for a body which is rotating and sliding are coupled through the two motions, an analytic solution is impossible. The usual practice is to consider the modes independently, and thus determine the upper bounds on the sliding motion and the tipping motion. If one wishes to approximate the load time history by an impulse, an exponential, or a linear curve, it is possible to generate analytic solutions. If, however, a more accurate description of the loading is desired, one must resort to numerical methods and a computer solution to the equations for the sliding or tipping motions. In this case, one may as well go one step further and include the coupled equations of motion for simultaneous sliding and tipping. Such a program (called VANDY, for VAN DYnamics) was developed for the U. S. Army Satellite Communications Agency as part of a project [1] to study the vulnerability of transportable satellite communications ground stations.

The basis of the digital computer simulation is outlined in this paper, and an example problem will be presented which clearly demonstrates the significant increase in resistance to overturning if sliding also occurs. This effect should be considered in future vulnerability studies of unanchored structures.

SIMULATION

The input parameters necessary to describe the physical properties of a typical boxlike structure (hereafter referred to as a van) are shown in Fig. 1. The description of the broadside loading on the van from the blast appears elsewhere [2]. The horizontal load on the front face of the van is considered separately from the load on the back face. Vertical loads and variations of drag coefficients are assumed to be negligible. Figure 2 shows the pressure load history for the front face of a van, and Fig. 3 shows the pressure load history for the back face of a van.

The front face loading begins at the reflected pressure p_r and decays linearly until the clearing time t_s when the initial air particles have moved off the face. This time is computed by $t_s = 3S/U$ where S is the clearing distance and U is the shock velocity. The shock front reaches the edges of the back face at time w/U and increases linearly to a time t_b as the shock wave moves over and off the back face. The slope of the curve is the back face buildup

*Now at Booz, Allen Applied Research, Inc., Chicago, Illinois.

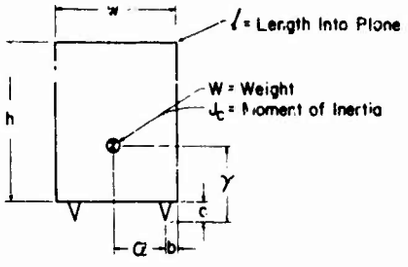

Fig. 1. Physical properties of typical van

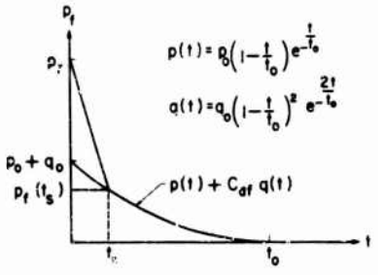

Fig. 2. Pressure load of front face of van

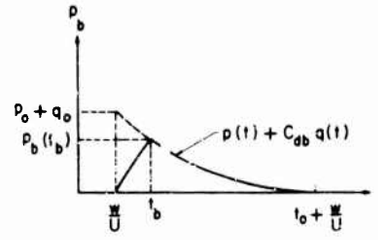

Fig. 3. Pressure load of back face of van

coefficient n. Inputs to the computer to specify the pressure loading are S, n, C_{df}, C_{db}, p_o, and t_o. The parameters C_{df} and C_{db} are the front and back face drag coefficients, respectively. The peak overpressure is p_o and the positive phase duration is t_o. All other quantities on Figs. 2 and 3 are computed within the program.

The net horizontal load F(t) is then computed from

$$F(t) = 144\,hl\left[p_f(t) - p_b(t)\right].$$

From the free-body diagram of Fig. 4, the center of pressure is assumed to remain halfway up the horizontal projected area of the van. The equations of motion for sliding and tipping together, assuming that the pivot remains in contact with the ground, are

$$F - \mu N = \frac{W}{g}(\ddot{x} + r\ddot{\theta}\cos\beta + r\dot{\theta}^2\sin\beta),$$

$$N - W = \frac{W}{g}\,r(\ddot{\theta}\sin\beta - \dot{\theta}^2\cos\beta),$$

$$Fd - Wr\sin\beta = \frac{W}{g}\ddot{x}r\cos\beta + J\ddot{\theta}.$$

The coefficient of friction μ is an input constant, and the moment of inertia J about the pivot point is computed from $J = J_c + Wr^2/g$. The program assumes both sliding and tipping at the beginning of a simulation.

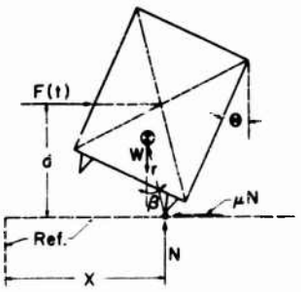

Fig. 4. Van free-body diagram

If $\dot{x} < 0$, the program switches to tipping only, and computes the motion from

$$Fd - Wr\sin\beta = J\ddot{\theta}.$$

If $\dot{\theta} < 0$, the program switches to sliding only, and computes the motion from

$$F - \mu W = W\ddot{x}/g.$$

If both conditions above are satisfied, or if $\pi/2 < \theta$ at any time, the program starts a new case or stops if no other input is found. Figure 5 illustrates this logic.

Comparing the third equation above for the coupled motion with the equation of motion for tipping only, one readily sees the term involving $\ddot{x}$ which resists the overturning motion when the van is accelerating forward.

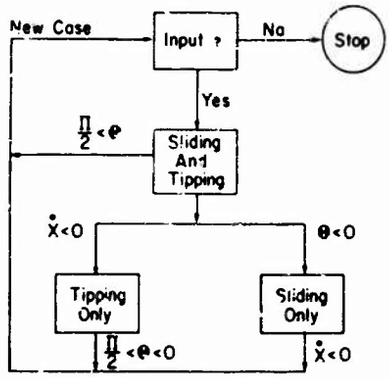

Fig. 5. Basic program logic

EXAMPLE OF EFFECT

To illustrate the effect which sliding motion has on the blast loads required to overturn vans, a 10-ft-square box weighing 5000 lb was simulated on the computer. The details of the configuration are presented in Table 1. The coefficients of friction between the van and ground were taken as 0.5, 0.75, and 1.0, and the peak overpressure p_o and corresponding positive phase durations t_o for a 1-megaton surface burst were varied until overturning occurred. A feature of the program which allows for running a case with an assumed fixed pivot was also utilized. This provides a lower bound on the loads required to overturn a van.

A summary of the results is presented in Table 2, which shows the last run before overturning, together with the first run which produced overturning. Figure 6 shows the effect of sliding in the form of a graph. It is seen that a coefficient of friction of 1.0 produces very little sliding, and the peak overpressure to overturn is negligibly greater than for the fixed pivot case. As the coefficient of friction is decreased, however, the peak overpressure to overturn increases rapidly. At $\mu = 0.5$, an 80 percent greater peak overpressure is required than for the fixed pivot case. Note also the rapid increases in distance slid and maximum velocity as the coefficient of friction is decreased. Indeed, for $\mu = 0.5$, the sliding motion could logically be considered intolerable before overturning occurs.

It is readily shown from momentum considerations that the velocity above which the van would overturn should it strike an immovable object is

$$V_{cr} = \frac{r_0}{y}\sqrt{gaf},$$

where

$$g = 32.2 \text{ ft/sec}^2,$$

$$r_0 = \sqrt{\frac{J_c g}{W} + a^2 + y^2},$$

and

$$\phi = \tan^{-1}\frac{a}{y}.$$

TABLE 1
Input for Computer Simulation of Van Overturn

Column	First Card			Second Card		
	Parameter	Units	Value	Parameter	Units	Value
1	h	ft	10	b	ft	0
11	ℓ	ft	10	c	ft	0
21	w	ft	10	W	lb	5000
31	a	ft	5	μ		1.0 (typ.)
41	y	ft	4	C_{df}		1.0
51	J_c	slug-ft^2	2600	C_{db}		-1.0
61	n		2.7	p_o	psi	3.0 (typ.)
71	S	ft	5	t_o	sec	3.6 (typ.)

TABLE 2
Results of Computer Simulation of Van Overturn

μ	p_o (psi)	θ_{max} (rad)	$t(\theta_{max})$ (sec)	x_{max} (ft)	$t(x_{max})$ (sec)	$\dot{x}_{max}$ (fps)
Last Run before Overturn						
0.5	5.1	0.2275	0.98	187.8	5.46	59.0
0.75	3.8	0.1482	0.99	29.7	2.31	17.9
1.0	2.9	0.3678	1.30	0.8	0.70	3.1
Fixed pivot	2.8	0.3635	1.18			
First Run Producing Overturn						
0.5	5.2	$\pi/2$	1.99			
0.75	3.9	$\pi/2$	1.76			
1.0	3.0	$\pi/2$	2.81			
Fixed pivot	2.9	$\pi/2$	2.87			

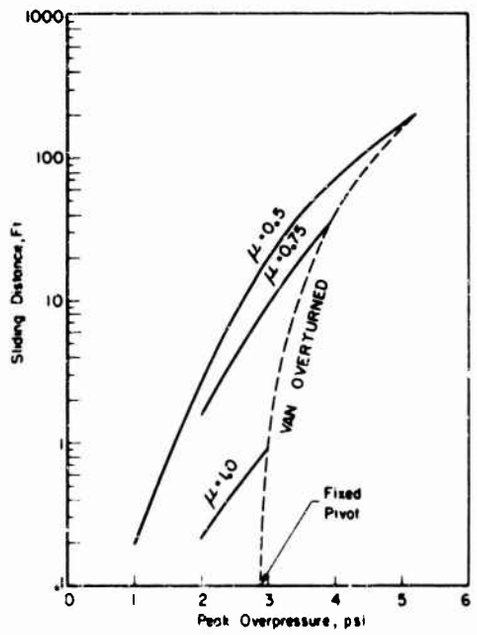

Fig. 6. Sliding distance vs peak overpressure for various friction coefficients

For the example van the critical velocity is 20.4 fps, which is exceeded for coefficients of friction below about 0.7.

CONCLUSIONS

It may be concluded that sliding motions of structures significantly decrease the tendency to overturn because of blast loads. The combined motion should therefore be considered if an accurate estimate of loads required to overturn an unanchored structure is desired. The computer program VANDY, described and demonstrated in this paper, provides a rapid and inexpensive method of evaluating the complete dynamics of boxlike structures subjected to blast loads.

The results of the example problem presented should not be extrapolated to imply the order of magnitude of the effect on any other structure. Variables such as coefficient of friction, van shape, height above ground, center of gravity position, moment of inertia, center of pressure position, and drag coefficients, may create considerable variation of the overturning motions. Experience has shown, however, that if the sliding motions are predominant or of primary interest, it is sufficient to assume sliding only, since the rotation affects the translation negligibly.

REFERENCES

1. "Design of a Survivable Mobile Link Terminal," IITRI, Contract No. DAAB07-C-0088, U. S. Army Electronics Command, Oct. 1966
2. Samuel Glasstone (Ed.), The Effects of Nuclear Weapons (rev. ed.) pp. 177-188 (U. S. Atomic Energy Commission, Washington, D.C.), 1962

* * *

USE OF DETONABLE GAS EXPLOSIONS FOR BLAST AND SHOCK STUDIES

Milton R. Johnson and Marion J. Balcerzak
General American Research Division
Niles, Illinois

Detonation waves, which can be initiated in certain mixtures of combustible gases, can be used to generate shock waves in air or other test gases. Plane detonation waves can be generated in tubes and used to develop high-pressure loadings by reflection of the wave, or to develop high-overpressure shock waves in a test gas. Large-scale spherical detonation waves can be generated in gas mixtures which are contained in spherical or hemispherical envelopes.

Successful spherical detonation experiments have been conducted with gas mixtures in above-ground spherical balloons up to 32 ft in diameter and in ground-level hemispheres up to 125 ft in diameter. These experiments have shown that the air shock-wave phenomena resulting from the gaseous detonation are much clearer and distinct in the high-pressure region than those normally observed on detonations of high explosives. This may be explained in terms of a Taylor instability and the fact that the combustion products of a detonable gas explosion are initially less dense than the surrounding air, whereas with a high explosive they are more dense.

INTRODUCTION

The moratorium on atmospheric nuclear testing has given impetus to the development of techniques for simulating nuclear blast effects. Simulation techniques using the effects of detonation phenomena in detonable gas mixtures have proved to be particularly advantageous for generating high-overpressure blast waves in large-diameter shock tubes and for producing spherically symmetric air-blast waves. Feasibility studies have also shown that there are promising applications for detonable gas phenomena in creating high-altitude and underground explosive environments.

This paper describes the use of detonable gas phenomena for shock tube applications and free air explosions. The results obtained on Project SLEDGE (Simulating Large Explosive Detonable Gas Experiment), which was initiated by the Defense Atomic Support Agency in 1965 to study the feasibility of using the explosion of detonable gas mixtures for providing high-yield air-blast phenomena, are emphasized.

DETONABLE GAS MIXTURES

Detonation waves can be initiated in certain mixtures of combustible gases. A detonation wave is a shock wave which propagates through an explosive medium and is sustained by the release of chemical energy. The exothermic chemical reaction is initiated by the shock compression of the combustible mixture.

A detonation wave is similar to a shock wave; the detonation front propagates with supersonic velocity and there is a discontinuous change in properties across the detonation front. The propagation of a detonation wave is not influenced by the flow behind the detonation front, because its velocity is equal to the sum of the acoustic and flow velocities in the gas immediately behind the front. In contrast to this the propagation of a shock wave is influenced by the flow behind the detonation front because its velocity is less than the sum of the acoustic and flow velocities in the gas behind the front.

Gas mixtures of propane and oxygen, methane and oxygen, and hydrogen and oxygen are particularly useful for blast and shock studies, because they will detonate over a wide range of mixture ratios, they are readily available, and they are low in cost.

Propane-oxygen detonable gas mixtures are nonbuoyant and are applicable to ground-level experiments. Methane-oxygen and

hydrogen-oxygen detonable gas mixtures are buoyant and are applicable to above-ground tests.

PROPERTIES OF DETONATION WAVES

The velocity of the detonation front and properties of the gas mixture immediately behind the detonation front, namely the pressure, flow velocity, temperature, molecular weight, etc., may be determined analytically from the conservation equations of mass, momentum, and energy across the detonation front and a thermochemical analysis describing the chemical reactions taking place within the detonation front. Detonation parameters for mixtures of hydrogen and oxygen, methane and oxygen, and propane and oxygen at atmospheric pressure are given in Table 1. For a given mixture the detonation pressure is approximately proportional to the initial pressure. Detonation front velocity and the flow velocity and temperature immediately behind the front are not significantly affected by the ambient gas pressure.

The pressure, temperature, and flow velocity begin to decay immediately behind the detonation front, because the head of a rarefaction wave in the flow behind the front can keep up with the front. The rate of decay of the properties is inversely proportional to the length of detonation wave propagation from the point of ignition. Thus, the duration of flow velocity and pressure behind the front increases with increasing length of wave propagation.

The rate of decay of properties behind the detonation front also depends on whether the wave is propagating as a plane wave or as a spherically symmetric wave. The rate of decay of properties is much greater for spherical detonation waves than for plane waves. This is shown by comparing the decay of pressure and flow velocity for both types of waves in Figs. 1 and 2. The front velocity, peak pressure, and peak flow velocity do not change, in either case, with increasing length of propagation.

The properties of detonation waves can be determined analytically, but these calculations have significance only if detonation waves can be initiated and maintained in the detonable gas mixture. There is no analytic technique presently available for determining whether a stable detonation wave can be initiated and maintained in a given gas mixture. Detonation limits can be determined only by experiment. The two basic parameters affecting detonability are the composition of the mixture and its initial pressure. If the mixture is either too oxygen rich or too fuel rich, or if the initial pressure is too low, it is impossible to obtain a steady detonation wave.

The mixture ratios within which spherical detonations can be obtained in propane-oxygen and methane-oxygen mixtures at atmospheric pressure have been determined on project SLEDGE [1,2]. Also, tests to determine the detonability limits of methane-oxygen and hydrogen-oxygen at low pressures, which simulate high-altitude ambient conditions, have been conducted in the Ballistic Research

TABLE 1
Detonation Parameters for Mixtures of Oxygen and Fuel Gases at 1-Atm Initial Pressure

Fuel Gas	Oxygen-to-Fuel-Gas Mole Ratio	Detonation Pressure (atm)	Detonation Velocity (fps)	Peak Flow Velocity (fps)	Peak Acoustic Velocity (fps)
Methane	1.5	30.07	8169	3581	4588
Methane	2	27.97	7719	3375	4344
Propane	3	41.77	8267	3629	4638
Propane	3.5	40.03	8132	3566	4566
Propane	5	34.38	7603	3326	4277
Hydrogen	0.5	18.86	9367	4094	5273
Hydrogen	1.0	17.87	7653	3341	4312
Hydrogen	1.5	16.94	6870	2990	3879
Hydrogen	2.0	16.09	6384	2769	3615
Hydrogen	3.0	14.54	5752	2476	3276

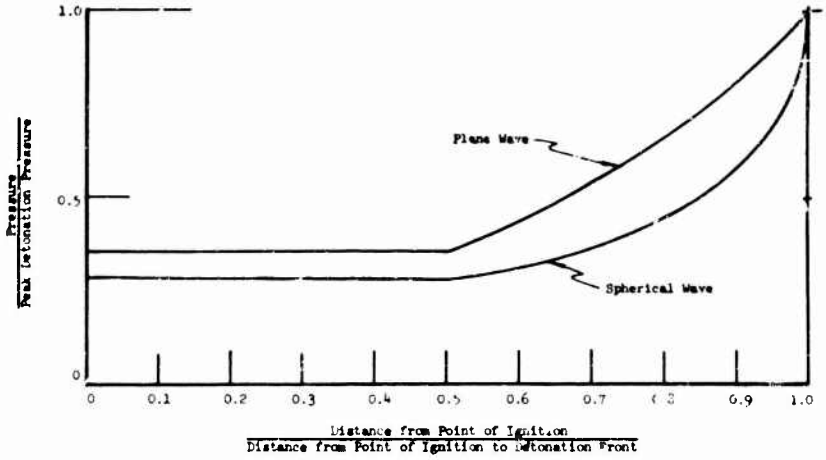

Fig. 1. Comparison of detonation wave pressures, plane and spherical waves

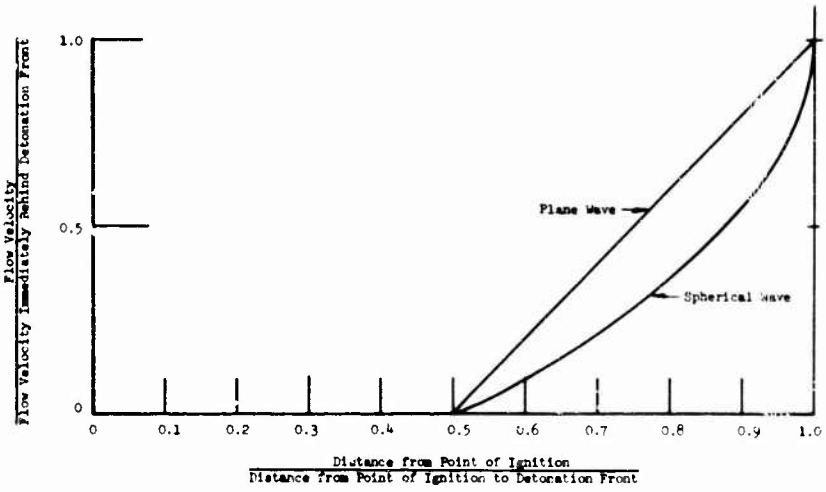

Fig. 2. Comparison of detonation wave flow velocities, plane and spherical waves

Laboratories blast sphere at Aberdeen Proving Ground, Maryland. The tests have shown that both methane-oxygen and hydrogen-oxygen gas mixtures will detonate at an initial pressure corresponding to 30,000-ft altitude if the ignition energy is large enough.

APPLICATIONS OF DETONATION WAVE PHENOMENA

Plane Detonation Waves

Detonation Tube – Plane detonation waves may be used to develop high-pressure shock loadings with infinitesimal rise times. The technique is shown schematically in Fig. 3. The detonable gas mixture is confined in a large tube. When the gas is ignited, a detonation wave quickly develops and propagates away from the point of ignition at high velocity. If care is taken regarding the method of ignition, the detonation wave will rapidly assume a planar orientation perpendicular to the axis of the tube. This wave can then be used to impose an impulsive load on the far end of the tube, where the test item is located. The detonation wave propagates from the point of ignition with a constant velocity and uniform peak detonation pressure.

As the detonation wave progresses down the tube, its duration increases with increasing

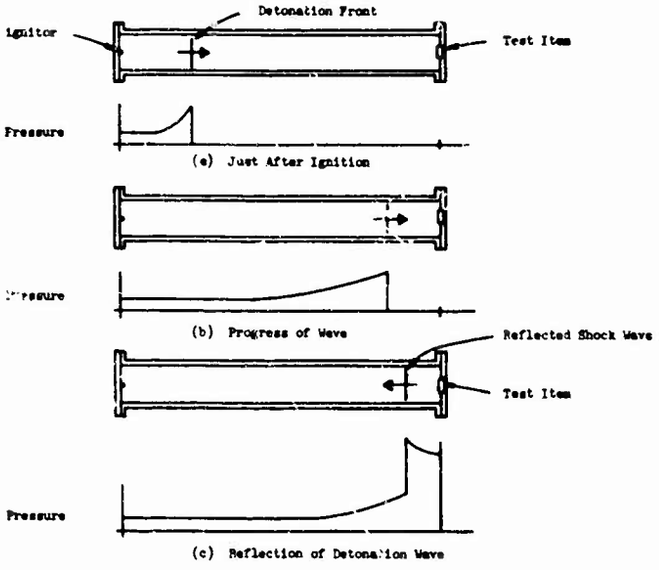

Fig. 3. Detonation tube shock loading

propagational distance. When it reaches the end of the tube, it will be reflected. The reflected pressure is what actually loads the test item. The reflected pressure will vary, depending on the value of the specific heat ratio behind the incident wave, from 2.6 to 2.3 times the incident pressure. The reflected wave will then travel back toward the other end of the tube. The loading pulse will have an instantaneous rise to peak pressure, followed by an exponential decay. Thus, the pulse is quite similar to the air blast wave from a nuclear explosion in the high-overpressure region.

Sigmon [3] has described the use of this type of loading to provide high accelerations in mechanical shock tests.

Detonation Shock Tube — The application of plane detonation waves to the shock-tube generation of high-overpressure blast waves is described in detail in Ref. [4] and [5]. A detonation-driven shock tube is illustrated in Fig. 4. It consists of a detonation chamber containing a detonable gas mixture and an expansion chamber containing the test gas. These two chambers are separated by a frangible diaphragm.

When a detonable gas mixture is ignited at the end of the detonation chamber, a detonation wave will form and move at high velocity toward the other end of the chamber. On reaching the end of the detonation chamber, the

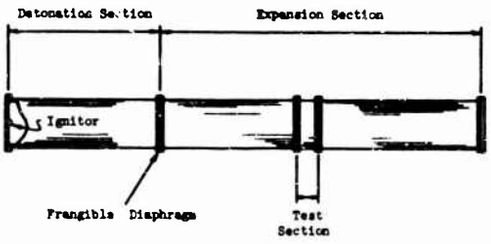

Fig. 4. Schematic Diagram of detonation shock tube

detonation wave bursts the diaphragm and causes the formation of a shock wave in the test gas.

There are three major advantages of using detonation wave drive which are especially important when high-overpressure shock waves are required in large-diameter tubes. The first advantage is that the end of the detonation chamber where the detonable gas mixture is ignited does not have to remain closed after the initiation of the detonation wave. Only a light diaphragm is required to contain the gas mixture. The diaphragm will break open immediately after ignition and allow the gases to exhaust into the atmosphere without affecting the properties behind the detonation wave front. This eliminates the recoil force on the tube caused by the unbalanced gas pressures.

A second advantage is the relatively low maximum pressure of the detonation wave which is required to generate high-overpressure shock waves. To produce a given shock pressure in the test gas, the detonation pressure is usually much less than the pressure of a driver gas initially at rest. This is a result of the high velocity of the gas behind the detonation front.

A third advantage is that there is no limit to the establishment of plane detonation waves in large-diameter tubes. Because of this, detonation drivers are paricularly applicable to large-diameter shock tubes.

Spherical Detonation Waves

Project SLEDGE – Spherically expanding air-blast waves can be produced by spherical detonation waves. The detonable gas mixture may be contained in a spherical balloon for above-ground testing or in a hemispherical envelope for ground-level tests. In each case the detonation wave is initiated in the center of the mixture.

Experiments have shown that using free-air, spherical, detonable gas explosives overcomes one of the disadvantages of using high explosives to provide air blast phenomena. This disadvantage is the lack of distinct shock phenomena in the high-shock-strength region near the charge. A clearly defined spherically symmetric shock wave is usually not observed with TNT explosions at distances closer than 30 charge radii. Even beyond this distance protrusions from the main shock wave often exist.

There are two principal reasons for the lack of clear shock phenomena in the high-shock-strength region. The first is that it is difficult to cast and handle spheres of high explosives larger than 10 tons. Large charges, therefore, have to be made up of smaller blocks of explosives. The junctions between the blocks of explosives affect the advance of the detonation front. While effects are unknown in detail; they are known to lead to nonuniform detonation velocities and hence an unevenly expanding detonation front from the central ignition point. A second reason is that the interface is basically unstable during the early phases of fireball growth. A classical Taylor instability [6] exists as the outwardly expanding detonation products are decelerated by the less dense surrounding air. With detonable gas explosions, the Taylor instability is removed; shock phenomena are clear and distinct in the high-shock-strength region.

Peak air-blast overpressure vs range for a methane-oxygen detonation, a propane-oxygen detonation, and TNT is compared in Fig. 5. The horizontal region on the gas detonation curves is the detonation pressure within the balloon. This figure shows that the air-blast effect from a detonable gas explosion is about the same as from the same weight of TNT.

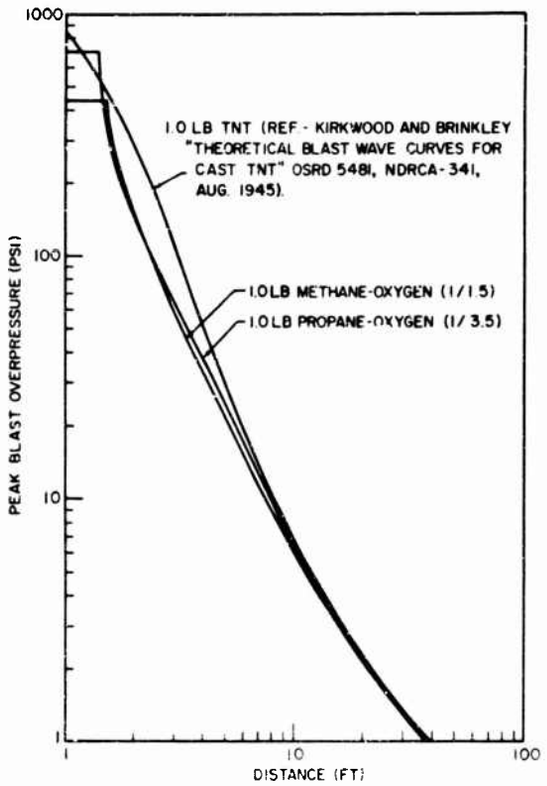

Fig. 5. Comparison of overpressure vs distance at sea level from 1 lb of TNT, methane-oxygen mixture (1:1.5 mole ratio), and propane-oxygen mixture (1:3.5 mole ratio)

Pressure, particle velocity, and density vs range are shown in Figs. 6 through 11 for both methane-oxygen and propane-oxygen detonations. Nondimensional parameters are used in these figures. Range R is shown in terms of balloon radii:

$$R = \frac{r}{r_0} .$$

where r is distance from the balloon center and r_0 is the radius of the gas-containing balloon. Pressure P is given in atmospheres:

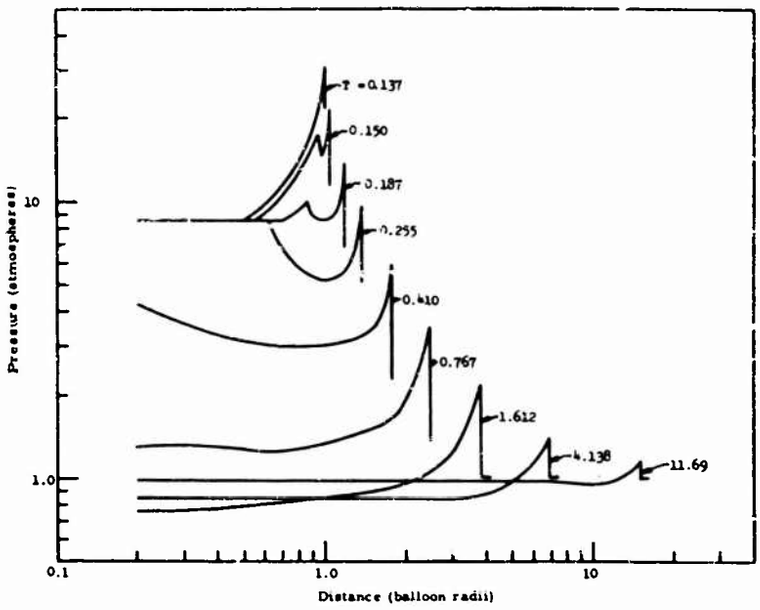

Fig. 6. Pressure vs distance for sea-level free-air detonation of methane-oxygen mixture (1:1.5 mole ratio)

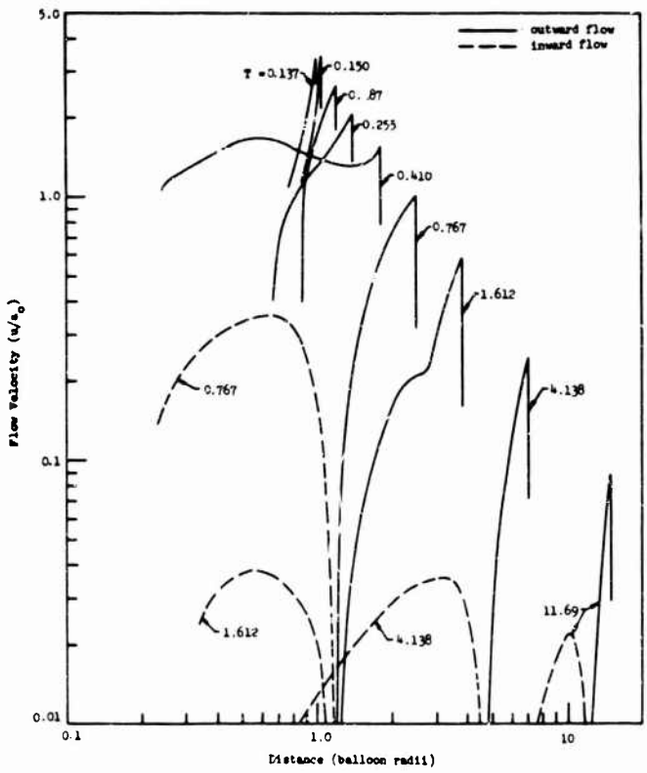

Fig. 7. Particle velocity vs distance for sea-level free-air detonation of methane-oxygen mixture (1:1.5 mole ratio)

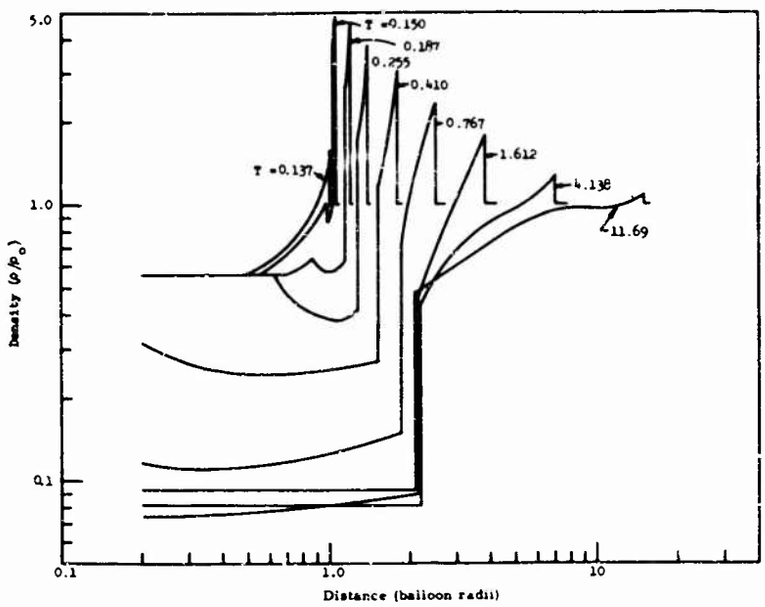

Fig. 8. Density vs distance for sea-level free-air detonation of methane-oxygen mixture (1:1.5 mole ratio)

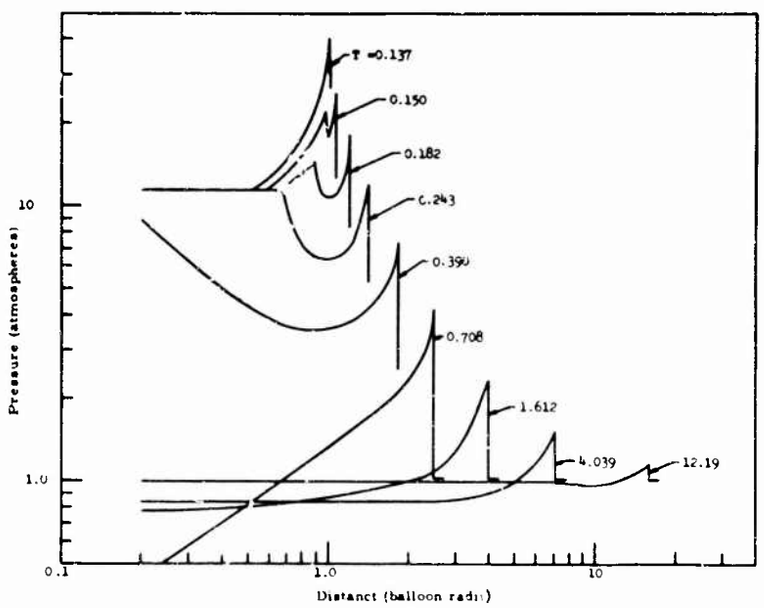

Fig. 9. Pressure vs distance for sea-level free-air detonation of propane-oxygen mixture (1:3.5 mole ratio)

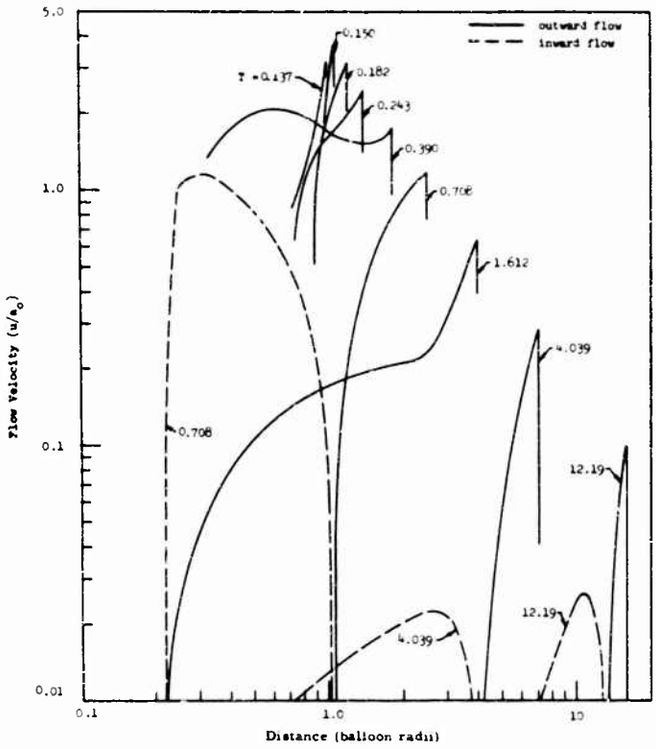

Fig. 10. Particle velocity vs distance for sea-level free-air detonation of propane-oxygen mixture (1:3.5 mole ratio)

$$P = \frac{p}{p_0} ,$$

where p is pressure and p_0 is ambient atmospheric pressure. Flow velocity U is normalized by the ambient sonic velocity,

$$U = \frac{u}{a_0} ,$$

where u is velocity and a_0 is the speed of sound in the ambient air. Density D is given in terms of the ambient air density,

$$D = \frac{\rho}{\rho_0} ,$$

where ρ is density and ρ_0 is the initial air density. The vertical line on the density curves represents the interface between the air and combustion products of the detonation wave. Time T is nondimensionalized as follows:

$$T = \frac{a_0 t}{r_0} ,$$

where t is time from the initiation of the detonation wave.

Project SLEDGE: High Altitude Application — Developmental programs are currently underway to apply the technology Project SLEDGE to a high-altitude blast-generation system. Preliminary feasibility studies have established the technical and economic feasibility of the SLEDGE system in this application. Applications of this test technique include missile air-blast interaction tests, aircraft air-blast interaction tests, and height-of-burst experiments.

Underground Detonable Gas Explosions — Studies have also been completed to determine the feasibility of generating detonable gas explosions in underground cavities [7]. Initial gas pressures much higher than one atmosphere can be considered for this application. Thus, high peak detonation pressures can be attained. Parameters which can be used to describe underground explosion phenomena quantitatively are (a) the peak reflected pressure on the cavity wall, (b) the energy released by the explosion,

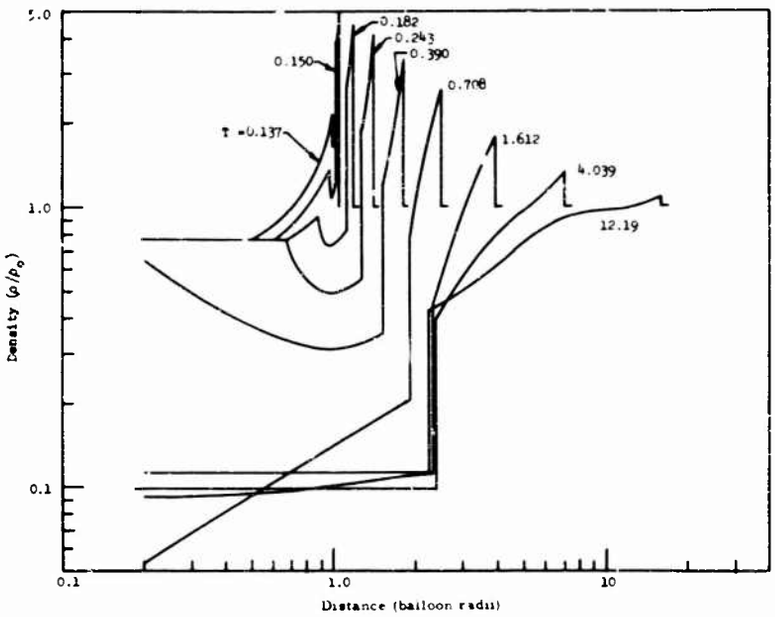

Fig. 11. Density vs distance for sea-level free-air detonation of propane-oxygen mixture (1:3.5 mole ratio)

(c) the size of the cavity, (d) the average pressure on the cavity wall, (e) the impulse delivered to the cavity wall, and (f) the oscillation frequency of the shock wave with the cavity, i.e., the reciprocal of the time between successive pressure peaks. It is impossible to have an underground detonable gas explosion which duplicates all the parameters of a nuclear underground explosion in a cavity. It is possible, however, to match any two of these parameters with a detonable gas explosion. Meaningful seismic signal data could be obtained from an underground detonable gas explosion.

EQUIPMENT FOR FREE-AIR DETONABLE AIR EXPLOSIONS

To produce a suitable free-air explosion of detonable gases, equipment must be available for delivering and containing the gas mixtures. The development of the most suitable test equipment has been emphasized during project SLEDGE.

The gases are contained with light balloon-like membranes prior to detonation. The experience gained with deploying high-altitude balloons is of little value in this regard because the problems of handling and filling balloons with detonable gas are very different from the problems encountered with high-altitude balloons. The usual procedure is to inject the oxygen into the balloon first. Because of safety considerations, the balloon must be handled remotely while the methane or hydrogen is injected and while the balloon is deployed to altitude. If methane or hydrogen is used, the balloons do not become buoyant until most of the fuel gas has been injected. One must also plan for relatively long filling times if large quantities of gas are used.

The balloon is susceptible to wind damage during the filling process. To overcome this problem a ballonet-balloon technique has been developed. A ballonet is an impermeable membrane inside the balloon which compartmentalizes the balloon into a detonable gas side and an air side (see Fig. 12). The balloon is first rapidly inflated with air. This pushes the ballonet to one side of the balloon. Then, after the balloon has been filled with air, the oxygen and fuel gases are injected into the balloon at a slower rate. This forces the ballonet toward the other side of the balloon expelling the air. This technique allows the balloon to remain stable, presenting a clean aerodynamic shape to the wind, during oxygen and fuel gas filling.

Efforts are now underway to develop equipment and procedures for decreasing filling times. Gases like oxygen and propane are normally delivered to the test site in the liquid

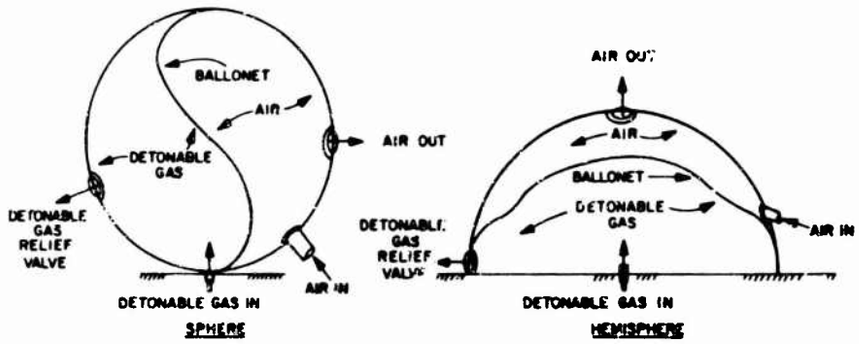

Fig. 12. Design of balloon with ballonet

state. Large vaporizers are required for high filling rates. If filling times are sufficiently reduced it may be possible to eliminate the need for the ballonet, thus decreasing the cost of the balloons.

PROJECT SLEDGE EXPERIMENTS

A number of tests have been performed with the SLEDGE technique to obtain the correlation between the predicted and experimental results. The largest experiments are described below.

Detonation of a 1000 Pound Methane-Oxygen Mixture

The largest methane-oxygen detonation achieved under project SLEDGE was 1000 lb of gas mixture in October 1965. The balloon filled with methane and oxygen is shown in Fig. 13. It was 32 ft in diameter and its center was located 25 ft above the surface of the ground. Two pictures from a high-speed film record are shown in Figs. 14 and 15. These photographs show the distinct spherically symmetric shock front and the well-defined interface between the detonation products and the surrounding air. The irregularities in shock front development and the fireball growth from a comparable TNT explosion are shown in Fig. 16. This figure shows the detonation of a 1000-lb charge made up of blocks of TNT, which was also at a burst height of 25 ft.

Detonation of 40,000-Pound Propane-Oxygen Mixture

The largest detonation achieved was the detonation of 20 tons of propane and oxygen in a 125-ft-diam hemisphere in Operation DISTANT PLAIN [8,9] in July 1966. The balloon filled with the detonable gas mixture is shown in Fig. 17. Figure 18 shows the resulting explosion. This test demonstrated that stable detonation waves can be obtained in a large detonable gas volume and that the balloon containment technique

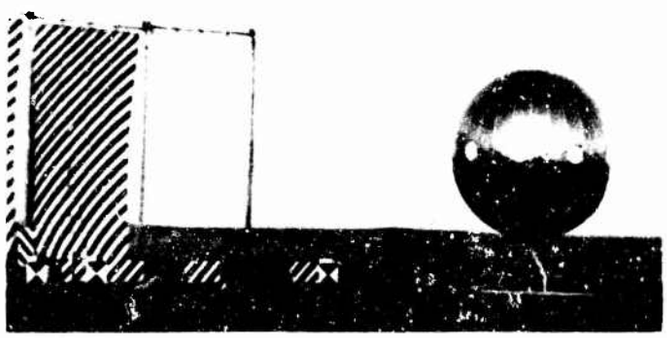

Fig. 13. Methane-oxygen balloon of 32-ft-diam

Fig. 14. Fireball and air-blast shock front from 32-ft-diam methane-oxygen explosion

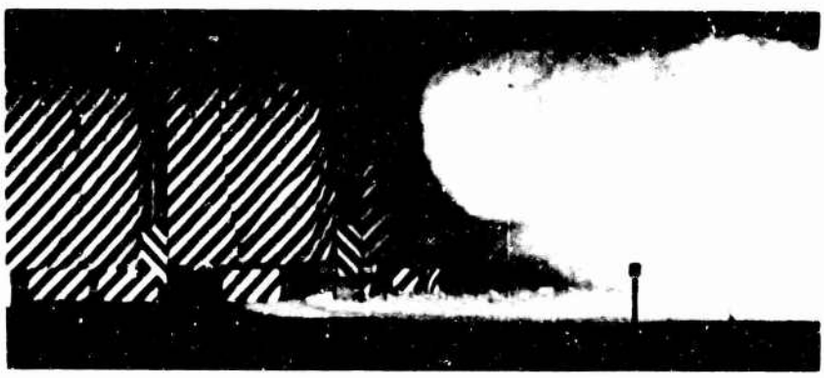

Fig. 15. Fireball and air-blast shock front from 32-ft-diam methane-oxygen explosion

is sound. The test again demonstrated that clear and distinct shock phenomena are obtained from detonable gas explosions.

A notable feature of this detonation was that no crater was formed, even though the base of the hemisphere was on the surface of the ground. A comparable surface explosion of TNT would have produced a large crater. The ejecta from the crater would have interfered with air-blast effects tests near the charge in the high-overpressure region.

CONCLUSIONS

The results of shock tube tests with plane detonation waves and free-air explosions with spherical detonation waves have agreed with predictions. The experiments have demonstrated that detonable gas explosion phenomena can be used to provide blast and shock environments. The principal advantages of detonable gases are ability to generate high-overpressure shock waves in shock tubes and ability to produce clear, distinct phenomena in the high-overpressure regions of free-air explosions.

More developmental work is required to obtain greater reliability in field-test operations using spherical balloons. Field-test operations have revealed deficiencies in the early designs of large spherical balloons. Another problem is that of obtaining reliable protection against a static electrical discharge when using balloon materials which accumulate static electrical charges. A premature detonation during the fuel gas filling foiled an attempt to detonate a 110-ft-diam spherical balloon filled with methane and oxygen on Operation DISTANT PLAIN. This preignition was attributed to a static electrical discharge, although precautions

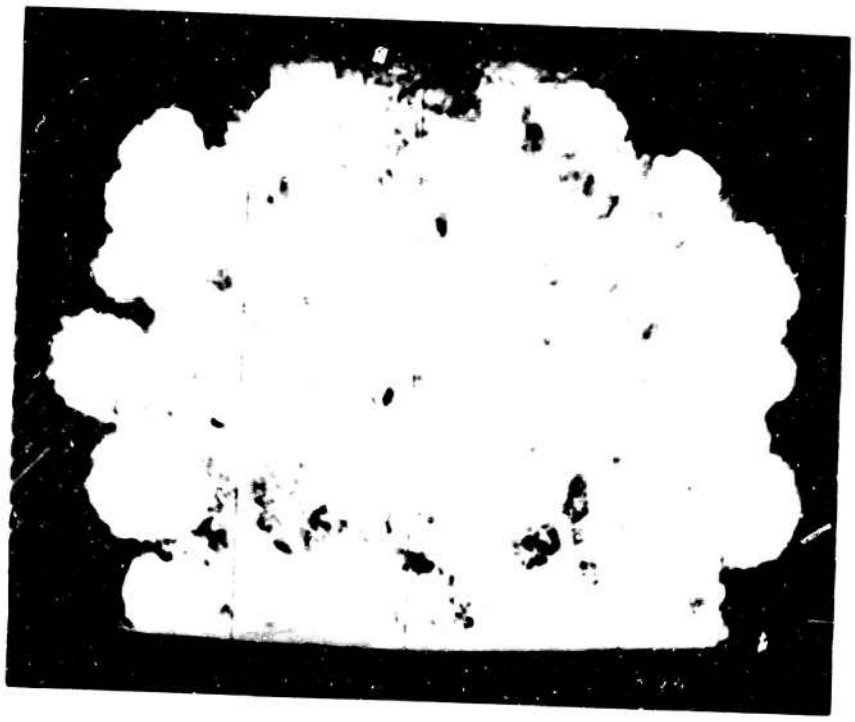

Fig. 16. Fireball and air-blast shock front from 1000 lb of TNT

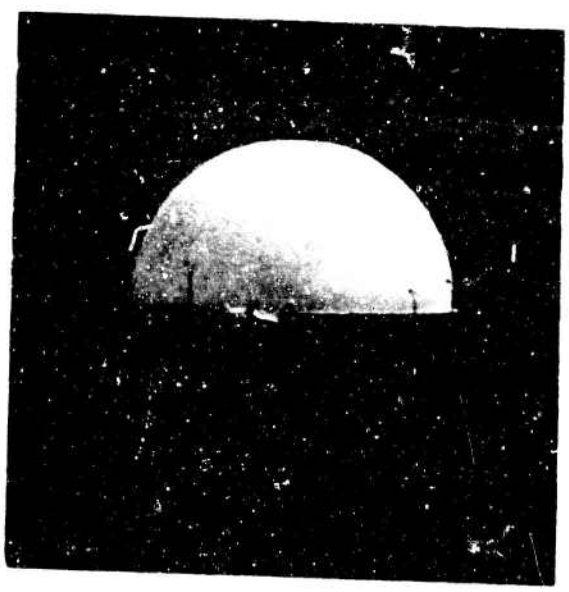

Fig. 17. Fully inflated 125-ft-diam hemispherical balloon filled with propane-oxygen mixture

Fig. 18. Detonation of 125-ft hemispherical balloon

had been taken to guard against such an event. Subsequent studies revealed that the particular scheme which was used to ground the balloon surfaces could be defeated under certain conditions. Prospects for developing methods to overcome this problem are excellent.

REFERENCES

1. J. R. Kelso and J. Choromokos, Jr., "Project SLEDGE," Military Eng., No. 385: pp. 355-356, Sept-Oct. (1966)

2. M. J. Balcerzak, M. R. Johnson, and F. R. Kurz, "Nuclear Blast Simulation, Part I, Detonable Gas Explosion," Defense Atomic Support Agency Rept. 1792-1, July 1966

3. W. M. Sigmon, Jr., "Shock Testing with Explosive Gases," Shock and Vibration Bull. 34(Part 3):pp. 311-327, Dec. (1964)

4. M. R. Johnson and M. J. Balcerzak, "A Detonation Tube Drive for Producing Hypersonic Flows in a Shock Tube," Proc. 3rd Hypervelocity Techniques Symp., Mar. 1964

5. M. J. Balcerzak and M. R. Johnson, "The Gaseous-Detonation Driver and its Application to Shock Tube Simulation Techniques," Proc. 5th International Shock Tube Symp., Apr. 1965

6. G. I. Taylor, "The Instability of Liquid Surfaces when Accelerated in a Direction Perpendicular to Their Planes. I," Proc. Roy. Soc. (London), Ser. A, 201:192 (1950)

7. F. E. Ostrem and L. E. Fugelso, "Feasibility of Underground Detonable Gas Explosions," Defense Atomic Support Agency Rept. 1919, Apr. 1967

8. M. J. Balcerzak and M. R. Johnson, "Operation DISTANT PLAIN Preliminary Report, Volume I," Defense Atomic Support Agency Rept. 1876-1, Dec. 1966, pp. 214-243

9. M. J. Balcerzak, M. R. Johnson, and S. W. Lucole, "Nuclear Blast Simulation, Detonation Gas Explosion, Operation Distant Plain," Defense Atomic Support Agency Rept. 1945, Apr. 1967

DISCUSSION

Voice: I understand that this is supposed to be a simulation of a nuclear bomb or something like that. How does the pressure-time curve compare to that of a nuclear detonation?

Mr. Johnson: First of all, it is an explosion in its own right and, of course, one can compare it with TNT or nuclear explosive. In a scale sense it compares very well with a nuclear pressure wave.

* * *

INCORPORATION OF SHOCK PROTECTION IN EXISTING ABOVEGROUND CYLINDRICAL STRUCTURES SUBJECTED TO NUCLEAR BLAST*†

Edward Cohen, Samuel Weissman, and Louis Sanchez
Ammann & Whitney, Consulting Engineers
New York, New York

The contents of existing small-diameter, aboveground, multistory cylindrical structures, housing equipment and personnel, will be provided with shock protection consistent with the blast capacity (10 to 50 psi for megaton weapon yields) of the concrete structural shell. Large horizontal and rotational motions, in addition to vertical motions, will occur in the cylinder because of its configuration and flexibility. In the development of appropriate shock-mounting schemes, every interior component and system was investigated to determine where shock protection was required to assure the survival and postattack operation of all essential electronic components and key personnel. Many restrictions were imposed by the requirement for incorporating shock isolation within small, confined areas in which the equipment requiring protection is already installed.

Vertical, horizontal, and rotational shock response spectra at each floor level were used as input to design various shock protection schemes to meet shock tolerance and fragility criteria. Typical designs are illustrated and discussed. These include. (a) spring-suspended group platforms to protect sensitive electronic equipment and personnel operating this equipment; (b) individual spring-mounted service equipment such as air conditioners and electric panel boxes; (c) rigid-mounted items such as fire extinguishers and tools; (d) ruggedized replacements including stronger partition walls and metal toilet units; (e) additional clamps and supports for piping, and flexible utility and power lines connected to spring-mounted equipment; and (f) energy-absorbing padding.

INTRODUCTION

The critical system components on the interior of existing small-diameter, aboveground, multistory cylindrical structures, housing sensitive electronic equipment, personnel, and service equipment, are being upgraded by the provision of shock mounting consistent with the blast protective capacity of the concrete structural shell and floor slabs. Figure 1 shows a cross section of a typical structure. The tower portion of the structures is approximately 27 ft in diameter and extends up to 100 ft above ground. Most story heights are 10 ft 3 in., with one or two levels below ground. The structures are founded on rock.

The overpressure levels for the various structures range from 10 to 50 psi for megaton weapon yields. Because of the configuration and flexibility of the structures, the direct-blast and ground-shock loading will result in relatively large horizontal motions. Flexural distortion of the structures, with the cylinder acting as a cantilever, resulted in the major contribution to horizontal motion, and caused an additional vertical component at points away from the neutral axis of the cylinder.

Peak horizontal structure motions, at the upper floors, are in the order of 6-in. displacement, 150-ips velocity, and 20-g acceleration. Peak vertical structure motions, at the upper floors, are in the order of 1-in. displacement, 50-ips velocity, and 10-g acceleration. Motions are somewhat higher at the roof and are much lower at the lower floors and underground levels.

Shock response spectra were furnished for each floor level of the structures. In addition

*This project was performed for the Department of the Navy, Naval Facilities Engineering Command.
†This paper was not presented at the Symposium.

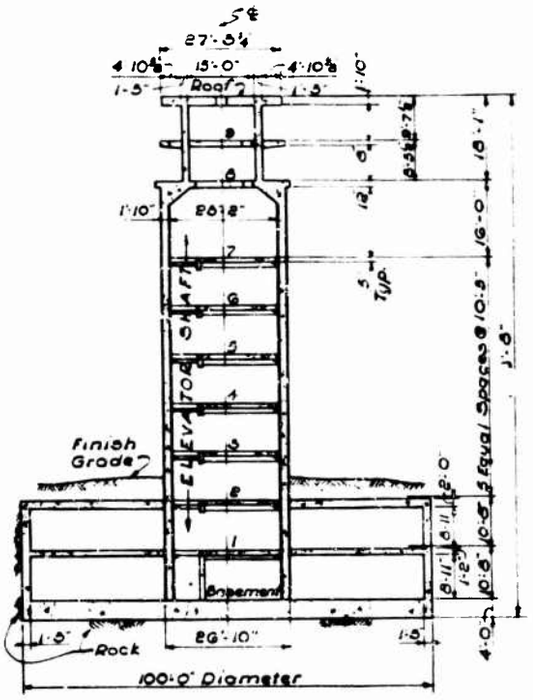

Fig. 1. Cross section of structure

to the horizontal and vertical spectra normally considered for shock isolation in hardened facilities, rotational spectra were required because of the large flexural distortions of the cylinder. The potential dynamic response of existing equipment without shock isolation, on the middle to upper floor levels, would be many times that of the tolerance values. Moreover, large amplifications of the peak structure motions from resonance would result at certain frequency ranges. Personnel within the structures also require shock protection.

In the development of appropriate shock-mounting systems, it was important that every interior component and system be investigated to determine where protection was required to assure the survival and postattack operation of all essential electronic components and systems. A failure in critical components or injury to key personnel would disrupt the entire system. Many restrictions were imposed by the task of incorporating shock isolation within small, confined areas in which the equipment requiring protection is already installed.

This paper describes and discusses some of the various conceptions which were designed to meet the shock protection requirements. These designs are being presently installed in the structures.

GENERAL SHOCK-MOUNTING CONCEPTIONS

Shock-mounting conceptions, used to provide the required shock protection, include the following general types: spring mounted, rigid mounted, ruggedized replacements, and padding. Spring-mounted systems include such items as group platforms, air conditioners, dehumidifiers, electric service panels, and storage racks and cabinets. Rigid-mounted conceptions apply to such items as piping, conduit, tools, fire extinguishers, fire hoses, and water coolers. Ruggedized replacements include new walls, toilet facilities, and light bulbs. Padding has been provided along sharp edges where impact may cause injury, and also in combination with other mounting conceptions.

Spring-mounted items undergo a dynamic displacement of several inches when subjected to shock effects. Therefore, necessary clearances and flexible utility lines have been provided to permit motion in any direction. It is essential that the amount and distribution of weight considered in the design of the spring-mounted conceptions be maintained to assure proper dynamic balance and clearances. Where future equipment changes are required, adjustment of springs and use of ballast may be required.

Protection for operators of electronic equipment is provided by the spring-suspended group platforms. Other personnel will generally be safe if they are on the lower floors of the structures.

Rigid mountings have been provided to restrain rugged or expendable items and prevent damage which would otherwise be caused by impact or collision resulting from the structure motions. Rigid mountings for piping serve to reduce span lengths and thereby reduce stresses induced by structure accelerations.

Ruggedized replacements include the elevator-shaft walls on those floors where masonry or plaster walls are replaced with steel walls capable of resisting acceleration forces. On certain floors, vitreous water closets and lavatories will be replaced with stronger metal units. Standard incandescent lamps will be replaced with shock-resistant lamps. Padding has been provided to protect against secondary impact effects within spring- and rugged-mounted conceptions, and to protect personnel against injury resulting from impact of the head with hazardous sharp edges. The design of necessary shock protection for the elevators is being currently performed and is not covered here.

SPRING-SUSPENDED GROUP PLATFORMS

Banks of electronic equipment and personnel operating this equipment require shock protection on certain aboveground floor levels of the structures. Various combinations of individually shock-isolated platforms and base-mounted vs pendulum-mounted isolation systems were considered. A spring-suspended group platform was found to afford the most effective protection.

A typical platform framing plan is shown in Fig. 2. The six hanger locations required to suspend the platform are indicated. This system provides protection for the equipment and for personnel in any posture, standing or sitting, and is adaptable for the different quantities and layouts of equipment existing on the various floors. Moreover, future changes in equipment layout can be accomplished with the use of ballast and spring adjustments. A minimum horizontal clearance, between the platform and the cylinder wall, of 10 in. is provided for horizontal displacements. Figure 3 illustrates a section through an edge of the platform. The platform framework is 8 in. deep with a steel plate subfloor covered by a tile finish. Three inches of vertical clearance is provided to accommodate the dynamic motion and variations in the static displacement. Power lines and other

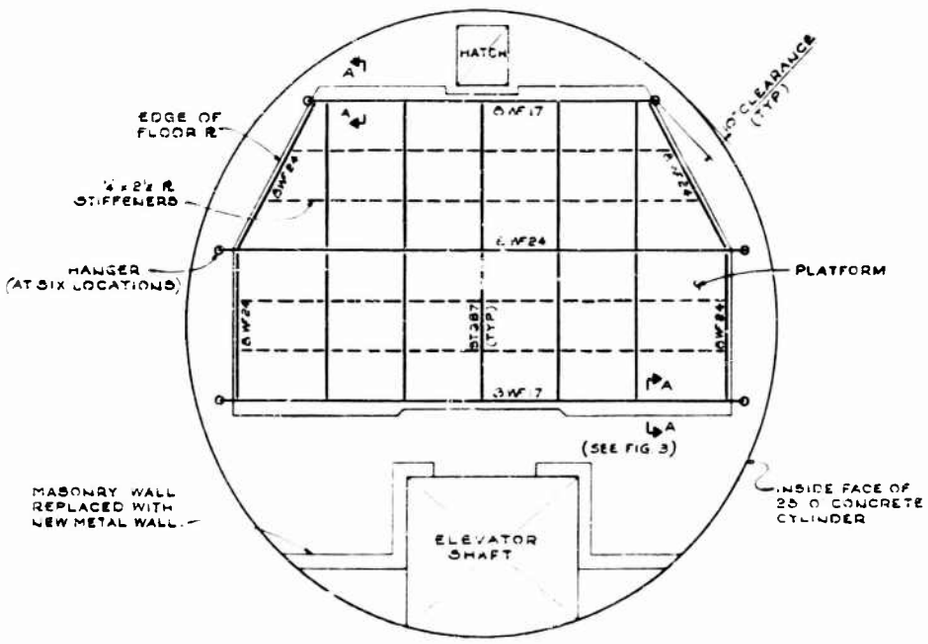

Fig. 2. Typical platform framing plan

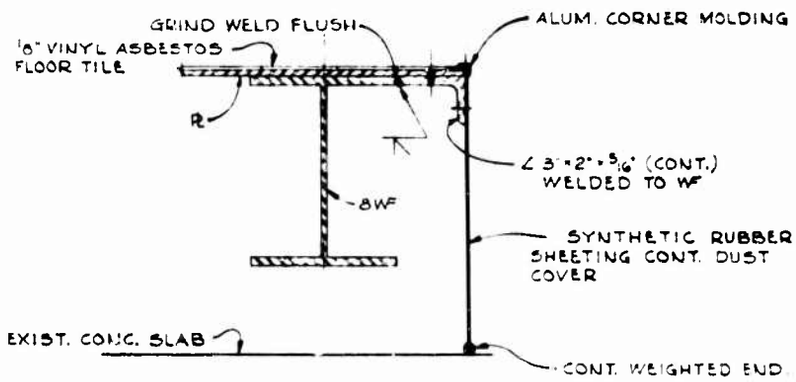

Fig. 3. Section through edge of platform

conduit connected to equipment mounted on the platform have been provided with flexible connections to allow for free movement of the platform.

Figure 4 shows a typical platform hanger detail. Under the dead and live loads, a point attachment of the suspension rods to the slab above would result in an overstress in the slab. Thus, it was necessary to distribute each hanger reaction over a length of about 3 ft. The shackles provide a hinge at the top and bottom of each hanger, thereby assuring perfect pendulum action. The low pendulum frequencies (about 0.3 cps) result in considerable attenuation of the horizontal structure accelerations (platform responses less than 0.5 g). Soft helical compression springs are provided to obtain vertical frequencies, varying from 1 to 1.5 cps, which limit the vertical component of acceleration to less than 1 g at all points on the platform. These frequencies are below the frequencies of the concrete structure, and resonance does not occur; special damping devices are not required.

The dynamic analysis to calculate the response of the suspended platform involved a modal analysis for shock motions acting in a vertical plane passing through the center of gravity. The equipment-platform system was considered as a rigid body attached to the structure with flexible supports. The shock environment at the points of attachment to the structure was as specified by the vertical, horizontal, and rotational spectra. The dynamic system comprises six degrees of freedom: a vertical mode, two translational modes, two rocking modes, and a twisting mode. The twisting mode is not activated since the shock motion passes through the center of twist. Similar analyses were performed for the other spring-mounted equipment described below.

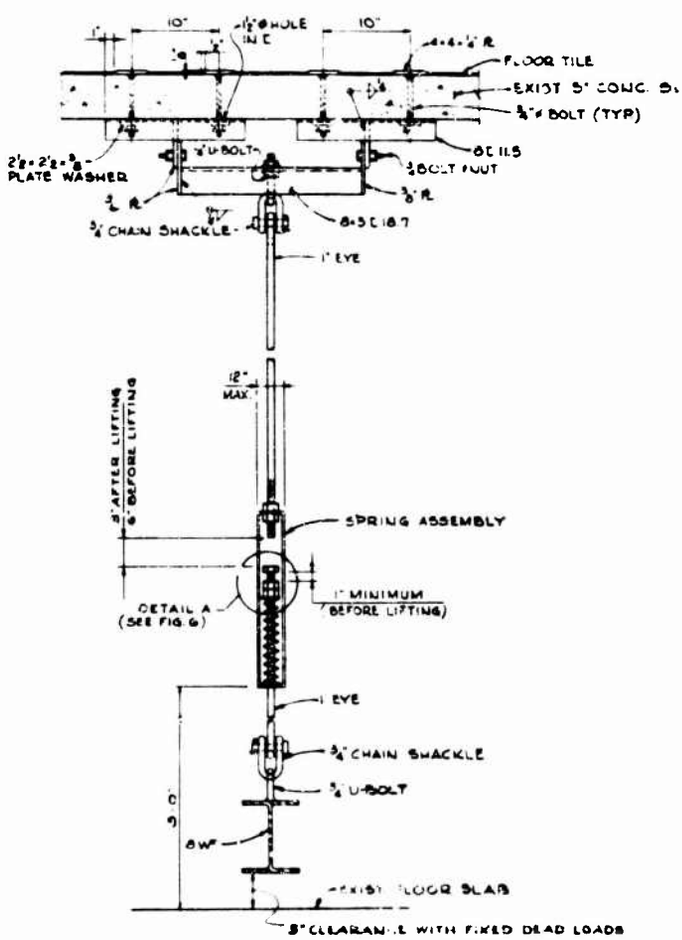

Fig. 4. Typical platform hanger detail

For a platform on any particular floor, each of the six springs has the same spring properties, which further effects a nearly uniform distribution of load to the slab above. The spring design and dynamic analyses were based on the assumption that the location of the center of gravity in its horizontal plane coincides with the center of vertical stiffness of the springs. The equipment layout on each platform has been prearranged (refer to Fig. 5 for example layout) so that the center of gravity is as close to the center of stiffness as practicable. The ballast indicated is used to correct eccentricities.

After the equipment is placed on the platform, the platform will be lifted by turning the adjusting nut (Figs. 4 and 6) on the spring assemblies until the necessary vertical clearance is obtained. To assure that a true dynamic balance exists, the ballast is adjusted until each spring is compressed the same amount. Figure 6 shows the calibrator used to read the compression in each spring.

The springs were designed so that the platform-suspension system has the proper dynamic properties under the present equipment

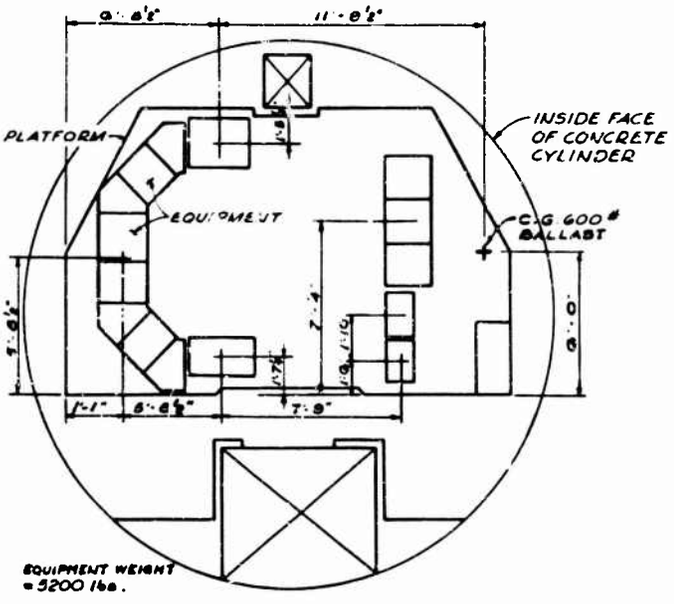

Fig. 5. Example of equipment layout on platform

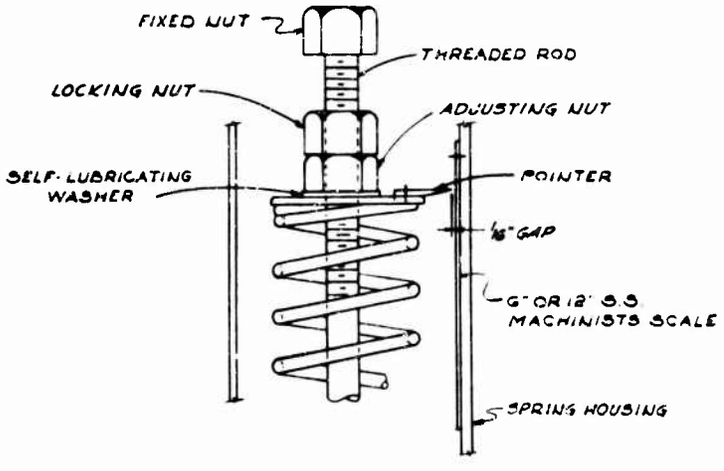

Fig. 6. Detail of platform lifting mechanism

weight, and also for a 25 percent excess weight represented by future additions. If equipment weight is reduced, ballast will be used to maintain the required frequencies. Figure 7 is a detail of the typical platform ballast. It is seen that increments of weight can be removed or added as necessary to accommodate future changes in equipment and to provide a further means for balancing the system.

INDIVIDUAL SPRING-MOUNTED EQUIPMENT

Certain items of equipment requiring shock isolation cannot be placed conveniently on the group platforms, or are located on floors where group platforms are not required. In these cases individual spring-mounted conceptions, either wall or ceiling mounted, were designed.

Figure 8 illustrates a typical ceiling-suspended configuration as shown for an air-conditioning unit originally rigid mounted to the ceiling. The unit is bolted to a support framework hung from the ceiling with four wire-rope hangers, which provide a pendulum suspension system for attenuation of horizontal accelerations. Compression springs shown in Fig. 9 are used for isolation of vertical motion. Conventional high-frequency isolators have been provided to attenuate the transmission of vibration and noise caused by the air conditioner itself. Rotational effects resulting from the large vertical eccentricity of the center of gravity with respect to the pendulum attachment points of the unit were considered in the spring design. Vertical and horizontal clearance and flexible utility lines are provided for the dynamic displacements expected.

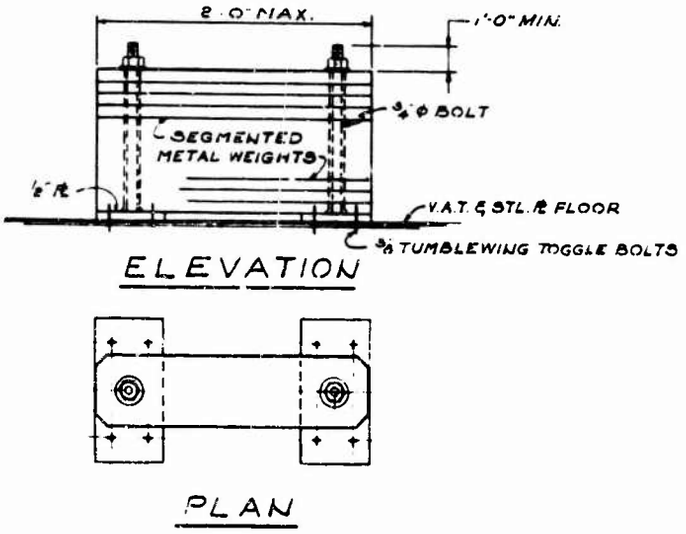

Fig. 7. Typical platform ballast detail

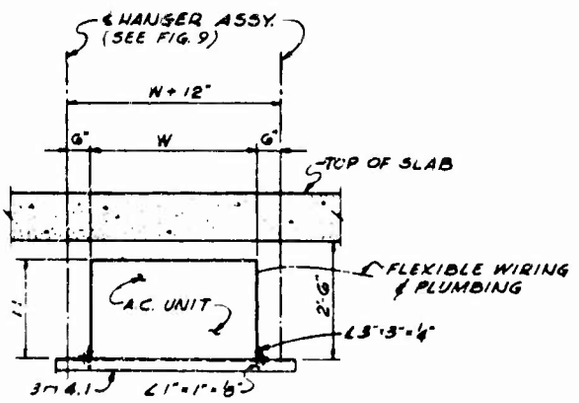

Fig. 8. Air conditioner shock mounting

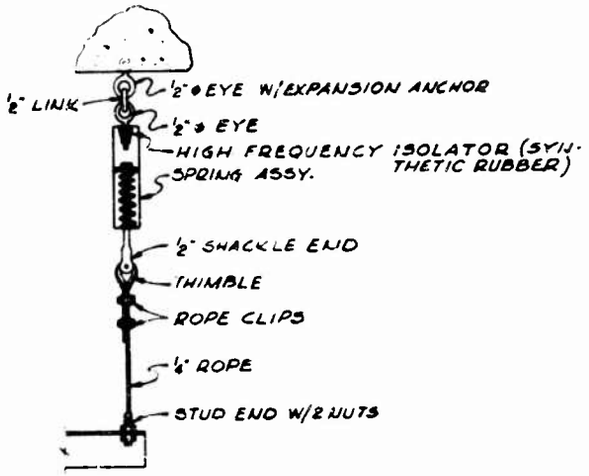

Fig. 9. Air conditioner hanger detail

Figure 10 shows a spring-suspended electric service panel bracketed off the wall. This panel contains miscellaneous items requiring shock isolation, including telephone, speaker box, thermostat, alarm bell, blast horn, air-conditioner control, and lighting circuit-breaker panel box. These items were originally at different locations on each floor. Four suspension hangers similar to that shown in Fig. 9 are used, without the high-frequency isolators.

Figure 11 illustrates a typical ceiling-mounted scheme used for shock isolating storage items so that they can be lowered to the floor when the items are to be used. In this case a single spring hanger was sufficient to attenuate the accelerations. The suspension point is located near the center of the cylinder to minimize, or completely eliminate, the effect of direct rotational motion of the structure.

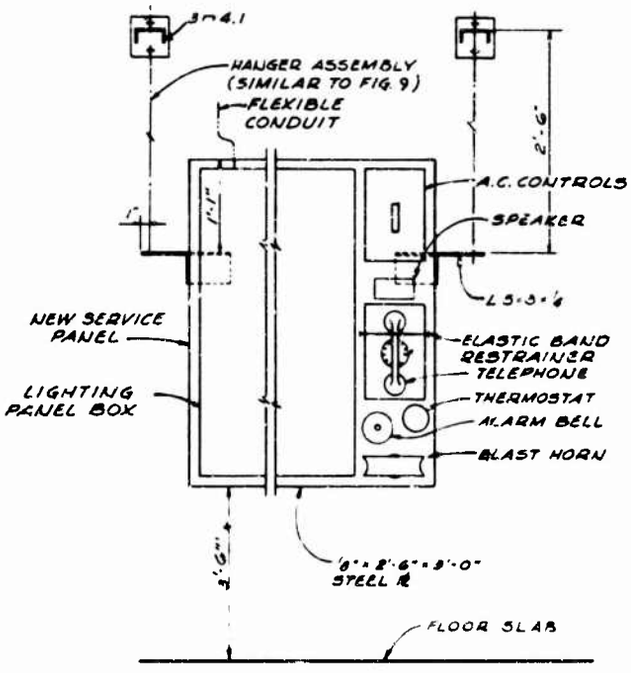

Fig. 10. Service panel shock mounting

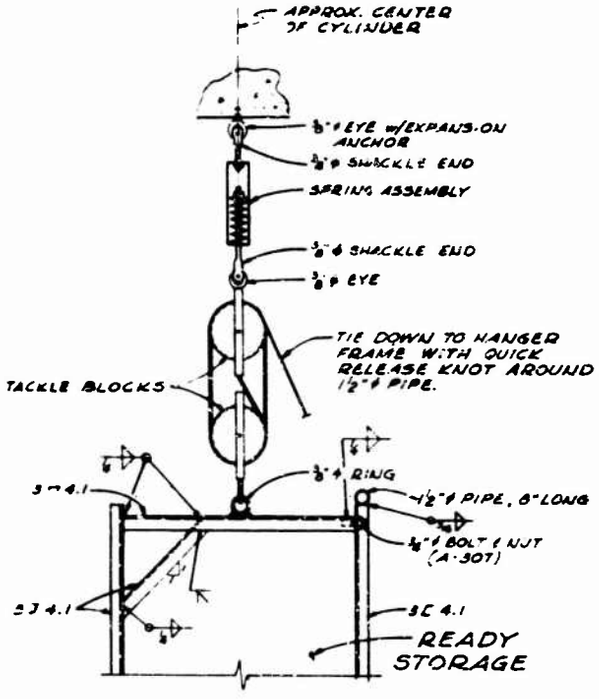

Fig. 11. Detail of overhead storage shock mounting

RIGID-MOUNTED ITEMS, RUGGEDIZED REPLACEMENTS, AND PADDING

Rigid-Mounted Items

Various equipment items and piping and conduit do not require shock isolation (spring mountings), but their connection to the structure walls or floors must be strengthened to resist acceleration forces, to reduce span lengths, and, in some cases, to maintain stability. Some of the contents of the structures can be damaged without impairing the operation of the facility, and the only protective requirement was to restrain these items to prevent damage or injury caused by impact with nearby critical equipment or personnel. Other items which are inherently rugged enough not to be damaged will also be anchored or restrained to prevent impact damage.

Water coolers, heavy tools, fire extinguishers, pressure tanks, etc., will be clamped or strapped to the cylinder wall. All of these items, except the water coolers, are sufficiently rugged not to be damaged by the direct acceleration forces. Damage to the water cooler can be tolerated, since the cutoff valves to the coolers will be turned off during an emergency period, thereby preventing flooding. Figure 12 shows a typical rigid mounting for an electric water cooler. It is necessary that the water cooler, and the other rigid-mounted items, be mounted to the main concrete cylinder wall rather than to an interior partition wall, which could not resist the horizontal acceleration forces required to restrain the water cooler.

To prevent breakage or disconnection of rigid piping and conduit, additional clamps and hangers are required. To provide the necessary protection, heavy-duty supports generally have been specified. Where piping is directly up against the wall or ceiling, rubber padding is used between the structure and the piping to prevent local shock damage. Existing faucets will be removed from sinks and lavatories and will be wall mounted above the units to prevent possible damage to the piping.

Ruggedized Replacements

For certain existing items which would be damaged by the shock, the most practicable solution is to use ruggedized replacements capable of resisting the acceleration forces without special shock-isolation devices. The existing masonry or plaster walls surrounding

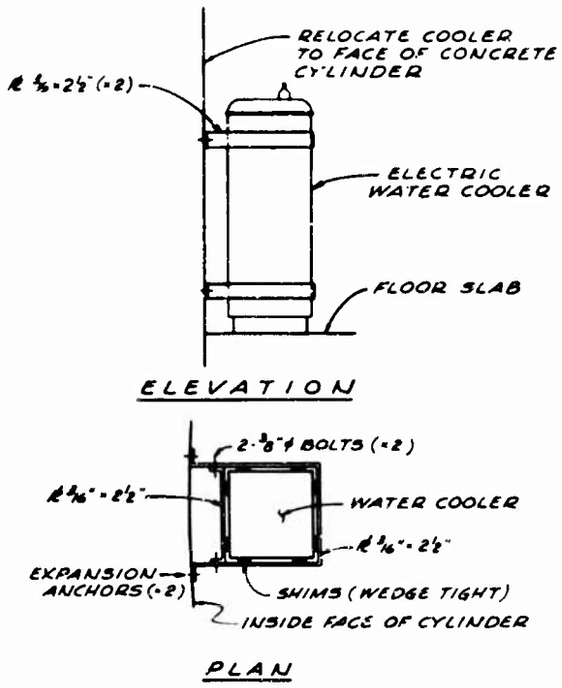

Fig. 12. Typical rigid mounting for water cooler

the elevator shaft are too stiff and weak to resist the high lateral acceleration forces without developing serious damage which would interfere with the postattack operation of the elevator and also cause damage to adjacent equipment. On the middle to upper floors, these walls (Fig. 2) will be replaced with stronger, lighter, more flexible metal units.

Existing vitreous china water closets and lavatories on certain floors require shock isolation to prevent damage. A spring mounting was considered, but it would be too flexible for normal use. These units will be replaced with aluminum units capable of resisting the acceleration forces. Where incandescent light are used on the upper floors, the standard lamps will be replaced with a shock-resistant type.

Padding for Personnel Protection

Personnel on the middle and upper floors will be protected on the group platforms. On the underground levels, the shock environment is sufficiently low so that general protection is not required. However, as a precaution to protect against possible injury resulting from impact with adjacent sharp edges, energy-absorbing padding will be added.

* * *

* U.S. GOVERNMENT PRINTING OFFICE 1960 O—289 460